

Durham E-Theses

Probing the Electronic Structure and Dynamics of Anions in the Gas Phase

ANSTOTER, CATE,SARA

How to cite:

ANSTOTER, CATE,SARA (2019) *Probing the Electronic Structure and Dynamics of Anions in the Gas Phase*, Durham theses, Durham University. Available at Durham E-Theses Online:
<http://etheses.dur.ac.uk/13313/>

Use policy

The full-text may be used and/or reproduced, and given to third parties in any format or medium, without prior permission or charge, for personal research or study, educational, or not-for-profit purposes provided that:

- a full bibliographic reference is made to the original source
- a [link](#) is made to the metadata record in Durham E-Theses
- the full-text is not changed in any way

The full-text must not be sold in any format or medium without the formal permission of the copyright holders.

Please consult the [full Durham E-Theses policy](#) for further details.

Probing the Electronic Structure and Dynamics of Anions in the Gas Phase

A thesis submitted in partial fulfilment for the degree of Doctor of
Philosophy in Chemistry

Cate Sara Anstöter
Department of Chemistry
Durham University

2019

This thesis is dedicated to my Grandad

William Leathem

who remains my biggest cheerleader

despite having no idea what I'm talking about

CONTENTS

1.	
INTRODUCTION.....	11
1.1 ANIONS IN THE GAS PHASE.....	11
1.2 PRINCIPLES OF PHOTOELECTRON SPECTROSCOPY	14
1.2.1 VELOCITY MAP IMAGING.....	18
1.2.2 PHOTOELECTRON ANGULAR DISTRIBUTIONS	18
1.3 ADVANCES IN ANION PHOTOELECTRON SPECTROSCOPY	21
1.3.1 ELECTROSPRAY IONISATION	21
1.3.2 IMPROVING ENERGY RESOLUTION	22
1.4 EXCITED STATES OF ANIONS	23
1.4.1 NON-VALENCE STATES	24
1.4.2 RESONANCES	26
1.4.3 FATES OF EXCITED STATES	27
1.4.4 TWO-DIMENSIONAL PHOTOELECTRON IMAGING	28
2 THEORETICAL CONSIDERATIONS.....	35
2.1.1 THE HARTREE-FOCK APPROXIMATION	37
2.1.2 POST HARTREE-FOCK METHODS	39
2.1.3 NOTE ON THE CHOICE OF BASIS SET	43
2.1.4 MULTICONFIGURATIONAL SCF.....	45
2.1.5 DENSITY FUNCTIONAL THEORY.....	54
2.1.6 THE DIFFICULTIES OF ANIONS AND RESONANCES.....	55
2.1.7 THEORETICAL TREATMENTS OF NON-VALENCE STATES	57
2.1.8 CONCLUDING REMARKS	58
2.2 AIMS.....	59
2.3 REFERENCES	60
METHODS: FREQUENCY-, ANGLE- AND TIME-RESOLVED PHOTOELECTRON SPECTROSCOPY AND ELECTRONIC STRUCTURE CALCULATIONS	65
3 GAS-PHASE PHOTOELECTRON SPECTROSCOPY OF ANIONS	67
3.1 THE ELECTROSPRAY IONISATION SOURCE MACHINE	67
3.1.1 GENERATION OF ANIONS	67
3.1.2 SELECTION OF ANIONS.....	68
3.1.3 DETECTION OF ANIONS	69
3.1.4 IMAGING PHOTOELECTRONS	71
3.1.5 CALIBRATING PHOTOELECTRON IMAGES: Γ^-	72
3.2 LASER SYSTEM	73
3.3 THE CLUSTER MACHINE	75
4 ELECTRONIC STRUCTURE CALCULATIONS: A COMPUTATIONAL TOOLKIT	76

4.1	VERTICAL DETACHMENT ENERGY	79
4.2	ADIABATIC DETACHMENT ENERGY	80
4.3	SIMULATING PHOTOELECTRON SPECTRA.....	80
4.4	EXPLORING THE GROUND STATE POTENTIAL ENERGY SURFACE	81
4.5	MODELLING PHOTOELECTRON ANGULAR DISTRIBUTIONS	82
4.6	EXCITED STATE CALCULATIONS.....	82
4.7	NON-VALENCE STATES	83
4.7.1	BINDING ENERGIES OF DIPOLE BOUND STATES	83
4.8	REFERENCES.....	84
5	RESULTS.....	87
SECTION A PHOTOELECTRON ANGULAR DISTRIBUTIONS		87
5.1	TESTING THE SENSITIVITY OF THE DYSON ORBITAL APPROACH.....	88
5.2	THE SENSITIVITY OF PHOTOELECTRON ANGULAR DISTRIBUTIONS TO MOLECULAR CONFORMATIONS OF A SERIES OF PARA-SUBSTITUTED PHENOLATES	93
5.2.1	INTRODUCTION	93
5.2.2	METHODOLOGY	94
5.2.3	FREQUENCY- AND ANGLE-RESOLVED PHOTOELECTRON SPECTRA	95
5.2.4	PHOTOELECTRON ANGULAR DISTRIBUTIONS AS A PROBE OF CONFORMATION.....	99
5.2.5	EXPLORING THE POTENTIAL ENERGY SURFACE OF pEtPh ⁻	101
5.2.6	RELATING THE CONFORMATIONAL FREEDOM TO PHOTOELECTRON ANGULAR DISTRIBUTIONS.....	104
5.2.7	CONCLUSIONS	105
5.3	PROBING WAVEPACKET MOTION ON THE BOUND EXCITED STATE OF A PYP CHROMOPHORE.....	107
5.3.1	INTRODUCTION	107
5.3.2	METHODOLOGY	112
5.3.3	TIME-RESOLVED PHOTOELECTRON SPECTRA	115
5.3.4	EXPLORATION OF THE S ₁ POTENTIAL ENERGY SURFACE	119
5.3.5	INTERPRETING WAVEPACKET MOTION ON THE S ₁ SURFACE.....	120
5.3.6	TIME-RESOLVED PHOTOELECTRON ANGULAR DISTRIBUTIONS	123
5.3.7	CONCLUSIONS AND FURTHER WORK	126
5.4	SECTION A CONCLUSIONS AND OUTLOOK	126
5.5	REFERENCES.....	128
SECTION B EXCITED STATE DYNAMICS		131
5.6	A BOTTOM-UP HÜCKEL PICTURE OF THE EXCITED STATES OF PHOTOACTIVE PROTEINS	132
5.6.1	INTRODUCTION	132
5.6.2	METHODOLOGY	134
5.6.3	FREQUENCY- AND ANGLE-RESOLVED PHOTOELECTRON SPECTRA	135
5.6.4	WHAT THE HÜCK?	139
5.6.5	EXTENSION TO EXCITED STATE DYNAMICS OF BIOCHROMOPHORES	145
5.6.6	CONCLUSIONS.....	147

5.7	ELECTRONIC STRUCTURE AND DYNAMICS OF THE PARA-DINITROBENZENE ANION	148
5.7.1	INTRODUCTION	148
5.7.2	METHODOLOGY	150
5.7.3	FREQUENCY- AND ANGLE-RESOLVED PHOTOELECTRON SPECTRA	153
5.7.4	MODELLING RESONANCES USING XMCQDPT2	155
5.7.5	EVIDENCE FOR EXCITED STATE DYNAMICS IN pDNB ⁻	157
5.7.6	PHOTODISSOCIATION OF NO ₂ ⁻	160
5.7.7	CONCLUSIONS	164
5.8	SECTION B CONCLUSIONS AND OUTLOOK	165
5.9	REFERENCES	166
	SECTION C NON-VALENCE STATES	169
5.10	INVESTIGATING THE STRENGTH OF THE ANION-II BOND	170
5.10.1	INTRODUCTION	170
5.10.2	METHODS	171
5.10.3	INDIRECT MEASUREMENT OF THE ANION-II BOND WITH PHOTOELECTRON SPECTROSCOPY	172
5.10.4	DETERMINING THE STRENGTH OF THE ANION-II BOND	173
5.10.5	DISENTANGLING THE CONTRIBUTIONS TO THE ANION BINDING ENERGY	176
5.10.6	CONCLUSIONS	178
5.11	THE NITROBENZENE ANION: 2D PHOTOELECTRON AND ELECTRON ENERGY LOSS SPECTROSCOPY STUDY	179
5.11.1	INTRODUCTION	179
5.11.2	METHODOLOGY	180
5.11.3	COMPARISON OF 2D PHOTOELECTRON AND ELECTRON ENERGY LOSS SPECTRA	183
5.11.4	INTERPRETING STRUCTURED LOW ENERGY ELECTRON EMISSION	185
5.11.5	MODE-SPECIFIC VIBRATIONAL AUTODETACHMENT	191
5.11.6	CONCLUSIONS	195
5.12	PROBING THE DIPOLE BOUND STATE OF A NOVEL ORGANIC ANION	195
5.12.1	INTRODUCTION	195
5.12.2	METHODOLOGY	196
5.12.3	GAS-PHASE SYNTHETIC CHEMISTRY	198
5.12.4	EVIDENCE OF A DIPOLE BOUND STATE?	202
5.12.5	CONCLUSIONS	208
5.13	SECTION C CONCLUSIONS AND OUTLOOK	208
5.14	REFERENCES	209
6	CONCLUSION AND OUTLOOK	213

Declaration

The material contained within this thesis has not previously been submitted for a degree at Durham University or any other university. The research reported within this thesis has been conducted by the author unless indicated otherwise.

Copyright Notice

The copyright of this thesis rests with the author. No quotation from it should be published in any format, including electronic and the internet, without the author's prior written consent. All information derived from this thesis must be acknowledged appropriately.

Acknowledgements

I would like to begin by thanking my supervisor, Jan, for his excellent supervision, constantly supplying me with requests for ‘quick and easy’ calculations, and for allowing me to abscond to Moscow on multiple occasions. Thank you not only for your support and guidance over the past few years, but also for being a good F&B.

I would also like to extend my thanks over to my incredibly welcoming surrogate group at Moscow State University, especially to Anastasia, who has provided friendship and many Russian adventures, as well as vastly improving my understanding of quantum chemistry.

Special thanks also go to past and present members of the Verlet group, specifically; Josh for his help with collecting experimental data, explaining the inner workings of the machines and his friendship outside of the office; James for his wisdom and insight into both experiment and theory; and Golda for retaking data for me and her extensive working knowledge of KUWTK. I would also like to thank Basile for coffee, scientific chats and his advice over the past few years.

My final academic thank you goes to Patrick Fowler, for inspiring, supporting and encouraging me.

Outside of work, I would like to thank my family and friends for providing me with chemistry free entertainment. To my Mam, for her support in all things I do, and my sisters, Sophie and Lucy, thank you for always being there. Special thanks also go to Blinky, Pal, Hannah and Tanor for chatting nonsense whenever I needed a break. To my husband Tom, thank you for everything you do, including but not limited to listening to me harp on about dipole bound states and feeding me. Finally, to my daughter Odette, for whom I do everything for and ensures any academic achievements pale in comparison, thank you for making me appreciate there are more important things in life than electrons.

Publications

Parts of this thesis are based on the following publications:

1. C. S. Anstöter, J. N. Bull and J. R. R. Verlet
Ultrafast dynamics of temporary anions probed through the prism of photodetachment
Int. Rev. Phys. Chem. **35**, 509 (2016)
2. C. S. Anstöter, C. R. Dean and J. R. R. Verlet
Sensitivity of photoelectron angular distributions to molecular conformations of anions
J. Phys. Chem. Lett. **8**, 2268 (2017)
3. C. S. Anstöter, C. R. Dean and J. R. R. Verlet
Chromophores of chromophores: a bottom-up Hückel picture of the excited states of photoactive proteins
PCCP **19**, 29772 (2017)
4. C. S. Anstöter, T. E. Gartmann, L. H. Stanley, A. V. Bochenkova and J. R. R. Verlet
Electronic structure of the para-dinitrobenzene radical anion: A combined 2D photoelectron imaging and computational study
PCCP **20**, 24019 (2018)
5. C. S. Anstöter, J. P. Rogers and J. R. R. Verlet
Spectroscopic Determination of an Anion- π Bond Strength
J. Am. Chem. Soc. **141**, 6132 (2019)

Additional publications:

6. C. S. Anstöter, C. W. West, J. N. Bull and J. R. R. Verlet
The Vitamin E radical probed by anion photoelectron imaging
J. Phys. Chem. B **120**, 7108 (2016)
7. L. H. Stanley, C. S. Anstöter and J. R. R. Verlet
Resonances of the Anthracenyl anion probed by frequency-resolved photoelectron imaging of collision-induced dissociated anthracene carboxylic acid
Chem. Sci. **8**, 3054 (2017)
8. J. P. Rogers, C. S. Anstöter and J. R. R. Verlet
Ultrafast dynamics of low-energy electron attachment via a correlation-bound state
Nature Chem. **10**, 341 (2018)
9. J. P. Rogers, C. S. Anstöter and J. R. R. Verlet
Evidence for Electron Capture of an Outgoing Photoelectron Wave by a Non-Valence State in $(\text{C}_6\text{F}_6)_n^-$
J. Phys. Chem. Lett. **9**, 2504 (2018)
10. J. P. Rogers, C. S. Anstöter, J. N. Bull, B. F. E. Curchod and J. R. R. Verlet
Photoelectron Spectroscopy of the Hexafluorobenzene Cluster Anions: $(\text{C}_6\text{F}_6)_n^-$ $n=1-5$ and $\Gamma\text{C}_6\text{F}_6$
J. Phys. Chem. A **123**, 1602 (2018)
11. J. N. Bull, C. W. West, C. S. Anstöter, G. da Silva, E. J. Bieske and J. R. R. Verlet
Ultrafast Photoisomerization of an Isolated Retinoid
PCCP **21**, 10567 (2019)

Abstract

The electronic structure and dynamics of a number of anions in the gas phase have been investigated through joint experimental and computational methods. Photoelectron imaging was used to obtain both frequency-, time- and angle-resolved photoelectron spectra. Quantum chemistry calculations modelled different experimental parameters and provided insight into the complex photoelectron signatures observed. A particular emphasis on advancing the understanding and interpretation of the photoelectron angular distributions in both the frequency- and time-domain was made.

The need for caution and understanding of the considerations one needs to make, and the requirement to be flexible with the theoretical model used to interpret a specific problem are presented. This was emphasized throughout the results section, where the complexity of models required ranged from a simple Hückel model to a multi-configurational multi-reference model. An analysis of the sensitivity of the parameters used in the calculation of photoelectron angular distributions with the Dyson orbital approach was presented.

The results were presented within three broad themes. Section A presented results in which the photoelectron angular distributions were modelled and interpreted to give novel insight into the character and structure of the molecular anions investigated. Analysis of the photoelectron angular distributions was presented both in the frequency- and time-domain. Section B presented studies in which the ‘bottom-up’ approach was used to elucidate information on the structure-function dynamics of small components of more complex systems. Finally, Section C presented results in which the prevalence and importance of non-valence states were probed.

.

1. Introduction

1.1 Anions in the Gas Phase

An anion is an atom or molecule that has a net negative charge. This means the physical and chemical properties of an anion are inherently different from those of neutral molecule and cations. For example, the negative charge of an anionic species will perturb the chemical environment differently to neutral or cations and will interact with the opposite orientation of the dipole moment of a molecule or solvent system.

From an electronic structure point of view, an anion is created through the addition of an electron to an unfilled or partially filled atomic or molecular orbital. The excess electron is bound by an attractive potential that is qualitatively different from that of neutral and cationic species, resulting in a valence electron density that is weakly bound. The difference in energy between the neutral and anionic species is known as the electron affinity (EA) and is a direct measure of the stability of the anion. If the EA of a molecule is positive, then the anion formed is stable with respect to electron loss. When an anion has a negative EA, the anionic species may still survive long enough to be detected experimentally. Such anions are referred to as being metastable, as spontaneous electron loss to form the neutral parent plus a free electron is always an open channel (autodetachment). The electron affinity of a molecule represents a key physical parameter: its importance is not limited to gas phase spectroscopy but extends to many research areas ranging from astrochemistry, to material science and to biology, where electron transfer pathways are ubiquitous.

The accurate determination of EAs proved difficult prior to 1970.^{1,2} The most direct experimental techniques to measure electron affinities involve using a tunable light source, $h\nu$, to photodetach an electron from an atomic or molecular anion, A^- . The minimum $h\nu$ needed to detach an electron and form the neutral is equivalent to the electron affinity. Major improvements in laser sources and photodetachment spectroscopy techniques led to a wealth

of studies and brought the number of measured electron affinities from tens to hundreds of anionic systems.³ For example, whereas electron capture or ion-molecule reaction strategies in the 1960s and 1970s might claim accuracy of 10-20%, laser photodetachment spectroscopy (especially on cold targets) can routinely claim accuracy of better than 1%.

Accurate determination of electron affinities is most effective when using experimental methods that employ the photoelectric effect.^{4,5} The photoelectric effect states that when an incident photon, $h\nu$, has energy equal to or exceeding the electron affinity of an anionic species then an electron will be photodetached;



It is typically far easier to photodetach an electron from an anion than to photoionise a neutral species because EAs are generally lower than ionisation potentials.

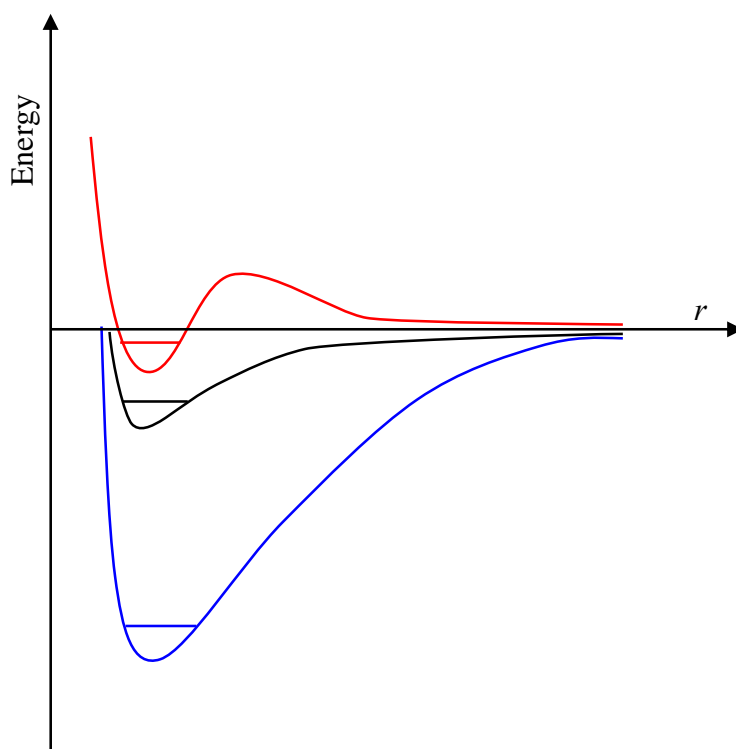


Figure 1 Qualitative description of effective potentials experienced by valence electrons in neutrals and cations (blue), singly charged anions (black), and multiply charged anions (red). The potentials are as a function of the electron-nuclear distance between the excess electron and the parent species, r .

The valence electrons in anions experience very different potential energies compared with those of neutrals and cations, Figure 1. Specifically, in the asymptotic regions where the distance between the electron and the nuclear core (r) is large, electrons in the valence regions of anions experience no net Coulomb attraction. However, the corresponding electrons of a neutral or cationic system do experience net Coulomb attraction ($-Ze^2/r$). For singly charged anions the longest-range attractive potentials arise from charge-dipole $(-\boldsymbol{\mu} \cdot \mathbf{r}e/r^3)$, charge-quadrupole $(-\mathbf{Q} \cdots (\mathbf{3}\mathbf{r}\mathbf{r} - r^2\mathbf{1})e/3r^5)$, and charge induced-dipole $(-\boldsymbol{\alpha} \cdots \mathbf{r}e^2/2r^6)$ potentials, where \mathbf{r} is the position vector of the excess electron and $\boldsymbol{\mu}$, \mathbf{Q} and $\boldsymbol{\alpha}$ are the dipole moment vector, quadrupole moment tensor, and polarizability tensor of the corresponding neutral molecule, respectively, and $\mathbf{1}$ is the unit tensor. The most important consequence of this is that the large- r attractive potential falls off as $-Ze^2/r$ for neutral and cations, whereas it falls off as a higher power of $1/r$ for anions. It is these differences that are responsible for the major differences in radial size, electron binding energy and pattern of bound electronic states of anion, compared to neutrals and cations. At shorter range, inner valence-range potentials also have regions of space where the extra electron experiences net attraction to the nucleus leading to overall binding.

Experimentally it is advantageous to work with anions for two principal reasons: firstly, the weaker binding of the excess electron (e.g. $< 4\text{eV}$) means that their photophysics can be probed with visible or near-UV light; and secondly, anions of a single mass to charge ratio (m/z) can be easily isolated using mass spectrometry.

Anion photoelectron spectroscopy is a versatile technique that allows the study of the neutral by means of photodetachment from the parent anion. Many pioneering studies of atomic and molecular anions by photoelectron spectroscopy were performed by the research group of Carl Lineberger at JILA.^{6,3,7-10} Photoelectron spectroscopy was showcased as a means of extracting accurate electron affinities, as well as vibrational information of both the anion and

neutral species. Studies from Lineberger's group have laid the foundations for many of the experimental techniques used throughout the experimental section of this thesis.

1.2 Principles of Photoelectron Spectroscopy

Photoelectron spectroscopy is an electronic spectroscopic technique based upon the photoelectric effect described in equation 2. The liberated photoelectrons are collected and recorded with respect to their electron kinetic energies (eKE). The electron affinity is then determined as the difference in energy between the incident photon, $h\nu$, and the eKE of the electron detached from the ground vibrational state of the anion to form the ground vibrational state of the neutral

$$EA = h\nu - eKE(0,0). \quad (2)$$

In photoelectron spectroscopy, the electron affinity is also referred to as the adiabatic detachment energy (ADE).

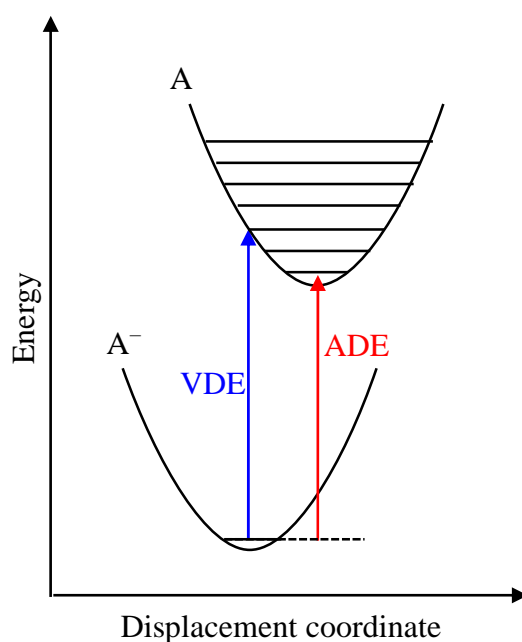


Figure 2 Qualitative diagram of the potential energy surfaces for a molecular anion, A^- , and its neutral counterpart, A . The transitions shown represent the adiabatic detachment energy (ADE), or electron affinity, and the vertical detachment energy (VDE).

The electron affinity represents the minimum energy required to produce a photoelectron, however, at higher $h\nu$ photoelectrons will still be produced. As $h\nu$ increases above the energetic threshold for photodetachment, the excess energy will be conserved in the electron kinetic energy (eKE), which must be equal to the difference in energy of $h\nu$ and the binding energy of the electron (eBE),

$$\text{eKE} = h\nu - \text{eBE} . \quad (3)$$

As $h\nu$ increases, different energies of the neutral state can be probed (Figure 2). The removal of an electron from the parent anion causes a change in electron density, which consequently requires a change in the geometry of the corresponding neutral species as shown by the horizontally displaced potential energy curves in Figure 2. The difference in energy between the minimum energy geometry of the anion and neutral at the equilibrium geometry of the anion is the vertical detachment energy (VDE). It is extracted experimentally by identification of the peak with highest intensity.

The magnitude of change in geometry between the anion and neutral can often be inferred by the difference in adiabatic and vertical detachment energies. In systems with a substantial change in geometry between the anion and neutral species, there may be no overlap of the ground vibrational level wavefunctions. In such a case, the adiabatic detachment energy cannot be observed in the spectrum.¹¹ Conversely, for systems with little change between the anion and neutral geometries, the adiabatic and vertical detachment energies are similar and only a single transition will be visible.

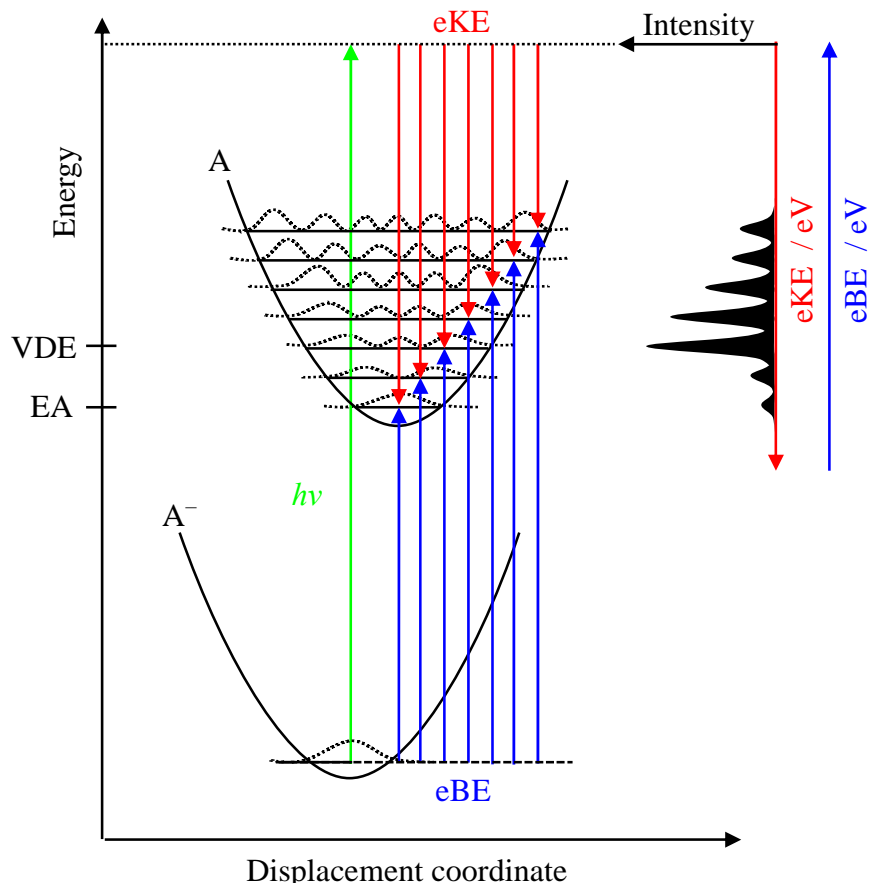


Figure 3 Schematic of photodetachment from an anionic species, A^- , to form the corresponding neutral, A , following absorption of a photon of light, $h\nu$. The photoelectrons originate from an initial ground state vibrational state in the anion, and photodetach to form various final vibrational states in the neutral. The kinetic energy of the photoelectron, eKE , is detected, and from this the binding energy, eBE , of the transition can be determined. The intensity of the specific vibronic transition is determined by the Franck-Condon overlap of the initial vibronic wavefunction of the anion, ψ_v^i , and the final vibronic wavefunction of the neutral, ψ_v^f . The ADE is the peak with the highest eKE (lowest eBE), and the VDE is the peak with highest intensity.

Under the Born-Oppenheimer approximation (BOA) approximation,¹² the photodetachment process can be understood as the projection of an initial vibrational wavefunction, ψ_v^i , defined by the nuclear coordinates of the equilibrium geometry of the anion, onto the final states of the neutral, ψ_v^f . The overlap of the initial and final vibrational wavefunction is described by a Franck-Condon factor,¹³ $\left| \langle \psi_v^f | \psi_v^i \rangle \right|^2$, and governs the relative intensities of different vibrational levels of an electronic state observed in the photoelectron spectrum as shown in Figure 3. The vibrational quantum number may change for Franck-

Condon allowed transitions. In the case of totally symmetric vibrational modes, this may be $\Delta v = 0, \pm 1, \pm 2, \dots$. While for non-totally symmetric mode, this may be $\Delta v = 0, \pm 2, \pm 4, \dots$. Franck-Condon forbidden modes may also be observed in photoelectron spectra, arising through borrowed intensity from Herzberg-Teller vibronic coupling between electronic states or vibrational autodetachment mediated by an excited state of the anion.^{14,15}

For systems with a finite geometric change between the anion and neutral, a vibrational progression will be recorded in the photoelectron spectrum. This vibrational progression will appear as a series of narrow peaks, with discrete eKEs and an intensity modulated by the Franck-Condon overlap of the specific transition (Figure 3). When there is a change in geometry between the anion and neutral ground states, there may be specific vibrational modes that have large Franck-Condon factors that correspond to motion along the displacement vector that connect the two equilibrium geometries. Hence, the eKE and relative intensity of the outgoing electron contains a wealth of information about the electronic and vibrational structure of both the anion and neutral species.^{16–20}

Photoelectron spectroscopy has less stringent selection rules compared to other optical spectroscopic methods. Any neutral state can be formed by removal of an electron from an atomic or molecular orbital, providing there is sufficient energy for photodetachment, including states of the neutral that may have different multiplicities.

The cross-section, σ , of a photoelectron detached near threshold can be expressed by the Wigner threshold law,^{21,22}

$$\sigma \propto \text{eKE}^{l+1/2}, \quad (4)$$

where l is the angular momentum of the outgoing photoelectron wave.²³ This shows that as $\text{eKE} \rightarrow 0$, $\sigma \rightarrow 0$. Furthermore, at low eKE, low l partial waves will dominate.

1.2.1 Velocity Map Imaging

In addition to kinetic energies, photoelectron angular distributions relative to a linear polarisation axis of a light field can provide complimentary information about the character of the orbital from which the photoelectron is ejected. Both the kinetic energies and angular distributions of photoelectrons are provided in photoelectron imaging techniques.

Velocity Map Imaging is a technique developed by Chandler and Houston,²⁴ and refined by Eppink and Parker,²⁵ in order to measure the velocity of charged particles following a photoionisation/detachment event. In the case of photoelectron spectroscopy, a cloud of photoelectrons is produced following the irradiation of the anion with a laser pulse. VMI focusses charged-particles (the electrons) with a given velocity vector onto a specific point on a two-dimensional plane, irrespective of the origin of the charged particle within a relatively large photodetachment volume. As a velocity vector is probed using VMI, the collected data contains information regarding the speed (energy) and direction of the charged particle. The directional information is usually with respect to the linearly polarised light field used to photodetach the electron. In VMI, the Newton sphere of photoelectrons expands and is projected onto 2D detector.

VMI with photoelectron spectroscopy is an attractive pairing. It combines high collection efficiency with the ability to collect photoelectrons with low eKEs and allows for the measurement of photoelectron angular distribution.

1.2.2 Photoelectron Angular Distributions

The angular distribution of photoelectrons produced in a single-photon process by linear polarised light, has the general form²⁶

$$I(\theta) = \frac{\sigma}{4\pi} (1 + \beta_2 P_2 \cos(\theta)), \quad (5)$$

where θ is the angle of the ejected photoelectron relative to the polarisation axis of the light, σ is the total photodetachment cross section, $P_2 \cos(\theta)$ is the second-order Legendre polynomial, and β_2 is the unitless anisotropy parameter. The β_2 parameter is constrained to between the bounds of +2 and -1 and contains important information about the angular momentum of the photoelectron, and by extension the molecular orbital from which the electron was ejected from. The limiting values of β_2 correspond to a photoelectron angular distribution with a $\cos^2(\theta)$ or a $\sin^2(\theta)$ distribution relative to the polarisation vector, respectively.

The physical significance of the photoelectron angular distribution arises from consideration of the angular momentum of the selection rule. If the photoelectron is detached from an orbital for which l is a good quantum number, and the laser is linearly polarised, then the outgoing photoelectron angular distribution will have a momentum of $l \pm 1$.²⁷ Therefore, photodetachment from an s- or σ -like atomic or molecular orbital will produce an outgoing p-wave, of which the β_2 parameter will be positive up to the value of +2. In the case of an initial p- or π -type atomic or molecular orbital, the outgoing wave will yield a combination of s- and d-waves and the β_2 parameter will be negative, up to the value of -1. The β_2 parameter is energy dependent, because partial-wave cross sections are energy dependent and because the ultimate photoelectron angular distribution is determined by the phase between contributing partial waves which also changes with energy. In general, from the Wigner law, close to threshold, electrons with low angular momentum values dominate, giving rise to broadly isotropic photoelectron angular distributions.

1.2.2.1 Dyson Orbitals and Modelling Photoelectron Angular Distributions

The experimental β_2 parameter inherently contains information about the electronic structure and dynamics of the system the photoelectron is ejected from. It is desirable to be able to quantitatively or qualitatively model and interpret the complementary information encoded in the photoelectron angular distribution. Sanov *et al.* developed a non-perturbative model for predicting the energy dependent photoelectron angular distributions of molecular anions from a mixed *sp*-state, based on symmetry arguments.^{28–30} For molecular anions, l is not a rigorous quantum number as it is for atomic anions. In some cases, molecular orbitals may be approximated to atomic *s*-, *p*- or *d*-like functions and l is a good quantum number. In other cases, a single value of l is not sufficient. Instead, a superposition of two or more atomic-like orbitals should be used. The net observed photoelectron angular distribution from the *s-p* mixed model is an incoherent superposition of the distributions. Modelling the parent orbital as a linear combination of *s*- and *p*-states becomes less rigorous for large molecular systems.

Recently, progress has been made toward the development of a quantitative *ab initio* framework for predicting the photoelectron angular distributions by Krylov and co-workers.^{31–33} This electronic structure method uses the Dyson orbital approach to model the photoelectron angular distributions as a function of energy for a specific photodetachment channel. Conceptually, Dyson orbitals can be thought of as the one-electron wavefunction of the leaving electron, before photodetachment.^{34–37} For an anionic system, the Dyson orbital, $\Psi_{\text{Dyson}}(1)$, represents the overlap between an N electron molecular wavefunction and the N^{-1} electron wavefunction of the corresponding anion,

$$\Psi_{\text{Dyson}}(1) = \sqrt{N} \int \Psi_i^N(1, \dots, n) \int \Psi_f^{N-1}(2, \dots, n) d2 \dots dn, \quad (6)$$

where *i* and *f* refer to the initial and final states, respectively. As such, the molecular orbital from which the outgoing electron is ejected provides a good approximation of the Dyson

orbital. The photoelectron angular distributions can be predicted through calculation of the transition dipole moments between the Dyson orbital and a free electron, Ψ_k^{el} , with appropriate averaging of the molecular frame. This is achieved through calculation of the photoelectron dipole matrix element, D_k^{if} ,

$$D_k^{\text{if}} = \boldsymbol{\mu} \left\langle \Psi_{\text{Dyson}}(1) \left| \hat{r} \right| \Psi_k^{\text{el}} \right\rangle, \quad (7)$$

where k is the magnitude of the photoelectron wave vector \mathbf{k} , \hat{r} is the dipole moment operator and $\boldsymbol{\mu}$ is a unit vector in the direction of the polarisation of light.

The Dyson orbital approach has been applied in the results section of this thesis and was found to be relatively robust. However, the methodology has several limitations, foremost the inability to model photodetachment channels from states embedded in the anion continuum. Another limitation is the current treatment of the outgoing electron; for anions this is a plane wave, while for neutrals this is a Coulomb wave. These are first-order approximations, and do not take into account the physical properties of the parent core. The Dyson orbital approach may fail in cases where certain physical properties of the parent core are pronounced, for example a large dipole moment of the neutral core may influence the outgoing electron of an anionic system in ways that are not described by a simple plane wave.

1.3 Advances in Anion Photoelectron Spectroscopy

1.3.1 Electrospray Ionisation

There are many different methods that can be used to generate anions in the gas phase. Generally, the ion source chosen is dependent upon the type of ionic system one wants to probe experimentally. Molecular beam methods are commonly used to generate ions and clusters in the gas phase.³⁸ However, this method has limitations if one studies larger molecular species

because many such systems are not volatile and decompose upon heating. In order to study larger systems in the gas phase, a ‘soft ionisation’ technique is required.³⁹

‘Soft ionisation’ refers to a class of methods that produce anions with low internal energies, minimising fragmentation. One of the most commonly used soft ionisation techniques is electrospray ionisation (ESI). ESI has been developed into an invaluable tool allowing the study of large fragile complexes,^{40,41} paving the way for a number of studies on proteins and biomolecules,^{42–47} and more exotic charged species, such as multiply-charged anions.^{48–51} The latter is not readily achievable through hard ionisation methods, due to Coulombic repulsion.

1.3.2 Improving Energy Resolution

Historically, photoelectron imaging has been limited by the energy resolution of eKE detection and high internal temperatures of molecular anions. The original Eppink-Parker VMI design reported an energy resolution of $\Delta eKE/eKE \sim 3\%$.²⁵ This is sufficient resolution to measure electronic transitions, and vibrational structure for systems with high frequency vibrational modes. There are noted limitations to resolution of vibrational features for warm ions and systems with many Franck-Condon active low frequency modes. Experimentally, vibrational resolution is often only close to threshold, where the eKE of the electron is lowest. Alterations have been made to improve the energy resolution. Notably, the adaptation of zero electron kinetic energy (ZEKE) spectroscopy of neutral molecules^{52,53} to anions by the Neumark group⁵⁴ and the photodetachment microscopy method of Blondel and co-workers.^{55,56} Anion ZEKE yielded far better resolution,^{57–59} but was far more experimentally challenging due to the vanishing cross section at zero kinetic energy (Wigner Law). Photodetachment microscopy has the ability to image photoelectrons with high precision but has so far been limited to atomic systems and relatively narrow energy ranges.⁶⁰

To address limitations in energy resolution while retaining the simplicity of anion photoelectron spectroscopy, an adaptation of slow photoelectron velocity map imaging (SEVI)

was applied to cryogenically cooled anions. Slow photoelectron velocity-map imaging (SEVI) is a high-resolution variant of anion photoelectron spectroscopy. Using SEVI, photodetachment is carried out close to threshold and the slowest electrons are detected selectively using low VMI extraction voltages, providing the best energy resolution.^{18,61,62}

In cyro-SEVI, ions generated in a pulsed ion source are trapped in a cryogenically cooled radio-frequency trap, held at 5 K.^{63,64} Ions are then thermalized to their ground vibrational and electronic states through collisions with buffer gas,⁶⁵ eliminating hot bands, sequence, and rotational broadening.⁶² This drastically improves energy resolution to $\sim 2\text{-}3\text{ cm}^{-1}$ for molecular anions.^{66,67} This has been demonstrated to improve the capabilities of anion photoelectron spectroscopy to extract accurate ADEs, vertical excitation energies of excited states and fundamental vibrational frequencies.^{66,68–71}

There are other research groups able to collect high-resolution photoelectron images, using similar adaptations. Wang's group combine an anion photoelectron spectrometer ESI ion source with a cryogenically-cooled Paul trap.^{72,73} Spectra of the cooled anions have an improved energy resolution of $\sim 1\text{-}2\text{ cm}^{-1}$, due to the removal of spectral congestion, and they have also used photodetachment action spectroscopy, which has proven to be very sensitive to the presence of non-valence excited states of molecular anions.^{74,75}

1.4 Excited States of Anions

The anion states discussed in the previous sections lie energetically below the ground state of the neutral molecule. As such, they are stable with respect to electron loss. It is possible for excited states of an anion to lie below the detachment threshold; however, anions typically have few bound excited states due to low electron affinities. A special class of loosely bound excited states of anions are discussed in section 1.4.1.

If the anion state lies energetically above the ground state of the neutral molecule, they are known as temporary anion states, metastable states or resonances. Temporary anion states are embedded in the continuum of the neutral plus electron and are susceptible to spontaneous electron loss. A full discussion of temporary states of anions, known as resonances, is given in section 1.4.2.

1.4.1 Non-Valence States

While the discussion so far has considered predominantly valence orbitals mostly defined by short-range interactions, there are a class of electrons states that are bound by the long-range potential only. For neutral atoms and molecules, these are Rydberg states which are bound by the $-1/r$ Coulomb potential between the cationic core and the electron. As a result, these non-valence states are essentially hydrogenic atomic orbitals. In anions, the long-range potentials described in Section 1.1 can also bind an electron if they are sufficiently large. Section 1.4.2 discussed how temporary anion states may facilitate electron capture and the formation of stable anions; non-valence states provide an alternate route to anion formation, whereby a low-energy electron may be temporarily captured by long-range interaction between the neutral core and the free electron.⁷⁶⁻⁷⁹

1.4.1.1 Dipole Bound States

The strongest long-range interaction between an anion and neutral core is through the permanent dipole-moment of the core, forming a dipole-bound state. In a dipole bound state the excess electron is located in a very diffuse s- or sigma type orbital, off the positive side of the molecular dipole.⁸⁰ Fermi and Teller first proposed the minimum dipole moment required to bind an electron in a dipole bound state to be 1.625 Debye,⁸¹ within the Born-Oppenheimer approximation.¹² Under the Born-Oppenheimer approximation it was predicted that any

species with this minimum dipole moment would have an infinite number of bound states the excess electron could attach to.^{82,83} However, unless the dipole is very large, only the lowest of these states will be energetically bound. Crawford and Garrett demonstrated that when electronic-rotational coupling is included for molecular anions, the “rule of thumb” first critical dipole moment is ~ 2.4 D.^{84–86}

Wang and co-workers have probed mode-specific vibrational autodetachment from the dipole bound state of anions of interest using cryo-SEVI (section 1.3.2). This technique has been used to obtain the autodetaching vibrational energies of the dipole bound state in addition to the Franck-Condon forbidden vibrational structure of the neutral ground state for a number of molecular anions.^{74,87–91}

1.4.1.2 Correlation Bound States

For molecular anions that lack a sufficiently large permanent multipole moment, the excess electron may still be bound in a correlation-bound state by dispersion forces. For this non-valence state, the binding energy of the excess electron is determined by the polarizability and dynamic correlation of the molecule. While the nature of the non-valence orbital has similarities to that of the dipole bound state, i.e. large and diffuse, the density is more uniformly distributed over the entirety of the molecule, engulfing the valence system. Correlation-bound states have been observed experimentally for molecular anions and clusters that do not have permanent multipole moments.^{11,92,93}

1.4.1.3 Photoelectron Signatures of Non-valence States

Non-valence states have characteristic signatures in photoelectron spectroscopy that are distinct from valence bound anions. Photodetachment from non-valence states is usually seen as sharp, atomic like, peaks with very low binding energies, while photodetachment from valence bound anions tend to have a broad Franck-Condon envelope. Photodetachment from

non-valence states yields photoelectron angular distributions with positive β_2 values, with little energy dependence. The origin of the sharp peak of non-valence states arises from the similarity in geometry between the non-valence and neutral core, while the angular distribution arises from the very diffuse s-like non-valence orbital.

Regardless of the specific binding interaction of the electron in non-valence states, conceptually there are similarities. Namely, the excess electron is bound in a large and diffuse orbital which has very little spatial overlap with the valence electrons of the neutral core, the non-valence state is just below the threshold for electron detachment and the interaction of the excess electron has little perturbative effect on the neutral molecular core. This introduces an additional caveat to consider when modelling the electronic structure, which is discussed in Section 2.1.7, following broad introductions to dipole and correlation bound states.

1.4.2 Resonances

Resonances are electronically excited states of anions embedded in the detachment continuum. Although electron loss from resonances can be very fast, a potential energy barrier prevents instantaneous ejection of the excess electron. Resonances have both a valence component, defined by the molecular orbitals involved in the electronic transition from the anion ground state, and a free electron component, a part of the wavefunction that decays through the barrier to the continuum. The temporal width, Δt , of a resonance can be expressed by the relation

$$\Delta E \Delta t > \frac{\hbar}{2}. \quad (8)$$

Generally, resonances have lifetimes ranging from femtoseconds to picoseconds, depending on the strength of coupling of the excited state to the neutral continuum and the character of the resonance.

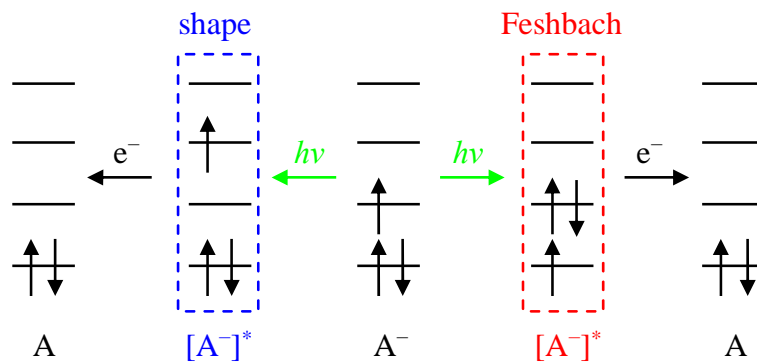
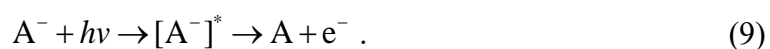


Figure 4 Schematic showing the electronic configurations that define shape and Feshbach resonances of a radical anion, A^- .

Resonances of anions are classified as either shape or Feshbach resonances. The difference between the two types of resonances is shown schematically in Figure 4. If the electron lost leads to the ground state electronic configuration, then the resonances is a shape resonance. Feshbach resonances require an electronic rearrangement in addition to electron loss to form the neutral ground state. The two-electron transition required for electron loss from a Feshbach resonance imposes a larger potential energy barrier on formation of the neutral ground state, leading to a smaller continuum contribution and a longer lifetime.

1.4.3 Fates of Excited States

Resonances are understood to facilitate electron attachment to isolated neutral species. When an incoming electron has an eKE resonant with an excited state of the anion in the continuum, then it may be temporarily captured. These resonance dynamics determine the fate of the system. When a resonance is formed, electron loss may occur directly from this state, known as autodetachment



While autodetachment is always an open channel for resonances, there are other mechanisms that may be in competition. For example, an initial excitation may create a wavepacket on the potential energy surface of a resonance. If the barrier to electron loss is sufficiently high, the wavepacket may have time to propagate and spread. In the case that there is an energetically accessible conical intersection, a portion of the wavepacket may internally convert to a lower lying resonance or a bound electronic state. This implies that non-adiabatic processes, involving nuclear dynamics, are able to compete with electron loss. Whether electron loss occurs promptly, by autodetachment from the initially formed resonance, or following nuclear dynamics by delayed autodetachment, will be reflected in the outgoing eKE.

In addition to autodetachment and internal conversion processes, there are other non-adiabatic processes that may occur. An example is dissociative electron attachment, in which initial electron capture leads to fragmentation to yield a neutral and anionic fragment. In this case, the photoelectron spectrum of the anionic fragment may also be recorded in the photoelectron spectrum.

Finally, in extreme cases, the ground state of the anion may be reformed following internal conversion. This is commonly the case for large conjugated molecules, which have a high density of coupled states. Internal vibrational energy redistribution will then lead to a statistical electron loss from the vibrationally hot anion ground state. This so-called thermionic emission leads to a characteristic statistical photoelectron signature, with electrons with a very-low eKE Boltzmann distribution.^{94–97}

1.4.4 Two-Dimensional Photoelectron Imaging

1.4.4.1 Frequency- and Angle-Resolved Photoelectron Spectroscopy

It is possible to probe the electronic structure of the neutral and the resonances embedded in its continuum, through photoexcitation of the ground state anion, A^-

$$A^{-} + h\nu \rightarrow [A^{-}]^{*} \rightarrow \text{products} . \quad (10)$$

If, $h\nu$ is resonant with a transition of the anion, photoelectron spectroscopy may be used to probe the dynamics of this resonance. While a single photoelectron spectrum may contain information about the anion-neutral system, it is often insensitive to the identification and characterisation of the dynamics of anion resonances.

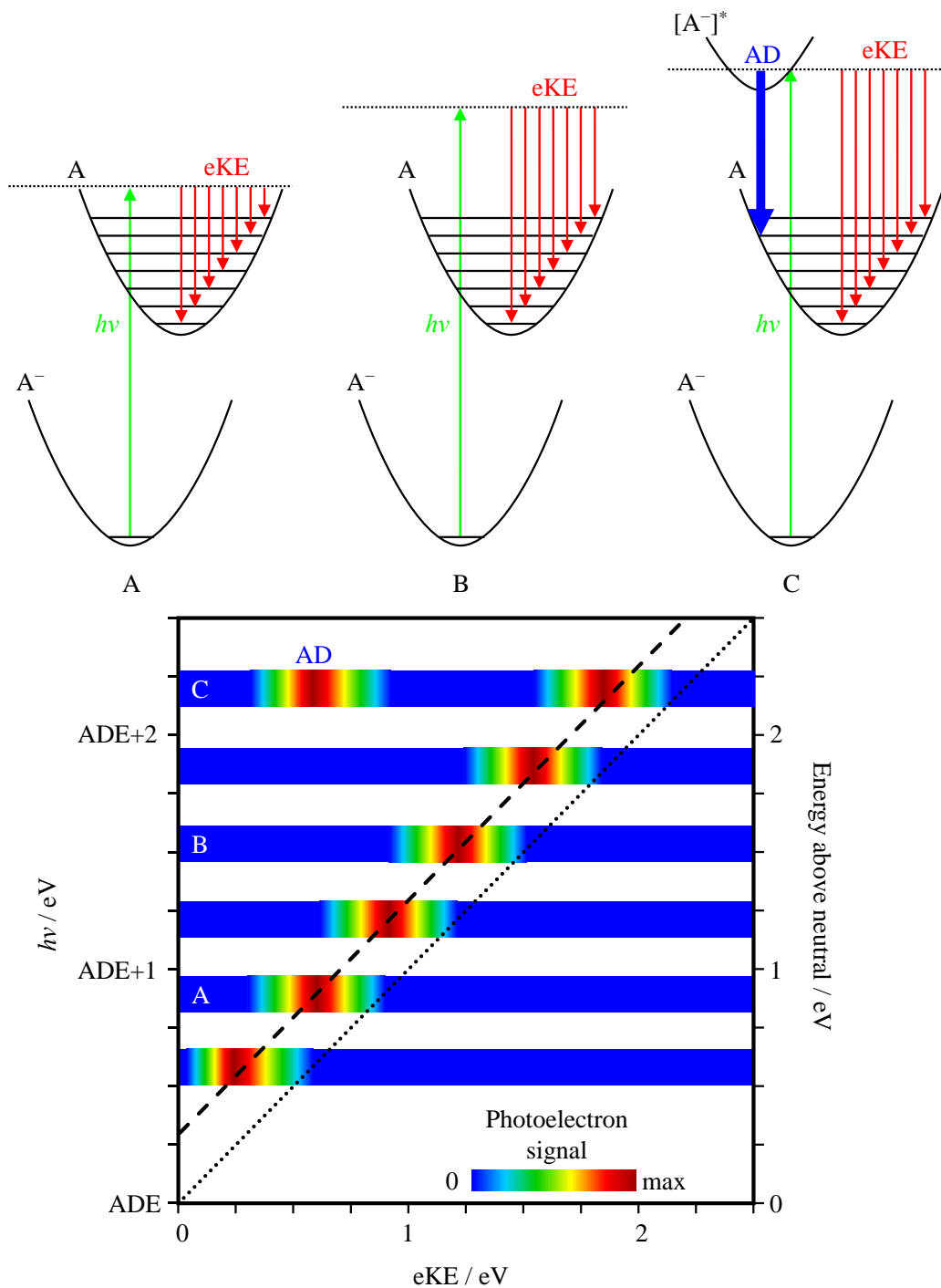


Figure 5 Pictorial representation of frequency-resolved photoelectron spectroscopy. The top panel depicts the photodetachment as $h\nu$ increases from left to right (A) – (C), leading to an increase in the eKE of the outgoing electron responsible for the direct detachment feature. The frequency-resolved spectra, made from stacking photoelectron images at each $h\nu$, is shown in the 2D map. If $h\nu$ is resonant with a transition that accesses an excited state of the anion in embedded in the continuum, then autodetachment (AD) from this resonance may occur. If the resonance is sufficiently long-lived, then the autodetachment feature will be at lower eKE than

the direct detachment feature, as indicated in the 2D graph. The dotted and dashed lines with unit gradient represent the adiabatic and vertical detachment energies, respectively.

In photoelectron spectroscopy, direct detachment produces an eKE distribution that increases relative to $h\nu$ by a proportional amount. Measuring the photoelectron spectra as a function of $h\nu$, plotted as a false-colour 2D map, allows us to visualise how the eKE distribution changes with increasing $h\nu$. If $h\nu$ is sufficient to access a resonance, $[A^-]^*$, the ensuing dynamics can have a profound effect on the measured photoelectron spectra and the photoelectron angular distributions. With reference to Figure 5, the eKE distribution from the direct detachment channel is shown as a diagonal feature, where the dotted and dashed lines correspond to the adiabatic and vertical detachment energies as a function of $h\nu$ (Section 1.2). Changes to the eKE distribution imply dynamics of resonances. Commonly, this will result in a red-shift to the outgoing electron, and a photoelectron features will appear at lower side of the direct detachment eKE distribution. Following photoexcitation to $[A^-]^*$, if autodetachment has a lifetime comparable to or slower than nuclear motion on the potential energy surface of $[A^-]^*$, then the Franck-Condon factors to the neutral ground state will differ, leading to a different final internal energy content in the neutral. Such dynamics will be reflected in the photoelectron spectrum, due to conservation of energy. By scanning the $h\nu$ across the detachment continuum and taking sequential photoelectron spectra, one is able to monitor the signatures of resonances and their observed dynamics. It is then possible to stack these photoelectron images to make a set of frequency-resolved spectra, building a 2D map of the electronic structure of the anion-neutral system.

2D photoelectron spectroscopy is in many ways complementary to 2D electron energy loss spectroscopy (EELS).^{98–101} In this, the kinetic energy of the incoming electron is scanned and for each of these the outgoing electrons kinetic energy spectrum measured. The key difference of 2D EELS is that it measures the “full” reaction. In 2D photoelectron spectroscopy, the resonance is accessed with a photon and so only the corresponding “half” reaction is

monitored. Additionally, the initial geometries differ. But there are some key advantages to performing 2D photoelectron spectroscopy.

For each $h\nu$, the photoelectron image taken has the complementary photoelectron angular distributions for any photoelectron features present in the spectra. As the photoelectron angular distributions are inherently sensitive to the molecular orbital from which the photoelectron is ejected, they are very responsive to any changes in electron loss channels. Resonances can be inferred through sudden changes to the photoelectron angular distributions as a function of $h\nu$. Sudden changes to photoelectron angular distributions can be rationalised through consideration of what is happening during excitation to a resonance. Firstly, the molecular orbital the outgoing electron is ejected from is changing. Secondly, formation of the resonance will have an associated transition dipole moment such that photoexcitation may lead to some initial alignment in the laboratory frame. Such changes have been observed previously in a number of photoelectron imaging experiments.^{44,102–104} It should be noted that the observation of no dramatic change in photoelectron angular distribution does not negate the presence of resonances. Many large or low-symmetry systems have predominantly isotropic angular distributions, regardless of any dynamics.

1.4.4.2 Time-Resolved Photoelectron Spectroscopy

Frequency- and angle-resolved photoelectron spectroscopy allow identification of the vertical energetic range over which resonance dynamics occur. It is straightforward to extend the investigation of the dynamics of resonances into the time-domain using photoelectron spectroscopy. This is particularly desirable for the unravelling the activity of biomolecules, for which an understanding of the ultrafast dynamics of the anionic chromophores provides baseline measurements for understanding how a condensed phase environment (e.g. solution or protein) influences the inherent photochemical dynamics.^{46,105–108}

Nuclear motion occurs on a timescale in the order of femtoseconds (10^{-15} seconds). In order to gain insight direct into chemical dynamics that occur on this timescale state-of-the-art experimental methods have been developed. Pivotal work in the 1980s led to the development of laser systems able to produce light pulses of only a few hundred femtoseconds.^{109–111} The commercial availability of femtosecond laser systems and the development of the pump-probe methodology laid the foundation for a wealth of ground-breaking studies, able to unravel chemical reactions in new detail.^{110,111}

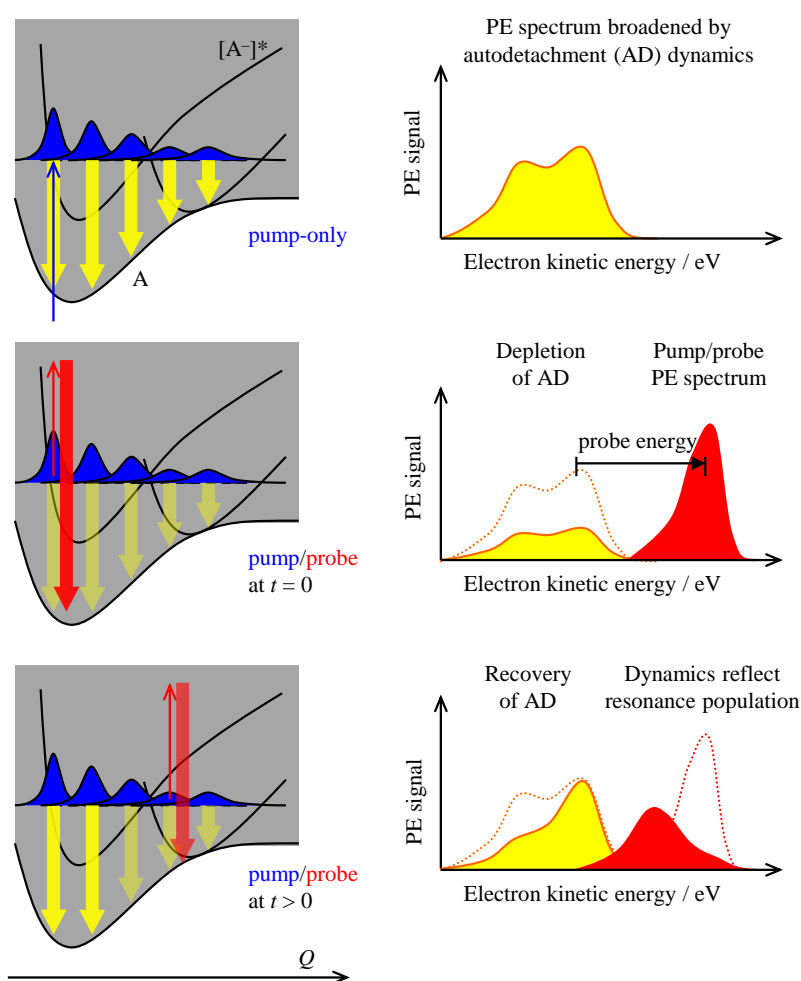


Figure 6 Pictorial representation of time-resolved photoelectron spectroscopy applied to the study of anionic resonances. The top panel shows the initial photoexcitation of a resonance, by a femtosecond pump pulse. If the autodetachment (AD) lifetime of the resonance is long compared to the nuclear vibrations of the system, then AD may occur along some intermolecular coordinate, Q , as indicated by the downward arrows. Following a time delay a second probe pulse samples the population from the resonance, shown in the central panel, leading to depletion in AD and the appearance of higher eKE feature. Through varying the pump-probe time delay, as shown in the bottom panel, the dynamics of the resonance can be probed in real time.

The basic principles of time-resolved anion photoelectron spectroscopy applied to resonances are summarised pictorially in Figure 6. An ultrashort femtosecond laser pulse, at an identified $h\nu$, is used to photoexcite the anion ground state to some excited state. Following a time delay, Δt , a second ultrashort pulse arrives, photodetaching the electron. The two pulses are referred to as the pump and probe pulses, respectively. The delay between the pump and probe pulses is varied to allow temporal evolution of the photoelectron spectra. The photoelectron spectra taken allow direct monitoring of the nuclear dynamics and autodetachment from the resonance. As there are no stringent selection rules in photoelectron spectroscopy, the entire reaction coordinate can be monitored.

The photoelectron spectrum is determined by the energetic difference between the excited state and final neutral ground state potential energy surfaces as a function of nuclear coordinate. That is to say, if the final state photodetached remains the same, the time-resolved dynamics are probed by the changes in Franck-Condon factors to this final neutral state.¹¹² There are cases in which the final state or states accessed by photodetachment differ. This may occur when there are additional neutral states or multiple resonances involved in the dynamics. This idea has been applied to the interpretation of a many time-resolved studies of bound states.¹¹³ The former caveat is often unimportant in interpretation of dynamics of resonances of radical anions as the closed-shell neutral is typically more than a few eV above that of the anion. As such, only a single final neutral state needs to be considered.

The decay mechanisms of resonances can be probed through the depletion induced by the probe pulse, and the resultant new photoelectron signal at higher eKE (Figure 6). If the ultimate fate of the system is electron loss on a timescale shorter than the temporal resolution of the experimental arrangement, the total integrated photoelectron signal will be constant, and the lifetime of the dynamics cannot be determined unless the electrons are dispersed in energy.

2 Theoretical Considerations

Quantum chemical calculations aid the interpretation and unravelling of experimental data. All quantum chemistry methods rely on approximations in order to be able to solve the electronic Schrödinger equation, Equation 11, the first of which are time-independence,

$$\hat{H}_{\text{elec}} \Psi(r; R) = E_{\text{elec}}(R) \Psi(r; R). \quad (11)$$

There are three additional basic approximations underpinning electronic structure theory; the Born-Oppenheimer approximation, the independent particle approximation, and the formation of molecular orbitals from linear combination of atomic orbitals (LCAO-MO).

A single electronic wavefunction, $\Psi(r; R)$, depends explicitly only on the coordinates of the electrons, denoted as r , for a given nuclear configuration (R). A different wavefunction describes the position of the nuclei, $\chi(R)$. The separation of the molecular wavefunction into an electronic and nuclear wavefunction arises from the Born-Oppenheimer approximation. Under the independent particle approximation all electrons experience a ‘field’ of all other electrons as a group, rather than individually. Finally, molecular orbitals are constructed from superpositions of atomic orbitals belonging to atoms in a molecule, known as the LCAO-MO approach.

The partitioning of contributions to the total electronic energy under the Born-Oppenheimer approximation massively reduces the complexity of the calculation, making calculation of molecular systems feasible, and introduces the concept of potential energy surfaces. Potential energy surfaces are complex hypersurfaces defined by the nuclear degrees of freedom of the molecule ($3N - 6$) and considering a distortion in a single coordinate R allows the construction of 1D slices, shown qualitatively in earlier figures.

The independent particle approximation is sometimes referred to as the molecular orbital approximation, whereby $\Psi(r)$ can be written as a product of wavefunctions for single electrons in an n electron system,

$$\Psi(r_1, r_2, \dots, r_n) \cong \psi_1(r_1)\psi_2(r_2)\dots\psi_n(r_n) . \quad (12)$$

The single electron wavefunctions, $\psi_n(r_n)$, are called molecular orbitals. Determination of molecular orbitals is far simpler than the overall wavefunction. It is important to note that this approximation, as written above, fails immediately for electrons as it is not antisymmetric. Additionally, this approximation inherently neglects explicit electron-electron interactions (electron correlation). Many-body electron correlation arises from symmetry and repulsion.¹¹⁴ The former is referred to as Fermi correlation and the latter as Coulomb correlation.

LCAO-MO is a simple method that yields a qualitative picture of MOs in a molecule, forming approximate N -electron wavefunctions as linear combinations of anti-symmetrized products of MOs. Modifications must be made to the electronic wavefunction to ensure that combined spatial and spin variables of any given electron, x_i , is properly represented, such that the overall wavefunction is antisymmetric with respect to swapping the coordinates of any two of the electrons. This condition satisfies the Pauli principle. For a system of n electrons, the combination of one-electron spin orbitals, $\chi_i(x)$, antisymmetrised, can be written as the determinant of a $n \times n$ matrix. Within Hartree-Fock theory, these determinants are referred to as Slater determinants

$$\Psi(x_1, x_2, \dots, x_n) = \frac{1}{\sqrt{n!}} \begin{vmatrix} \chi_1(x_1) & \chi_2(x_1) & \cdots & \chi_n(x_1) \\ \chi_1(x_2) & \chi_2(x_2) & \cdots & \chi_n(x_2) \\ \vdots & \vdots & \ddots & \vdots \\ \chi_1(x_n) & \chi_2(x_n) & \cdots & \chi_n(x_n) \end{vmatrix} . \quad (13)$$

The use of a Slater determinant to represent the electronic wavefunction is beneficial as interelectronic interactions and the motion of electrons becomes correlated with respect to the spin and permutation symmetry conditions of the wavefunction (Fermi correlation).

Despite the deceptive simplicity of the electronic Schrödinger equation shown in Equation 11, calculating accurate solutions remains a complex problem. The art of quantum chemistry is choosing how to balance approximations in calculations. The remainder of this section outlines the main approximations and pitfalls associated with a variety of electronic structure methods, with attention paid to the calculation of anions and resonances.

2.1.1 The Hartree-Fock Approximation

The central starting point for most computational methods is the Hartree-Fock (HF) approach, also referred to as the self-consistent field (SCF) method.^{115,116} While the HF approximation is able to return a solution to the electronic Schrödinger equation, it is important to appreciate that this is not an exact solution. The HF energy can be defined as E_{approx} calculated from the approximate HF wavefunction, Ψ_{approx} and must be higher than the true ground-state energy of the system

$$E_{\text{approx}} = \int \Psi_{\text{approx}}(r) \hat{H}_{\text{elec}} \Psi_{\text{approx}}(r) dr . \quad (14)$$

The HF wavefunction of a system is defined as the Slater determinant that returns the lowest energy. From a HF calculation one can retrieve a HF wavefunction, or Slater determinant, molecular orbitals with their associated energies, ε_i , and the overall energy of the system. All three of the calculated terms are of interest when trying to understand the properties of a system. In the complete basis set limit, the HF energy differs from the true energy due to two factors, neglect of electron correlation and neglect of relativistic corrections.

The orbital energies are of particular importance when considering the chemical properties of a system. The influence of frontier orbitals in determining chemical properties

and reactivity of a system has been widely documented.^{117–120} Using Koopmans’ theorem the energy of the lowest unoccupied molecular orbital (LUMO) can be used to provide a rough estimate of the electron affinity of a system¹²¹

$$EA \approx -\epsilon_{\text{LUMO}}. \quad (15)$$

While the energies of HF orbitals are relatively poor, their shape can provide qualitative insight into the chemical properties of a system and can provide a reliable qualitative description of a ground state system in an equilibrium geometry, if the ground state has a closed-shell electronic structure.

Introductory statements to many books on electronic structure begin with a statement of the general content ‘most stable molecules have closed-shell electronic structures’. This statement is not of much comfort for those trying to perform calculations on anions. As anion photoelectron spectroscopy probes the electronic structure of both the anion parent and the neutral daughter, inherently there is an open-shell electronic structure to consider. This has implications in the type of HF calculation that is needed. Closed-shell systems can be represented using a simplified restricted HF approach. There are two main ways to represent an open-shell system, one can either use a restricted open-shell (ROHF) or an unrestricted HF (UHF) calculation. In the former, pairs of opposite-spin electrons exist in doubly occupied ‘closed-shell’ orbitals, while any remainder electrons exist in singly occupied ‘open-shell’ orbitals. In the latter, the spatial components of orbitals for opposite-spin electrons (e.g. α and β) are allowed to differ. There are reasons for preference for one of these formalisms over the other (e.g. avoidance of spin contamination using ROHF or correct dissociation character using UHF) but further discussion of the specifics of the two methods is not offered here. Rather, the different HF formalisms are mentioned to highlight the consideration needed when designing a calculation to render physically meaningful results.

2.1.2 Post Hartree-Fock Methods

The HF method is an approximate method as it is based upon the calculation of an approximate wavefunction from a single Slater determinant. The HF energy is always higher than the true ground state energy, due to the variational principle. The difference between the two energies is known as the correlation energy.

A plethora of *ab initio* methods, which invoke varying degrees of approximations, have been developed to recover the missing (Coulomb) electron correlation in calculations of the electronic ground state.^{115,122–125} Coulombic electron correlation tends to be broken down into non-dynamic (static) and dynamic correlation, but it should be noted there is no unified robust definition of these terms. For example, in many multireference calculations performed in this thesis, the CASSCF component takes into account static correlation from near-degeneracies, while the perturbation theory part of an XMCQDPT2 calculation takes into account dynamic correlation. Both correlation components are missing from the HF model; the dynamic due to the failure of accurately describing the short distance interelectronic interaction, and the static by considering that a single Slater determinant can be used to describe the electronic configuration of the molecule.

There are two different ways to improve the electronic energy, through recovery of the correlation energy, based on the HF approach. The first class of methods focuses on improving the approximate form of the wavefunction (Equation 14). The description is improved through introducing many-electron character into the wavefunction, increasing flexibility. Under this approach additional linear combinations of excited determinants are used to form the approximate wavefunction. These methods are discussed in Sections 2.1.2.1, 2.1.2.3 and 2.1.4.1. The second class of methods tries to improve the description of the wavefunction, through applying a small perturbation to the approximate Hamiltonian of the HF reference (a

Fock operator). These methods are discussed in Sections 2.1.2.2 and 2.1.4.2.1. Both methods use the HF reference as a starting point for subsequent calculations.

2.1.2.1 Configuration Interaction

Mathematically, electron correlation can be included by increasing the flexibility of the wavefunction by adding more Slater determinants. LCAO-MO coefficients are first determined through a single-reference HF calculation, finding the lowest energy for N -orbitals. Configuration interaction (CI) is then used to find the excited Slater determinants, allowing the many-electron wavefunction to be written as a linear combination of determinants

$$|\psi_{\text{CI}}\rangle = c_{\text{HF}} |\Psi_{\text{HF}}\rangle + \sum_{ia} c_i^a |\Psi_i^a\rangle + \sum_{i>j,a>b} c_{ij}^{ab} |\Psi_{ij}^{ab}\rangle + \dots \quad (16)$$

The components of the CI wavefunction are shown qualitatively in Figure 7.

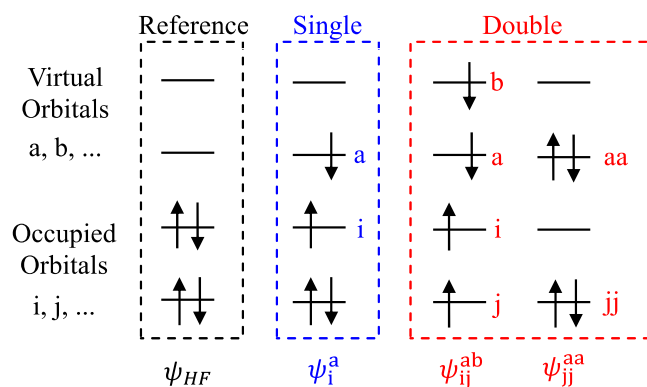


Figure 7 Schematic representation of the components of the configurational interaction wavefunction.

In principle full CI, with an infinite basis set, would yield the exact solution to the electronic Schrödinger equation. However, even with a finite basis set, full CI is too computationally expensive. It is for this reason that the expansion is normally truncated to single and double excitations (singles and doubles), referred to as CISD.

CI is a systematic procedure for going beyond the HF approach. It is a variational approach, advantageous as it is able calculate the upper bounds of energy, excited states and

recover some dynamic correlation energy. However, this method has the disadvantage of not being size-extensive, as such the energy does not scale properly with the number of particles. Additionally, the number of determinants scales rapidly with level of excitations, even for systems with a small number of electrons, and the convergence is slow.

2.1.2.2 Many-Body Perturbation Theory

Møller-Plesset perturbation theory (MP)¹²² is a different approach to accounting for electron correlation, through treating it as a perturbation to the Hartree-Fock wavefunction. Under this approach the total Hamiltonian of a system is partitioned into two parts; a zeroth-order part with known eigenfunctions and eigenvalues, H_0 and a perturbation, V . A reference is often used to form the zeroth-order component, while the perturbed component is a two-electron operator. The electronic energy is improved by systematic improvement of the zeroth-order Hamiltonian, so that it becomes closer in energy to the total Hamiltonian,

$$\hat{H} = \hat{H}_0 + \lambda \hat{V} \quad (17)$$

through application of a dimensional perturbation parameter, λ . The zeroth order eigenfunctions and eigenvalues are expanded as a Taylor series. The first meaningful correction is the second-order correction, MP2,

$$E_{\text{MP2}} = \sum_{i < j}^{\text{occ}} \sum_{a < b}^{\text{virt}} \frac{[\langle \psi_i \psi_j | \psi_a \psi_b \rangle - \langle \psi_i \psi_j | \psi_a \psi_b \rangle]^2}{\epsilon_i + \epsilon_j - \epsilon_a - \epsilon_b}. \quad (18)$$

Perturbation theory is size-consistent at each level and recovers a large amount of correlation energy. While perturbation theory offers an improved description of the energy in almost all cases, it does have limitations. Perturbation theory is not variational, which can lead to overcorrections and energies lower than the total electronic energy. Overcorrection of energies is particularly prominent for systems with small energy gaps between frontier orbitals.

Additionally, perturbation theory does not perform well in cases of spin contamination of states and convergence is not smooth for higher order expansions (e.g. MP4).

2.1.2.3 Coupled-Cluster Theory

The coupled-cluster method (CC) takes the basic Hartree-Fock molecular orbital approach and constructs multi-electron wavefunctions using an exponential cluster operator. A CC wavefunction can be expressed as a product,

$$\psi_{\text{CC}} = e^{\hat{T}} \psi_{\text{HF}}, \quad (19)$$

where the exponential operator \hat{T} generates the excited Slater determinants,

$$e^{\hat{T}} = 1 + \hat{T} + \frac{1}{2}\hat{T}^2 + \frac{1}{6}\hat{T}^3 + \dots = \sum_{k=0}^{\infty} \frac{1}{k!} \hat{T}^k. \quad (20)$$

While perturbation methods add all types of corrections to a given order, CC methods includes all corrections of a given type to an infinite order,

$$\hat{T} = \hat{T}_1 + \hat{T}_2 + \hat{T}_3 + \dots + \hat{T}_N \quad (21)$$

$$e^{\hat{T}} = \hat{1} + \hat{T}_1 + (\hat{T}_2 + \frac{1}{2}\hat{T}_1^2) + (\hat{T}_3 + \hat{T}_2\hat{T}_1 + \frac{1}{6}\hat{T}_1^3) \dots \quad (22)$$

The difference between MP and CC arises from the way in which the excited determinants are generated. CC excited determinants are generated using interacting and non-interacting pairs. If all cluster operators up to \hat{T}_N were to be included, the energetic solution would be equivalent in accuracy to full CI. As with CISD, CC is normally truncated at single and double excitations (CCSD).¹²⁶ However, the CCSD wavefunction will also include triple and quadruple excitations as products of the single and double amplitudes

$$e^{\hat{T}_1 + \hat{T}_2} = \hat{1} + \hat{T}_1 + (\hat{T}_2 + \frac{1}{2}\hat{T}_1^2) + (\hat{T}_2\hat{T}_1 + \frac{1}{6}\hat{T}_1^3) + (\frac{1}{2}\hat{T}_2^2 + \frac{1}{2}\hat{T}_2\hat{T}_1^2 + \frac{1}{24}\hat{T}_1^4) \quad (23)$$

The triples term, \hat{T}_3 , improves the description of the wavefunction dramatically. This can be included perturbatively, with modest cost, to yield the CCSD(T) model. The CCSD(T) wavefunction is very accurate, with the solution approaching that of full CI.

The advantage of the CC method has been highlighted in Equation 23, truncation to singles and doubles yields an excitation operator that contains products equivalent to higher order excitations. These disconnected excitations are often more important than some of the higher CI solutions, and the convergence is much faster for CC methods. The CCSD(T) method is widely regarded as the gold standard for dynamic electron correlation, with a complete basis set.

While CCSD(T) may be heralded as the gold standard, this does not make it the appropriate choice for every problem. There are systems that may be adequately treated by much lower levels of theory, saving much computational cost. Conversely, there are systems for which CCSD(T) will fail, and different approaches are necessary. An additional caveat that must be mentioned is that CCSD(T) requires the use of a large basis set in order to truly be considered capable of producing results of ‘gold standard’. For example, the results yielded by the use of CCSD(T) with a minimal basis set will be physically unmeaningful, while a CCSD(T) with a complete basis set represents the true gold standard.

2.1.3 Note on the Choice of Basis Set

As highlighted above, a limitation with any electronic structure method is the choice of basis set used to perform the calculation. In electronic structure theory, the ‘level of theory’ used in calculations has two components that the user must define: the treatment of electron correlation, and the basis set. In actuality, the choice of basis set may also aid the recovery of electron correlation.

For efficient calculation, molecular orbitals, $\psi(r)$, can be expressed as combinations of simpler functions, known as basis functions $\varphi(r)$,

$$\psi_i(r) = \sum_{j=1}^{n_{\text{basis}}} c_{ij} \varphi_j(r), \quad (24)$$

where the set of n_{basis} functions are chosen to represent each of the occupied atomic orbitals of the atoms making the molecular system. The collection of basis functions is known as the basis set and is chosen prior to carrying out any calculation. Basis sets provide the building blocks to the many-electron wavefunction, and as such, the choice of basis set is extremely important. These basis functions are often taken to be Gaussian-type functions.

When choosing a basis set, there is a compromise to be made between accuracy and computational time. An appropriate basis set for calculations on molecular anions needs to be able to accommodate the radial extent and polarizability of the anion. The radial extent of a basis function is determined by an exponent factor, normally denoted the ζ -factor. The accuracy of the description, and the computational time, increases for higher ζ -factors. However, a second-order or higher-order ζ -factor is not enough to describe the diffuse electron density of anions and excited states. These also require additional diffuse functions. Additional basis functions of different angular quanta must be added to the basis set to describe the polarisation of atoms. Polarisation functions are crucial for an accurate description of electron correlation.

Basis set choice is relatively straightforward for the problems in this thesis. Dunning basis sets are accepted as being the gold standard for calculations on anions.¹²⁷ This family of basis sets is a correlation-consistent basis set, written as cc-pVXZ, where X refers to the order of ζ -factor. When using these basis sets for anions augmented with diffuse functions, aug-cc-pVXZ, is used.

2.1.4 Multiconfigurational SCF

The correlation energy may be improved through use of the single-reference methods described in Sections 2.1.2.1 - 2.1.2.3, however, there are cases in which a single-reference wavefunction cannot accurately describe a chemical system. A notable example is when bonds distort and elongate. The origin of this limitation is that the electronic configuration and shape of the MOs are determined by a single Slater determinant. In order to obtain more accurate results, the shape of the orbitals needs to be optimized. To do this, a variational approach is needed for the coefficients that describe the contributions of Slater determinants and the coefficients that describe the weighting of atomic orbitals in molecular orbitals.

A family of methods known as multiconfigurational SCF (MCSCF) are able to treat electron correlation in cases where the HF reference is insufficient. As discussed previously, single reference methods are able to provide an accurate description of the wavefunction when a system is close to the equilibrium geometry. MCSCF methods are required when considering geometries that lie further away from the equilibrium geometry and excited determinants contribute significantly to the wavefunction. The methodology of MCSCF methods is discussed in the next section.

2.1.4.1 Complete Active Space SCF

Complete active space SCF (CASSCF)¹²⁸ is the most commonly used MCSCF method. Briefly, CASSCF is essentially a full CI method for a restricted space, where all possible configurations for a given number of ‘active’ electrons in a given ‘active’ orbital space are constructed. The active orbitals and electrons in a defined CAS space are referred to as CAS(n_{el} , m_{orb}). This yields a wavefunction with comparable accuracy to full CI, but that is

computationally tractable provided the chosen active space is limited. The typical active space limitation is 18 or less active electrons in 18 active orbitals.¹²⁹

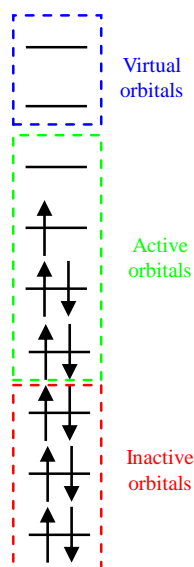


Figure 8 Schematic representation of the subspaces used to form a CASSCF wavefunction

The methodology of CASSCF is similar in principle to CI, whereby the multiconfigurational wavefunction is constructed as a linear combination of single-configurational wavefunctions. The single-configurational wavefunctions may be referred to as configurational state functions (CSFs), if the determinants are spin-adapted. The determinants are defined by dividing orbitals into three distinct subspaces; the inactive subspace, in which all orbitals are doubly occupied, the active subspace, comprised of the n electrons and m orbitals on which the full CI is carried out, and the virtual space, in which all orbitals are unoccupied and are kept unoccupied. This is shown qualitatively in Figure 8. The electrons and orbitals included in the active space are those deemed to contribute the most to the multireference character of the system studied. The occupation number of the orbitals in the active space will be a non-integer number between 0 and 2.

CASSCF is able to provide a better description of the electronic structure of a system, before recovering the correlation energy. This MCSCF method provides accurate reference states for recovering large fractions of dynamic correlation energies and is size-consistent.

Additionally, CASSCF is able to handle more exotic systems, such as zwitterions, biradicals, transition states and conical intersections between two or more potential energy surfaces. Unlike the previously discussed single-reference states, CASSCF is applicable to ground and excited states within a single framework. This latter property is crucial when modelling photochemical processes.

While there are numerous advantages of CASSCF, this method cannot be considered as ‘black box’. The choice of active space is not always obvious but is crucial to returning a reasonable wavefunction. There are no rigorous rules for the choice of a balanced active space:¹³⁰ while one can use chemical intuition and experience, this is not always enough. Often some prior knowledge of the system is required.

2.1.4.2 Second-Order Multireference Perturbation Theory

There are a hierarchy of second-order multireference perturbation theory (MRPT2) methods used to correct the secondary space, improving the dynamic electron correlation. The first level of the MRPT2 methods consists of multi-reference state-specific methods, the second and third levels of multi-reference multi-state methods. These will be briefly discussed in the following sections.

Prior to discussing the specific of MRPT2 methods it is pertinent to outline some general considerations. Briefly, all perturbation methods are single reference in origin, and any expansion of these methods requires the orbital energies to be defined. The need to define orbital energies originates from the denominator of equation 18 and requires the use of semi-canonical orbitals. When moving to second-order corrections to PT there are more parameters that may be varied, and so different methods develop in different ways. All methods begin with CASSCF reference wavefunctions that describe the zeroth-order wavefunctions. A detailed analysis is beyond the scope of this thesis, but a brief discussion will be given in order to

highlight which comparisons can be made, and which methods can be considered reliable for modelling the parameters of anion photoelectron spectroscopy.

2.1.4.2.1 Multireference State Specific MRMP2

State specific MRMP2 methods dynamically correlate only one target space, based on a single reference state described by CASSCF. There are two branches of development of method that will be considered; MRMP2^{131,132} and CASPT2.^{133,134} CASPT2 is simply CAS with perturbation theory at second-order and is a popular choice of second-order correction method.

The methods differ in definition of the secondary space, MRMP2 includes all determinants in the secondary space, while CASPT2 only includes the diagonal elements of the Hamiltonian. The former is a totally uncontracted method, while the latter is internally contracted. The consequence of contracting the secondary space is that states cannot interact, this in turn means that the description of the zeroth-order wavefunction cannot be improved.

For both methods problems are encountered if the CASSCF is not a good reference space. This can arise in cases for which CASSCF is insufficient to describe states correctly, leading to an incorrect ordering of states due to lack of dynamic correlation.

2.1.4.2.2 Multireference Multistate MRMP2

State specific MRMP2 methods are limited in the amount of dynamic correlation they can return. In order to introduce more dynamic correlation, multistate extensions are incorporated within the effective Hamiltonian framework. Within this extension a multidimensional reference space, spanned by state-averaged CASSCF (SA-CASSCF) states, is generated. States are obtained through diagonalization of the effective Hamiltonian within the reference space, based on a linear combination of the initial CASSCF wavefunction. The wavefunctions obtained are still zeroth-order wavefunctions, however, their description is

improved as states are allowed to interact through the perturbative calculation of the effective Hamiltonian. Allowing states to interact is particularly important in regions of energetic space in which states lie close together, such as conical intersections.

While the description of the wavefunctions is improved through this extension, there are still notable problems. Particularly problematic is the artificial couplings, seen as large off-diagonal elements of the effective Hamiltonian, that arise in cases where a low-dimensional reference space is used to calculate states that lie close in energy.

The extension of MRMP2 is called multiconfigurational quasi-degenerate perturbation theory (MCQDPT2),¹³⁵ while the analogous extension to CASPT2 is known as MS-CASPT2.¹³⁶ Both methods should give comparable results.

To approximately correct for the unphysical large off-diagonal elements, a stabilization technique was developed for MCQDPT2.¹³⁷ In order to quench the artificial couplings, the number of zeroth-order wavefunctions needs to be drastically increased. This method (aug-MCQDPT2) sequentially enlarged the reference space of an augmented Hamiltonian, enabling the calculation of target electronic states that gave good agreement to experimental values.¹⁰⁵

2.1.4.2.3 Third Generation Corrections

While the aug-MCQDPT2 method was able to yield results comparable to experimental values, the size of the secondary space needed reduces the applicability of the method drastically. A third generation of MRMP2 methods was developed by Granovsky in order to address the large off-diagonal artefacts in the effective Hamiltonian. This method is known as extended multiconfigurational quasi-degenerate perturbation theory (XMCQDPT2).¹³⁸ A similar analogous extension has been made to MS-CASPT2, XMS-CASPT2.¹³⁹

XMCQDPT2 is invariant with respect to the rotation of orbitals in the active space or vectors in the model space. The major advantage of XMCQDPT2 is that through allowing states to interact the quality of the wavefunction improves from that of the CASSCF

wavefunction. The eigenvalues of the effective Hamiltonian are now able to accurately describe the mixing of states. The energetic description of XMCQDPT2 states become more accurate, even in cases where states become near degenerate in energy. Furthermore, the energies are stable with respect to extension of a model space, allowing application to large molecular systems.^{46,140–142}

2.1.4.2.4 Choice of MRMP2 Method

As with any other branch of methods, there is not a simple solution for choice of MRMP2 method. This is because the application is always different, so the choice needs to be the most beneficial to the particular experimental parameter modelled and is often state dependent.

CASPT2 is a method that has enjoyed great popularity. This method is indeed capable of producing accurate vertical excitation energies for systems with large energetic separations. In these cases, the off-diagonal elements of the effective Hamiltonian should, in principle, be small. In this scenario, as there is negligible mixing of states, the accuracy of the CASPT2 energies should be comparable to XMCQDPT2. In reality, and particularly the reality of the energetic landscape of anions, states are not separated by such large energies that the couplings become negligible. Additionally, CASPT2 often requires application of an ‘IPEA correction’^{143,144} to systematic errors in order to improve the IP and EA energies of active orbitals. This pitfall is avoided in multistate methods.

Furthermore, as CASPT2 does not improve the description of the zeroth-order wavefunction, there are obvious cases where the CASSCF wavefunction will not be adequate, and the error will propagate through. Such cases include neutrals with low-lying $n\pi^*$ states that are incorrectly ordered at CASSCF and states involving two-electron excitations. As the errors are introduced because of an artefact of the CASSCF method, they cannot be removed by a CASPT2 calculation, and a multistate approach is required.

In principle, it is possible to envisage scenarios in which the CASSCF provides an adequate description of the states of interest, e.g. the ground and first excited state of a system which is dominated by a single one-electron excitation. In these cases, the state specific CASPT2/MRMP2 methods should be sufficient to return good energetics. However, for more complex systems, or to accurately model the experimental parameters of anion photoelectron spectroscopy in both the frequency- and time-domain, a multistate reference method is needed (XMCQDPT2/XMS-CASPT2). This is because there will be states that interact, and the MRMP2 method chosen needs to be able to accurately handle state mixing.

The limitations of state specific methods have been highlighted for the case of the anionic photoactive yellow chromophore,¹⁰⁵ a derivative of which is the subject of Section 5.3. For this system, the CASSCF description was determined to be highly insufficient, resulting in overestimation of excitations. It was found that the target state lay fairly high in energy at the CASSCF level, requiring multistate methods to correctly reorder states and improve the quality of the target state.

Finally, care must be taken to ensure remove intruder states from the active space of MRMP2 methods, as their inclusion leads to troublesome convergence and incorrect energies.^{145,146} While a range of methods have been developed to correct the intruder problem in MRMP2 methods,^{147–150} in the scope of this thesis the use of multistate XMCQDPT2 ‘perturb then optimize’ approach and natural orbitals is enough to diagnose and overcome the so-called intruder state problem.

2.1.4.3 The Equation-of-Motion Coupled-Cluster Method for Excited, Ionized and Electron-attached States

Equations-of-motion (EOM)^{151,152} is an elegant electronic structure method that allows the description of multiconfigurational wavefunctions within a single-reference formalism.

This method is used extensively throughout this thesis; however the details of this method have been extensively covered in a number of publications^{31,151,153,154} and so are only briefly described.

Conceptually, EOM methods are similar to CI, but EOM is numerically superior as correlation effects are ‘folded into’ the transformed Hamiltonian. EOM methods are also rigorously size-extensive. Target states, Ψ_0 , are described as excitations from a reference state, Ψ ,

$$\Psi_{\text{EOM}} = \hat{R}\Psi_0, \quad (25)$$

where \hat{R} is a general excitation operator. This method allows treatment of electronically excited states at a level of theory similar to CC for the ground state.

There are a number of EOM variants; electronic excitations (EOM-EE) describes electronically excited states, while the ionized potential and electron attachment (EOM-IP/EA) methods describe electron detachment and attachment to a reference wavefunction. For the first method R is electron conserving, for the latter two methods R is electron annihilating and creating, respectively. These three EOM-CCSD methods are shown schematically in Figure 9. These models can accurately treat ground and excited states of open-shell systems, avoiding the reliance upon the unstable HF solution for open-shell systems.

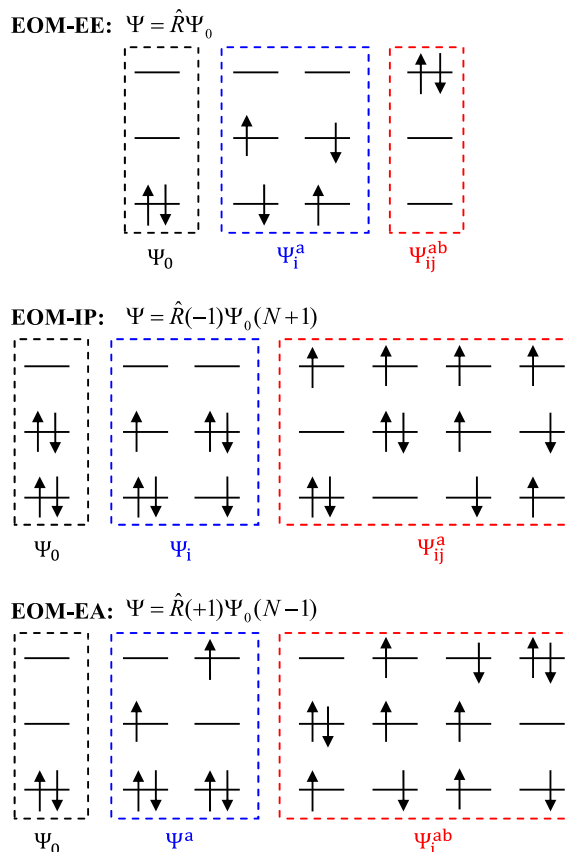


Figure 9 Schematic representation of the electronic excitation (EE), ionisation potential (IP) and electron attachment (EA) EOM-XX-CCSD methods.

EOM-EE-CCSD has been demonstrated to be very accurate for systems that are primarily single one-electron transitions. However, the accuracy is much lower for states that have substantial double excitation character. The description of such states arises from truncation of the excitation operator, and can be improved through inclusion of triples, but this increases the computational cost substantially.

While the EOM-XX-CCSD suite of methods are moderately expensive, their current implementation allows calculations of medium-size molecules. In principle, it is possible to obtain Dyson orbitals using all three of the EOM-XX-CCSD methods shown in Figure 9.^{31,32} The Dyson orbital for direct detachment channels shows little difference from a HF orbital when modelling photoelectron angular distributions. However, in order to model the photoelectron angular distributions from electronically excited state it is necessary to obtain a Dyson orbital optimized to the target excited state.

2.1.5 Density Functional Theory

Density functional theory (DFT)^{155–158} represents a conceptually different approach to incorporating electron correlation, whereby the electronic energy is written as a functional of the electron density, rather than the many-electron wavefunction,

$$E = E[\rho], \quad (26)$$

$$E[\rho] = E_T[\rho] + E_V[\rho] + E_J[\rho] + E_X[\rho] + E_C[\rho], \quad (27)$$

where the energy is partitioned into kinetic (T), Coulombic attraction of the electron to the nucleus (V), Coulombic energy of electrons moving independently and repelling itself (J), exchange (X) and correlation (C). Exchange and correlation effects are gathered together in an exchange-correlation (XC) functional, which is in principle exact. In practice, functionals are fitted empirically to experimental data or known physical properties.

DFT can be extended to consider excited states through time-dependent DFT (TD-DFT).^{159,160} TD-DFT is widely applied to the calculation of excited state properties, including excitation energies, oscillator strengths and geometries, for a number of medium to large molecules. Of all the excited state methods discussed in this section, TD-DFT is the most commonly utilised, however this does not speak to the accuracy of this method. While TD-DFT performs well for bound valence excited states, there are well-documented failures with non-valence and charge-transfer states.^{161–163} These failures arise from the incorrect long-range asymptotic behaviour of approximate exchange correlation functionals.

There are functionals that have been optimized to correct the long-range behaviour, known to be important for anionic systems, such as CAM-B3LYP and ω B97XD.^{164,165} With use of these functional and appropriate basis sets, DFT and TD-DFT may yield reasonable ground state geometries and qualitative excited state information. The main advantages of DFT are the reduced computational cost compared to *ab initio* methods and “black box” style usage

in many computational packages, allowing the calculation of very large complexes. It is worth noting that, because the choice of functional massively dictates the accuracy of any computed results, this may undermine the speed of this method. A single DFT calculation may run faster but benchmarking with several functionals to ensure the results are physically meaningful is often required, undermining improvements to computational time and cost.

2.1.6 The Difficulties of Anions and Resonances

Anions and their excited states present a difficult challenge to theoretical models. The problems can be broadly summarized as:^{166,167}

- there will always be an open-shell electronic configuration to consider for photodetachment processes;
- the excess electron is far more diffuse in nature than valence electrons;
- anions have high polarizability;
- electron correlation is non-negligible;
- dispersion becomes important in specific cases;
- resonances are embedded in the neutral plus free electron continuum;
- calculation of accurate vertical excitation energies and oscillator strengths require multiconfigurational and multireference methods.

Resonances cannot be robustly modelled using conventional quantum chemical methods as there are discrete energy levels that correspond to the valence resonances embedded in the neutral plus free electron continuum of states, where the energy of the free electron is not quantized.¹⁶⁸ The resonance wavefunction has large amplitude in the valence region, Figure 10, indicating that the electron is rather localised. However, the wavefunction decays exponentially into the classically forbidden tunnelling region, and beyond this region is a free

electron. It is the latter component of the resonance wavefunction that makes it clear that the orbital energy of the resonance state is not a sufficient description.

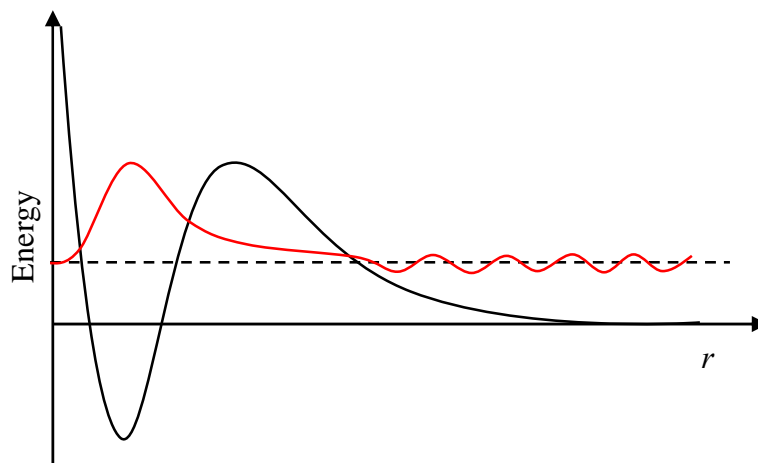


Figure 10 Qualitative representation of the effective radial potential and wavefunction of a metastable state.

Proper theoretical treatment of metastable states requires special techniques able to describe both the quasi-bound valence and the free-electron continuum components of their wavefunctions. An additional caveat arises when considering the dynamics of resonances, in which there are two processes involved, a fast electronic motion and a slower nuclear motion. The adiabatic coupling of these two processes in energetic regions where potential energy surfaces approach one another represent the breakdown of the Born-Oppenheimer approximation, introducing further complications.

Throughout the results sections, care has been taken to negate the problems associated with anions and resonances. Unfortunately, there is no one single method used to do this, as the severity of the problems is very much dependent on the system. For example, the nitrobenzene anion and related para-dinitrobenzene anion have open shell ground states and resonances, presenting real challenges to many electronic structure methods discussed in the previous sections. For these systems it was necessary to use XMCQDPT2, to restrict the active

space ensuring the calculation of resonances were physically meaningful and of quantitative value.

2.1.7 Theoretical Treatments of Non-valence States

In order to model non-valence states, special care must be taken theoretically. Non-valence states will be unbound in the Hartree-Fock approximation, but through proper treatment of electron correlation it is possible to model the excess electron binding. In addition to this, the diffuse character of the non-valence orbital requires careful choice of custom basis functions with very low orbital exponents.¹⁶⁹ It should be noted that the choice of basis set for the neutral core is also important, and one should ensure that this is flexible enough to accurately describe first the static charge distribution of the neutral, and second, the polarisation and dispersion stabilization of the anion upon electron attachment. The latter term outlines the importance for the inclusion of dynamic electron correlation within the method.

Electron correlation effects drastically alter the properties of dipole-bound states of anions.^{82,170–172} The main contribution to correlation arises from a dispersion-type interaction between the excess electron and the valence electrons of the polar molecule.¹⁷³ It has been demonstrated that high-order correlation effects play a major role in describing the electron binding energies of non-valence states, highlighting the need for accurately incorporating electron correlation in any computational method.^{76,170,171,174,175}

Pioneering theoretical work on calculation of the binding energies of electrons in non-valence states was carried out by Simons, Jordan, Skurski and Gutowski.^{169–171} One-electron models able to recover most of correlation contributions to electron binding energies were developed and shown to be able to accurately model non-valence states.^{176–178}

Correlation bound anions have been characterised by a number of theoretical groups.^{179–181} Through these studies it has been shown that it is crucial to use a theoretical method that allows the single occupied orbital to relax in response to the dispersion-type

correlation effects. Recent computational explorations of non-valence states by Jordan *et al.* have shown the strength and versatility of EOM-EA-CCSD and EOM-MP2 methods.¹⁸²

While EOM-EA-CCSD provides a powerful method of calculating non-valence states, one needs to be cautious when the reference state is open shell. In such cases, it is imperative to choose a ROHF neutral reference. Care also needs to be taken to minimize linear dependence on the orbital exponents chosen to represent the non-valence state.

2.1.8 Concluding Remarks

The aim of the previous sections was to provide a broad overview of the complexity of the problems and the care that must be taking for calculations of anions, resonances and non-valence states. More detailed exploration of methods used to model and investigate the properties of excited states are the subject of a number of publications.^{134,135,138,153,159,183,184} These sections were not intended to provide a complete guide to all methods for calculation of anions and resonances, indeed state-of-the-art techniques such as the complex absorbing potential method¹⁸⁵ and the stabilisation technique^{186,187} have been excluded in the interest of space.

This section demonstrates the complexity of the problems associated with theoretical investigations of anions. While there are some recommendations about the computational tools that may be optimal to represent properties of a molecular anion, there is no specific single method that is recommended. There are only a few aspects that are common to any good computational method; the necessity for incorporation of polarisation and diffuse functions in the basis set, agreement that Dunning basis sets represent the gold standard for calculations of molecular anions, and an appreciation for how to design the correct calculation for a specific problem. When considering more complex photoelectron signatures, there are circumstances in which each method performs well, and circumstances in which it performs poorly. This statement is not intended to criticize the methods available for calculation, rather to provide a

context for the breadth of different computational methods used through the results section of the thesis. Further broad considerations are provided in the Electronic Structure Calculation methods section, while more detailed discussions can be found in individual results chapters.

2.2 Aims

There is a wealth of studies that exploit photoelectron spectroscopy as a versatile tool for probing the electronic structure of anions. However, the focus is often on the information yielded from the kinetic energy of the photoelectron. The information encoded in the photoelectron angular distributions appears considerably less appreciated. This is particularly true of 2D anion photoelectron spectroscopy. This powerful technique has provided insight into the intrinsic dynamics of a number of anions of biological and astrochemical relevance. Photoelectron angular distributions are intrinsically sensitive to the character of an electronic state and provide a powerful insight into nuclear dynamics. It is possible to extract information about the initial and final electronic wavefunctions, the nature of the electronic state and geometry that undergoes photodetachment and the orientation of the departing photoelectron. As such, they are inherently more sensitive to ultrafast changes in electronic structure than the energetics. The aims of this thesis are to:

- Quantitatively model photoelectron angular distributions for frequency- and time-resolved photoelectron spectra;
- Develop 2D photoelectron spectroscopy and imaging;
- Investigate the role of resonances and non-valence states in electron capture processes.

The results section is organised by theme; Section A groups studies that showcase the importance of the information contained in the photoelectron angular distributions; Section B contains studies that focus on excited state dynamics; and Section C groups studies that investigate non-valence states of anions.

2.3 References

- 1 R. J. Zollweg, *J. Chem. Phys.*, 1969, **50**, 4251–4261.
- 2 J. P. Lowe, *J. Am. Chem. Soc.*, 1977, **99**, 5557–5570.
- 3 H. Hotop and W. C. Lineberger, *J. Phys. Chem. Ref. Data*, 1975, **4**, 539–576.
- 4 A. Einstein, *Ann. Phys.*, 1905, **17**, 132–148.
- 5 D. W. Turner, *Philos. Trans. R. Soc. Math. Phys. Eng. Sci.*, 1970, **268**, 7–31.
- 6 W. C. Lineberger and B. W. Woodward, *Phys. Rev. Lett.*, 1970, **25**, 424–427.
- 7 H. Hotop and W. C. Lineberger, *J. Phys. Chem. Ref. Data*, 1985, **14**, 731–750.
- 8 D. G. Leopold, A. E. S. Miller and W. C. Lineberger, *J. Am. Chem. Soc.*, 1986, **108**, 1379–1384.
- 9 C. T. Wickham, Jones, K. M. Ervin, G. B. Ellison and W. C. Lineberger, *J. Chem. Phys.*, 1989, **91**, 2762–2763.
- 10 K. M. Ervin and W. C. Lineberger, *J. Phys. Chem.*, 1991, **95**, 1167–1177.
- 11 J. P. Rogers, C. S. Anstöter and J. R. R. Verlet, *Nat. Chem.*, 2018, **10**, 341–346.
- 12 M. Born and R. Oppenheimer, *Ann. Phys.*, 1927, **389**, 457–484.
- 13 E. Condon, *Phys. Rev.*, 1926, **28**, 1182–1201.
- 14 J. Simons, *J. Am. Chem. Soc.*, 1981, **103**, 3971–3976.
- 15 A. Weaver, D. W. Arnold, S. E. Bradforth and D. M. Neumark, *J. Chem. Phys.*, 1991, **94**, 1740–1751.
- 16 R. F. Gunion, M. K. Gilles, M. L. Polak and W. C. Lineberger, *Int. J. Mass Spectrom. Ion Process.*, 1992, **117**, 601–620.
- 17 L.-S. Wang, *J. Chem. Phys.*, 2015, **143**, 040901.
- 18 D. M. Neumark, *J. Phys. Chem. A*, 2008, **112**, 13287–13301.
- 19 P. G. Wenthold and W. C. Lineberger, *Acc. Chem. Res.*, 1999, **32**, 597–604.
- 20 J. H. Hendricks, S. A. Lyapustina, H. L. de Clercq, J. T. Snodgrass and K. H. Bowen, *J. Chem. Phys.*, 1996, **104**, 7788–7791.
- 21 E. P. Wigner, *Phys. Rev.*, 1948, **73**, 1002–1009.
- 22 D. Dill, *J. Chem. Phys.*, 1976, **65**, 1130–1133.
- 23 J. Marks, P. S. Drzaic, R. F. Foster, D. M. Wetzell, J. I. Brauman, J. S. Uppal and R. H. Staley, *Rev. Sci. Instrum.*, 1987, **58**, 1460–1463.
- 24 D. W. Chandler and P. L. Houston, *J. Chem. Phys.*, 1987, **87**, 1445.
- 25 A. T. J. B. Eppink and D. H. Parker, *Rev. Sci. Instrum.*, 1997, **68**, 3477–3484.
- 26 J. Cooper and R. N. Zare, *J. Chem. Phys.*, 1968, **48**, 942–943.
- 27 K. L. Reid, *Annu. Rev. Phys. Chem.*, 2003, **54**, 397–424.
- 28 A. Sanov, *Annu. Rev. Phys. Chem.*, 2014, **65**, 341–363.
- 29 D. Khuseynov, C. C. Blackstone, L. M. Culberson and A. Sanov, *J. Chem. Phys.*, 2014, **141**, 124312.
- 30 E. R. Grumbling and A. Sanov, *J. Chem. Phys.*, 2011, **135**, 164302.
- 31 C. M. Oana and A. I. Krylov, *J. Chem. Phys.*, 2007, **127**, 234106.
- 32 C. M. Oana and A. I. Krylov, *J. Chem. Phys.*, 2009, **131**, 124114.
- 33 S. Gozem, A. O. Gunina, T. Ichino, D. L. Osborn, J. F. Stanton and A. I. Krylov, *J. Phys. Chem. Lett.*, 2015, **6**, 4532–4540.
- 34 B. T. Pickup, *Chem. Phys.*, 1977, **19**, 193–208.
- 35 R. McWeeny and B. T. Pickup, *Rep. Prog. Phys.*, 1980, **43**, 1065–1144.
- 36 M. Deleuze, B. T. Pickup and J. Delhalle, *Mol. Phys.*, 1994, **83**, 655–686.
- 37 G. M. Seabra, I. G. Kaplan, V. G. Zakrzewski and J. V. Ortiz, *J. Chem. Phys.*, 2004, **121**, 4143–4155.
- 38 G. Scoles, Ed., *Atomic and molecular beam methods*, Oxford University Press, New York, 1988.
- 39 E. de Hoffmann and V. Stroobant, *Mass Spectrometry - Principles and Applications.*, John Wiley & Sons, Chichester, Second Edi., 2007.
- 40 J. B. Fenn, M. Mann, C. K. Meng, S. F. Wong and C. M. Whitehouse, *Science*, 1989, **246**, 64–71.
- 41 R. B. Cole, Ed., *Electrospray ionization mass spectrometry: fundamentals, instrumentation, and applications*, Wiley, New York, 1997.
- 42 S. Daly, M. Porrini, F. Rosu and V. Gabelica, *Faraday Discuss.*, 2019, **217**, 361–382.

- 43 C. R. S. Mooney, D. A. Horke, A. S. Chatterley, A. Simperler, H. H. Fielding and J. R. R. Verlet, *Chem. Sci.*, 2013, **4**, 921–927.
- 44 D. A. Horke, A. S. Chatterley, J. N. Bull and J. R. R. Verlet, *J. Phys. Chem. Lett.*, 2015, **6**, 189–194.
- 45 A. S. Chatterley, C. W. West, G. M. Roberts, V. G. Stavros and J. R. R. Verlet, *J. Phys. Chem. Lett.*, 2014, **5**, 843–848.
- 46 A. V. Bochenkova, C. R. S. Mooney, M. A. Parkes, J. L. Woodhouse, L. Zhang, R. Lewin, J. M. Ward, H. C. Hailes, L. H. Andersen and H. H. Fielding, *Chem Sci*, 2017, **8**, 3154–3163.
- 47 J. L. Woodhouse, M. Assmann, M. A. Parkes, H. Grounds, S. J. Pacman, J. C. Anderson, G. A. Worth and H. H. Fielding, *Phys. Chem. Chem. Phys.*, 2017, **19**, 22711–22720.
- 48 J. R. R. Verlet, D. A. Horke and A. S. Chatterley, *Phys. Chem. Chem. Phys.*, 2014, **16**, 15043.
- 49 X.-B. Wang, C.-F. Ding and L.-S. Wang, *Phys. Rev. Lett.*, 1998, **81**, 3351–3354.
- 50 L.-S. Wang, C.-F. Ding, X.-B. Wang and J. B. Nicholas, *Phys. Rev. Lett.*, 1998, **81**, 2667–2670.
- 51 A. S. Chatterley, D. A. Horke and J. R. R. Verlet, *Phys. Chem. Chem. Phys.*, 2014, **16**, 489–496.
- 52 K. Muller-Dethlefs and E. W. Schlag, *Annu. Rev. Phys. Chem.*, 1991, **42**, 109–136.
- 53 K. Müller-Dethlefs, E. W. Schlag, E. R. Grant, K. Wang and B. V. McKoy, in *Advances in Chemical Physics*, eds. I. Prigogine and S. A. Rice, John Wiley & Sons, Inc., Hoboken, NJ, USA, 2007, pp. 1–104.
- 54 T. N. Kitsopoulos, I. M. Waller, J. G. Loeser and D. M. Neumark, *Chem. Phys. Lett.*, 1989, **159**, 300–306.
- 55 C. Blondel, C. Delsart and F. Dulieu, *Phys. Rev. Lett.*, 1996, **77**, 3755–3758.
- 56 C. Valli, C. Blondel and C. Delsart, *Phys. Rev. A*, 1999, **59**, 3809–3815.
- 57 C. C. Arnold, D. M. Neumark, D. M. Cyr and M. A. Johnson, *J. Phys. Chem.*, 1995, **99**, 1633–1636.
- 58 G. R. Burton, C. Xu, C. C. Arnold and D. M. Neumark, *J. Chem. Phys.*, 1996, **104**, 2757–2764.
- 59 C. C. Arnold and D. M. Neumark, *J. Chem. Phys.*, 1993, **99**, 3353–3362.
- 60 C. Delsart, F. Goldfarb and C. Blondel, *Phys. Rev. Lett.*, 2002, **89**, 183002.
- 61 A. Osterwalder, M. J. Nee, J. Zhou and D. M. Neumark, *J. Chem. Phys.*, 2004, **121**, 6317–6322.
- 62 C. Hock, J. B. Kim, M. L. Weichman, T. I. Yacovitch and D. M. Neumark, *J. Chem. Phys.*, 2012, **137**, 244201.
- 63 D. Gerlich, in *Advances in Chemical Physics*, eds. C.-Y. Ng, M. Baer, I. Prigogine and S. A. Rice, John Wiley & Sons, Inc., Hoboken, NJ, USA, 2007, pp. 1–176.
- 64 R. Wester, *J. Phys. B At. Mol. Opt. Phys.*, 2009, **42**, 154001.
- 65 J. Doyle and W. Campbell, in *Cold Molecules*, eds. W. Stwalley, R. Krems and B. Friedrich, CRC Press, 2009.
- 66 M. L. Weichman, J. A. DeVine, D. S. Levine, J. B. Kim and D. M. Neumark, *Proc. Natl. Acad. Sci.*, 2016, **113**, 1698–1705.
- 67 Z. Luo, X. Chen, J. Li and C. Ning, *Phys. Rev. A*, 2016, **93**, 020501.
- 68 K. M. Ervin, T. M. Ramond, G. E. Davico, R. L. Schwartz, S. M. Casey and W. C. Lineberger, *J. Phys. Chem. A*, 2001, **105**, 10822–10831.
- 69 M. L. Weichman, J. B. Kim, J. A. DeVine, D. S. Levine and D. M. Neumark, *J. Am. Chem. Soc.*, 2015, **137**, 1420–1423.
- 70 J. Zhou, E. Garand, W. Eisfeld and D. M. Neumark, *J. Chem. Phys.*, 2007, **127**, 034304.
- 71 J. A. DeVine, M. L. Weichman, S. J. Lyle and D. M. Neumark, *J. Mol. Spectrosc.*, 2017, **332**, 16–21.
- 72 X.-B. Wang, H.-K. Woo, B. Kiran and L.-S. Wang, *Angew. Chem. Int. Ed.*, 2005, **44**, 4968–4972.
- 73 X.-B. Wang and L.-S. Wang, *Rev. Sci. Instrum.*, 2008, **79**, 073108.
- 74 H. T. Liu, C. G. Ning, D. L. Huang, P. D. Dau and L. S. Wang, *Angew. Chem. - Int. Ed.*, 2013, **52**, 8976–8979.
- 75 G. Z. Zhu, Y. Liu and L. S. Wang, *Phys. Rev. Lett.*, 2017, **119**, 1–5.
- 76 G. L. Gutsev and R. J. Bartlett, *J. Chem. Phys.*, 1996, **105**, 8785–8792.

- 77 R. N. Compton, H. S. Carman, C. Desfrancois, H. Abdoul-Carime, J. P. Schermann, J. H. Hendricks, S. A. Lyapustina and K. H. Bowen, *J. Chem. Phys.*, 1996, **105**, 3472–3478.
- 78 L. Lehr, *Science*, 1999, **284**, 635–638.
- 79 J. H. Hendricks, S. A. Lyapustina, H. L. de Clercq and K. H. Bowen, *J. Chem. Phys.*, 1998, **108**, 8–11.
- 80 K. D. Jordan and W. Luken, *J. Chem. Phys.*, 1976, **64**, 2760–2766.
- 81 E. Fermi and E. Teller, *Phys. Rev.*, 1947, **72**, 399–408.
- 82 K. D. Jordan and F. Wang, *Annu. Rev. Phys. Chem.*, 2003, **54**, 367–396.
- 83 K. D. Jordan, *Acc. Chem. Res.*, 1979, **12**, 36–42.
- 84 W. R. Garrett, *Phys. Rev. A*, 1971, **3**, 961–972.
- 85 W. R. Garrett, *Chem. Phys. Lett.*, 1970, **5**, 393–397.
- 86 O. H. Crawford and W. R. Garrett, *J. Chem. Phys.*, 1977, **66**, 4968–4970.
- 87 D.-L. Huang, H.-T. Liu, C.-G. Ning and L.-S. Wang, *J. Chem. Phys.*, 2015, **142**, 124309.
- 88 H.-T. Liu, C.-G. Ning, D.-L. Huang and L.-S. Wang, *Angew. Chem. Int. Ed.*, 2014, **53**, 2464–2468.
- 89 D.-L. Huang, H.-T. Liu, C.-G. Ning, P. D. Dau and L.-S. Wang, *Chem. Phys.*, 2017, **482**, 374–383.
- 90 D.-L. Huang, H.-T. Liu, C.-G. Ning, G.-Z. Zhu and L.-S. Wang, *Chem. Sci.*, 2015, **6**, 3129–3138.
- 91 G.-Z. Zhu, L. F. Cheung, Y. Liu, C.-H. Qian and L.-S. Wang, *J. Phys. Chem. Lett.*, 2019, **10**, 4339–4344.
- 92 S. M. Ciborowski, R. M. Harris, G. Liu, C. J. Martinez-Martinez, P. Skurski and K. H. Bowen, *J. Chem. Phys.*, 2019, **150**, 161103.
- 93 J. N. Bull and J. R. R. Verlet, *Sci. Adv.*, 2017, **3**, e1603106.
- 94 A. Amrein, R. Simpson and P. Hackett, *J. Chem. Phys.*, 1991, **95**, 1781–1800.
- 95 A. Amrein, R. Simpson and P. Hackett, *J. Chem. Phys.*, 1991, **94**, 4663–4664.
- 96 B. Baguenard, J. C. Pinaré, C. Bordas and M. Broyer, *Phys. Rev. A*, 2001, **63**, 023204.
- 97 J. U. Andersen, E. Bonderup and K. Hansen, *J Phys B Mol Opt Phys*, 2002, **35**, R1–R30.
- 98 K. Regeta and M. Allan, *Phys. Rev. Lett.*, 2013, **110**, 203201.
- 99 F. Currell and J. Comer, *Phys. Rev. Lett.*, 1995, **74**, 1319–1323.
- 100 T. Reddish, F. Currell and J. Comer, *J Phys E Sci Instrum*, 1988, **36**, 203–207.
- 101 M. Allan, K. Regeta, J. D. Gorfinkiel, Z. Mašín, S. Grimme and C. Bannwarth, *Eur. Phys. J. D*, 2016, **70**, 123.
- 102 C. L. Adams, H. Schneider and J. M. Weber, *J. Phys. Chem. A*, 2010, **114**, 4017–4030.
- 103 D. B. Dao and R. Mabbs, *J. Chem. Phys.*, 2014, **141**, 154304.
- 104 L. H. Stanley, C. S. Anstöter and J. R. R. Verlet, *Chem. Sci.*, 2017, **8**, 3054–3061.
- 105 L. H. Andersen and A. V. Bochenkova, *Eur. Phys. J. D*, 2009, **51**, 5–14.
- 106 I.-R. Lee, W. Lee and A. H. Zewail, *Proc. Natl. Acad. Sci.*, 2006, **103**, 258–262.
- 107 T. E. Meyer, G. Tollin, J. H. Hazzard and M. A. Cusanovich, *Biophys. J.*, 1989, **56**, 559–564.
- 108 R. Schoenlein, L. Peteanu, R. Mathies and C. Shank, *Science*, 1991, **254**, 412–415.
- 109 A. H. Zewail, *Angew Chem Int Ed*, 2000, **39**, 2586–2631.
- 110 A. H. Zewail, *Science*, 1988, **242**, 1645–1653.
- 111 A. H. Zewail, *J. Phys. Chem. A*, 2000, **104**, 5660–5694.
- 112 A. Stolow, A. E. Bragg and D. M. Neumark, *Chem. Rev.*, 2004, **104**, 1719–1758.
- 113 V. Blanchet, M. Z. Zgierski, T. Seideman and A. Stolow, *Nature*, 1999, **401**, 52–54.
- 114 I. Shavitt and R. J. Bartlett, *Many-body methods in chemistry and physics: MBPT and coupled-cluster theory*, Cambridge University Press, Cambridge ; New York, 2009.
- 115 A. Szabo and N. S. Ostlund, *Modern quantum chemistry: introduction to advanced electronic structure theory*, Dover Publications, Mineola, N.Y, 1996.
- 116 R. McWeeny, *Methods of molecular quantum mechanics*, Academic Press, London, 2nd edn., 1992.
- 117 I. Fleming, *Molecular orbitals and organic chemical reactions*, Wiley, Hoboken, N.J, Reference ed., 2010.
- 118 E. Steiner and P. W. Fowler, *J. Phys. Chem. A*, 2001, **105**, 9553–9562.
- 119 W.-C. Chen and I. Chao, *J. Phys. Chem. C*, 2014, **118**, 20176–20183.

- 120 K. Liu, C.-L. Song, Y.-C. Zhou, X.-Y. Zhou, X.-J. Pan, L.-Y. Cao, C. Zhang, Y. Liu, X. Gong and H.-L. Zhang, *J. Mater. Chem. C*, 2015, **3**, 4188–4196.
- 121 T. Koopmans, *Physica*, 1934, **1**, 104–113.
- 122 Chr. Møller and M. S. Plesset, *Phys. Rev.*, 1934, **46**, 618–622.
- 123 W. Kutzelnigg, *J. Mol. Struct. THEOCHEM*, 1988, **181**, 33–54.
- 124 B. O. Roos, R. Lindh, P. Å. Malmqvist, V. Veryazov and P.-O. Widmark, *Multiconfigurational quantum chemistry*, 2016.
- 125 P. Čársky, J. Paldus and J. Pittner, Eds., *Recent progress in coupled cluster methods: theory and applications*, Springer, Dordrecht, 2010.
- 126 G. D. Purvis and R. J. Bartlett, *J. Chem. Phys.*, 1982, **76**, 1910–1918.
- 127 T. H. Dunning, *J. Chem. Phys.*, 1989, **90**, 1007–1023.
- 128 B. O. Roos, P. R. Taylor and P. E. M. Sigbahn, *Chem. Phys.*, 1980, **48**, 157–173.
- 129 J. Townsend, J. K. Kirkland and K. D. Vogiatzis, in *Mathematical Physics in Theoretical Chemistry*, Elsevier, 2019, pp. 63–117.
- 130 V. Veryazov, P. Å. Malmqvist and B. O. Roos, *Int. J. Quantum Chem.*, 2011, **111**, 3329–3338.
- 131 K. Hirao, *Chem. Phys. Lett.*, 1992, **190**, 374–380.
- 132 K. Hirao, *Chem. Phys. Lett.*, 1992, **196**, 397–403.
- 133 Kerstin. Andersson, P.-Åke. Malmqvist, B. O. Roos, A. J. Sadlej and Krzysztof. Wolinski, *J. Phys. Chem.*, 1990, **94**, 5483–5488.
- 134 K. Andersson, P. Malmqvist and B. O. Roos, *J. Chem. Phys.*, 1992, **96**, 1218–1226.
- 135 H. Nakano, *J. Chem. Phys.*, 1993, **99**, 7983–7992.
- 136 J. Finley, P.-Å. Malmqvist, B. O. Roos and L. Serrano-Andrés, *Chem. Phys. Lett.*, 1998, **288**, 299–306.
- 137 K. Bravaya, A. Bochenkova, A. Granovsky and A. Nemukhin, *J. Am. Chem. Soc.*, 2007, **129**, 13035–13042.
- 138 A. A. Granovsky, *J. Chem. Phys.*, 2011, **134**, 214113.
- 139 T. Shiozaki, W. Györfy, P. Celani and H.-J. Werner, *J. Chem. Phys.*, 2011, **135**, 081106.
- 140 H. V. Kiefer, E. Lattouf, N. W. Persen, A. V. Bochenkova and L. H. Andersen, *Phys Chem Chem Phys*, 2015, **17**, 20056–20060.
- 141 A. V. Bochenkova, B. Klærke, D. B. Rahbek, J. Rajput, Y. Toker and L. H. Andersen, *Angew. Chem. - Int. Ed.*, , DOI:10.1002/anie.201404609.
- 142 J. L. Knudsen, A. Kluge, A. V. Bochenkova, H. V. Kiefer and L. H. Andersen, *Phys. Chem. Chem. Phys.*, 2018, **20**, 7190–7194.
- 143 G. Ghigo, B. O. Roos and P.-Å. Malmqvist, *Chem. Phys. Lett.*, 2004, **396**, 142–149.
- 144 M. Schreiber, M. R. Silva-Junior, S. P. A. Sauer and W. Thiel, *J. Chem. Phys.*, 2008, **128**, 134110.
- 145 Y.-K. Choe, H. A. Witek, J. P. Finley and K. Hirao, *J. Chem. Phys.*, 2001, **114**, 3913–3918.
- 146 C. Camacho, H. A. Witek and S. Yamamoto, *J. Comput. Chem.*, 2009, **30**, 468–478.
- 147 B. O. Roos, K. Andersson, M. P. Fülscher, L. Serrano-Andrés, K. Pierloot, M. Merchán and V. Molina, *J. Mol. Struct. THEOCHEM*, 1996, **388**, 257–276.
- 148 B. O. Roos and K. Andersson, *Chem. Phys. Lett.*, 1995, **245**, 215–223.
- 149 S. Pathak, L. Lang and F. Neese, *J. Chem. Phys.*, 2017, **147**, 234109.
- 150 H. A. Witek, Y.-K. Choe, J. P. Finley and K. Hirao, *J. Comput. Chem.*, 2002, **23**, 957–965.
- 151 J. F. Stanton and R. J. Bartlett, *J. Chem. Phys.*, 1993, **98**, 7029–7039.
- 152 J. Geertsens, M. Rittby and R. J. Bartlett, *Chem. Phys. Lett.*, 1989, **164**, 57–62.
- 153 A. I. Krylov, *Annu. Rev. Phys. Chem.*, 2008, **59**, 433–462.
- 154 A. I. Krylov, in *Reviews in Computational Chemistry, Volume 30*, eds. A. L. Parrill and K. B. Lipkowitz, John Wiley & Sons, 2017, pp. 151–224.
- 155 R. G. Parr and W. Yang, *Density-functional theory of atoms and molecules*, Oxford University Press, New York, NY, 1st edn., 1994.
- 156 W. Kohn, A. D. Becke and R. G. Parr, *J. Phys. Chem.*, 1996, **100**, 12974–12980.
- 157 P. Hohenberg and W. Kohn, *Phys. Rev.*, 1964, **136**, B864–B871.
- 158 Tom. Ziegler, *Chem. Rev.*, 1991, **91**, 651–667.
- 159 A. Dreuw and M. Head-Gordon, *Chem. Rev.*, 2005, **105**, 4009–4037.

- 160 D. P. Chong, *Recent Advances in Density Functional Methods: (Part I)*, World Scientific, 1995, vol. 1.
- 161 D. J. Tozer, R. D. Amos, N. C. Handy, B. O. Roos and L. Serrano-Andrés, *Mol. Phys.*, 1999, **97**, 859–868.
- 162 A. L. Sobolewski and W. Domcke, *Chem. Phys.*, 2003, **294**, 73–83.
- 163 A. Dreuw and M. Head-Gordon, *J. Am. Chem. Soc.*, 2004, **126**, 4007–4016.
- 164 J.-D. Chai and M. Head-Gordon, *Phys. Chem. Chem. Phys.*, 2008, **10**, 6615.
- 165 M. J. G. Peach, E. I. Tellgren, P. Sałek, T. Helgaker and D. J. Tozer, *J. Phys. Chem. A*, 2007, **111**, 11930–11935.
- 166 J. Simons, *J. Phys. Chem. A*, 2008, **112**, 6401–6511.
- 167 J. C. Rienstra-Kiracofe, G. S. Tschumper, H. F. Schaefer III, S. Nandi and G. B. Ellison, *Chem. Rev.*, 2002, **102**, 231–282.
- 168 J. Simons and K. D. Jordan, *Chem. Rev.*, 1987, **87**, 535–555.
- 169 P. Skurski, M. Gutowski and J. Simons, *Int. J. Quantum Chem.*, 2000, **80**, 1024–1038.
- 170 M. Gutowski, P. Skurski, K. D. Jordan and J. Simons, *Int. J. Quantum Chem.*, 1997, **64**, 183–191.
- 171 M. Gutowski, P. Skurski, A. I. Boldyrev, J. Simons and K. D. Jordan, *Phys. Rev. A*, 1996, **54**, 1906–1909.
- 172 L. Adamowicz, *J. Chem. Phys.*, 1989, **91**, 7787–7790.
- 173 M. Gutowski and P. Skurski, *Chem. Phys. Lett.*, 1999, **300**, 331–338.
- 174 K. Yokoyama, G. W. Leach, J. B. Kim, W. C. Lineberger, A. I. Boldyrev and M. Gutowski, *J. Chem. Phys.*, 1996, **105**, 10706–10718.
- 175 C. Desfrancois, H. Abdoul-Carime, S. Carles, V. Périquet, J. P. Schermann, D. M. A. Smith and L. Adamowicz, *J. Chem. Phys.*, 1999, **110**, 11876–11883.
- 176 F. Wang and K. D. Jordan, *J. Chem. Phys.*, 2001, **114**, 10717–10724.
- 177 F. Wang and K. D. Jordan, *J. Chem. Phys.*, 2002, **116**, 6973–6981.
- 178 M. Šindelka, V. Špirko and P. Jungwirth, *J. Chem. Phys.*, 2002, **117**, 5113–5123.
- 179 V. K. Voora and K. D. Jordan, *J. Phys. Chem. A*, 2014, **118**, 7201–7205.
- 180 T. Sommerfeld, B. Bhattarai, V. P. Vysotskiy and L. S. Cederbaum, *J. Chem. Phys.*, 2010, **133**, 114301.
- 181 V. G. Bezchastnov, V. P. Vysotskiy and L. S. Cederbaum, *Phys. Rev. Lett.*, 2011, **107**, 133401.
- 182 V. K. Voora, A. Kairalapova, T. Sommerfeld and K. D. Jordan, *J. Chem. Phys.*, 2017, **147**, 214114.
- 183 H. Lischka, D. Nachtigallová, A. J. A. Aquino, P. G. Szalay, F. Plasser, F. B. C. MacHado and M. Barbatti, *Chem. Rev.*, 2018, **118**, 7293–7361.
- 184 T.-C. Jagau, K. B. Bravaya and A. I. Krylov, *Annu. Rev. Phys. Chem.*, 2017, **68**, 525–553.
- 185 U. V. Riss and H. D. Meyer, *J. Phys. B At. Mol. Opt. Phys.*, 1993, **26**, 4503–4535.
- 186 B. M. Nestmann and S. D. Peyerimhoff, *J. Phys. B At. Mol. Phys.*, 1985, **18**, 4309–4319.
- 187 A. F. Izmaylov, S. O. Adamson and A. Zaitsevskii, *J. Phys. B At. Mol. Opt. Phys.*, 2004, **37**, 2321–2329.

Methods: Frequency-, Angle- and Time-Resolved Photoelectron Spectroscopy and Electronic Structure Calculations

In order to elucidate information about the photochemical and intrinsic excited state dynamics of molecular anions, we have used gas phase photoelectron spectroscopy and a range of electronic structure methods. The following chapter gives a broad overview of the two experimental set-ups that have been used for data acquisition in this thesis, the methods and procedural workflows used to acquire and process data, and a summary of the type of information that could be extracted from that data. Further details of the instrumentation, including detailed descriptions of development and operation, are the subject of several publications and previous students' theses and can be found in these.¹⁻⁷ On the theoretical front, several levels of theory based on density functional theory, coupled-cluster electron correlation, and multireference perturbation theory, have been applied to best describe and assist in interpretation of the experimental data. In one significant study, a simple Hückel model was found to provide adequate qualitative insight into the evolution of electronic structure in a series of chromophores, however, reliable and quantitative analysis of photophysical properties such as the vertical energies of resonances or the binding energy of dipole bound states require more rigorous *ab initio* methods. The latter sections of this chapter provide an overview of the different levels of theory used, for which systems they are feasible or suitable, and the experimental parameter being modelled. The full details of calculations, including choice of basis set and/or functional and active space for multiconfigurational/multireference calculations, are given in each chapter.

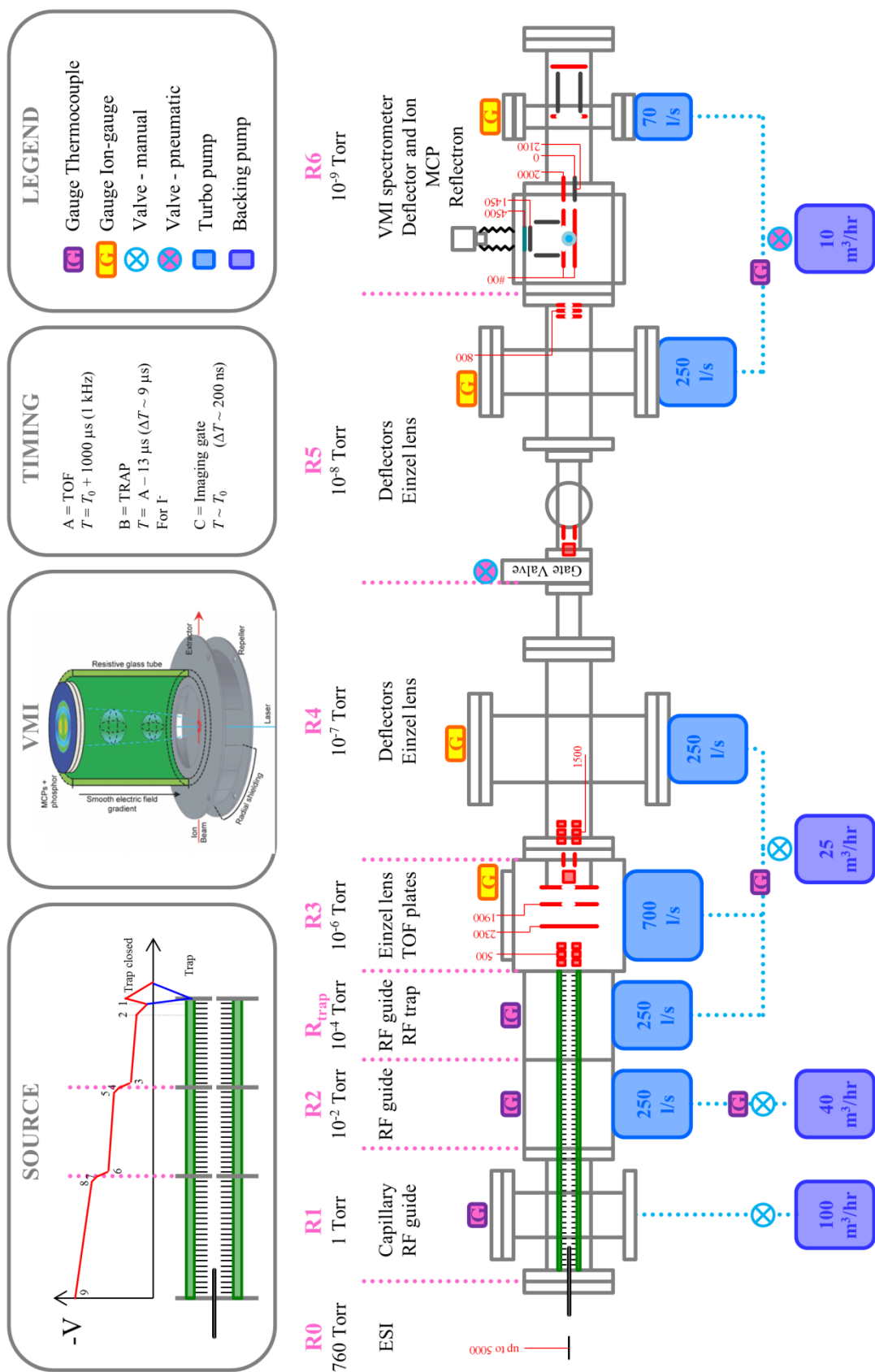


Figure 11 Schematic of the electrospray source ionisation (ESI) gas phase photoelectron spectrometer.

3 Gas-Phase Photoelectron Spectroscopy of Anions

3.1 The Electrospray Ionisation Source Machine

The design and operation of the Electrospray Ionisation Source Machine has been the subject of a number of past Verlet members PhD theses and publications.^{1-4,6,7} In this chapter, only a brief overview of the experiment is provided, which should be sufficient to understand all measurements and interpretation presented in later chapters.

3.1.1 Generation of Anions

In order to produce gaseous ions, our machine borrows an ionisation method prevalently used in the mass spectrometry community, electrospray ionisation (ESI).⁸ ESI is a ‘soft’ ionisation technique meaning that ions are gently ionized and introduced into the gas-phase with little fragmentation/ion activation, making it highly versatile and enabling the production of a wide range of parent ions, including macromolecules, polyanions and biomolecules.⁹⁻¹¹ The experimental set-up is illustrated schematically in Figure 11 and all discussion of the instrument is with reference to this diagram. In the ESI source, a dilute solution containing the molecule of interest (~1 mM) and a carrier solvent (e.g. methanol or acetonitrile for polar analytes) is pumped through a fine electrospray needle by a syringe pump at a steady flow rate (this region is defined by R0 in Figure 1). An adjustable negative high voltage is applied to the needle tip producing a vapour plume of anions. Ions become desolvated during the electrospray process, a process which can be aided with several (adjustable) streams of dry nitrogen gas over/along the ESI capillary. The needle is held in close proximity to a capillary tube that introduces ions into to the first vacuum region. The anions are drawn into the transfer capillary tube by a potential gradient formed from the high applied voltage on the ESI needle and by fluid dynamics of the gas-flow through the capillary into low pressure.

3.1.2 Selection of Anions

The electrosprayed anions pass through the transfer capillary and into the first of six vacuum regions. Region 1 is pumped to ~ 1 mbar and contains the first of a series of radio-frequency (RF) ring electrode guides. Region 2 and “trap” contain further RF ion guides and are held at pressures of $\sim 1 \times 10^{-2}$ mbar and $\sim 1 \times 10^{-4}$ mbar, respectively. These regions provide differentially pumped stages.

The ion guide applies both radially-confining RF fields and longitudinal DC ramps, which forms a gradual potential gradient along which the anions move. The final ring electrode in R_{trap} is held at a higher voltage in order to create a potential well to accumulate ions. In order to pulse the trapped ions into the TOF region, the final electrode voltage is rapidly decreased, changing the potential gradient profile. The voltages applied and the timing of the trap are adjusted using a digital delay generator to select the anion of interest and allowing optimum signal levels. An important consideration is that electrosprayed ions are trapped under conditions that produce a thermal ensemble, i.e. at ~ 298 K or laboratory temperature.

Once the trap is emptied, the ion packet travels from R_{trap} into the TOF mass spectrometry region, R3-R5. Before entering the TOF, the ion packet passes through an Einzel lens. The Einzel lens consists of three electrodes. The two outer electrodes are grounded, and the inner electrode is held at ~ -0.5 kV. An Einzel lens is analogous to an optical lens but for charged particles, with a voltage-variable focal length. Following the Einzel lens are the TOF plates. This arrangement consists of three steel ring electrodes in a collinear Wiley-McLaren arrangement.¹² The three ring electrodes are referred to as the repeller, accelerator and ground. All three electrodes are large, thin plates with holes in the centre. Both the accelerator and ground plates have a fine steel mesh covering the central hole, allowing for ion transmission with minimal distorting fringe fields. As the ion packet passes through the repeller and accelerator plates, they are pulsed from ground to -2.3 and -1.9 kV, respectively. The

difference in potential between the plates defines the focal length of the TOF system. The operating pressure in R3 is typically 1×10^{-6} mbar. In the TOF, the single ion packet injected by the trap becomes multiple ion packets separated according to the m/z ratio.

The remainder of the TOF region of the spectrometer is a 1.3 m drift tube. At the beginning of the drift tube is a set of x - y deflectors, followed by a second Einzel lens in R4. The deflectors consist of two pairs of parallel plates, in a square arrangement along the ion path, to which a potential of ± 50 V may be applied. Application of potentials to the deflectors allows correction to any misalignment in ion beam. The second Einzel lens is of the same arrangement as R3, with the inner electrode set to ~ 1.5 kV. The remainder of R4 is a TOF drift tube terminated by a pneumatic gate valve. The gate valve serves to isolate the ultrahigh vacuum regions (R5 and R6) from the lower vacuum regions when closed. This is important because the ESI source regions are regularly vented for maintenance. The detector chambers require ultra-high vacuum and can take weeks/months to reach ideal conditions if they are vented.

3.1.3 Detection of Anions

In R5, the ions pass through a second set of pairs of x - y deflectors, the remainder of the TOF drift tube and the final Einzel lens. The final Einzel lens is in the same arrangement as the preceding two and allows for focussing of the ion beam in the photodetachment and detection region (R6), which is held at a pressure of $<1 \times 10^{-9}$ mbar. This Einzel lens focuses the ions into the centre of the repeller and extractor electrodes of the velocity-map imaging (VMI) stack (R6).

In the VMI stack in R6, the ion packet is intersected with a light pulse from either an OPO or femtosecond laser, generating photoelectrons. The laser pulses enter the chamber through a 1 mm thickness calcium fluoride (CaF_2) window. The laser pulse and ion packet are timed to overlap allowing for irradiation of a mass-selected ion bunch. The laser pulse then

exits the chamber through a second 3 mm thickness CaF_2 window at the back of the chamber. The second window is mounted at Brewster's angle to minimise back reflection into the chamber.

The VMI set-up is loosely based upon the original design of Eppink and Parker.¹³ A complete description is given by Horke *et al.*²⁻⁴ At the bottom of the VMI stack, are two electrodes that are held at the same negative voltage. The first of the two electrodes is a solid plate, whereas the second plate has a hole in the central axis which leads from the grounded detector by a resistive glass tube. The resistive glass tube has an even gradient which minimizes any disruption to the electron path to the top electrode. The VMI lens is generated by the penetration of the field from the resistive glass through the central hole in the upper plate.⁴ The detector is a dual micro-channel plate (MCP) in a chevron arrangement. The chevron arrangement amplifies photoelectron strikes (e.g. by 10^6). The electron bursts are then projected onto a P43 phosphor screen generating a green flash of light, which is imaged by a charge-coupled device (CCD). The MCPs are gated by a ~ 200 ns pulse that is triggered to be coincidental with ion packet irradiation to reduce background noise. The voltages applied to MCPs and phosphor screen can be adjusted depending on photoelectron signal level (depends on photodetachment cross-section, laser fluence and ion signal), but typically the MCPs are operated with 0.7 kV across each and the phosphor with 3 kV above the back of the last MCP.

The TOF spectrum of the ions is measured by another MCP at the far end of the spectrometer, after ions have traversed through the VMI stack. Ions are deflected onto the MCP using an electrode held at ~ 2 kV. The mass spectrum of the ion beam is given by recording the output from the MCP as a function of time after TOF pulsing and is output to a digital oscilloscope. The laser pulse, imaging gate and TOF spectrum can all be visualised on the scope allowing delays to be appropriately adjusted to ensure the correct m/z ion packet is being investigated.

3.1.4 Imaging Photoelectrons

Following irradiation of the ion packet, a cloud of photoelectrons are produced. The photoelectron expand as a so-called Newton sphere from the photodetachment region toward the MCP detector under the influence of the electric field. This 3D sphere is then pancaked onto the detector, i.e. some of the velocity vector information is lost. Post-detection, the photoelectron Newton sphere needs to be reconstructed to extract the nascent velocities of the photodetached electrons, which we commonly interpret in terms of kinetic energy and angular distributions.

Raw ('pancaked') photoelectron images are captured using a lens and CCD camera which is interfaced to a computer and data acquisition program written in LabVIEW (8.5) on a desktop computer. The raw photoelectron image can be both processed on the fly for visualization and the final image offline using a polar onion peeling (POP) algorithm. This provides the 1D radial spectra and photoelectron angular distributions. The POP algorithm was developed in the Verlet group and is based on onion peeling in polar coordinates.¹ The radial spectra are then converted to photoelectron spectra through converting the radial axis, r , into eKE space by squaring all radii ($r^2 \propto \text{eKE}$), where r is the number of pixels from the centre of the photoelectron image. The energy axis is then calibrated using a spectrum with well-known photoelectron features to define a proportionality constant. Following the transformation from r to eKE space, the raw intensity must also be scaled. This is done through the relationship $I(\text{eKE}) = I(r)/r$, where $I(\text{eKE})$ refers to the signal intensity scale for the photoelectron spectra, and $I(r)$ to the signal intensity scale for the radial spectra. The spectral resolution photoelectron images acquired by the ESI machine is $\Delta\text{eKE}/\text{eKE} < 5\%$. Note that the POP reconstruction procedures require the laser polarization + VMI assembly to have cylindrical symmetry such that the laser(s) is horizontally polarized in the laboratory reference frame, i.e. the laser polarization is parallel to the imaging plane.

3.1.5 Calibrating Photoelectron Images: I⁻

The velocity and kinetic energy scale for velocity-map images (at a given extractor and repeller voltage) are calibrated using the atomic line photoelectron spectrum of iodide.

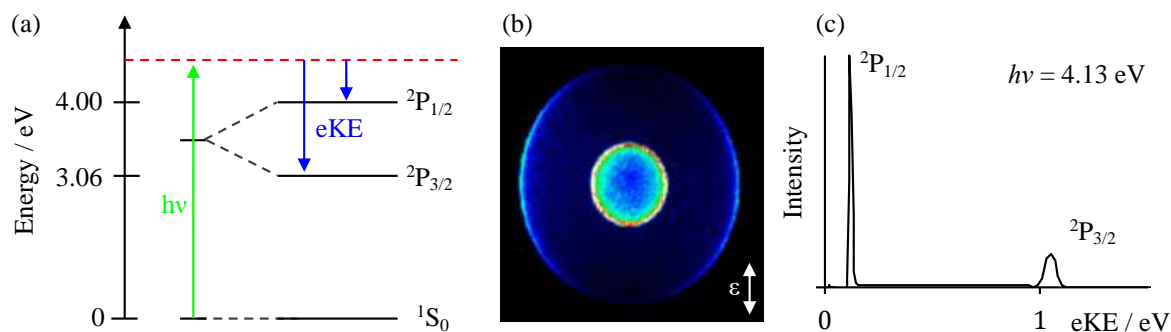


Figure 12 (a) Energy level diagram of the ground state of iodide, 1S_0 , and the two spin-orbit states, $^2P_{3/2}$ and $^2P_{1/2}$, of neutral iodine. The photodetachment process is shown schematically, with blue arrows showing the eKE of photoelectrons detached to the two spin-orbit states following irradiation by a laser pulse, $h\nu$, represented by the green arrow. (b) and (c) show the raw photoelectron image and the photoelectron spectrum of iodide taken at $h\nu = 4.13$ eV. The two peaks correspond to the photodetachment process shown in (a). The inner ring in the raw photoelectron image (b) corresponds to the feature at 0.12 eV in the photoelectron spectrum (b), and the outer ring corresponds to the feature at 1.06 eV. These photoelectron features correspond to photodetachment to form the $^2P_{3/2}$ and $^2P_{1/2}$ states, respectively.

A schematic showing the photodetachment events that lead to the raw photoelectron image and the consequent photoelectron spectrum used for calibration are shown in Figure 12 (a), (b) and (c), respectively. Photodetachment above 4 eV photon energy leads to a photoelectron spectrum with two characteristic photoelectron features, corresponding to electron loss from the ground state of iodide, 1S_0 , to form the two spin-orbit states of neutral iodine, $^2P_{3/2}$ and $^2P_{1/2}$. The peaks at 1.06 eV and 0.12 eV correspond to $^2P_{3/2}$ and $^2P_{1/2}$, respectively, with a defined splitting of 0.942648 eV.¹⁴ The inset raw photoelectron image, Figure 12(b), shows the relative anisotropies of the two photoelectron features.

3.2 Laser system

The experimental studies detailed in this thesis used two laser systems. The choice of laser for a given study depended on the type information desire, e.g. molecular properties and action spectra or direct measurement of excited state dynamics.

The nanosecond laser system is tunable over a large range of wavelengths (190 – 2700 nm, 6.53 – 0.56 eV). Laser pulses are produced from a Nd:YAG laser (Surelite-II, Continuum) pumped optical parametric oscillator (Horizon I, Continuum). The pulses produced are ~6 ns in duration and have a bandwidth of $<10 \text{ cm}^{-1}$.

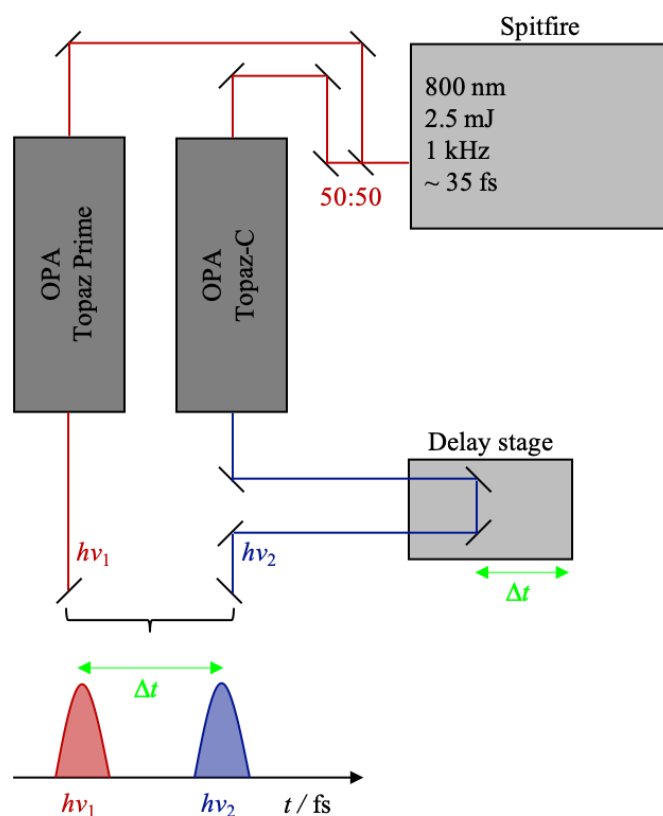


Figure 13 Layout of the output and partitioning of the fundamental output from the Spectra-Physics Spitfire XP-Pro chirp pulse amplifier used in conjunction with the photoelectron spectrometer for time-resolved photoelectron imaging studies. The beam from the Spitfire oscillator is passed through a 50:50 beam splitter to produce two beams, $h\nu_1$ and $h\nu_2$, the former will be used to generate the pump pulse and the latter will be used as the probe pulse. Both the pump and probe pass through tunable OPAs, details of the energies of pump and probe available are given in Table 1.

In order to have direct measurements of the excited state dynamics of a target anion, a commercial femtosecond laser system is used, which is illustrated schematically in Figure 13. Laser pulses (800 nm, 35 fs, 2.5 mJ, 1 kHz) were generated using a commercial chirp pulse amplified femtosecond system (Spectra Physics Spitfire XP-Pro). The pulse is then split into two beams, $h\nu_1$ and $h\nu_2$, by a 50:50 beam splitter and guided into two separate tunable optical parametric amplifiers, OPAs (Topas Prime and Topas-C). After passing through the respective OPAs, $h\nu_2$ is directed onto a set of mirrors on a motorised delay stage before being aligned to overlap temporally and spatially with $h\nu_1$. Both $h\nu_1$ and $h\nu_2$ are then directed through to the interaction region of the VMI spectrometer. At t_0 the beams are temporally concurrent ($\Delta t = 0$), and both the pump and probe, $h\nu_1$ and $h\nu_2$, respectively, irradiate the ion packet simultaneously. The delay stage can then be moved in the forwards and backwards direction, changing the path length of the probe pulse. This causes the probe pulse to arrive before and after the pump pulse – the speed of light is $\sim 3 \times 10^8 \text{ m s}^{-1}$ so a complete time-resolved experiment with delay times extending to 10's or 100's of picoseconds requires a delay stage mirror to move by millimeters (noting that the light beam travels twice the distance of the mirror movement). The temporal offset of the pump and probe pulses is characterized by Δt .

Time-resolved experiments often follow a frequency-resolved study, which might be completed in one or two days for an anion with good photoelectron signal. That is, the frequency-resolved experiment provides insight into the appropriate excitation and detachment energies for the pump and probe beams, allowing the excited state dynamics in interesting regions to be investigated further. Details of the available energetic ranges and the processes used to generate these energies are provided in Table 1.

λ / nm	$h\nu$ / eV	Process
800	1.55	Block OPA generation stages
400	3.10	Double fundamental output
1150 - 1600	1.08 – 0.77	Signal from OPA
575 - 800	2.16 – 1.55	Double signal
288 - 400	4.31 – 3.10	Quadruple signal
1600 - 2500	0.77 – 0.50	Idler from OPA
800 - 1250	1.55 – 0.99	Double idler
400 - 625	3.10 – 1.98	Quadruple idler
472 - 533	2.63 – 2.33	Mix signal and fundamental

Table 1 The full spectral range of energies accessible by the femtosecond laser system. The process for producing the different energies are given.

3.3 The Cluster Machine

The Verlet lab has a second gas phase anion photoelectron spectrometer, which was used in the study of the nitrobenzene anion. The design and operation of this machine was the subject of the recent thesis of J. P. Rogers, and the full details can be found therein and in a subsequent publication.^{5,15} A brief overview of the operation is provided here for completeness.

The method for generation of anions is different between the two gas phase photoelectron spectrometers, but the mass-selection, detection and imaging of anions and the detached photoelectrons use the same logic and have similar design. In the cluster machine, anions are produced using a pulsed valve source that generates a cold molecular beam. Analytes of interest can be seeded into the molecular beam as neutral molecules by mixing a small amount of the sample gas or liquid vapour (< 1%) into the carrier gas (usually He or Ar). The principal advantage of a molecular beam is the sample is cooled (e.g. 20-50 K in vibrational degrees of freedom) though jet-cooling during the molecular beam expansion. The disadvantages are that it is difficult to seed molecules that normally exist as solids because they have to be first heated to produce vapour; many organics such as the biochromophores studied

in the Verlet group will thermally decompose before sufficient yields of parent neutrals can be obtained. Anions are produced through secondary electron capture by crossing the expanding molecular beam with an electron beam. For example, an electron beam of 100-300 eV ionises carrier gas (Ar) producing photoelectrons. These photoelectrons can be captured by the target molecules. Because the molecule beam supersonic expansion is still occurring during this process, the nascent anions are cooled and thus liberate the vibrational energy associated with electron capture. Note, electron capture typically occurs on a closed-shell molecule, so that it is often simple to produce radical anions but very hard or impossible to produce deprotonated anions (which are simple with electrospray). Following generation, the m/z selection, detection and VMI of the anions proceeds in much the same way as detailed for the ESI machine. The VMI spectrometer – which is more akin to a conventional VMI stack with a shaped repeller to flatten the imaging plane – means that the photoelectron images obtained are higher resolution, with $\Delta eKE/eKE < 3\%$ (c.f. 5% for the ESI machine).

4 Electronic Structure Calculations: A Computational Toolkit

As with experimental methods, there are a variety of electronic structure methods that can be applied to the target anion, with the choice depending on the desired property and accuracy, and the computational resources available. The ultimate goal of most electronic structure calculations is to solve the Schrödinger equation. Unfortunately, because analytical solutions of the many-electron Schrödinger equation are not possible for polyatomic systems, various approximations need to be invoked. It is the reliability of these approximations – for the system and molecular property desired – that must be considered when undertaking electronic structure calculations to support experiment. In many instances, gas-phase experiments actually provide ideal data to calibrate and test electronic structure methods. The remainder of this chapter will detail the electronic structure methods used as part of this thesis and rationalise why these particular methods were chosen.

Modern electronic structure methods can be divided into two main classes, *ab initio* and non-*ab initio*, where the latter refers to density functional theory (DFT).^{16–19} While DFT methods have seen immense growth, development and adoption over the last decade, due to efficient computational scaling with the size of the problem ($\sim N^4$ as limited by a Hartree-Fock step, where N is the number of atoms), it has drawbacks in crucial areas, such as complex electronic structures, excited states and photochemistry. Moreover, many of its shortfalls are particularly serious for anions, e.g. unphysical self-interaction and poor or erratic description of charge-transfer excitations, inability to describe excited states/resonances in the detachment continuum with diffuse basis sets, and time-dependent DFT providing only singles excitation character.^{20–26} When dealing with modelling anion resonances and excited states, which are associated with a large component of the experimental work in this thesis, it is necessary to instead use *ab initio* methods. As indicated above, anions and their excited states that lie embedded in the continuum pose a complex problem and require careful handling. The main complication with *ab initio* methods is the computational cost associated with post-Hartree-Fock electron correlation; this is the major point of compromise between the accuracy of the chosen model and the computational cost. For example, MP2 calculations scale as N^5 , CCSD as N^6 and CCSD(T) as N^7 . Ultimately, one of the first questions is: should a rigorous model be developed to provide a qualitative interpretation of the experimental data, or should quantitative calculations be performed to aid understanding. One must also be careful of fortuitous or “Pauling point” agreement where cancellation of errors due to approximations in the model lead to a good agreement between theory and experiment. While this might be the case for one parameter for an anion and a given geometry and state, it might not be so for another!

There are many computational packages available for electronic structure calculations. Most of the calculations in this thesis were carried out using the QChem 5.0 package,²⁷ with

the exception of XMCQDPT2 calculations which were performed using the Firefly 8.2 quantum chemistry package, which is partially based on the GAMESS-US source code.²⁹ There was occasional use of the Gaussian 16.A03 computational package.³⁰ Simulation of the photoelectron spectra has been carried out using Gaussian 16 and ezSpectrum v3.³¹ Modelling of the photoelectron angular distributions using Dyson Orbitals as implemented in the ezDyson v4 program.³² Both ezSpectrum and ezDyson are developed by Krylov and co-workers and made available by the iOpenshell project.

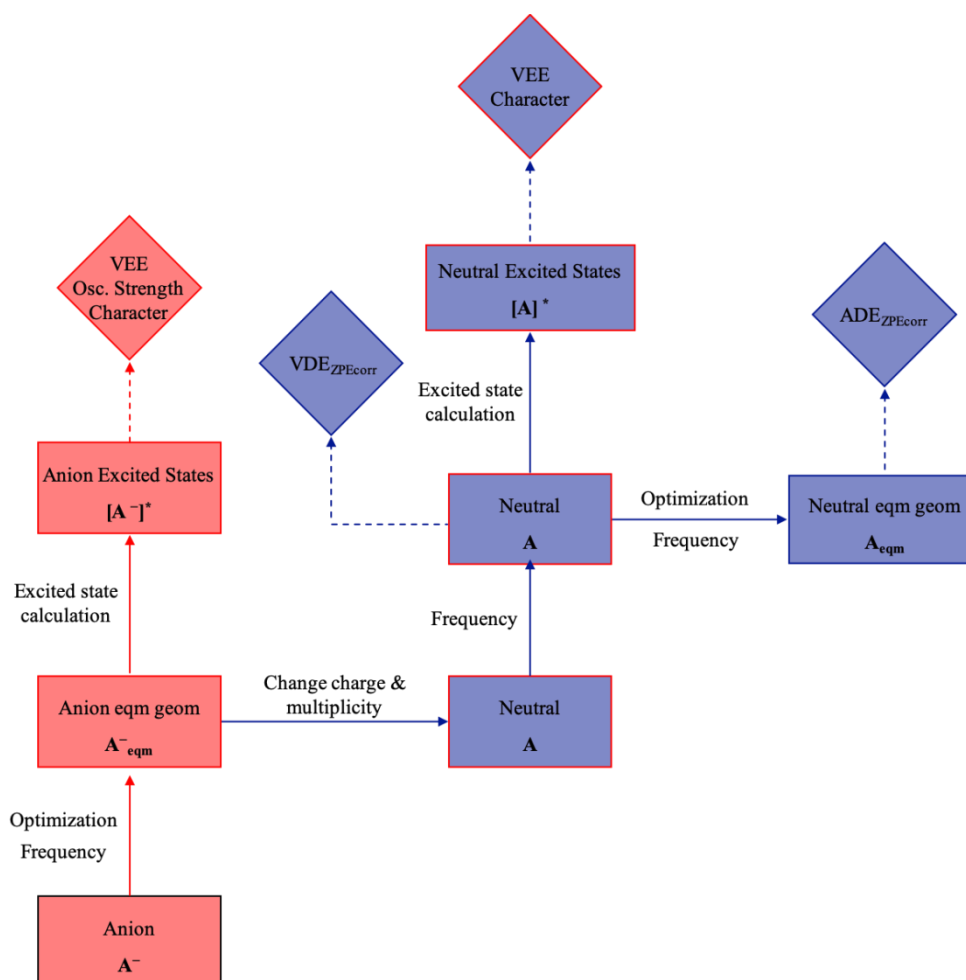


Figure 14 Schematic of the types of calculations routinely run and the experimental variables calculated. Calculations run to model parameters of the anion and neutral species are indicated by red and blue boxes, respectively. Calculations run using the anion equilibrium geometry are denoted with red borders, while calculations using the neutral equilibrium geometry are indicated by blue borders.

4.1 Vertical Detachment Energy

The starting point for most calculations is to obtain an accurate minimum energy geometry of the anion in its electronic ground state. This will also provide an absolute energy (within the approximations of the calculation) for the anion. Note that this value is not of use by itself because all experimental techniques characterise some difference in energy, but it provides a reference to which other calculations can be performed to obtain an energy difference. The total electronic energy of a given molecule in a specific electronic state as a function of nuclear positions is defined by its potential energy surface. In other words, the potential energy surface can be thought of as a complex and multidimensional map of interatomic forces.

A schematic of the workflow that was followed when investigating the properties of the anions in this thesis is shown in Figure 14. Ground state optimizations of the anion are first carried out using DFT, due to the low computational cost, availability of analytical gradients, and good performance/parameterization for geometrical parameters.

Vibrational frequency analysis is used to confirm a given structure represents a geometric minimum. In order to calculate the harmonic vibrational frequencies, the force constants of the molecule must first be determined. The force constants are second derivatives of the total electronic energy with respect to the nuclear coordinates, grouped to form the Hessian matrix. When a global minimum energy structure is found, this can be characterised by very shallow gradient near zero and no imaginary frequencies.

Following the identification of the geometric minimum of the anion, noting that fluxional species might have many local minima and one global minimum, a frequency calculation of the neutral is performed in this geometry. The difference in total energy of the neutral and anion in the anion equilibrium geometry is equivalent to the vertical detachment energy, VDE. This value is corrected to account for the zero-point energy (ZPE), $\text{VDE}_{\text{ZPEcorr}}$.

It is crucial to note that comparison of absolute energies is only physically meaningful if the same level of theory (basis set and electron correlation) have been used in the calculations.

4.2 Adiabatic Detachment Energy

In order to calculate the adiabatic detachment energy (ADE), a subsequent geometry optimisation and frequency calculation is performed on the neutral species. The $ADE_{ZPE_{corr}}$ is then equal to the relative difference in total energy between the anion and neutral in their respective equilibrium geometries, corrected for ZPE. In conventional photoelectron spectra showing only direct photodetachment features, the ADE is the lowest energy discernible detaching vibration (excluding hot bands). The VDE is the most intense feature as part of the photoelectron peak.

4.3 Simulating Photoelectron Spectra

When simulating photoelectron spectra it is important to have neutral and anion geometries in comparable reference frames. In the first step, the neutral geometry optimisation is initiated from the anion minimum energy geometry. This ensures that comparable sections of the two potential energy surfaces are sampled. The calculation of frequencies for both species allows simulation of the detaching transition intensities or Franck-Condon factors, i.e. stick spectra. This requires evaluation of the overlap integrals of the initial and final vibrational wavefunctions of the anion and neutral electronic states. If desired, the stick spectra can be convoluted with Gaussian/Lorentzian functions with a given width to approximate temperature smearing and/or experimental spectral resolution.

Simulations of photoelectron spectra in this thesis were performed with ezSpectrum v3.0,³¹ using either the parallel normal modes approximation or Duschinsky rotations. The former approximation calculates the Franck-Condon factors analytically as products of one-dimensional harmonic wavefunctions, while the latter approximation includes Duschinsky

rotations of the normal modes as full-dimensional integrals. The parallel approximation is appropriate for use when the normal modes of the initial and final electronic states are parallel, and the Duschinsky rotation is required for cases in which these electronic states are significantly non-parallel. The temperature can be altered within both methods, allowing direct comparison of the modelled stick photoelectron spectrum with the experimental photoelectron spectrum. The physics incorporated in ezSpectrum are suitable for modelling the photoelectron spectra to reproduce direct detachment channels but are not suited to describing autodetachment from resonances. In the cases where broadening from autodetachment is reproduced, the modelled photoelectron spectra were produced by Dr Anastasia V. Bochenkova, Moscow State University.

4.4 Exploring the Ground State Potential Energy Surface

Further exploration of the potential energy surface of the ground state of the target anion has been required for studies in Sections A and C. In these cases, a rigid potential energy scan was carried out using the same level of theory as the initial geometry optimisation. It should be noted that in order to perform a full quantitative exploration of the ground state potential energy surface a relaxed scan is required. In the studies in which the rigid potential energy surface scans were run, it was determined sufficient as the region of the potential energy surface we wished to explore was well represented by a series of distortions around a single degree of freedom, and so all other nuclear motion was frozen. In a relaxed potential energy surface scan, the geometry would be reoptimized at each point with respect to all degrees of freedom, providing more accurate energetics, but would have a correlating increase the computational time. The rigid approximation was considered to be sufficient in both Sections A and C as the exploration of the potential energy surfaces was done with respect to hindered rotation of a single bond and the distance of an anion from a planar heteroaromatic ring. In both cases the

distortions investigated caused very little rearrangement in the remainder of the parent anion, and as such was considered to be robust enough to provide semi-quantitative analysis.

4.5 Modelling Photoelectron Angular Distributions

Photoelectron angular distributions are modelled through computation of Dyson orbitals which are then input into the ezDyson v4 code, written by Krylov and co-workers.³² Dyson orbitals in this thesis were calculated using the equation-of-motion coupled cluster singles and doubles method (EOM-XX-CCSD), where XX is IP or EE.^{33–35} For photodetachment from anions, the ionisation potential implementation (EOM-IP-CCSD) was used to compute the Dyson Orbital. This method has been used to describe photodetachment channels from the ground and a bound excited state of the anion to form the ground and excited states of the neutral. In all these cases, the relationship between the initial and final wavefunctions can be represented by a single electron transition. In the case of the bound excited state of the anion an EOM-EE-CCSD calculation specifies the initial state. The Dyson orbital methodology is not suitable for cases where the single electron detaching transition approximation breaks down, including electron loss from Feshbach resonances.

The eigenvalues of the Dyson orbital are then run through ezDyson v4.³² The ezDyson program allows orbital specific photoelectron angular distributions and photodetachment cross-sections to be modelled as a function of kinetic energy of the photodetached electron. This allows direct comparison with the experimental angular-resolved photoelectron spectra.

4.6 Excited State Calculations

Once an equilibrium structure is found for the anion ground state, this may be used to begin building a picture of the vertical energies of electronic states of both the anion and the neutral. The vertical energies of electronic excited states of the anion and neutral (VEEs) are found using excited state calculations. In addition to the VEEs, an oscillator strength for the

formation of the excited states is calculated, and the character of the state can be considered through analysis of the active molecular orbitals.

The appropriate level of theory for excited state calculations is strongly dependent upon the chemical system. Systems with unbound/quasi-bound electronic states of the anion (i.e. shape and Feshbach resonances) provide a more complex challenge than those with bound states, due to the presence of the continuum. Time-dependent DFT (TD-DFT)^{36,37} on the whole provides a relatively good qualitative overview of the electronic structure of an anion, however there are well-documented cases in which TD-DFT fails.^{20,23} One such case is triplet instability. For this reason, all TD-DFT calculations within the report are run using the Tamm-Dancoff approximation (TDA).^{38,39}

For cases where the qualitative picture provided by TD-DFT fails, it becomes necessary to use a more robust wavefunction based method. The XMCQDPT2 method⁴⁰ has been shown to perform very well (typically within ± 0.1 eV) when calculating vertical excitation energies for resonances and the detachment threshold.⁴¹ XMCQDPT2 requires the careful consideration and selection of a balanced active space. Details on the selection of a balanced active space are provided in relevant sections. Prior to the selection of an active space, the geometry obtained from DFT geometry optimizations is repeated at the MP2 level of theory and verified to be a minimum using vibrational analysis. The MP2 equilibrium geometry is used as the reference geometry for the XMCQDPT2 calculations.

4.7 Non-Valence States

4.7.1 Binding Energies of Dipole Bound States

Dipole bound states (DBSs) are the most common type of non-valence state for an anion, in which the excess electron is weakly bound by the dipole moment of the neutral core. The binding energy of a dipole bound state is low, with values normally in the range of 10-100s of meV.⁴² The long-range electrostatic interaction between the neutral core and electron

requires both a suitable diffuse basis set and high degree of electron correlation for an accurate description.^{42–44}

Within Section C, calculation of the binding energy of the DBS have been attempted within two different theoretical models, using both a full and a reduced active space. The former uses the electron affinity implementation of EOM-CCSD, EOM-EA-CCSD, shown by Jordan and co-workers to perform well for non-valence states.^{45,46} The latter method expands the selected active space in XMCQDPT2 to include both ‘continuum’ and DBS orbitals. Both methods allow direct calculation of the binding energy of the DBS.

In both methods a ghost atom is added in the centre of mass or off the end of the dipole moment vector. The ghost atom is affixed with a set of very diffuse functions to represent the DBS. The coefficients for the DBS were chosen by supplementing the standard Dunning basis set describing the valence system with a set of diffuse *s*, *p* and, in some cases, *d* primitive Gaussian functions. The exponents of these Gaussians were chosen to be in geometric ratios from 0.022010 to 0.000070, 0.017845 to 0.000056, and 0.100000 to 0.000158 for *s*, *p*, and *d* functions, respectively. The number of *s*, *p* and *d* functions is then increased until the binding energy calculated stabilises.

4.8 References

- 1 G. M. Roberts, J. L. Nixon, J. Lecointre, E. Wrede and J. R. R. Verlet, *Rev. Sci. Instrum.*, 2009, **80**, 053104.
- 2 G. M. Roberts, PhD Thesis, Durham University, 2010.
- 3 J. Lecointre, G. M. Roberts, D. A. Horke and J. R. R. Verlet, *J. Phys. Chem. A*, 2010, **114**, 11216–24.
- 4 D. A. Horke, G. M. Roberts, J. Lecointre and J. R. R. Verlet, *Rev. Sci. Instrum.*, 2012, **83**, 063101.
- 5 J. P. Rogers, PhD Thesis, Durham University, 2017.
- 6 L. H. Stanley, PhD Thesis, Durham University, 2017.
- 7 L. H. Stanley, C. S. Anstöter and J. R. R. Verlet, *Chem. Sci.*, 2017, **8**, 3054–3061.
- 8 J. B. Fenn, M. Mann, C. K. Meng, S. F. Wong and C. M. Whitehouse, *Mass Spectrom. Rev.*, 1990, **9**, 37–70.
- 9 J. B. Fenn, M. Mann, C. K. Meng, S. F. Wong and C. M. Whitehouse, *Science*, 1989, **246**, 64–71.
- 10 L.-S. Wang, *J. Chem. Phys.*, 2015, **143**, 040901.
- 11 L.-S. Wang, C.-F. Ding, X.-B. Wang and S. E. Barlow, *Rev. Sci. Instrum.*, 1999, **70**, 1957–1966.

- 12 W. C. Wiley and I. H. McLaren, *Rev. Sci. Instrum.*, 1955, **26**, 1150–1157.
- 13 A. T. J. B. Eppink and D. H. Parker, *Rev. Sci. Instrum.*, 1997, **68**, 3477–3484.
- 14 G. Piani, M. Becucci, M. S. Bowen, J. Oakman, Q. Hu and R. E. Continetti, *Phys. Scr.*, 2008, **78**, 058110.
- 15 J. P. Rogers, C. S. Anstöter, J. N. Bull, B. F. E. Curchod and J. R. R. Verlet, *J. Phys. Chem. A*, 2019, **123**, 1602–1612.
- 16 P. Hohenberg and W. Kohn, *Phys. Rev.*, 1964, **136**, B864–B871.
- 17 W. Kohn and L. J. Sham, *Phys. Rev.*, 1965, **140**, A1133–A1138.
- 18 M. Levy, *Proc. Natl. Acad. Sci.*, 1979, **76**, 6062–6065.
- 19 R. G. Parr, in *Horizons of Quantum Chemistry*, eds. K. Fukui and B. Pullman, Springer Netherlands, 1980, pp. 5–15.
- 20 D. J. Tozer, R. D. Amos, N. C. Handy, B. O. Roos and L. Serrano-Andrés, *Mol. Phys.*, 1999, **97**, 859–868.
- 21 J. C. Rienstra-Kiracofe, G. S. Tschumper, H. F. Schaefer III, S. Nandi and G. B. Ellison, *Chem. Rev.*, 2002, **102**, 231–282.
- 22 A. L. Sobolewski and W. Domcke, *Chem. Phys.*, 2003, **294**, 73–83.
- 23 A. Dreuw and M. Head-Gordon, *J. Am. Chem. Soc.*, 2004, **126**, 4007–4016.
- 24 J. Simons, *J. Phys. Chem. A*, 2008, **112**, 6401–6511.
- 25 A. J. Cohen, P. Mori-Sanchez and W. Yang, *Science*, 2008, **321**, 792–794.
- 26 W. Koch and M. C. Holthausen, *A chemist's guide to density functional theory*, Wiley-VCH, Weinheim, 2nd ed., 5. reprint., 2008.
- 27 Y. Shao, Z. Gan, E. Epifanovsky, A. T. B. Gilbert, M. Wormit, J. Kussmann, A. W. Lange, A. Behn, J. Deng, X. Feng, D. Ghosh, M. Goldey, P. R. Horn, L. D. Jacobson, I. Kaliman, R. Z. Khaliullin, T. Kuš, A. Landau, J. Liu, E. I. Proynov, Y. M. Rhee, R. M. Richard, M. A. Rohrdanz, R. P. Steele, E. J. Sundstrom, H. L. Woodcock, P. M. Zimmerman, D. Zuev, B. Albrecht, E. Alguire, B. Austin, G. J. O. Beran, Y. A. Bernard, E. Berquist, K. Brandhorst, K. B. Bravaya, S. T. Brown, D. Casanova, C.-M. Chang, Y. Chen, S. H. Chien, K. D. Closser, D. L. Crittenden, M. Diedenhofen, R. A. DiStasio, H. Do, A. D. Dutoi, R. G. Edgar, S. Fatehi, L. Fusti-Molnar, A. Ghysels, A. Golubeva-Zadorozhnaya, J. Gomes, M. W. D. Hanson-Heine, P. H. P. Harbach, A. W. Hauser, E. G. Hohenstein, Z. C. Holden, T.-C. Jagau, H. Ji, B. Kaduk, K. Khistyayev, J. Kim, J. Kim, R. A. King, P. Klunzinger, D. Kosenkov, T. Kowalczyk, C. M. Krauter, K. U. Lao, A. D. Laurent, K. V. Lawler, S. V. Levchenko, C. Y. Lin, F. Liu, E. Livshits, R. C. Lochan, A. Luenser, P. Manohar, S. F. Manzer, S.-P. Mao, N. Mardirossian, A. V. Marenich, S. A. Maurer, N. J. Mayhall, E. Neuscamman, C. M. Oana, R. Olivares-Amaya, D. P. O'Neill, J. A. Parkhill, T. M. Perrine, R. Peverati, A. Prociuk, D. R. Rehn, E. Rosta, N. J. Russ, S. M. Sharada, S. Sharma, D. W. Small, A. Sodt, T. Stein, D. Stück, Y.-C. Su, A. J. W. Thom, T. Tsuchimochi, V. Vanovschi, L. Vogt, O. Vydrov, T. Wang, M. A. Watson, J. Wenzel, A. White, C. F. Williams, J. Yang, S. Yeganeh, S. R. Yost, Z.-Q. You, I. Y. Zhang, X. Zhang, Y. Zhao, B. R. Brooks, G. K. L. Chan, D. M. Chipman, C. J. Cramer, W. A. Goddard, M. S. Gordon, W. J. Hehre, A. Klamt, H. F. Schaefer, M. W. Schmidt, C. D. Sherrill, D. G. Truhlar, A. Warshel, X. Xu, A. Aspuru-Guzik, R. Baer, A. T. Bell, N. A. Besley, J.-D. Chai, A. Dreuw, B. D. Dunietz, T. R. Furlani, S. R. Gwaltney, C.-P. Hsu, Y. Jung, J. Kong, D. S. Lambrecht, W. Liang, C. Ochsenfeld, V. A. Rassolov, L. V. Slipchenko, J. E. Subotnik, T. Van Voorhis, J. M. Herbert, A. I. Krylov, P. M. W. Gill and M. Head-Gordon, *Mol. Phys.*, 2015, **113**, 184–215.
- 28 A. A. Granovsky, *Firefly v8.2.1*, <http://classic.chem.msu.su/gran/firefly/index.html>.
- 29 M. W. Schmidt, K. K. Baldridge, J. A. Boatz, S. T. Elbert, M. S. Gordon, J. H. Jensen, S. Koseki, N. Matsunaga, K. A. Nguyen, S. Su, T. L. Windus, M. Dupuis and J. A. Montgomery, *J. Comput. Chem.*, 1993, **14**, 1347–1363.
- 30 M. J. Frisch, G. W. Trucks, H. B. Schlegel, G. E. Scuseria, M. A. Robb, J. R. Cheeseman, G. Scalmani, V. Barone, G. A. Petersson, H. Nakatsuji, X. Li, M. Caricato, A. V. Marenich, J. Bloino, B. G. Janesko, R. Gomperts, B. Mennucci, H. P. Hratchian, J. V. Ortiz, A. F. Izmaylov, J. L. Sonnenberg, Williams, F. Ding, F. Lipparini, F. Egidi, J. Goings, B. Peng, A. Petrone, T. Henderson, D. Ranasinghe, V. G. Zakrzewski, J. Gao, N. Rega, G. Zheng, W. Liang, M. Hada, M. Ehara, K. Toyota, R. Fukuda, J. Hasegawa, M. Ishida, T. Nakajima, Y. Honda, O. Kitao, H. Nakai, T. Vreven, K. Throssell, J. A. Montgomery Jr., J. E. Peralta, F. Ogliaro, M. J. Bearpark, J. J. Heyd, E. N. Brothers, K.

- N. Kudin, V. N. Staroverov, T. A. Keith, R. Kobayashi, J. Normand, K. Raghavachari, A. P. Rendell, J. C. Burant, S. S. Iyengar, J. Tomasi, M. Cossi, J. M. Millam, M. Klene, C. Adamo, R. Cammi, J. W. Ochterski, R. L. Martin, K. Morokuma, O. Farkas, J. B. Foresman and D. J. Fox, *Gaussian 16 Rev. A.01*, Wallingford, CT, 2016.
- 31 V. Mozhayskiy and A. I. Krylov, *ezSpectrum v3.0*, <http://iopenshell.usc.edu/downloads>
- 32 S. Gozem and A. I. Krylov, *ezDyson v4*, <http://iopenshell.usc.edu/downloads/ezdyson>.
- 33 A. I. Krylov, *Annu. Rev. Phys. Chem.*, 2008, **59**, 433–462.
- 34 K. B. Bravaya, D. Zuev, E. Epifanovsky and A. I. Krylov, *J. Chem. Phys.*, 2013, **138**, 124106.
- 35 S. Gozem, A. O. Gunina, T. Ichino, D. L. Osborn, J. F. Stanton and A. I. Krylov, *J. Phys. Chem. Lett.*, 2015, **6**, 4532–4540.
- 36 E. Runge and E. K. U. Gross, *Phys. Rev. Lett.*, 1984, **52**, 997–1000.
- 37 M. A. L. Marques and E. K. U. Gross, in *A Primer in Density Functional Theory*, eds. C. Fiolhais, F. Nogueira and M. A. L. Marques, Springer Berlin Heidelberg, Berlin, Heidelberg, 2003, pp. 144–184.
- 38 S. Hirata and M. Head-Gordon, *Chem. Phys. Lett.*, 1999, **314**, 291–299.
- 39 M. J. G. Peach, M. J. Williamson and D. J. Tozer, *J. Chem. Theory Comput.*, 2011, **7**, 3578–3585.
- 40 A. A. Granovsky, *J. Chem. Phys.*, 2011, **134**, 214113.
- 41 A. V. Bochenkova, C. R. S. Mooney, M. A. Parkes, J. L. Woodhouse, L. Zhang, R. Lewin, J. M. Ward, H. C. Hailes, L. H. Andersen and H. H. Fielding, *Chem Sci*, 2017, **8**, 3154–3163.
- 42 M. Gutowski, P. Skurski, K. D. Jordan and J. Simons, *Int. J. Quantum Chem.*, 1997, **64**, 183–191.
- 43 K. D. Jordan and F. Wang, *Annu. Rev. Phys. Chem.*, 2003, **54**, 367–396.
- 44 P. Skurski, M. Gutowski and J. Simons, *Int. J. Quantum Chem.*, 2000, **80**, 1024–1038.
- 45 V. K. Voora and K. D. Jordan, *J. Phys. Chem. A*, 2014, **118**, 7201–7205.
- 46 V. K. Voora, A. Kairalapova, T. Sommerfeld and K. D. Jordan, *J. Chem. Phys.*, 2017, **147**, 214114.

5 Results

Section A Photoelectron Angular Distributions

Frequency-, angle- and time-resolved photoelectron imaging yields velocity map images of the photoelectrons, containing not only the eKE but also information about the angular distribution of the ejected electron relative to the photodetachment field polarisation, ϵ , and how these change with temporal evolution of a molecular anion. This chapter presents studies which have attempted to model and use the photoelectron angular distributions to gain insight into the intrinsic dynamics of a family of phenolate-based chromophores.

Work in this Section is based on the publication below, and unless stated otherwise I performed the experimental and computational work.

1. C. S. Anstöter, C. R. Dean and J. R. R. Verlet
Sensitivity of photoelectron angular distributions to molecular conformations of anions
J. Phys. Chem. Lett. **8**, 2268 (2017)

5.1 Testing the Sensitivity of the Dyson Orbital Approach

Prior to delving into comparison of photoelectron angular distributions calculated using the Dyson orbital approach to experimental results, a brief analysis of the sensitivity of the parameters of the calculation of the Dyson orbital is presented. All calculations presented in this section are on the direct detachment channel of the phenolate anion leading to the ground state of the neutral (D_0) for which the HOMO is the Dyson orbital. The modelled photoelectron angular distributions are modelled using ezDyson v4.¹ Phenolate is a common chromophore in all of the systems presented in this section.

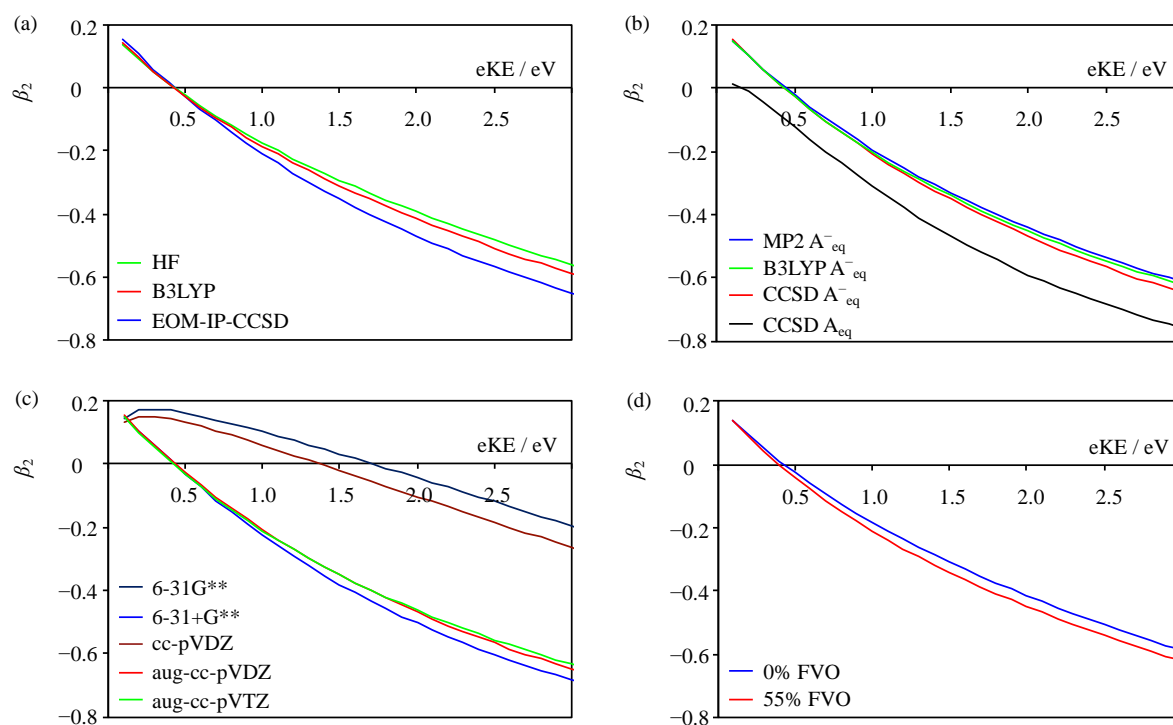


Figure 15 The photoelectron angular distributions modelled as a function of energy are shown for the phenolate anion, with respect to variation of (a) the method used to obtain the orbital, (b) the method used to optimize the geometry, (c) the basis set and (d) the percentage of frozen virtual orbitals (FVO). The aug-cc-pVDZ basis set was used in (a), (b) and (d). The full EOM-IP-CCSD calculation was used to obtain the Dyson orbital used to model the photoelectron angular distributions with respect to percentage of FVO, (d).

As outlined in Section 1.2.2.1, the Dyson orbital used to model photoelectron angular distributions can be approximated as the molecular orbital from which the outgoing photoelectron is ejected from. This suggests, that in principle, a full high-level EOM-IP-CCSD

calculation is not required to model the photoelectron angular distributions. As long as it is possible to identify a single MO, then the calculation may be done using any electronic structure method. The sensitivity of the modelled photoelectron angular distributions to three very different methods (HF, DFT, EOM-IP-CCSD) used to calculate the MO are summarised in Figure 15(a) and shows a general insensitivity. For $eKE < 1$ eV, very good quantitative agreement is seen between the levels of theory. At higher energy, qualitative trends are similar although there are minor quantitative deviations. Within the scope of modelling the experimental photoelectron angular distributions, it is reasonable to use the less expensive methods to obtain the Dyson orbital. As noted in Section 1.2.2.1, once detachment from resonances is encountered, it is not possible to model the PAD using the Dyson orbital approach. For this reason, the slight deviation at higher eKE in the behaviours of modelled photoelectron angular distributions in Figure 15(a) is of little consequence.

It is important to have a feeling for the importance of the parameters of modelling photoelectron angular distributions when applying this approach to larger or more complex systems. For example, being able to use HF or DFT orbitals to approximate the Dyson orbital would be of particular benefit for larger systems, as it avoids a more costly full Dyson orbital calculation. However, one should be cautious of using HF or DFT orbitals for systems which the respective methods are known to perform poorly for.

Figure 15(b) shows the sensitivity to the initial geometry of the anion, optimised at different levels of theory, while the Dyson orbital was obtained from HF/aug-cc-pVDZ. While, at first glance, it may appear that Figure 15(b) shows no sensitivity to the method used to obtain the geometry of the anion, the change in photoelectron angular distributions between the equilibrium geometry of the anion and neutral ground states serves as a cautionary tale. Although the phenolate anion is a small molecule, with reduced conformational freedom due to its delocalised ring structure, the changes in geometry following electron loss cause large

changes to the modelled PAD. For systems with greater conformational freedom, an accurate ground state geometry is crucial for modelling the PAD. In such cases, the MO may be artificially perturbed due to limitation of the method used, impacting the accuracy of the modelled photoelectron angular distributions.

Figure 15(c) shows the effect of basis sets using the HF method on the calculated photoelectron angular distributions. The basis set choice shows a dramatic variation in modelled photoelectron angular distributions. Comparable Dunning and Pople basis sets (i.e. aug-cc-pVDZ and 6-31+G**) show similar trends in the photoelectron angular distributions. It should be noted that improving the basis set for either family results in insignificant quantitative changes in calculated β_2 values. However, exclusion of the diffuse functions, the aug- and '+' the Dunning and Pople basis set, respectively, results in dramatically different modelled photoelectron angular distributions. Such a dependence is perhaps to be expected given the considerations one must make when accurately representing an anion with electronic structure methods (Section 2).

The final parameter investigated was the sensitivity of the modelled photoelectron angular distributions to the freezing of virtual orbitals, when obtaining the Dyson orbital via a full EOM-IP-CCSD calculation. Figure 15(d) shows that freezing up to 55% of the virtual orbitals results in negligible changes to the modelled photoelectron angular distributions. This provides a means for obtaining the full Dyson orbital at reduced computational cost for larger systems for which HF or DFT will not suffice.

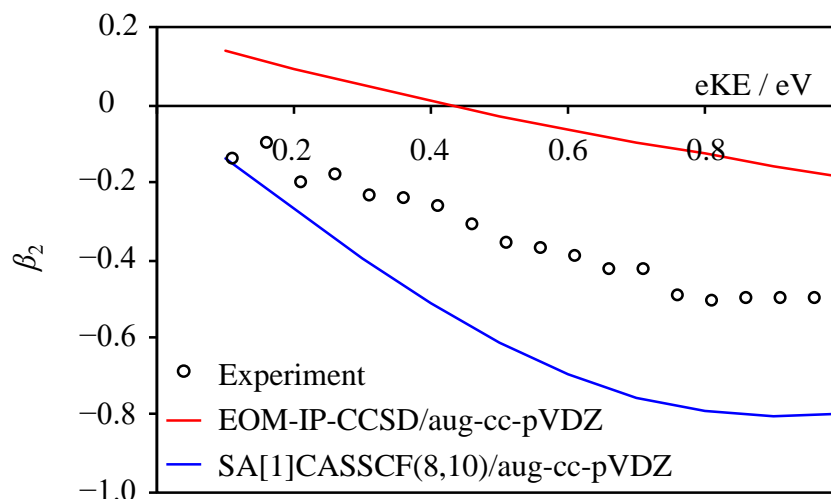


Figure 16 The modelled photoelectron angular distributions (red solid line) are shown in comparison with the experimentally obtained photoelectron angular distributions (black circles) for the direct detachment channel of the phenolate anion. A reduced energetic range is shown, to ensure perturbation due to the presence of resonances is omitted.

From inspection of all of the modelled photoelectron angular distributions in Figure 15(a-d), it appears that the correct behaviour of the D_0 channel of the phenolate anion is a broadly negative anisotropy. This is in qualitative agreement with the π -HOMO used in all cases as the Dyson orbital. It should be noted that while the correct trend of negative anisotropy observed in the experimental photoelectron angular distributions is reproduced by the Dyson approach, there is a systematic discrepancy for the phenolate anion (Figure 16). Most notably the modelled PADs have positive anisotropies at low eKEs, before becoming broadly negative. All the methods investigated in Figure 15 are single reference electronic structure methods, a final investigation into the influence of using a multi-reference method to obtain a Dyson orbital was performed. The natural orbital obtained from a SA[1]-CASSCF(8,10)/aug-cc-pVDZ calculation, in which the orbital was optimised by averaging over the ground state only. While the natural orbital still does not quantitatively capture the behaviour of the experimental PADs, it is noted that it behaves more reasonably at low eKEs than the Dyson orbitals calculated by single reference approaches. The use of natural orbitals obtained by SA-CASSCF calculation

provides an alternative method of calculating PADs for open shell systems that are known to misbehave within single-reference frameworks.

Further detailed discussion of the possible physical origin of this discrepancy is not offered here, and comparison of the phenolate anion is omitted throughout the remainder of this section.

5.2 The Sensitivity of Photoelectron Angular Distributions to Molecular Conformations of a Series of para-Substituted Phenolates

An anion photoelectron imaging study probing the sensitivity of the photoelectron angular distributions to conformational changes is presented. The photoelectron angular distributions of a series of para-substituted phenolate anions is compared with those calculated using the Dyson orbital approach. Good agreement was attained for the two observed direct detachment channels of all anions, except for the lowest energy detachment channel of para-ethyl phenolate for which two conformations exist that yield dramatically different photoelectron angular distributions. The conformational freedom leads to an observed PAD that is the incoherent sum of the photoelectron angular distributions from all possible conformers. In contrast, a second detachment channel shows no sensitivity to the conformational flexibility of para-ethyl phenolate. The results show that photoelectron angular distributions can provide detailed information about the electronic structure of the anion and its conformations.

5.2.1 Introduction

Molecular conformation plays a key role in determining chemical reactivity or biomolecular function and structure. The measurement and understanding of intrinsic interactions that lead to specific conformations represents an important branch of physical chemistry, which impacts many branches of science. The development of new methods that can probe conformations and conformational change may provide new insights. Gas-phase ion spectroscopy in particular has provided a wealth of insight into the intrinsic interactions leading to specific conformations in biological, chemical and catalytic contexts.^{2–8} Electronic structure is of course closely linked to the nuclear framework of a molecule and, generally, specific geometric structures can have very different electronic structures that in turn lead to differing

physical or chemical properties. Anion PE spectroscopy is a powerful and well-established method that probes electronic structure directly and, by comparison with calculations and vibrational analysis of the Franck-Condon profiles of the PE spectra, can also probe geometric structure.^{9–12} Many experimental implementations of PE spectroscopy also measure the PAD; here we consider how sensitive these photoelectron angular distributions are to geometric changes in a molecular anion.

In this section, the sensitivity of the photoelectron angular distributions to changes in molecular structure that might be considered to have small effects on the electronic structure is explored. The sensitivity of photoelectron angular distributions to *gauche*- and *anti*-conformers of neutral species has previously been noted and was used to assign PE spectral bands.¹³ Here, a combined PE imaging and computational study on a series of para-substituted phenolate anions shown in Figure 17 is performed: para-methyl phenolate (pMPh[−]), para-ethyl phenolate (pEPh[−]), and para-vinyl phenolate (pVPh[−]). These three phenolate anions have similar geometric structures, which may in turn be anticipated to have broadly similar electronic structure.

5.2.2 Methodology

The full methodology for the PE spectrometer has been detailed in Section 3.1. Only details pertinent to this study are included here. Briefly, ESI was used to produce deprotonated anions from ~1 mM solutions of phenol, p-methyl-phenol or p-ethyl-phenol (Ph[−], MPh[−] and EPh[−], respectively) in methanol. The p-vinyl-phenolate anion, VPh[−], was produced from para-coumaric acid (pCA[−]) that underwent collisional-induced dissociation to lose CO₂ in the ion guide. The anionic fragment was then mass-selected, and PE imaged.

Preliminary electronic structure calculations were performed using B3LYP/aug-cc-pVDZ, in the QChem computational package.¹⁴ These calculations obtained the minimum

energy geometries of both the anion and neutral ground states, and the vertical excitation energies of relevant anion and neutral excited states.

The B3LYP/aug-cc-pVDZ geometries were reoptimized at the CCSD/aug-cc-pVDZ level, prior to EOM-IP-CCSD/aug-cc-pVDZ calculations to obtain the Dyson orbitals for two direct detachment channels (see Section 5.2.3 for details). The Dyson orbitals were then used to model the photoelectron angular distributions as a function of excitation energy using ezDyson v4.¹ Details on the calculation of photoelectron angular distributions using ezDyson can be found in Section 1.2.2.1).

5.2.3 Frequency- and Angle-Resolved Photoelectron Spectra

Figure 17(a) - (d) shows the frequency- and angle-resolved PE spectra for the four para-substituted phenolates studied, Ph⁻, pMPh⁻, pEPh⁻ and pVPh⁻, respectively. While distinct similarities can be seen between the spectra for all phenolates, there are notable differences in both the frequency- and angle-resolved PE spectra. Discussion of these differences is divided into discussion of the origins of the differences in the angle-resolved PE spectra and the differences in the frequency-resolved PE spectra, in this section and Section B, respectively.

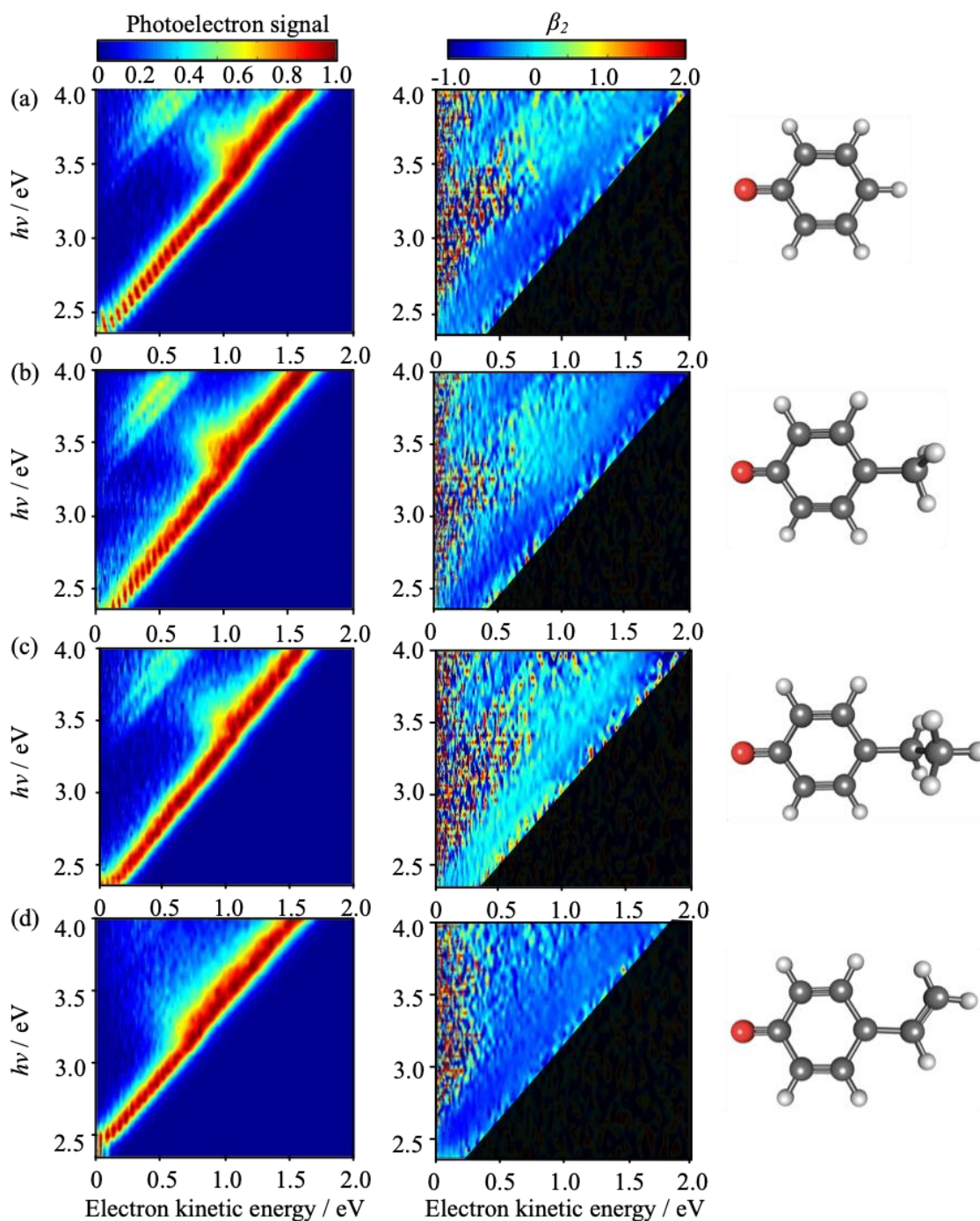


Figure 17 The 2D frequency resolved PE spectra of (a) Ph^- , (b) pMPh^- , (c) pEPh^- and (d) pVPh^- , are shown as false colour plots in the left column. To emphasize spectral changes as a function of $h\nu$ the PE spectra have been normalised to a maximum intensity of one. The 2D β_2 spectra of the four para-substituted phenolates are shown in the central column. The shaded region is ignored as there is insufficient PE signal to define physically meaningful photoelectron angular distributions. The structures of the four para-substituted phenolates are shown in the right column.

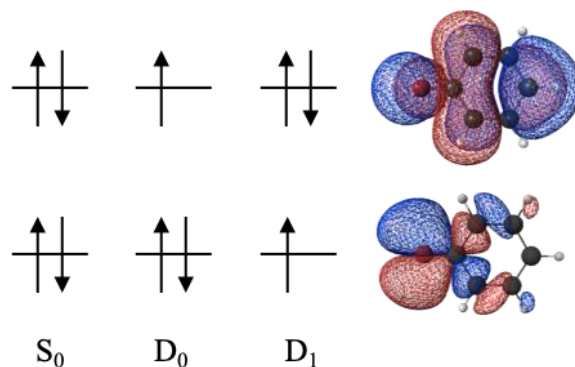


Figure 18 The electronic configurations of the ground states of the anion, S_0 , neutral, D_0 , and the first excited state of the neutral are shown schematically. The two MOs from which photodetachment occurs (D_0 and D_1 channel Dyson orbitals) are indicated.

Briefly, the FR-PE spectra for all para-substituted phenolates have a single dominant PE feature at all $h\nu$. This feature increases linearly with increasing $h\nu$, corresponding to a direct detachment channel. This direct detachment channel corresponds to the loss of an electron from the anion ground state to form the neutral ground state, $S_0 + h\nu \rightarrow D_0 + e^-$. A second direct detachment channel is seen for Ph^- , pMPh^- and pEPh^- , with an onset of $h\nu \sim 3.2$ eV. This direct detachment channel corresponds to electron loss from the ground state of the anion to form the first excited state of the neutral, $S_0 + h\nu \rightarrow D_1 + e^-$. While not as evident in the 2D spectra for pVPh^- , this channel is present in the 1D spectra (Figure 19(d)). In the following section, these two photodetachment processes will be referred to as the D_0 or the D_1 detachment channel, respectively. Both channels are represented qualitatively in Figure 18.

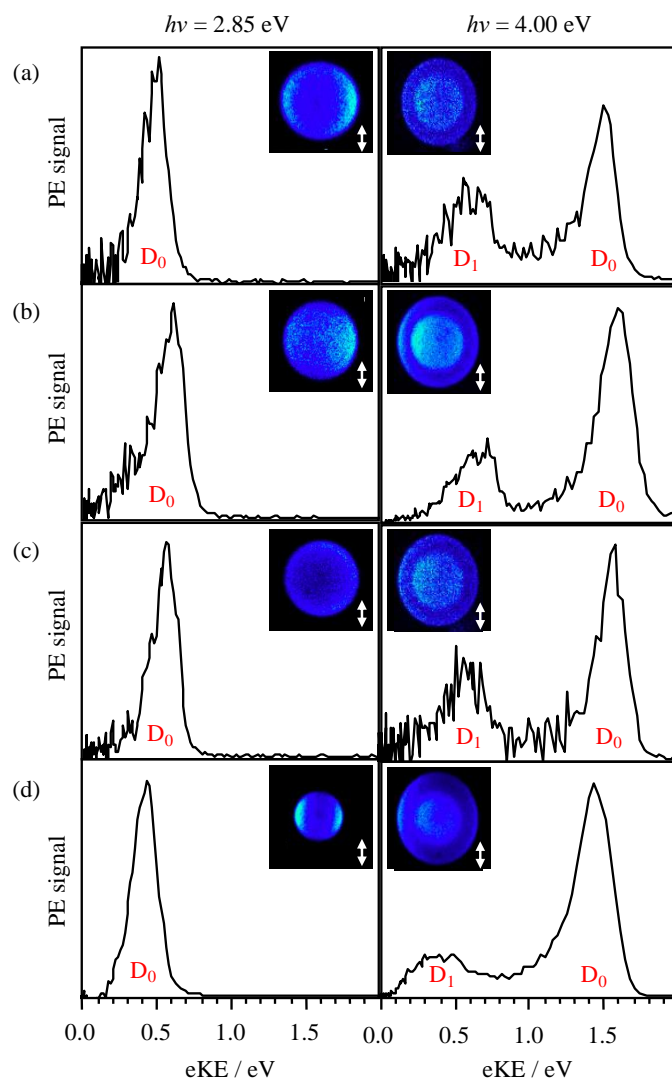


Figure 19 Photoelectron spectra acquired at $h\nu = 2.85$ and 4.00 eV for (a) Ph^- , (b) pMPh^- , (c) pEPh^- , and (d) pVPh^- . Respective raw images are inset with the polarization axis of the laser shown by the double arrow. The photoelectron features corresponding to the D_0 and D_1 channels are indicated.

Figure 19 shows the PE images and spectra of the four phenolate anions at the two photon energies $h\nu = 2.85$ and 4.00 eV . The PE spectra at $h\nu = 2.85 \text{ eV}$ show a single direct detachment feature, while the $h\nu = 4.00 \text{ eV}$ shows an additional higher binding energy peak. These spectra are consistent with previous measurements on phenolate anions by the Lineberger group, albeit at lower resolution.^{15,16} The highest eKE feature corresponds to the D_0 detachment channel. The peak at lower eKE that is only visible at $h\nu = 4.00 \text{ eV}$ corresponds to the D_1 detachment channel.

5.2.4 Photoelectron Angular Distributions as a Probe of Conformation

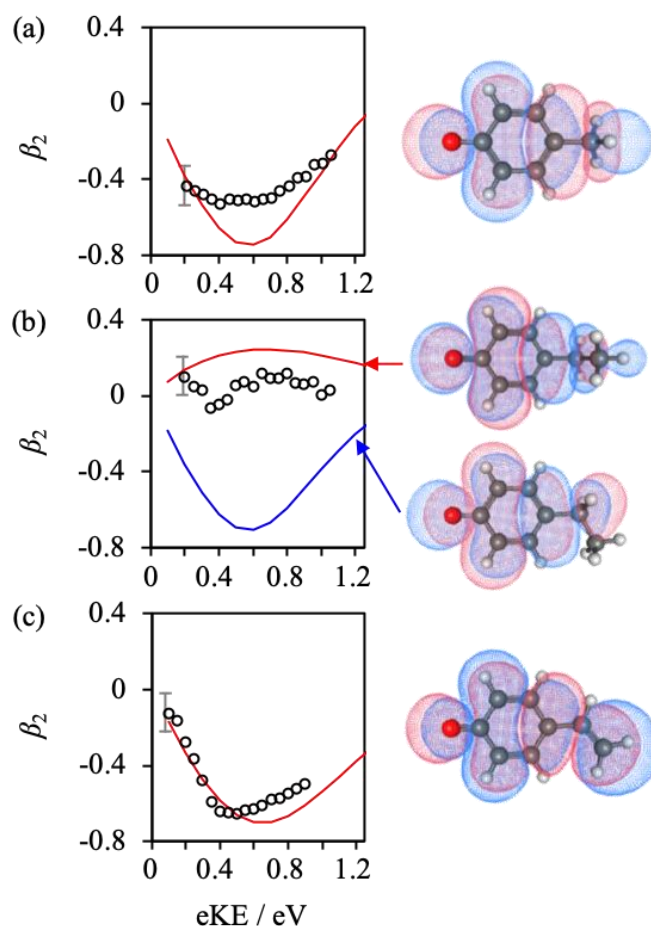


Figure 20 Plots of the experimental (circles) and computed (solid lines) β_2 parameters as a function of eKE for the D_0 detachment channel for (a) pMPh⁻, (b) pEP⁻ and (c) pVPh⁻. For pEP⁻ two computed photoelectron angular distributions are shown corresponding to global (red) and local (blue) minimum energy structures. The right-hand side shows the relevant Dyson orbitals.

The experimental photoelectron angular distributions of both detachment channels were quantified using the β_2 parameter (Equation 5). The photoelectron angular distributions were determined from a series of PE images taken over a range of $h\nu$ with 50 meV intervals. The β_2 values across the highest intensity of the peaks were averaged and plotted as a function of eKE above the threshold of each channel. The measured β_2 parameters for the D_0 and D_1 detachment channel covering a range of nearly 1 eV in eKE are plotted in Figure 20 and Figure 21, respectively. The error associated with the β_2 values is on the order of ± 0.1 . Also shown in

Figure 20 and Figure 21 are the calculated β_2 parameters including the relevant Dyson orbital corresponding to the detachment channel. For pEPh⁻, two β_2 parameters were calculated (Figure 20(b)), corresponding to different conformers. The eKE range over which β_2 was measured has been restricted because of the presence of electronic resonances. Resonances have been shown to cause changes in the PE spectra of both pMPh⁻ and the phenolate anion^{15,16} and many other molecular anions, as well as in photoelectron angular distributions.^{17–20} photoelectron angular distributions from resonances are not accounted for within the current calculations.

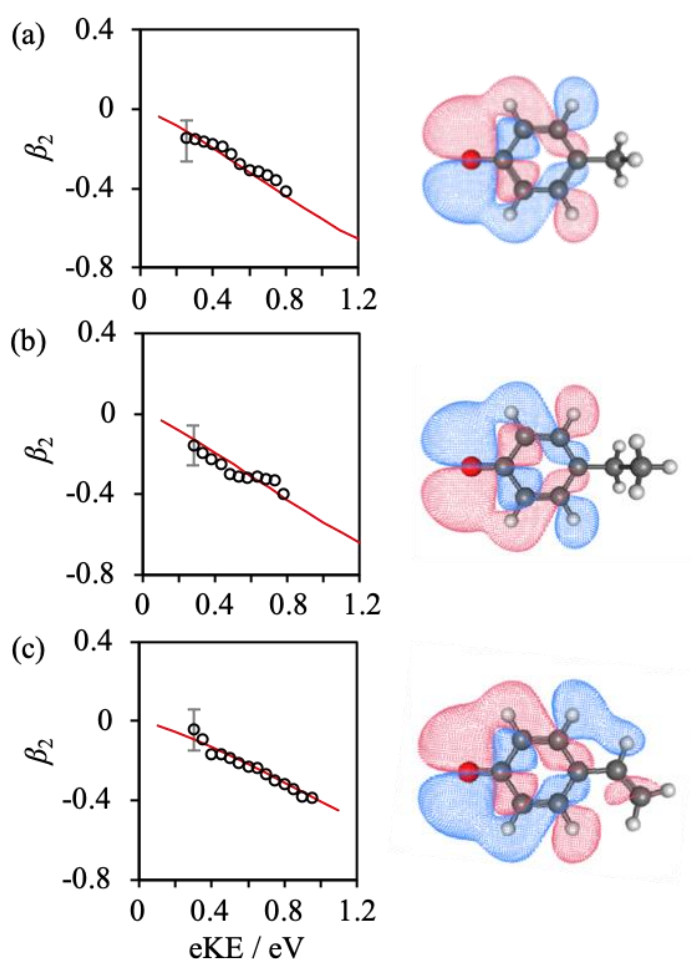


Figure 21 Plots of the experimental (circles) and computed (solid lines) β_2 parameters for (a) pMPh⁻, (b) pEPh⁻ and (c) pVPh⁻, as a function of eKE for the D₁ detachment feature. The right-hand side shows the relevant Dyson orbitals.

For the D_1 detachment channel, the computed photoelectron angular distributions are in very good agreement with those experimentally observed (Figure 21). For the three phenolate anions, the PAD is characterized by a negative β_2 value. Previous studies have confirmed the nature of the D_1 state,^{16,21} which is in good agreement with the experimental onset observed here and our electronic structure calculations. The Dyson orbitals corresponding to the D_1 detachment channel for pMPh^- , pEPh^- , and pVPh^- are shown in Figure 21(a), (b), and (c), respectively. These show that the electron density is primarily localized to the phenolate-motif in all molecules. The dominant character of this Dyson orbital is a lone pair of the oxygen atom (p-character), which qualitatively agrees with the experimentally observed negative β_2 values. The convergence of $\beta_2 \rightarrow 0$ as $e\text{KE} \rightarrow 0$ arises from the Wigner law,²² see Section 1.2.

5.2.5 Exploring the Potential Energy Surface of pEtPh^-

The D_0 detachment channels for pMPh^- and pVPh^- have negative experimental β_2 values and vary more rapidly with $e\text{KE}$ compared to the D_1 channel as shown in Figure 20(a) and (c), respectively. For these two anions, there is again very good agreement with the calculated photoelectron angular distributions. Qualitatively, a negative value of β_2 is indicative of p- or π -character of the MO from which the electron is detached, which is consistent with the calculated Dyson orbitals for the D_0 detachment channel (See Figure 20). For pEPh^- , β_2 is observed to be broadly isotropic with a value close to 0. At first glance, the striking difference between the photoelectron angular distributions of pEPh^- and pMPh^- or pVPh^- is surprising. Firstly, one might envisage a larger change in electronic structure between pVPh^- and the other two because of the increased conjugation. Secondly, similar differences are not seen for the D_1 detachment channel. Indeed, the calculated photoelectron angular distributions for pEPh^- with a similar planar geometry as for pMPh^- and pVPh^- indicates that a negative PAD is expected for this too (see Figure 21(b)). However, pEPh^- has

greater conformational flexibility than pMPh⁻ and pVPh⁻, due to the saturated ethyl chain. A second conformation was found to be the global minimum energy structure, related by torsion about a single bond as shown in Figure 22. The calculated PAD of the lowest energy conformer is dramatically different, showing an inversion of sign with respect to all other calculated photoelectron angular distributions in this energy range. This observation is more consistent with the experimentally observed anisotropy, although not quantitatively correct.

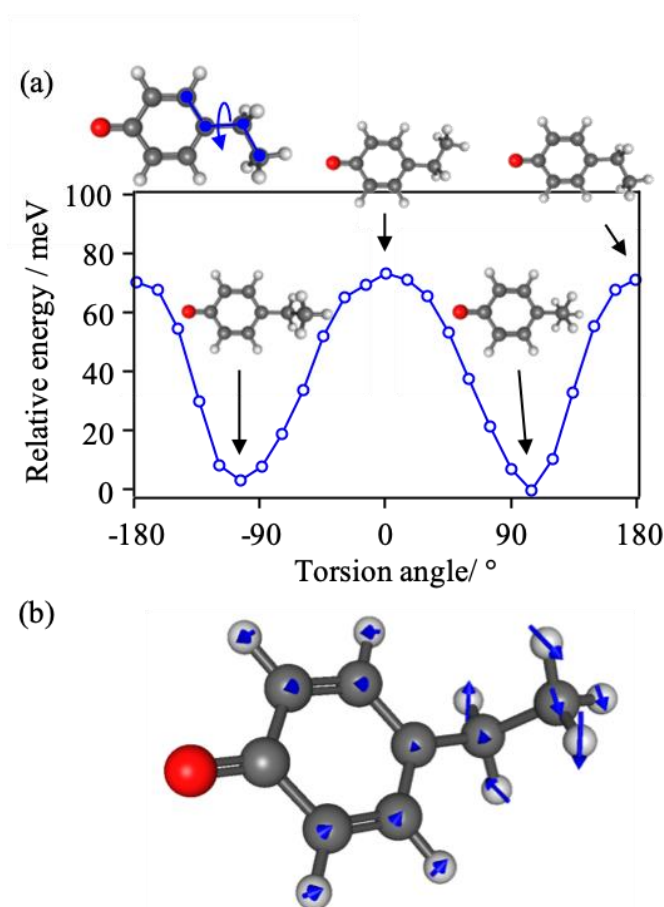


Figure 22 (a) A rigid potential energy scan of pEPh⁻ as a function of the torsion angle around the ethyl chain as shown. Above and below are shown snapshots of conformations where the ethyl-chain is in the plane and out of the plane of the phenolate, respectively. (b) Calculated torsional mode for pEPh⁻ indicating the displacement vectors of the atoms.

A rigid potential energy scan as a function of the torsion angle to the ethyl-chain is shown in Figure 22(a). The out-of-plane structure is the lowest energy with a 70 meV (565 cm⁻¹) barrier to the planar conformation. The torsional mode connecting the two

geometries can be readily identified from the calculations (see Figure 22(b)) and the (harmonic) frequency of the mode is 56.4 cm^{-1} in the out-of-plane geometry (64.7 cm^{-1} for the planar geometry). Hence, the zero-point energy associated with this torsion is $\sim 30\text{ cm}^{-1}$ ($\sim 3.5\text{ meV}$). In principle, the wavefunctions of the torsional levels can be calculated from this potential.²³ The square of these wavefunctions then provides a distribution of possible conformations and the photoelectron angular distributions for these conformations can be calculated from their Dyson orbitals. If the PAD of each conformation is correctly represented, then the weighted sum of these photoelectron angular distributions can be used to reproduce the experimentally observed PAD. However, the present experiments were conducted with ions thermalized in a $\sim 300\text{ K}$ ion trap. Although only a small fraction ($<10\%$) of the molecules have energies above the barrier, it is clear that on average, several quanta of energy are imparted in the torsional mode at 300 K . Hence, to quantitatively determine the conformational distribution would require a precise knowledge of the temperature and a high-level potential energy surface for the torsion based on spectroscopic data which is not available. Nevertheless, as most of the pEPh^- molecules are at energies well below the barrier, the out-of-plane conformation will have the highest probability and therefore, qualitatively, it is expected the overall PAD to predominantly represent that of the lowest-energy conformation in agreement with our observations. The use of temperature controlled cryogenic ion traps coupled with PE imaging^{24,25} would allow the molecules to be cooled so that only the lowest modes are populated which would greatly simplify a quantitative analysis.

5.2.6 Relating the Conformational Freedom to Photoelectron Angular Distributions

Based on the above discussion, the rigidity of the molecules impacts the observed photoelectron angular distributions. The most rigid of the three anions studied is pVPh^- . At elevated temperatures, the distribution of the Dyson orbital can be considered to be static and pVPh^- shows the closest agreement between experimental and predicted photoelectron angular distributions. For pMPh^- , good agreement between experimental and computational results are seen, however, the experimental values are generally less negative than the predicted ones. For pMPh^- at finite temperature, the methyl-group will have rotational freedom and such motion may have small, but important effects on the Dyson orbital. A similar point was noted in a previous publication on four tocopherol anions,²⁶ which have similar Dyson orbitals as the D_0 channel in this study. The photoelectron angular distributions were mostly isotropic except for δ -tocopherol in which the ring contains only H atoms in the ortho- and meta-positions. The other tocopherols have methyl groups in these positions that either lower the symmetry of the Dyson orbital, or in the case of α -tocopherol, may reduce the PAD anisotropy through rotational freedom. Overall, however, rotamers are likely to have a much smaller effect on photoelectron angular distributions than conformers, which is consistent with our observations for pMPh^- (Figure 20(a)). The flexibility in the ethyl-chain in pEPh^- yields two distinct conformers, for which the electron distribution of the MOs have some distinctive differences. The planar, higher energy, conformer has a Dyson orbital with the same nodal character as pMPh^- and pVPh^- and as a result, the predicted photoelectron angular distributions are very similar for the three molecules (see Figure 21). When the ethyl-chain in pEPh^- is bent out of the plane of the phenolate ring, its Dyson orbital shows an increase in the number of nodes. It appears that this change in MO character causes the drastic change in PAD, illustrating how

sensitive the photoelectron angular distributions are to such small changes in electronic structure caused by conformational flexibility.

The sensitivity of photoelectron angular distributions to conformation is starkly different for the two detachment channels. The D_1 channel shows no sensitivity to the conformational flexibility of pEP^- . Using similar arguments as used for the D_0 detachment channel, this may be rationalized by the lack of electron density in the Dyson orbital on the ethyl-chain. Calculations show that the photoelectron angular distributions are almost identical for both pEP^- isomers in the energy range shown here. The small additional Dyson orbital density on the vinyl chain of pVPh^- observed for the D_1 channel also does not appear to have altered the expected photoelectron angular distributions significantly compared to pMPh^- and pEP^- , because the overall nodal structure of the Dyson orbital remains unchanged.

5.2.7 Conclusions

In summary, a series of PE imaging studies of para-substituted phenolate anions have shown that conformation can subtly alter the electronic structure of certain MOs. photoelectron angular distributions can be extremely sensitive to these changes, which can be probed directly through PE imaging. Computation of the Dyson orbital corresponding to specific photodetachment channels allows the photoelectron angular distributions to be predicted and compared with experiment and shows very good overall agreement. Hence, by combining experiment and theory, the dominant conformation under experimental conditions can be determined through the photoelectron angular distributions. Moreover, the sensitivity of the PAD to the Dyson orbital provides detailed information concerning the electronic structure of the anion. Finally, the sensitivity of the photoelectron angular distributions to conformation may also be informative for dynamical processes in which time-resolved photoelectron imaging could track large amplitude motions of complex molecules through real-time changes in the photoelectron angular distributions.

5.3 Probing Wavepacket Motion on the Bound Excited State of a PYP Chromophore

The active form of the pCA-based chromophore in PYP is the deprotonated anion, making anion PE spectroscopy an ideal experimental technique to elucidate the intrinsic excited state dynamics. In this section a time-resolved photoelectron imaging study on the bound excited state of a derivative of the pCA⁻ chromophore is presented. The topology of potential energy surface of the bound excited state, S₁, was investigated by *ab initio* methods. An interpretation of the direction of the wavepacket on the S₁ potential energy surface is presented, through the application of arguments based on the energetics and photoelectron angular distributions.

5.3.1 Introduction

Photoactive proteins have garnered a large amount of attention, due to the pivotal role they play in facilitating various biological processes. The large proteins contain a chromophoric moiety that can undergo fundamental photochemical reactions, such as excited-state electron or proton transfer, or isomerisation.^{27–29} Photoisomerisation is a common photoresponse in photoactive proteins, such as rhodopsins and the photoactive yellow protein (PYP).^{30,31} As small structural changes of the chromophore, such as photoisomerisation, lead to larger-scale rearrangements in the protein scaffold, it can be understood that the photoactivity of the protein is determined by the chromophoric moiety.³² It is therefore of great benefit to first unravel the intrinsic reactivity and photoresponse of the chromophore in order to gain understanding of the photoactive protein it is embedded in.

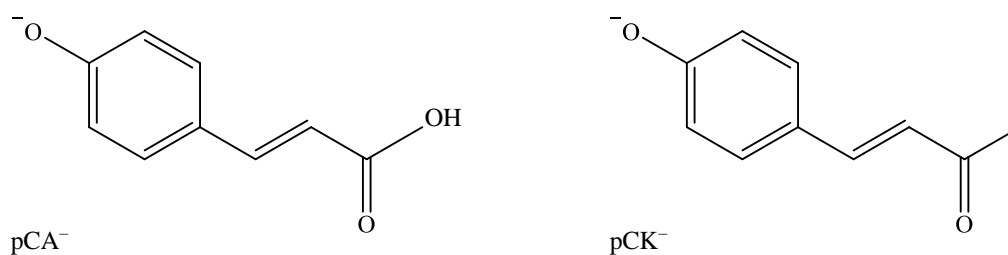


Figure 23 Skeletal representations of two derivatives of the anionic chromophore in PYP, para-coumaric acid (pCA⁻) and para-coumaric ketone (pCK⁻).

The chromophore commonly used to represent PYP is *trans*-para-coumaric acid anion (pCA⁻) and derivatives thereof. Photoexcitation of pCA⁻ leads to *trans*-*cis* isomerisation, which initiates a signalling cascade ultimately resulting in negative phototaxis in several halophilic purple bacteria.^{33–35} The initial isomerisation of the pCA⁻ chromophore causes a restructuring of the surrounding hydrogen-bonding network, that subsequently causes partial unfolding of the protein, to form the signalling structure. To gain a more detailed understanding of the initial events in this process there have been a number of experimental and computational studies on the chromophore photodynamics of pCA⁻ and its derivatives.^{36–38}

A derivative of the PYP chromophore was previously the subject of a time-resolved (TR) study by Zewail and co-workers.³⁹ The chromophore investigated was an isolated pCA⁻ derivative, terminated by a methyl group (Figure 23), pCK⁻. The isomerization dynamics of the S₁ excited state of pCK⁻ were probed using femtosecond pump-probe photoelectron (PE) spectroscopy. This study concluded that the chromophore undergoes ultrafast structural changes, involving twisting around the double bond.

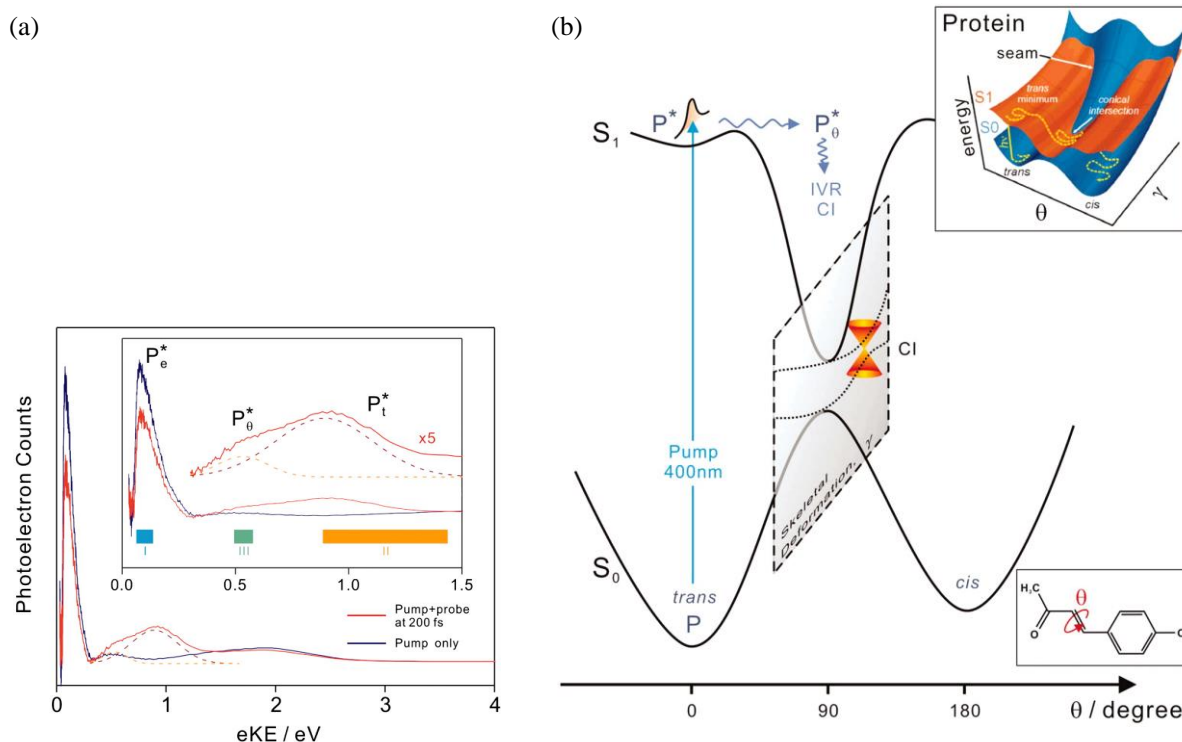


Figure 24(a) The photoelectron spectra of the pCK chromophore obtained with pump femtosecond pulse (blue trace) and pump+probe femtosecond pulses (red trace) at 200 fs delay. Inset is a blow-up of the energy region of 0-1.5 eV, in which energy windows for time-dependent transients are marked as I, II and III. The windows allowed for probing of P_e^* , P_t^* and P_θ^* . (b) Conceptual potential energy surface for the primary dynamics of pCK⁻. The rotation angle around the double-bond is indicated by θ . Reproduced with permission from Reference 39.

While the results of the study by Zewail and co-workers provide evidence for the primary steps in the isomerisation of the PYP chromophore, there are notable factors that lead to convolution of PE spectra. A 3.10 eV (400 nm) pump pulse was used to photoexcite pCK⁻ to the target excited state, S_1 . While the S_1 state is bound, the threshold for detachment to the neutral ground state, D_0 , lies close in energy. Consequently, a pump pulse of 3.10 eV is sufficient to form not only the S_1 , but also D_0 , through direct detachment. Therefore, the photoelectron spectra recorded contain both signatures of autodetachment, direct detachment, and isomerisation dynamics. The autodetachment process can be seen by the low energy peak in the time-resolved measurement. However, because a magnetic bottle was used as an electron energy analyser, their experiment was not sensitive to the lowest energy electrons (see Figure

24). There is also notable two photon signal evident. In order to aid any ambiguity in interpretation it is preferable to use a pump pulse resonant with S_1 but below D_0 .

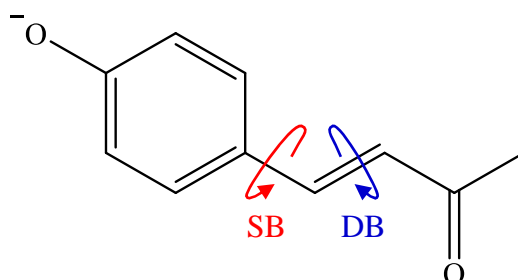


Figure 25 Rotation about the single bond (SB) and double bond (DB) are shown for the pCK anion.

Previous computational studies have focussed on calculation of the initial dynamics of the isolated PYP chromophores.^{36,40–45} An *ab initio* study by Groenhof and co-workers explored the potential energy surface of the bound excited state of pCK^- , with respect to rotation about the single bond (SB) and double bond (DB).⁴² The two rotations are shown in Figure 25. Exploration of the topology of the S_1 potential energy surface determined that, while photoisomerization about both the SB and DB is possible with 90° -rotated SB and DB geometries both representing energetic minima, the major relaxation channel was via the SB rotation. It was found that there was a negligible barrier to the SB minima from the Franck-Condon (FC) region (planar geometry), whereas there is a significant barrier in the direction of the DB minima.

While similar results have been found studying isolated pCK^- ,⁴⁴ it has been demonstrated that the DB rotation pathway can be made accessible through charge stabilization of the phenolic oxygen by hydrogen bonding.⁴³ The modulation of relaxation pathways of the S_1 state by the environment has been further explored in a number of trajectory studies in the gas-phase,^{40,46} in solution,⁴³ and in the protein.⁴⁷ Excited state wavepacket dynamics simulations of pCK^- in the gas-phase confirm that the S_1 SB minimum is reached, but that decay is inefficient due to the distance from the S_1/S_0 conical intersection.^{40,46} This is in

contrast to the photodynamics of pCK⁻ in solution, in which some decay via the DB rotation is seen in the simulations. The DB minimum lies closer to the S₁/S₀ intersection, causing faster decay. The modulation of the excited state pathways has been rationalised through examination of the charge distribution of the S₁ state. The SB rotation leads to complete charge transfer from the phenolate ring to the alkene tail, while the DB rotation leads to only a partial charge transfer in the same direction. Therefore, stabilisation of the phenolic oxygen through hydrogen bond formation is likely to influence the isomerisation pathway.

Conformational changes such as the SB and DB rotation have a large impact on the electronic structure of the system but may cause experimental challenges. This can be understood when considering designing an experiment to validate the theoretical work presented above. The wavepacket will initially be produced in the FC region of the S₁ state, and from here can propagate along two energetically accessible decay pathways, the minima of which are close in energy to one another. How can an experiment distinguish between the two pathways?

As the PE spectrometer used in this study utilises VMI it is possible to extract the photoelectron angular distributions alongside the PE spectra at all time delays. The development of the Dyson orbital approach has allowed for semi-quantitative interpretation of photoelectron angular distributions. It is possible to approximate a single molecular orbital from which a photoelectron is detached as the Dyson orbital, as long as the electron loss channels are defined by a single electron transition. The photoelectron angular distributions may then be modelled as a function of energy of the outgoing electron, using this Dyson orbital.

Photoelectron angular distributions have been demonstrated to provide powerful insight into the electronic structure of different conformers, the character of electronically excited states and the energetic onset of resonances.^{17,48–50} In principle, application of the Dyson orbital approach to the calculation of photoelectron angular distributions as a function of evolution of

a wavepacket on a potential energy surface would provide a novel insight into subtle changes in geometry, propagated through changes to electronic structure. The change in charge-transfer character between the S_1 SB and DB minima could be reflected in the photoelectron angular distributions, making pCK^- an ideal candidate for investigation of the sensitivity of photoelectron angular distributions to conformational changes in the time-domain.

Here we present a detailed study of the dynamics of the bound state of pCK^- , probed by TR-PE imaging and *ab initio* calculations. We model the photoelectron angular distributions as the wavepacket evolves along the potential energy surface of the bound S_1 state, in conjunction with TR-PAD measurements.

5.3.2 Methodology

The experimental setup and methodology have been detailed in Section 3.1, and only details relevant to the current experiment are provided herein. The pCK anion was generated through ESI of a $\sim 1\text{mM}$ sample of pCK in methanol, with a few drops of NH_3 added to aid deprotonation of the alcohol group.

Femtosecond laser pulses of 2.79 eV (444 nm) and 1.55 eV (800 nm) were used as pump and probe pulses, respectively. Further details of the femtosecond laser set-up, including generation of pulses at this energy can be found in Section 3.2. Pulses were delayed relative to one another (Δt) using a motorized delay stage.

All critical points of the potential energy surface for S_0 and S_1 – minima and minimum energy conical intersections – were located using SA2-CASSCF(12,11)/6-31G* in Molpro. Linear interpolation on internal coordinates (LIIC) pathways were obtained to link the different critical structure at the same level of theory. The common starting point employed for the LIIC pathways is the planar minimum on S_1 . These calculations were performed by Dr Basile F. E. Curchod.

Additionally, the S_1 , S_2 and D_0 states were calculated as VEEs from the S_0 geometries along the potential energy surface using XMCQDPT2 to correct for the lack of dynamic correlation at the CASSCF level. The $^1\pi\pi^*$ excited states of pCK^- were calculated using an active space of 12 valence π -orbitals and 12 electrons. The $\pi\pi^*$ active space is depicted in Figure 26. An additional extremely diffuse p-function was affixed to a carbon of the ring. A single π^* orbital of this highly diffuse shell was included in the active space and state averaging to mimic the continuum, D_0 . The XMCQDPT2[7]/SA[4]-CASSCF(12,12) method was used with a reference space spanned by 7 CASCI wavefunctions obtained through CASSCF-SA to ensure the states experimentally accessible were modelled. A DFT/PBE0-based one-electron Fock-type matrix was used to obtain energies of CASSCF semi-canonical orbitals used in perturbation theory, the FC geometry was run without this to improve the description of the detachment continuum. All XMCQDPT2 calculations used the (aug)-cc-pVTZ basis set, where the augmented function was only affixed to the oxygen atoms.

Finally, the PADs were calculated using EOM-EE/IP-CCSD/aug-cc-pVDZ to obtain the Dyson orbitals for critical geometries along the S_1 potential energy surface. The PADs were then modelled using ezDyson v4.¹ Further details on the calculation of PADs can be found in Section 1.2.2.1.

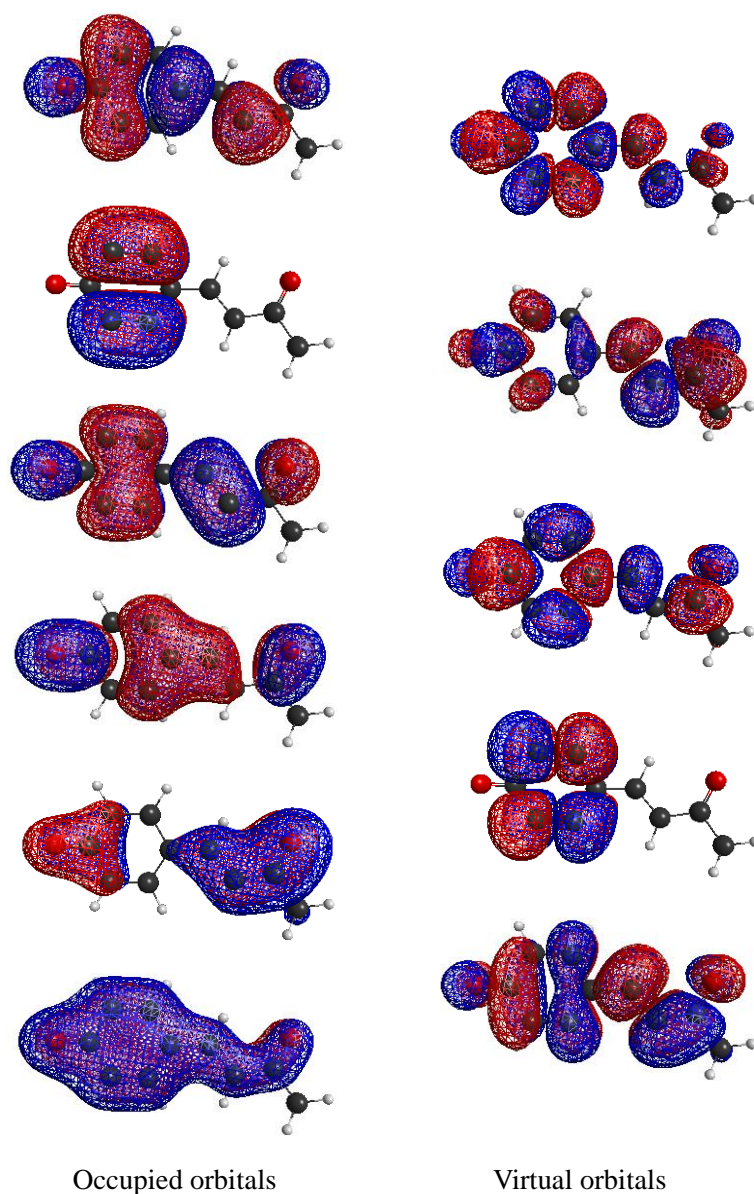


Figure 26 The orbitals used in all calculations. The extremely diffuse orbital used to represent the continuum in the XMCQDPT2 calculations is not visualized.

To provide qualitative insight into the photoelectron angular distributions of the S_1 along the calculated potential energy surface, natural orbitals from the XMCQDPT2 calculations optimized for the S_1 state were considered. The orbitals populated following excitation to the S_1 state (LUMO) were used as Dyson orbitals for photodetachment from the S_1 state along the calculated potential energy surface. This is qualitatively analogous to the Dyson orbital calculations of the ground state.

5.3.3 Time-Resolved Photoelectron Spectra

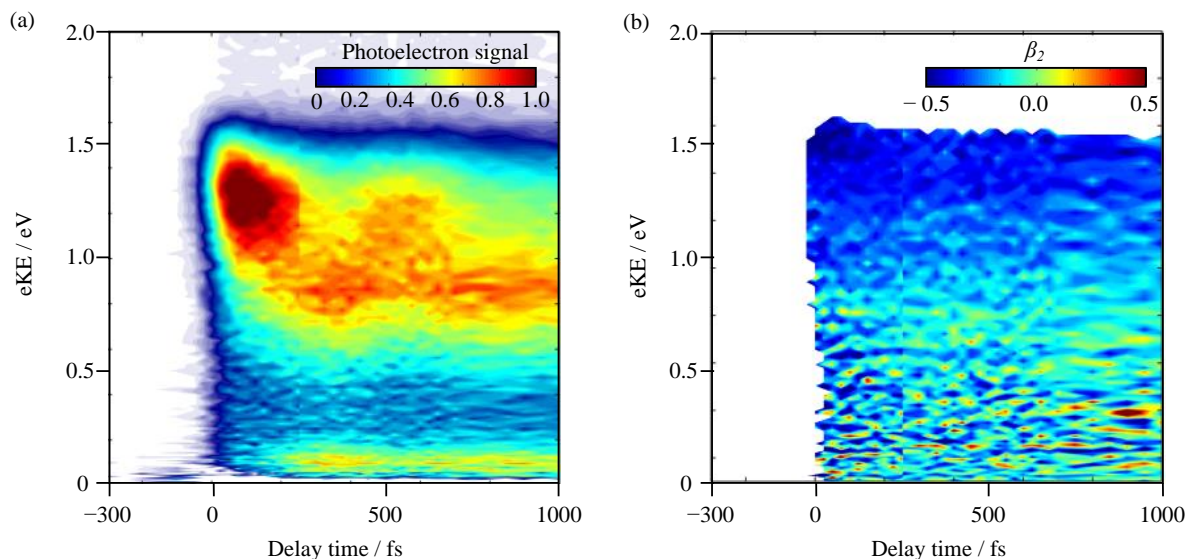


Figure 27(a) Time- and (b) angle-resolved PE spectra for pCK⁻, shown as false-colour intensity plots, over the first picosecond.

Figure 27 (a) shows the time-resolved photoelectron spectra, where each spectrum has had a $t \ll 0$ spectrum subtracted to leave only the time-resolved signal. At short times, (\sim first picosecond), wavepacket dynamics were observed in the time-resolved PE spectra, Figure 27(a). The complementary angle-resolved spectra are given alongside, in Figure 27(b). At time delays close to t_0 the PE spectra consists of a peak centred at ~ 1.40 eV. A representative photoelectron spectrum is shown in Figure 28(b). From $t = 100$ fs the initial PE feature shifts into a lower energy peak centred at ~ 0.75 eV. While both peaks remain present in the subsequent PE spectra, there is a clear oscillation between the initial, higher eKE, peak and the second, lower eKE, peak over the first picosecond. Representative photoelectron spectra of this motion are shown in Figure 28(b). Additionally, the dynamics that result in the feature at eKE ~ 0.75 eV also lead to the emissions of electrons with eKE ~ 0.15 eV. The signal from this feature is concurrent with the growth of the feature at eKE ~ 0.75 eV.

Figure 28 shows the integrated photoelectron signal over three energy windows that are representative of the photoelectron features discussed above as a function of time. The wavepacket oscillation is clearly visible in the peak around 1.4 eV and out-of-phase with the signal at 0.75 eV.

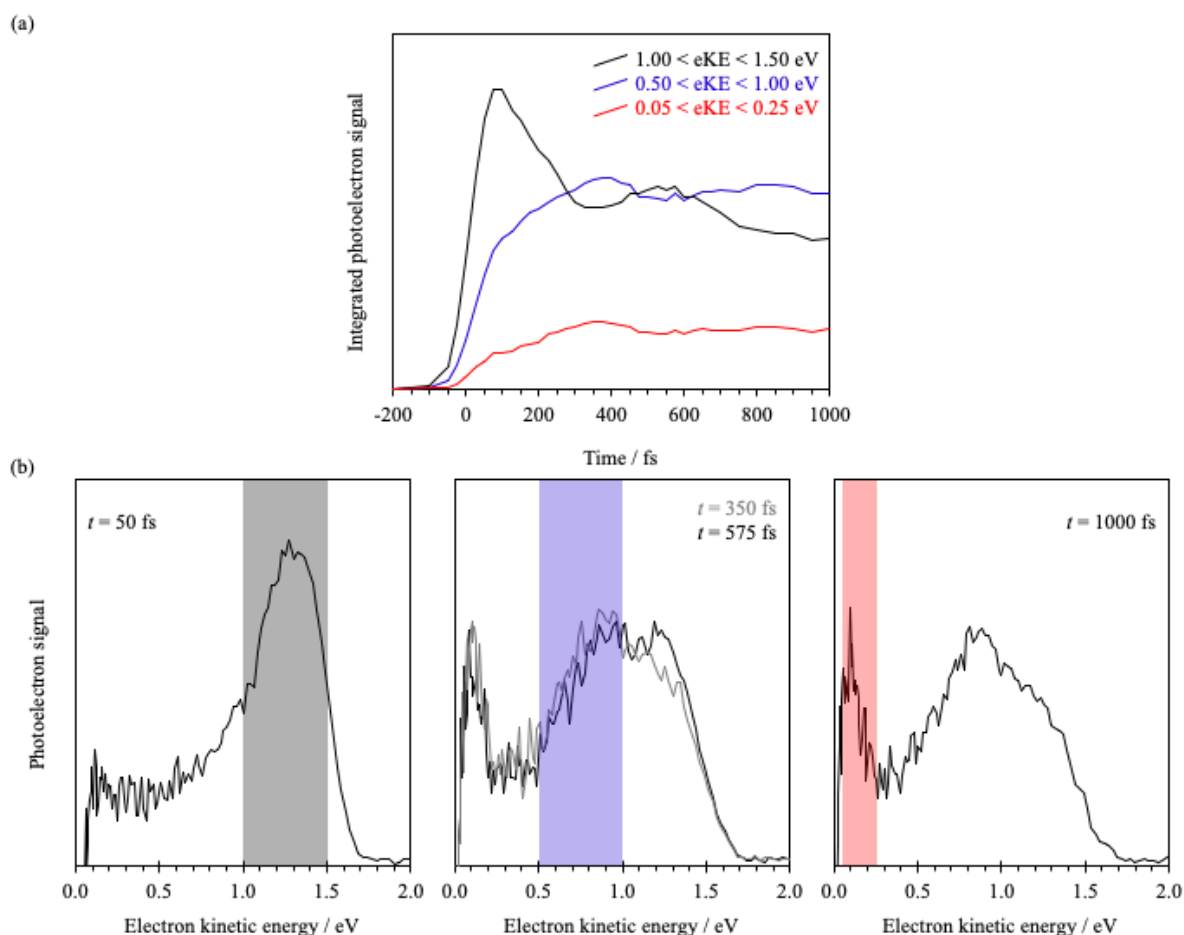


Figure 28(a) Integrated photoelectron signal over spectral windows, indicated by the inset parameters. Time-resolved photoelectron spectra at different t show the three spectral regions (b).

The oscillation between the two PE features occurs with a frequency $\sim 50 \text{ cm}^{-1}$. This behaviour has been seen previously and was interpreted to arise from some initial relaxation prior to wavepacket motion.⁵¹ It should be noted that an oscillation of $\sim 50 \text{ cm}^{-1}$ has also been seen in time-resolved fluorescence spectra of the PYP protein and this oscillation was assigned to some undefined protein mode.⁵² Our results and those of Zewail and co-workers clearly show that this is not the case and is an inherent motion in the chromophore.

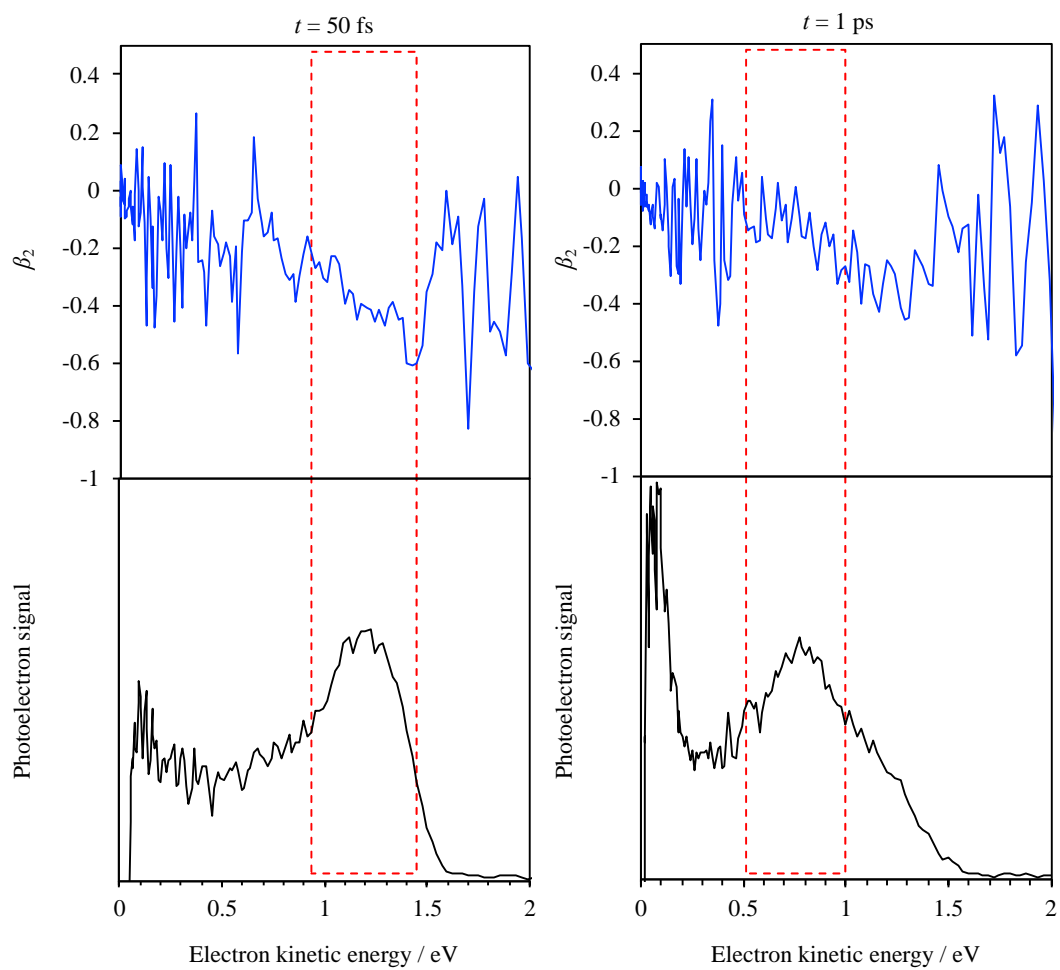


Figure 29 1D angle-resolved (blue) and time-resolved photoelectron spectra (black) at short- and long-times are shown on the left and right, respectively. The photoelectron angular distributions over the region of maximum photoelectron signal are indicated.

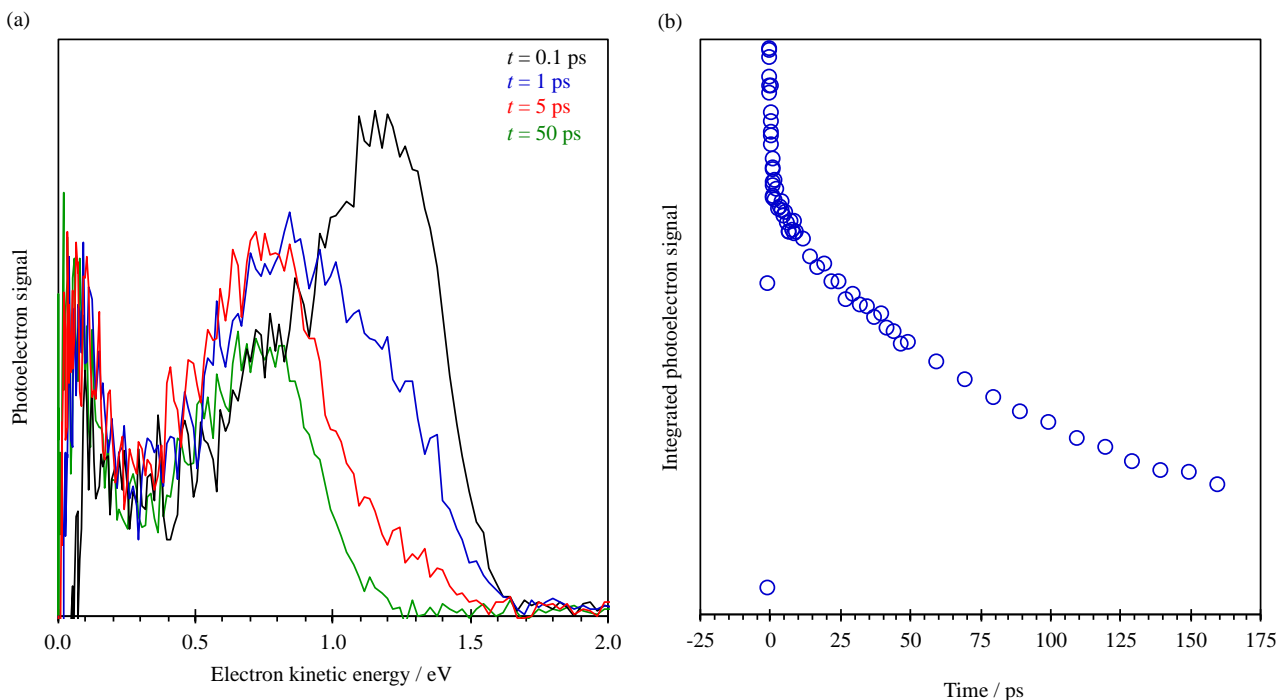


Figure 30 (a) Four example t background-corrected time-resolved spectra; (b) pump–probe signal with a fitted decay lifetime for the S_1 state.

In addition to the TR eKE spectra, it is possible to extract the TR-photoelectron angular distributions, Figure 27(b). A clear difference in anisotropy can be seen between the two oscillating PE features. Evaluation of the anisotropy of a specific photodetachment feature is done by averaging the measured β_2 values over the eKE range that corresponds to the maxima in PE signal, for a given Δt . Such an analysis is shown in Figure 29. The anisotropy of the higher eKE peak is negative, $\beta_2 \sim -0.41$, while the lower eKE peak has a less pronounced negative anisotropy, $\beta_2 \sim -0.14$.

At longer timescales the initial, higher eKE, peak decays and only the peak at 0.75 eV remains, Figure 30(a). This then decays with no further spectral evolution, with a lifetime of ~ 120 ps as shown in Figure 30(b).

5.3.4 Exploration of the S_1 Potential Energy Surface

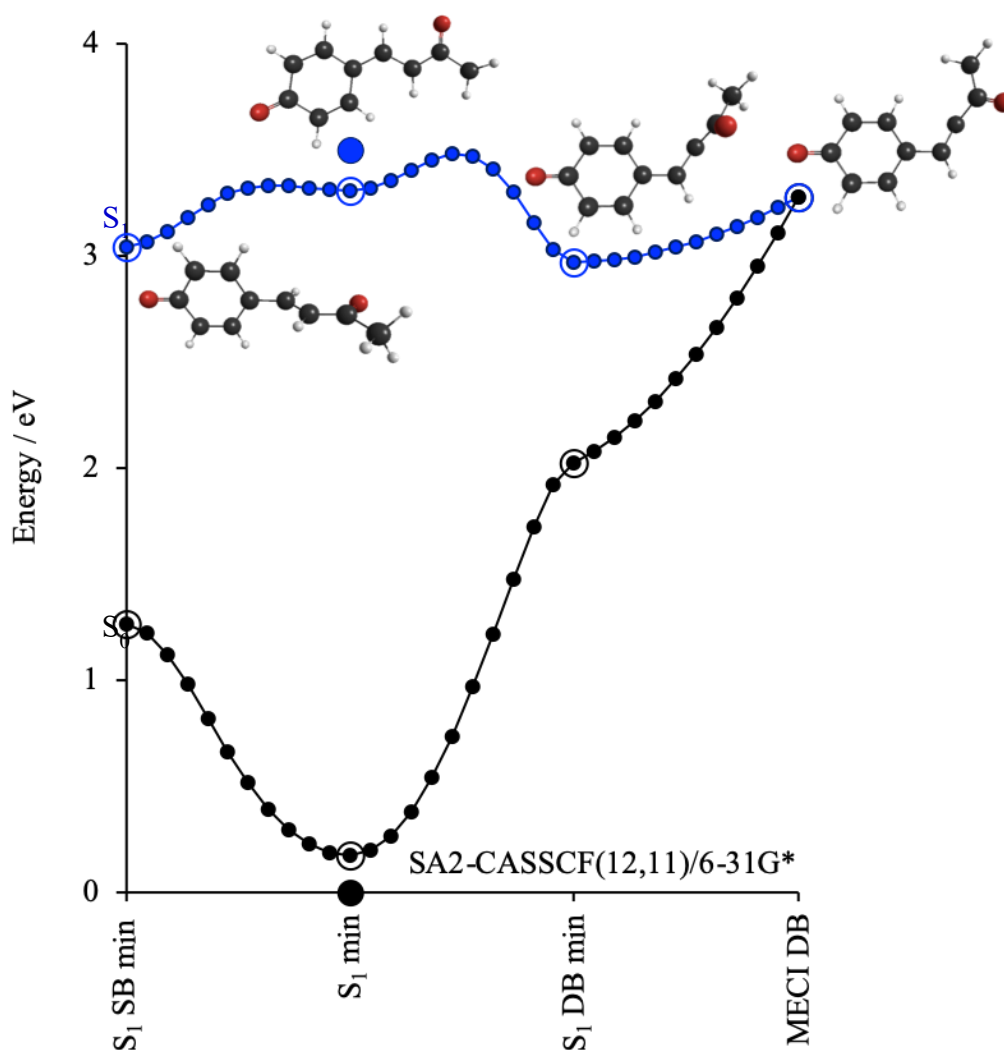


Figure 31 The potential energy surface of the bound excited state of the pCK anion, S_1 , is plotted as a function of rotation about the single bond (SB) and double bond (DB) from the Franck-Condon region. The ground state of the anion, S_0 , is plotted for the same geometries. Structures corresponding to the highlighted points along the potential energy surface are inset. These calculations were performed by B. F. E. Curchod.

To determine the motion of the wavepacket on the S_1 potential energy surface, electronic structure calculations were performed using SA-CASSCF. The initial geometry was the planar minimum in the S_1 geometry, as this represents the geometry with maximum overlap with the anion ground state. From the initial planar geometry, the potential energy surface was investigated with respect to motion around the SB and DB rotation of the para-substituted chain. The energetic profiles of the S_0 and S_1 states along the SA-CASSCF potential energy

surface were verified using XMCQDTP2, and the S_2 and D_0 states along this pathway were also calculated, for completeness. The overall agreement between the CASSCF and higher level XMCQDPT2 calculations are good, and the results of both are shown in Figure 31 and Figure 32, respectively.

From the results of both levels of theory it is evident that there is an energetic barrier in the direction of the DB minimum and MECI, in agreement with the results of Groenhof and co-workers.⁴² There is no substantial energetic barrier in the direction of the SB minimum. A rigid shift has been applied to the XMCQDPT2 D_0 potential energy surface in order to match the experimental values in the Franck-Condon region and the values calculated using semi-canonical orbital energies. The behaviour of the D_0 and S_2 states can be seen to be very similar to one another, along the trajectory of the S_1 potential energy surface.

5.3.5 Interpreting Wavepacket Motion on the S_1 Surface

From both the change in eKE of the main PE feature in the spectra, and the accompanying change in anisotropy, it is evident that there is motion of the wavepacket on the potential energy surface. The shift to lower eKE is indicative of nuclear motion, redistributing the initial excitation energy, resulting in lower energy photoelectrons. Previously, the photoelectron angular distributions have been shown to be very sensitive to changes in nuclear configuration that result in changes to electronic structure that impact the molecular orbital involved in photodetachment.

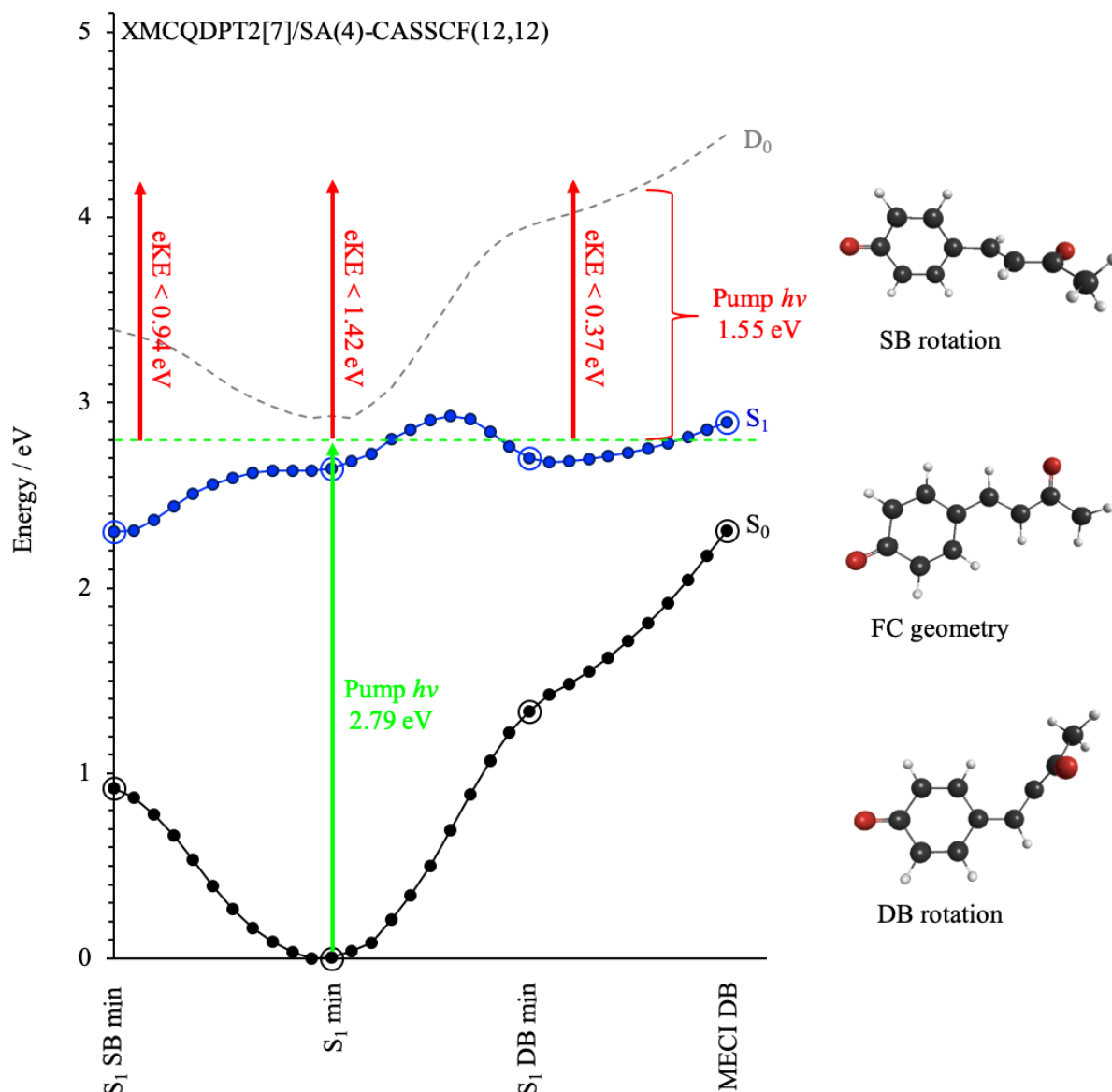


Figure 32 The potential energy surfaces for the ground and first excited states of the anion, S_0 and S_1 respectively, are plotted alongside the detachment continuum, D_0 . These surfaces were calculated using XMCQDPT2[7]/SA(4)-CASSCF(12,12), and detachment to the continuum was modelled through inclusion of an extremely diffuse orbital in the active space. A rigid shift has been applied to the D_0 potential energy surface to correct the value to be in line with experimental values, and the values calculated with semi-canonical orbital energies rather than the DFT/PBE0-based one-electron Fock-type matrix. The XMCQDPT2 potential energy surfaces for the S_0 , S_1 and D_0 states are used to provide a pictorial interpretation of the TR-PE spectra. A single pump pulse is indicated, whereas there are three possible probe pulses. Each of the possible probe pulses indicate the maximum expected kinetic energy of the photoelectron detached the indicated point on the S_1 potential energy surface. Representative geometries for each of the photodetachment regions are inset.

Figure 32 shows the two calculated pathways on the S_1 potential energy surface that the wavepacket might take, following photoexcitation. The relative energies of the S_0 , S_1 and D_0 are shown, with respect to the initial pump pulse energy. The expected maximum kinetic energies of the PE are indicated for photodetachment from the wavepacket in both the direction of the SB and DB rotation. There are several important energetic arguments highlighted schematically in Figure 32. Firstly, the D_0 detachment continuum is not energetically accessible at any point along the considered S_1 potential energy surface following excitation at 444 nm. Secondly, the initial energy of the pump pulse is not sufficient to overcome the barrier in the direction of the DB rotation, so only rotation about the SB should be possible. These two points were not the case in the experiments by Zewail and co-workers. Thirdly, the expected energies of the outgoing PE are quite distinct for the two different rotational directions.

The time-resolved photoelectron spectra are broadly consistent with Figure 32. The PE detached initially from the Franck-Condon region with a predicted maximum eKE of ~ 1.42 eV. Following motion in the direction of DB rotation, the expected maximum energy of an outgoing PE is eKE ~ 0.37 eV. PE detached following motion in the direction of the SB rotation are expected to have higher maximum eKE ~ 0.94 eV. Figure 30(a) shows PE spectra taken at four different delay times. The PE feature observed initially, $t = 0.1$ ps, is in agreement with the maximum eKE expected energy for photodetachment from the Franck-Condon region. Some population of this peak still remains at $t = 1$ ps alongside the lower energy PE feature. At the longer times, $t = 5$ and 50 ps (see Figure 30(a)), only the lower energy PE feature is seen. The PE feature centred eKE ~ 0.75 eV extends to eKE ~ 1.1 eV, in reasonable agreement with that expected for SB rotation. There is no clear PE feature between eKE ~ 0.20 and 0.50 eV suggesting that the peak due to DB rotation is not present. This energetic argument is consistent with the potential energy barrier that cannot be overcome in the direction of DB rotation.

5.3.6 Time-Resolved Photoelectron Angular Distributions

As photoelectron angular distributions are sensitive to the molecular orbital from which the outgoing photoelectron is detached, they provide a sensitive probe of changes to electronic structure, and by extension nuclear structure. This can, in principle, provide insight into nuclear dynamics that occur alongside wavepacket motion on the S_1 excited state.

The inherent sensitivity of photoelectron angular distributions to changes in conformation was previously demonstrated for a related molecule, $\text{pEP}^{\text{h-}}$, in the previous section. In this case, hindered rotation about the single bond of the ethyl-substituent resulted in two conformers, one planar and one with the ethyl-chain perpendicular to the phenolate plane. The rotation of the ethyl-chain was shown to result in a drastic change in photoelectron angular distribution, despite seemingly similar Dyson orbitals and small changes in relative energy. The para-ethyl phenolate anion represents a simplified, but related, structural model of $\text{pCK}^{\text{-}}$, with the hindered rotation about the single bond analogous with the proposed motion on the S_1 potential energy surface. It is therefore suggestive that the photoelectron angular distributions may provide further insight into the analysis of the motion of the wavepacket.

Figure 29 shows there is a change in the measured photoelectron angular distributions between the two PE features, the initial PE feature corresponding to autodetachment from the S_1 state in the Franck-Condon region has negative anisotropy, $\beta_2 \sim -0.41$. The PE feature at lower eKE has a less pronounced negative anisotropic PAD, $\beta_2 \sim -0.14$. The latter experimental PAD was extracted at $t = 1$ ps, when the peak at eKE ~ 1.4 eV has little PE signal. These PADs were chosen as they represented photodetachment from the initial Franck-Condon region and photodetachment following the wavepacket reaching a minimum on the S_1 surface.

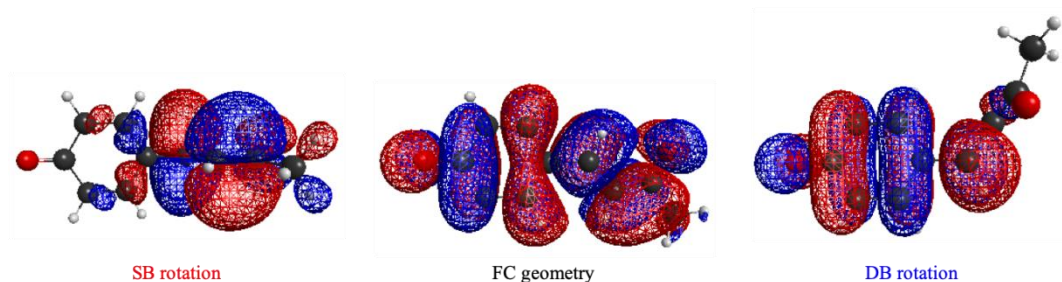


Figure 33 Representative Dyson orbitals and geometric structures for the three regions of the S_1 potential energy surface.

Figure 33 shows the molecular orbitals populated to form the S_1 state for three representative structures from the S_1 SB minimum, the Franck-Condon planar region and the S_1 DB minimum. The molecular orbitals are natural orbitals from the XMCQDPT2 calculations, and in principle these orbitals are representative of the Dyson orbitals. However, these orbitals are used only to offer qualitative insight into the changes in electronic density of the Dyson orbital as a function of nuclear motion in either direction from the Franck-Condon geometry. The negative anisotropy of the higher energy PE feature is consistent with qualitative interpretation of the Dyson orbital for a geometry in the Franck-Condon region and would be predicted to yield a negative modelled anisotropy. It can be seen from Figure 33, that the electron density of the Dyson orbital in the Franck-Condon region is not localised to the phenolate moiety, instead there is significant density delocalised across the entire molecular structure. Therefore, any substantial nuclear motion, i.e. rotation of either the single- or double-bond, will perturb this density and has the potential to cause drastic changes to the photoelectron angular distributions.

Rotation about the SB and DB yields two qualitatively different Dyson orbitals. As previously shown,^{40,46} rotation in the SB direction causes charge transfer in the S_1 state, reflected in the localisation of the Dyson orbital to the conjugated chain. Contrastingly, the Dyson orbital remains delocalised across the entirety of pCK⁻ following DB rotation. The latter scenario is reminiscent of the dramatic change in photoelectron angular distribution between

the two pEPh⁻ conformers in the previous study. Drawing on interpretation from the previous study, it would be expected that rotation in the DB direction would result in a dramatic change in the photoelectron angular distribution. Conversely, rotation in the SB direction would not be expected to cause such a dramatic change in photoelectron angular distributions as all the planarity of the Dyson orbital density is not perturbed. Based purely on this qualitative analysis, it is proposed that DB rotation is not reflected in the photoelectron angular distributions.

Preliminary photoelectron angular distributions modelled using EOM-EE/IP-CCSD support our qualitative analysis. The PAD of the initial Franck-Condon region is calculated to be $\beta_2 -0.28$, in reasonable agreement with the experimentally observed PAD. To represent the PADs following wavepacket motion to either the SB or DB rotation a number of geometries are required to provide further analysis. While this work is ongoing, two static geometries representing the minimum energy geometries in each direction have been calculated. The PADs following the SB rotation are broadly negative, while the PADs following DB rotation are broadly positive, further supporting the analysis presented above.

Based on the energetic and angular distribution arguments, we believe that we are monitoring wavepacket motion from the initially excited Franck-Condon region of the S₁ potential energy surface in the direction of the single-bond twist. While the MECI has not been calculated in the direction of the single-bond rotation, it is understood to be sufficiently high in energy that reformation of the anion ground state is slow. We propose that following initial excitation the wavepacket begins to move along the S₁ potential energy surface in the direction of the SB rotation until the energetic barrier to the MECI is encountered. The wavepacket has insufficient energy to leave the S₁ state, and so the wavepacket bounces between either side of the well, leading to the observed oscillation between the PE features. Following >1 ps, internal vibrational relaxation has taken place so that the wavepacket is left with insufficient energy to reach the FC, and becomes trapped in the lower energy SB well, leading to only

photodetachment yielding the PE feature at $eKE \sim 0.75$ eV. The energetic interpretation of the evolution of the wavepacket on the S_1 potential energy surface is supported by interpretation of the photoelectron angular distributions. Eventually, the population decays from the S_1 state to the ground state on a long 120 ps timescale by statistically sampling regions of the surface with strong nonadiabatic coupling.

5.3.7 Conclusions and Further Work

The interpretation of the findings presented are still ongoing. The arguments presented based upon energetic and photoelectron angular distributions indicate that the wavepacket was constrained to movement along only the direction of SB rotation on the S_1 potential energy surface. Preliminary modelling indicates that TR-photoelectron angular distributions are a sensitive probe of geometric changes and were used to infer wavepacket motion.

Further work is being carried out to provide quantitative analysis of the time-resolved photoelectron angular distributions, using Dyson orbitals obtained through both a single and multi-reference method. The bound state of pCK^- was described well through CASSCF calculations, which optimise the natural orbitals of specific states. Using natural orbitals to model the photoelectron angular distributions for excited states should provide a robust description of the Dyson orbital and allow quantitative analysis. This would in turn lay a foundation for application of photoelectron imaging to photoisomerisation processes in the time domain.

5.4 Section A Conclusions and Outlook

This section has presented an overview of the powerful insight photoelectron angular distributions affords to anion photoelectron spectroscopy. Through the two studies presented, the benefit of the application of the photoelectron angular distributions to aid interpretation of

photoelectron features that are not easily resolved in the energetic spectra has been demonstrated.

Both studies built upon an initial study on the tocopherol anions,²⁶ which had highlighted the ability of photoelectron angular distributions to distinguish between different structural isomers. Through routine extraction of the experimental photoelectron angular distributions alongside both frequency- and time-resolved photoelectron spectroscopy, new insights into the dynamics of the ground and excited states of anions have been made.

The sensitivity of parameters in the Dyson orbital approach have been analysed, and suggestions are outlined for considerations to be made when designing such a calculation. This approach has been shown be able to qualitatively model the experimental photoelectron angular distributions for direct detachment channels. The sensitivity of the photoelectron angular distribution to conformational change in the ground state was demonstrated in the first study. The use of this analysis is broadly applicable and has recently been used in interpretation of photoelectron angular distributions by Fielding and coworkers.⁴⁸

The foundation for development of this technique to model the time-resolved photoelectron angular distributions of a bound excited state of an anion were presented in the second study. The results presented are qualitative, but work is ongoing to quantitatively model the photoelectron angular distributions in the time domain.

There still exist some limitations to the methods currently used to model photoelectron angular distributions. Namely, it has not yet been possible to quantitatively model the photoelectron angular distributions for autodetachment from resonances. There are promising *ab initio* methods that could be applied to this problem. Development of a routine method to quantitatively model photoelectron angular distributions from resonances would unlock an extra dimension for both frequency- and time-resolved photoelectron studies. In principle,

photoelectron angular distributions could be used to fingerprint different electronic states in photoelectron spectra, with little ambiguity.

Finally, it should be noted that there are still cases, such as phenolate, in which the Dyson approach is only able to reproduce qualitative photoelectron angular distribution trends. This limitation may arise from the approximations made for the outgoing wave, which neglect physical properties of the neutral core. Investigation into modelling the outgoing wave with a dipole wave rather than a simple plane wave for molecules with pronounced dipole moments of the neutral core, may provide insight into the physical origin of the current limitations in the method presented.

5.5 References

- 1 S. Gozem and A. I. Krylov, *ezDyson v4*, <http://iopenshell.usc.edu/downloads/ezdyson>.
- 2 S. T. Park, S. K. Kim and M. S. Kim, *Nature*, 2002, **415**, 306–308.
- 3 T. R. Rizzo, J. A. Stearns and O. V. Boyarkin, *Int. Rev. Phys. Chem.*, 2009, **28**, 481–515.
- 4 A. B. Wolk, C. M. Leavitt, E. Garand and M. A. Johnson, *Acc. Chem. Res.*, 2014, **47**, 202–210.
- 5 S. Brøndsted Nielsen, C. Dedonder, G. Féraud and C. Jouvet, *Photophysics of Ionic Biochromophores*, Springer Berlin Heidelberg, Berlin, Heidelberg, 2013.
- 6 E. Garand, M. Z. Kamrath, P. A. Jordan, A. B. Wolk, C. M. Leavitt, A. B. McCoy, S. J. Miller and M. A. Johnson, *Science*, 2012, **335**, 694–698.
- 7 A. M. Rijs and J. Oomens, Eds., *Gas-Phase IR Spectroscopy and Structure of Biological Molecules*, Springer International Publishing, 1st edn., 2015, vol. 364.
- 8 E. M. Duffy, B. M. Marsh, J. M. Voss and E. Garand, *Angew. Chem. Int. Ed.*, 2016, **55**, 4079–4082.
- 9 W. C. Lineberger, *Annu. Rev. Phys. Chem.*, 2013, **64**, 21–36.
- 10 S. T. Stokes, X. Li, A. Grubisic, Y. J. Ko and K. H. Bowen, *J. Chem. Phys.*, 2007, **127**, 084321.
- 11 R. Mabbs, E. R. Grumbling, K. Pichugin and A. Sanov, *Chem. Soc. Rev.*, 2009, **38**, 2169–2177.
- 12 D. M. Neumark, *J. Phys. Chem. A*, 2008, **112**, 13287–13301.
- 13 C. Utsunomiya, T. Kobayashi and S. Nagakura, *Bull. Chem. Soc. Jpn.*, 1980, **53**, 1216–1220.
- 14 Y. Shao, Z. Gan, E. Epifanovsky, A. T. B. Gilbert, M. Wormit, J. Kussmann, A. W. Lange, A. Behn, J. Deng, X. Feng, D. Ghosh, M. Goldey, P. R. Horn, L. D. Jacobson, I. Kaliman, R. Z. Khaliullin, T. Kuš, A. Landau, J. Liu, E. I. Proynov, Y. M. Rhee, R. M. Richard, M. A. Rohrdanz, R. P. Steele, E. J. Sundstrom, H. L. Woodcock, P. M. Zimmerman, D. Zuev, B. Albrecht, E. Alguire, B. Austin, G. J. O. Beran, Y. A. Bernard, E. Berquist, K. Brandhorst, K. B. Bravaya, S. T. Brown, D. Casanova, C.-M. Chang, Y. Chen, S. H. Chien, K. D. Closser, D. L. Crittenden, M. Diedenhofen, R. A. DiStasio, H. Do, A. D. Dutoi, R. G. Edgar, S. Fatehi, L. Fusti-Molnar, A. Ghysels, A. Golubeva-Zadorozhnaya, J. Gomes, M. W. D. Hanson-Heine, P. H. P. Harbach, A. W. Hauser, E. G. Hohenstein, Z. C. Holden, T.-C. Jagau, H. Ji, B. Kaduk, K. Khistyayev, J. Kim, J. Kim, R. A. King, P. Klunzinger, D. Kosenkov, T. Kowalczyk, C. M. Krauter, K. U. Lao, A.

- D. Laurent, K. V. Lawler, S. V. Levchenko, C. Y. Lin, F. Liu, E. Livshits, R. C. Lochan, A. Luenser, P. Manohar, S. F. Manzer, S.-P. Mao, N. Mardirossian, A. V. Marenich, S. A. Maurer, N. J. Mayhall, E. Neuscamman, C. M. Oana, R. Olivares-Amaya, D. P. O'Neill, J. A. Parkhill, T. M. Perrine, R. Peverati, A. Prociuk, D. R. Rehn, E. Rosta, N. J. Russ, S. M. Sharada, S. Sharma, D. W. Small, A. Sodt, T. Stein, D. Stück, Y.-C. Su, A. J. W. Thom, T. Tsuchimochi, V. Vanovschi, L. Vogt, O. Vydrov, T. Wang, M. A. Watson, J. Wenzel, A. White, C. F. Williams, J. Yang, S. Yeganeh, S. R. Yost, Z.-Q. You, I. Y. Zhang, X. Zhang, Y. Zhao, B. R. Brooks, G. K. L. Chan, D. M. Chipman, C. J. Cramer, W. A. Goddard, M. S. Gordon, W. J. Hehre, A. Klamt, H. F. Schaefer, M. W. Schmidt, C. D. Sherrill, D. G. Truhlar, A. Warshel, X. Xu, A. Aspuru-Guzik, R. Baer, A. T. Bell, N. A. Besley, J.-D. Chai, A. Dreuw, B. D. Dunietz, T. R. Furlani, S. R. Gwaltney, C.-P. Hsu, Y. Jung, J. Kong, D. S. Lambrecht, W. Liang, C. Ochsenfeld, V. A. Rassolov, L. V. Slipchenko, J. E. Subotnik, T. Van Voorhis, J. M. Herbert, A. I. Krylov, P. M. W. Gill and M. Head-Gordon, *Mol. Phys.*, 2015, **113**, 184–215.
- 15 D. J. Nelson, W. K. Gichuhi, E. M. Miller, J. H. Lehman and W. C. Lineberger, *J. Chem. Phys.*, 2017, **146**, 074302.
- 16 R. F. Gunion, M. K. Gilles, M. L. Polak and W. C. Lineberger, *Int. J. Mass Spectrom. Ion Process.*, 1992, **117**, 601–620.
- 17 L. H. Stanley, C. S. Anstöter and J. R. R. Verlet, *Chem. Sci.*, 2017, **8**, 3054–3061.
- 18 C. S. Anstöter, J. N. Bull and J. R. R. Verlet, *Int. Rev. Phys. Chem.*, 2016, **35**, 509–538.
- 19 C. W. West, J. N. Bull, A. S. Hudson, S. L. Cobb and J. R. R. Verlet, *J. Phys. Chem. B*, 2015, **119**, 3982–3987.
- 20 C. W. West, J. N. Bull, E. Antonkov and J. R. R. Verlet, *J. Phys. Chem. A*, 2014, **118**, 11346–11354.
- 21 C.-W. Cheng, H. Witek and Y.-P. Lee, *J. Chem. Phys.*, 2008, **129**, 154307.
- 22 E. P. Wigner, *Phys. Rev.*, 1948, **73**, 1002–1009.
- 23 J. D. Lewis, T. B. Malloy, T. H. Chao and J. Laane, *J. Mol. Struct.*, 1972, **12**, 427–449.
- 24 L.-S. Wang, *J. Chem. Phys.*, 2015, **143**, 040901.
- 25 X.-B. Wang, *J. Phys. Chem. A*, 2017, **121**, 1389–1401.
- 26 C. S. Anstöter, C. W. West, J. N. Bull and J. R. R. Verlet, *J. Phys. Chem. B*, 2016, **120**, 7108–7113.
- 27 M. J. Thompson, D. Bashford, L. Noodleman and E. D. Getzoff, *J. Am. Chem. Soc.*, 2003, **125**, 8186–8194.
- 28 M. Mizuno, N. Hamada, F. Tokunaga and Y. Mizutani, *J. Phys. Chem. B*, 2007, **111**, 6293–6296.
- 29 H. Kuramochi, S. Takeuchi, K. Yonezawa, H. Kamikubo, M. Kataoka and T. Tahara, *Nat. Chem.*, 2017, **9**, 660–666.
- 30 T. E. Meyer, E. Yakali, M. A. Cusanovich and G. Tollin, *Biochemistry*, 1987, **26**, 418–423.
- 31 K. J. Hellingwerf, W. D. Hoff and W. Crielaard, *Mol. Microbiol.*, 1996, **21**, 683–693.
- 32 M. A. van der Horst and K. J. Hellingwerf, *Acc. Chem. Res.*, 2004, **37**, 13–20.
- 33 T. E. Meyer, *Biochim. Biophys. Acta BBA - Bioenerg.*, 1985, **806**, 175–183.
- 34 T. E. Meyer, G. Tollin, T. P. Causgrove, P. Cheng and R. E. Blankenship, *Biophys. J.*, 1991, **59**, 988–991.
- 35 M. Koh, G. Van Driessche, B. Samyn, W. D. Hoff, T. E. Meyer, M. A. Cusanovich and J. J. Van Beeumen, *Biochemistry*, 1996, **35**, 2526–2534.
- 36 C. Ko, B. Levine, A. Toniolo, L. Manohar, S. Olsen, H. J. Werner and T. J. Martinez, *J Am Chem Soc*, 2003, **125**, 12710–12711.
- 37 A. Henley, M. E. Diveky, A. M. Patel, M. A. Parkes, J. C. Anderson and H. H. Fielding, *Phys. Chem. Chem. Phys.*, 2017, **19**, 31572–31580.
- 38 I. B. Nielsen, S. Boyé-Péronne, M. O. A. El Ghazaly, M. B. Kristensen, S. Brøndsted Nielsen and L. H. Andersen, *Biophys. J.*, 2005, **89**, 2597–2604.
- 39 I.-R. Lee, W. Lee and A. H. Zewail, *Proc. Natl. Acad. Sci.*, 2006, **103**, 258–262.
- 40 E. V. Gromov, I. Burghardt, H. Köppel and L. S. Cederbaum, *J. Am. Chem. Soc.*, 2007, **129**, 6798–6806.
- 41 M. Boggio-Pasqua and G. Groenhof, *Comput. Theor. Chem.*, 2014, **1040–1041**, 6–13.
- 42 M. Boggio-Pasqua and G. Groenhof, *J. Phys. Chem. B*, 2011, **115**, 7021–7028.

- 43 E. V. Gromov, I. Burghardt, H. Köppel and L. S. Cederbaum, *J. Phys. Chem. A*, 2011, **115**, 9237–9248.
- 44 E. V. Gromov, *J. Chem. Phys.*, 2014, **141**, 224308.
- 45 F. F. García-Prieto, A. Muñoz-Losa, I. Fdez. Galván, M. L. Sánchez, M. A. Aguilar and M. E. Martín, *J. Chem. Theory Comput.*, 2017, **13**, 737–748.
- 46 M. Boggio-Pasqua, M. A. Robb and G. Groenhof, *J. Am. Chem. Soc.*, 2009, **131**, 13580–13581.
- 47 G. Groenhof, M. Buxin-Cademartory, B. Hess, S. P. de Visser, H. J. C. Berendsen, M. Olivucci, A. E. Mark and M. A. Robb, *J. Am. Chem. Soc.*, 2004, **126**, 4228–4233.
- 48 J. L. Woodhouse, A. Henley, M. A. Parkes and H. H. Fielding, *J. Phys. Chem. A*, 2019, **123**, 2709–2718.
- 49 C. S. Anstöter, T. E. Gartmann, L. H. Stanley, A. V. Bochenkova and J. R. R. Verlet, *Phys. Chem. Chem. Phys.*, 2018, **20**, 24019–24026.
- 50 C. S. Anstöter, C. R. Dean and J. R. R. Verlet, *Phys. Chem. Chem. Phys.*, 2017, **19**, 29772–29779.
- 51 J. P. Rogers, C. S. Anstöter and J. R. R. Verlet, *Nat. Chem.*, 2018, **10**, 341–346.
- 52 N. Mataga, H. Chosrowjan and S. Taniguchi, *J. Photochem. Photobiol. C Photochem. Rev.*, 2004, **5**, 155–168.

Section B Excited State Dynamics

The interaction of molecules with light drives many chemical, physical and biological processes. As molecules often exist in complex environments, it is difficult to decouple the strong interaction with the environment from the intrinsic dynamics of the molecule itself. In order to gain a better understanding of the interaction of molecules ubiquitous in nature with light it is favourable to adopt a ‘bottom-up’ approach to unravelling the structure-function dynamics. Previous gas-phase spectroscopy studies have shown how this approach offers a powerful method to study only the intrinsic dynamics of the *light-absorbing* structural motif. A particularly powerful method is 2D anion photoelectron spectroscopy. This chapter presents studies that have furthered this method. Here the bottom-up approach is applied to the phenolate chromophore (Section 5.1) and the para-dinitrobenzene (pDNB) anion (Section 5.2).

Work in this Section is based on the publications below, and unless stated otherwise I performed the experimental and computational work.

1. C. S. Anstöter, C. R. Dean and J. R. R. Verlet
Chromophores of chromophores: a bottom-up Hückel picture of the excited states of photoactive proteins
PCCP **19**, 29772 (2017)
2. C. S. Anstöter, T. E. Gartmann, L. H. Stanley, A. V. Bochenkova and J. R. R. Verlet
Electronic structure of the para-dinitrobenzene radical anion: A combined 2D photoelectron imaging and computational study
PCCP **20**, 24019 (2018)

5.6 A Bottom-up Hückel Picture of the Excited States of Photoactive Proteins

5.6.1 Introduction

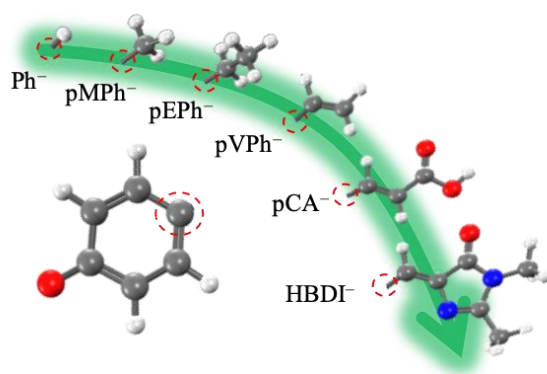


Figure 34 Schematic showing structures of chemically substituted para-phenolate chromophores with increasing complexity

At the core of most photoactive proteins is a small organic chromophore that acts as a light activated switch for the protein's function. Many of these natural chromophores contain the phenolate anion, Ph^- (Figure 34). In the green fluorescent protein (GFP), the chromophore is often taken to be the deprotonated p-hydroxybenzylidene-2,3-dimethylimidazolinone (HBDI $^-$, Figure 34), which is hindered from undergoing isomerisation in the protein and consequently fluoresces with a very high quantum yield.^{6,7} In the photoactive yellow protein (PYP), the chromophore is often taken to be deprotonated p-coumaric acid (pCA $^-$, Figure 34), which undergoes a trans-cis isomerisation upon near UV-excitation and serves as a mechanical switch to initiate the protein's response.^{8,9} The commonality of phenolates in many photoactive proteins arises from the biosynthetic pathways of chromophores that often involve tyrosine. The photophysics of photoactive protein chromophores has attracted much attention because of their underpinning role in the initial protein response to light.¹⁰⁻¹² Gas-phase spectroscopy has been particularly valuable as it provides an unperturbed view of the excited states of the chromophores and of their dynamics.^{2,13-16} Additionally, the gas-phase environment is

tractable by high-level electronic structure theory,^{1,5,17,18} which when combined with experiment, provides a detailed understanding of the excited state dynamics. However, the reliance on very high-level computational methods can mask some of the simple physical principles that are the foundation of the overall electronic structure of the chromophores. Such principles are central to the logical development of new light-activated proteins or macromolecules, and to understanding the natural selection based on nature's basic building blocks such as the amino acids. Here, gas-phase photoelectron imaging of the phenolate chromophores of HBDI⁻ and pCA⁻ is used. Based on our results, it is possible to provide a simple bottom-up picture of their bright excited states using Hückel theory together with electronic structure calculations. Specifically, a simple linear combination of MOs is shown to give rise to the characteristic spectroscopic features of these photoactive chromophores.

There is a wealth of experimental and computational studies on the photophysics of photoactive proteins and, specifically, their chromophores.^{16,19–34} These have largely focussed on the first singlet excited (S_1) state of the chromophores, because this is generally the excited state that is the most relevant to the biological function of the protein. For example, the pioneering work by Andersen and co-workers showed that the absorption spectrum of HBDI⁻ has a very similar appearance in vacuum as it does in the protein environment. The S_1 state of HBDI⁻ has been the focus of a large number of gas-phase studies.^{1,21,33,35–39} A very insightful picture of the electronic structure of the S_1 state was provided by Bravaya *et al.*, who rationalised the energetic shifts in different coloured photoactive proteins using a 3-centre allyl radical in a simple Hückel framework and a particle in the box model.⁴⁰

More recently, experimental and computational work has been directed to the higher-lying excited states in the UV spectral region. These are believed to be important in the photooxidation of the photoactive proteins. For example, in GFP a second optically bright state of HBDI⁻, S_3 , has been observed by action spectroscopy.²¹ Photoelectron spectroscopic

measurements with complementary computational studies suggest that the S_3 state leads to electron ejection from the protein to form hydrated electrons.¹ More generally, frequency-resolved photoelectron spectroscopy has provided valuable insight into the dynamics of resonances in the isolated chromophores, including HBDI⁻.^{1,41} High-level electronic structure calculations show that the S_3 resonance is formed by promotion of an electron from the HOMO to an unoccupied π^* MO localised almost exclusively on the phenolate chromophore. In a similar vein to the interpretation of the S_1 state, Bochenkova *et al.* viewed the MOs for the ground and excited electronic states using a cartoon Hückel picture to sketch the nature of transitions.²¹ While high-level calculations allow quantitative analysis of experimental data, the simple models based on Hückel theory allow qualitative analysis that provides deep insight into the nature of electronic states, which is critical in the rational design of new photoactive proteins and macromolecules. This is particularly so from a synthetic chemist's perspective who may not have the highly specialised skills required to perform high-level electronic structure calculations. In this study, a generalised Hückel picture is used to validate a bottom-up approach. The first two bright states of photoactive proteins are shown to arise from interaction of two chromophore moieties and that the phenolate chromophore is essential to describing the UV response of photoactive chromophores.

5.6.2 Methodology

The experimental details have been provided in Section 3.2 and Section 4.1.2.2.

Hückel theory calculations were performed using the HuLiS calculator.^{42,43} More extensive electronic structure calculations of the ground and excited state were carried out using the QChem 4.4 package.⁴⁴ Initial DFT calculations obtained geometries of the ground states of neutral and anions, using the B3LYP/aug-cc-pVDZ. TD-DFT calculations confirmed the character and energetics of the excited states of the anion and neutral accessed experimentally. Further calculations explored changes to the character of the bright excited

states of a series of para-substituted phenolates from phenolate to p-hydroxybenzylideneimidazolinone (HBI⁻), as shown in Figure 34. HBI refers to the HBDI chromophoric unit without the inclusion of two spectator methyl- groups, omitted to reduce the complexity of the model. These calculations were done using the B3LYP/cc-pVDZ, to exclude diffuse continuum states and simplify analysis of the molecular orbitals.

To model the PADs, all anions were reoptimized using CCSD/aug-cc-pVDZ. Using these optimized geometries, the Dyson orbitals were calculated using EOM-IP-CCSD/aug-cc-pVDZ, and the PADs were modelled using the ezDyson program v4.⁴⁵

5.6.3 Frequency- and Angle-Resolved Photoelectron Spectra

The frequency-resolved photoelectron spectra for Ph⁻, pEPh⁻, pVPh⁻ and HBDI⁻ are summarized as 2D false-colour plots in Figure 35(a)-(d), respectively. To emphasize spectral changes as a function of, $h\nu$, the photoelectron spectra have been normalised to a maximum intensity of one. At all $h\nu$, the photoelectron spectra are dominated by a feature with an eKE that increases linearly with increasing photon energy. This direct detachment channel corresponds to electron loss from the ground state of the anion to form the ground state of the corresponding neutral species, $S_0 + h\nu \rightarrow D_0 + e^-$. A second direct detachment feature for Ph⁻, pMPh⁻ and pEPh⁻, with an onset at $h\nu \sim 3.2$ eV, corresponds to the $S_0 + h\nu \rightarrow D_1 + e^-$ direct detachment channel. This channel is also seen for pVPh⁻, albeit relatively weaker and shifted to $h\nu \sim 3.5$ eV. It is not observable in HBDI⁻.

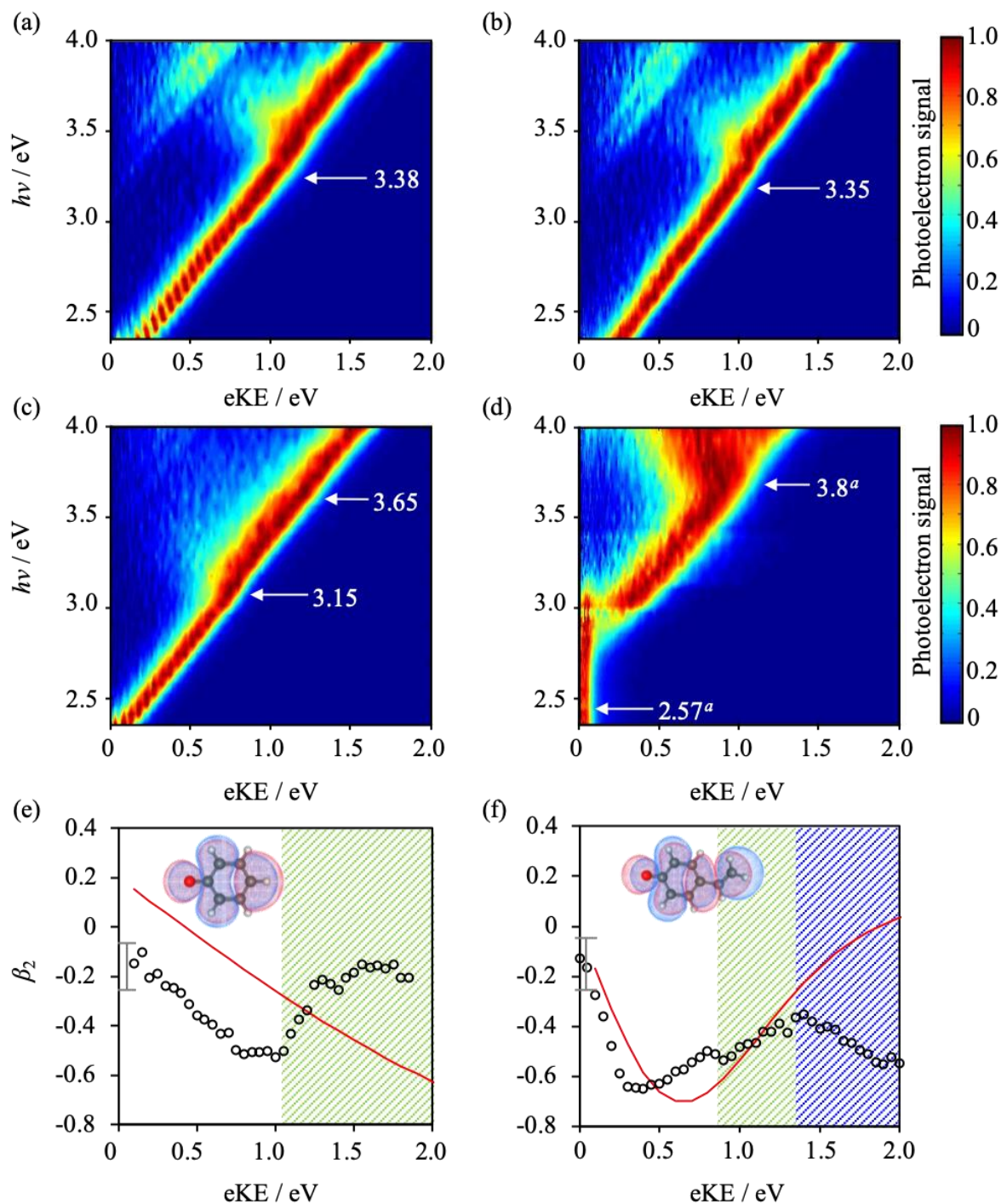


Figure 35 Frequency-resolved photoelectron spectra of (a) Ph^- , (b) pEPh^- , (c) pVPh^- , and (d) HBDI^- (taken from ref 33) are shown. All photoelectron spectra are normalised to a unit maximum. The horizontal arrows indicate the onsets of resonances in eV. For HBDI^- , these are taken from ref 19. Anisotropy parameters (β_2) for (e) Ph^- and (f) pVPh^- as a function of eKE.

In addition to the direct detachment features, spectral broadening is observed for all the anions, where photoelectron signal is observed at lower eKE than the direct detachment peak.

Such shifts have been observed in the photoelectron spectra of many anionic species,^{3,35,41,46–48} including several bio-chromophore derivatives based on phenolate.^{1,13,24,35,38,49} The shift towards lower eKE arises from the excitation of an electronic resonance of the anion. This resonance can undergo nuclear motion which leads to changing Franck-Condon factors with the final neutral states to which it autodetaches. The spectral features are broadly similar for all the phenolates including HBDI[−], suggesting that a common motif is responsible for the observed dynamics. However, the onset and width of the resonance features can be seen to change most significantly between Ph[−] and pEPh[−] to pVPh[−] and HBDI[−]. Additionally, the cross-section of excitation to the resonance appears to be larger for the latter two as evidenced by the larger proportion of photoelectrons lost from the autodetachment channel than from the direct channel leaving the neutral in the D₁ state.

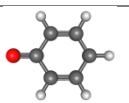
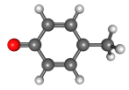
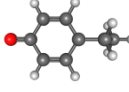
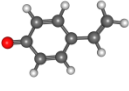
		VDE _{calc}	ADE _{calc}	D ₁ calc	VDE _{exp}	ADE _{exp}	D ₁ exp
	Ph [−]	2.27	2.21	3.28	2.30 ± 0.10	2.27 ± 0.10	3.29 ± 0.10
	pMPh [−]	2.15	2.07	3.19	2.24 ± 0.10	2.15 ± 0.10	3.21 ± 0.10
	pEPh [−]	2.18	2.12	3.22	2.23 ± 0.10	2.13 ± 0.10	3.22 ± 0.10
	pVPh [−]	2.02	1.97	3.11	2.45 ± 0.10	2.31 ± 0.10	3.47 ± 0.10

Table 2 The calculated and experimental VDEs, ADE, and onset of the D₁ channel of Ph[−], pMPh[−], pEPh[−] and pVPh[−]. All energies are in electron volts (eV).

The experimental data allows key properties of the phenolate derivatives to be determined. This includes the VDE and ADE, as well as the D₀-D₁ gap and the onset of the

resonances (Table 2). The resonance onsets were determined in two ways. They can be identified by the $h\nu$ at which the indirect autodetachment signal can be observed (see Figure 35(a) – (d)). They can also be determined from sudden changes in PADs as a function of $h\nu$. Figure 35(e) and (f) show the experimentally determined anisotropy parameters (β_2) for Ph^- and pVPh^- , respectively. The experimental β_2 parameter as a function of eKE were computed and their functionality followed the experimental values up to an eKE where a resonance can be accessed. The Dyson orbital approach fails to capture autodetachment from resonance leading to PADs rapid deviations from calculated behaviour.^{46,50} Examples of this are shown in Figure 35(e) and (f) for Ph^- and pVPh^- , respectively. There are two regions that show discontinuities for pVPh^- , suggesting that there are two resonances present. The onset of the resonance derived from the photoelectron spectra and the PADs agree remarkably well with each other, providing confidence of the assignment. However, it is noted that there is no clear indication of the second resonance for pVPh^- , except for the much greater range over which spectral broadening occurs in this anion, and in the PADs (Figure 35(f)) which shows a second deviation. We used the PAD data to estimate the location of the second resonance. The onsets of observed resonances have been included in Figure 35(a) – (d) as horizontal arrows. Those for HBDI^- are taken from the action spectrum of the Andersen group and agree with the values determined from the frequency-resolved photoelectron spectra in Figure 35(d).

In addition to ground state calculations, excited state calculations were performed. While the absolute energies are in poor agreement, the relative energies and patterns of states are expected to be less prone to large errors and these are used to provide a basis for the interpretation of the experimental data. The first bright resonance in Ph^- , pMPh^- and pEPh^- was calculated to be independent of substituent, in agreement with experimental observations. This resonance corresponded to the promotion of an electron from the HOMO

to an unoccupied antibonding MO localised on the phenol ring, π_{Ph}^* . The relevant orbital calculated by DFT for Ph^- is shown in Figure 36(a). Autodetachment from the resonance correlates with a one-electron process, in which loss of the electron from the π_{Ph}^* orbital produces the D_0 ground neutral state. The resonance is therefore of shape character. According to our calculations, for pVPh^- there are two bright excited states. Both have mixed character with a combination of a similar π_{Ph}^* orbital as well as an unoccupied MO, π_{R}^* on the vinyl unit (where R denotes the functional group attached to the para-position). For vinyl, this π_{R}^* orbital has the appearance of the π^* MO of ethene, as shown in Figure 36(b). The weights according to TD-DFT of the two excited states in terms of these orbitals are: $\Psi_+ = 0.60 \pi_{\text{Ph}}^* + 0.76 \pi_{\text{R}}^*$ and $\Psi_- = 0.75 \pi_{\text{Ph}}^* - 0.58 \pi_{\text{R}}^*$, where Ψ_+ is lower in energy than Ψ_- by 0.44 eV. The presence of two resonances in pVPh^- accounts for the large width observed for the resonance autodetachment seen in Figure 35(c) and the changes noted in the PADs in Figure 35(f).

5.6.4 What the Hück?

The frequency resolved photoelectron spectra for Ph^- , pMPh^- and pEPh^- are essentially identical, which allows us to conclude that the addition of an alkyl group (R) at the para position of the phenolate does not affect the π_{Ph}^* resonance energies, nor does it appear to affect the autodetachment dynamics from this resonance. This can be justified in a Hückel framework as the π_{Ph}^* orbital has no electron density on the oxygen or the para-carbon atom which binds to the R group. Hence, the π_{Ph}^* orbital essentially corresponds to a π^* orbital of benzene with a Hückel energy of $\varepsilon = \alpha - \beta$. As it is a localised excitation, there is also no reason to expect the dynamics to differ as R changes. However, in the case of pVPh^- and HBDI^- , the R group does perturb the excited state structure. The main difference in these cases is that the R group has its own π -system that is conjugated to the phenolate.

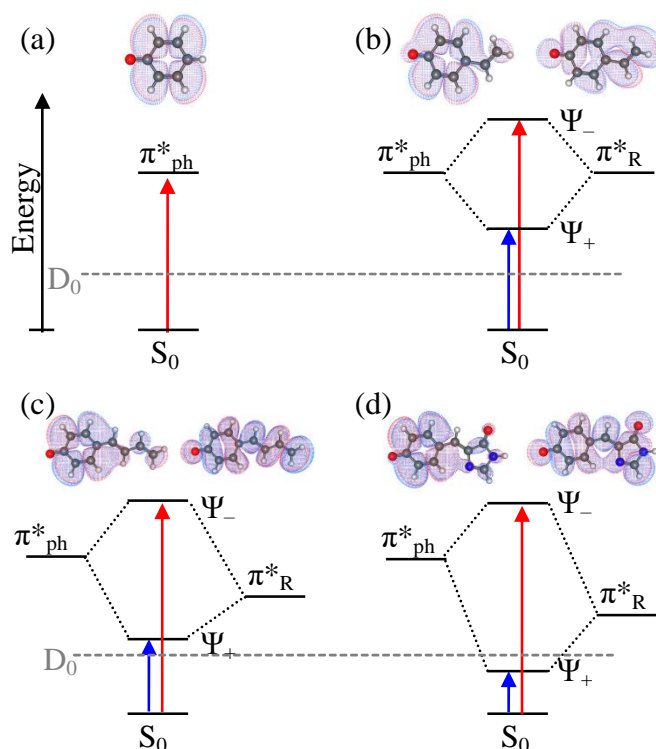


Figure 36 Relevant MOs and schematic MO diagram of excited states of (a) Ph^- , (b) pVPh^- , (c) pBPh^- , and (d) HBDI^- . The π^*_{ph} MO (left) produces a linear combination with the π^*_{R} MO (right) to produce the excited state structure of the chromophores. The neutral state, D_0 , is also indicated by the dashed grey line.

If the R group's π electron system is conjugated with the phenolate, then the HOMO becomes delocalised over the entire molecule. For pVPh^- the HOMO calculated using DFT is shown in Figure 36(b), while Figure 37(b) shows the results from a simple Hückel calculation. Both calculations show the delocalised π electron nature of the HOMO. However, inspection of the Hückel HOMO allows us to approximate it as a combination of the HOMO of the phenolate (shown in Figure 37(a)) and the allyl radical (highlighted region in Figure 37(b)) with the para-carbon providing a common contribution. Now the unoccupied MOs of pVPh^- within the Hückel framework is considered.

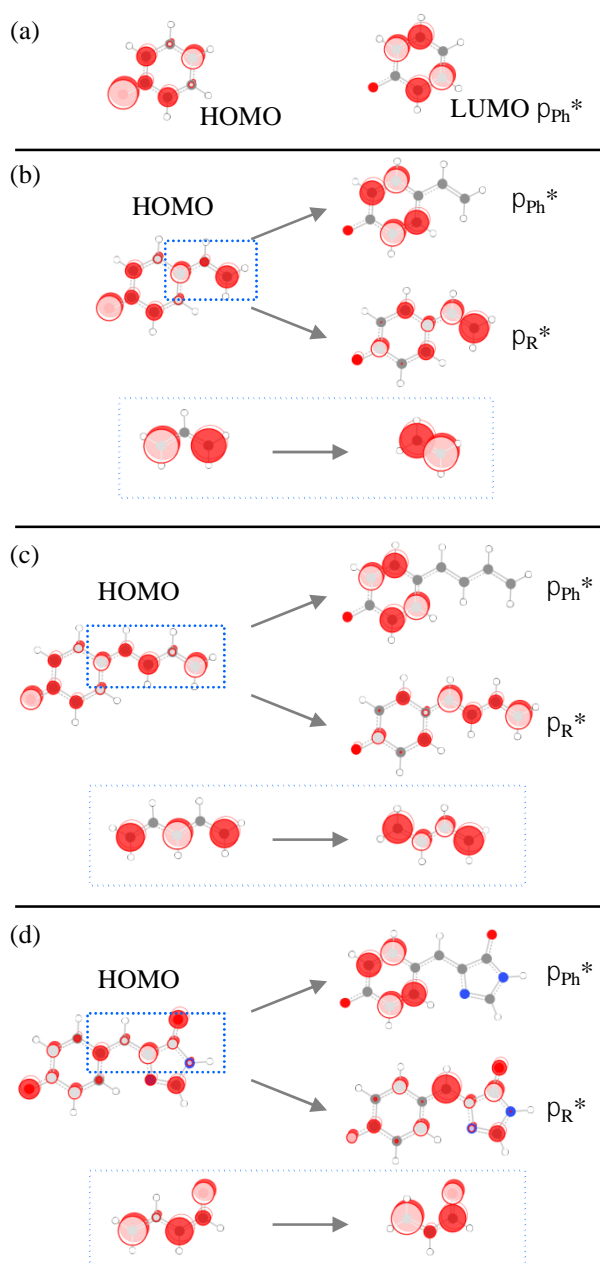


Figure 37 Highest occupied Hückel molecular orbital (HOMO) and lowest unoccupied molecular orbital (LUMO) and π_{Ph}^* and π_{R}^* MOs of (a) Ph^- , (b) pVPPh^- , (c) pBPh^- , and (d) HBI^- . Marked insets in (b) – (d) show the chromophoric MOs involved in the HOMO \rightarrow LUMO transition. It is noted that there is a small contribution of the second unoccupied π^* MO of phenolate (b), however this is the same in all molecule, so may be expected to have the same contribution in all anions considered.

The lowest-lying unoccupied MO has the appearance of the ethene antibonding orbital, π_{R}^* , as shown in Figure 37(b). The second unoccupied MO is the LUMO of phenolate, π_{Ph}^* , which is localised because of the very small coefficients (i.e. almost a node) at the para-carbon.

Assuming that π_R^* can be approximated as the ethene π^* MO, then the Hückel energies of the π_{Ph}^* and π_R^* are degenerate with an energy of $\varepsilon = \alpha - \beta$. It is possible now to construct a simple MO diagram involving these π_{Ph}^* and π_R^* orbitals, as shown in Figure 37(b). A linear combination of π_{Ph}^* and π_R^* MOs will lead to two new MOs: $\Psi_{\pm} = 0.71\pi_{Ph}^* \pm 0.71\pi_R^*$. This is in very good agreement with the TD-DFT calculations that yield $\Psi_+ = 0.60\pi_{Ph}^* + 0.76\pi_R^*$ and $\Psi_- = 0.75\pi_{Ph}^* - 0.58\pi_R^*$. The calculated energy gap is 0.44 eV. The Ψ_+ MO is lowered by ~ 0.2 eV compared to Ph^- , $pMPh^-$ and $pEPH^-$, in good agreement with the results shown in Figure 35. The Ψ_- solution is expected to increase in energy by ~ 0.2 relative to the π_{Ph}^* MO. This is close to the 0.3 eV from the experiment (Figure 35(c)).

In addition to the spectral agreement, the above analysis agrees with the observed experimental changes in the resonance dynamics. The autodetachment dynamics that can be ascertained from the spectral broadening appears to be similar for the two resonances of $pVPh^-$. This is in line with the fact that both have equal contributions from the π_{Ph}^* MO which is of shape character and is responsible for the autodetachment as seen in Figure 35(a) and (b). Additionally, the transition strength appears to have increased for both Ψ_+ and Ψ_- in $pVPh^-$ compared to the excitation to the pure π_{Ph}^* state in Ph^- . This can be rationalised by the $^1\pi\pi^*$ character in the excitation that comes about from the bright $n(\text{allyl}) \rightarrow \pi^*(\text{ethene})$ transition (see inset of Figure 37(b)).

It is also noted that energy gap between the HOMO and the π_{Ph}^* MO is not drastically affected by para-substitution. This can be appreciated by inspection of Figure 36(b), which shows that the HOMO of $pVPh^-$ is qualitatively the same as that of Ph^- because the conjugated R group is non-bonded due to a central allyl node. In fact, this argument essentially remains true for all phenolates discussed here.

This Hückel analysis can now be extended to larger conjugated molecules. We begin by considering 1,3-butadienylphenolate (BPh^-), Figure 36(c) and Figure 37(c). For this

molecule, R can be approximated as pentadiene bound to phenolate with the common para-carbon (see Figure 37(c) inset). The unoccupied MOs can be considered in a similar spirit as above. The π_{Ph}^* MO is the same as that of pVPh⁻ and Ph⁻. The π_{R}^* MO can be viewed as the first π^* MO of butadiene (see Figure 37 (c) inset), which has a Hückel energy $\varepsilon = \alpha - 0.62 \beta$. The reduction of the orbital energy of π_{R}^* relative to π_{Ph}^* means that their linear combination of π_{R}^* with π_{Ph}^* results in a lower energy of Ψ_+ , while Ψ_- will remain at approximately the same energy as Ψ_- in pVPh⁻. The linear combination of MOs will lead to Ψ_+ and Ψ_- with non-equal coefficients for the two contributing MOs. For Ψ_+ , the π_{Ph}^* MO is expected to have the largest contribution, while for Ψ_- , π_{R}^* is expected to have the largest coefficient. This is in agreement with TD-DFT calculations that shown that $\Psi_+ = 0.00 \pi_{\text{Ph}}^* + 0.95 \pi_{\text{R}}^*$ and $\Psi_- = 0.95 \pi_{\text{Ph}}^* - 0.00 \pi_{\text{R}}^*$. Hence, the modest lowering of the π_{R}^* orbital energy has drastically altered the nature of the excited states, with the lowest being almost exclusively of n(pentadiene) $\rightarrow \pi^*$ (butadiene) character (see Figure 37(c) inset). Experimentally, one would expect the photoelectron spectra to have similarities to that of Ph⁻ with the π_{Ph}^* resonance shifted to $h\nu \sim 3.7$ eV (as for pVPh⁻). The transition energy to the π_{Ph}^* resonance is expected to incur small changes because there is no significant perturbation to either the π_{Ph}^* orbital nor the HOMO from which the electron is excited with increased conjugation. In addition to the π_{Ph}^* resonance, we expect a lower-lying state to be observable because of the lower orbital energy of π_{R}^* in pBPh⁻. The TD-DFT calculations indicate the energy gap between the two electronic states is ~ 0.50 eV.

Using the above framework, the frequency-resolved photoelectron spectra of HBDI⁻, which have previously been recorded and reproduced in Figure 35(d), can also be interpreted. For convenience, we ignore the methyl groups of HBDI⁻ and only consider HBI⁻. With reference to Figure 37(d), HBI⁻ can be viewed as phenolate conjugated via an allyl bridge to the imidazole ring. As before, there are two important π^* orbitals: the phenolate π_{Ph}^* orbital

and the π_R^* , where R is the imidazole-ring with ethene in the 2-position (Figure 37(d) inset). The Hückel energy of the π_R^* orbital is $\varepsilon = \alpha - 0.35 \beta$ compared to $\varepsilon = \alpha - \beta$ for π_{Ph}^* . Hence, based on a comparison with pBPh⁻, we expect the lowest-lying excited state to be almost purely of π_R^* character, while at higher energy we expect to see a resonance similar to that of Ph⁻, but again shifted to $h\nu \sim 3.7$ eV. This is broadly consistent with experimental observation. The energy gap between S₁ and the higher lying π_{Ph}^* resonance is ~ 1.2 eV, based on the action spectra from Andersen and co-workers.²¹ Our calculations predict an energy gap of 0.77 eV, which is in reasonable agreement with experiment. The TD-DFT calculated excited states are defined by $\Psi_+ = 0.00 \pi_{Ph}^* + 0.95 \pi_R^*$ and $\Psi_- = 0.78 \pi_{Ph}^* - 0.59 \pi_R^*$. Hence, as anticipated from the pBPh⁻, the S₁ state is almost purely of π_R^* character. Note that the Ψ_- solution appears to have a larger than expected contribution from the π_R^* MO. This arises from excitation of HOMO-4 (the next lower-lying π_{Ph} MO) to the π_R^* MO, which is not accounted for in the current simple Hückel theory picture. Nevertheless, the dynamics of the predominantly π_{Ph}^* resonance in HBDI⁻ are consistent with those observed for the other systems studied here. The results from our TD-DFT calculations are consistent with the high-level calculations by Bochenkova *et al.*¹

The analysis for HBI⁻ can be compared with the Hückel interpretation of the S₁ state provided by the Krylov group.⁴⁰ They took an even more reductionist view of the S₁ state and argued that it can be viewed as a transition from the n(allyl) $\rightarrow \pi^*$ (ethene). Although this view is elegant in its simplicity, a slight extension of this depiction provides a much more detailed and far-reaching picture. We suggest that HBDI⁻ can be viewed as a phenolate unit and the crotonaldehyde radical (see Figure 37(d) inset). The S₁ state corresponds to a transition from the singly-occupied orbital of the crotonaldehyde radical (which has the appearance of the n(allyl) MO) to the lowest unoccupied π_R^* orbital, where R = acrolein, as shown in Figure 37 (d). Hence, the S₁ is best described by n(crotonaldehyde) $\rightarrow \pi^*$ (acrolein). The bright shape

resonance identified at $h\nu = 3.8$ eV corresponds a $\pi_{\text{Ph}} \rightarrow \pi_{\text{Ph}}^*$ transition localised on the phenolate and is remarkably close to the 3.7 eV that was anticipated from the simple bottom-up picture. The slight discrepancy can be attributed to the additional mixture of the HOMO-1 $\rightarrow \pi_{\text{R}}^*$ transition in the Ψ_- excited state for HBDI⁻. The dynamics of the S_3 state have been the subject of some controversy.^{1,35,38} In a previous study, it was argued that the frequency resolved photoelectron spectra were most consistent with autodetachment from S_3 and internal conversion to the lower-lying dark S_2 state which subsequently autodetached.³⁵ However, Bochenkova et al. showed that the spectral broadening observed in Figure 35(d) could be reproduced as an autodetachment from the S_3 state, without invoking any internal conversion.¹ Based on the above Hückel arguments, the fact that similar spectral broadening is seen in Ph and HBDI suggest that the dominant decay is simple autodetachment from the π_{Ph}^* orbital.

In principle, the above analysis is also valid for the PYP chromophore, pCA⁻. In fact, the Hückel structure of the relevant MOs in pCA⁻ is essentially identical to those of HBI⁻! Specifically, the same $n(\text{crotonaldehyde}) \rightarrow \pi^*(\text{acrolein})$ is expected to describe the S_1 state while the higher lying electronic resonances will be predominantly of π_{Ph}^* character. Hence, one may expect similar excited state structures and dynamics for the two. A study by Andersen and co-workers measured the lower lying (S_1) state of pCA⁻ to be at an excitation energy of 2.9 eV, which is very close to the experimental electron affinity of 2.91 ± 0.05 eV,²³ as in HBDI⁻.¹⁷ Based on our analysis, we expect the bright resonance to lie at $h\nu \sim 3.7$ eV.

5.6.5 Extension to Excited State Dynamics of Biochromophores

Although the Hückel picture is rudimentary, it provides useful insight into the basic electronic structure of bio-chromophores involving phenolates, which have been the subject of much recent interest. As the conjugation is extended further, the π_{R}^* MO is lowered in energy relative to the π_{Ph}^* MO, consistent with the particle in a box picture. This trivially explains why red fluorescent proteins absorb at longer wavelengths.⁴⁰ Overall, the lower the energy of

the π_R^* MO is relative to that of the π_{Ph}^* MO, the more dominant its contribution to the lower-lying excited state and the lower excitation energy to the Ψ_+ excited state.

A key result here is that the VPh^- chromophore is integral to building a bottom-up understanding of biochromophores, as it represents the species in which the characteristic spectroscopic properties of photoactive proteins emerge. The mixing of the two chromophore units produces the two bright states seen in several larger bio-chromophores. In particular the excited state around $h\nu = 3.7$ eV has been the subject of much recent interest. The autodetachment from this resonance has been discussed in terms of photo-oxidation of GFP.^{1,51} Our results show that this autodetachment process can be viewed quite simply as the loss of an electron from the lowest energy π_{Ph}^* of the phenolate (or benzene), in agreement with high-level electronic structure calculations.¹ Hence, to probe the dynamics and details of this autodetachment process, it appears not necessary to study the complex $HBDI^-$ molecule as the same dynamics can be observed in Ph^- . This is a pleasing conclusion and shows how simple chromophores of chromophores can provide exquisite insight into the dynamics of complex bio-molecules and how a gas-phase bottom-up approach can yield genuine insight into complex molecules. One must of course recognise that the Hückel approach has major limitations and does not provide quantitative insight. Additionally, the protein environment also plays a deterministic role. For example, the similarity in electronic structure of the PYP and GFP chromophores does not map onto their photophysical properties or biological function; in GFP, the protein structure inhibits isomerisation which leads to the fluorescent properties of the protein, while in PYP, it does not and isomerisation with internal conversion is the main decay mechanism. Nevertheless, the simple electronic structure and reductionist picture of photoactive protein chromophores may be useful in the development of new chromophores, particularly in synthetic laboratories that are often guided by qualitative electronic structure arguments rather than high-level *ab initio* calculations.

5.6.6 Conclusions

A combined frequency- and angle-resolved photoelectron and computational study of the phenolate chromophores that make up the biochromophores of photoactive proteins has been presented. A Hückel theory approach is employed to provide an understanding of the evolution of electronic structure as different para-substituents are incorporated into phenolate. For non-conjugated substituents, the electronic structure simply resembles that of bare phenolate. For conjugated substituents, a linear combination of molecular orbitals localised on the phenolate and substituent lead to the observed electronic excited states. For p-vinyl-phenolate, it is this effect that leads to the observation of a second bright excitation characteristic of chromophores in photoactive proteins. As the conjugation of the substituent increases, the lowering of its orbital energy defines the character of the first bright state, while the second bright state has predominantly phenolate π^* antibonding character. In these cases, the S_1 excited state can be described as a transition from the non-bonding orbital on the substituent including the para-carbon of phenolate to the first π^* antibonding orbital of the substituent excluding the para-carbon. Our results provide an intuitive and accessible framework for the logical design of photoactive chromophores.

5.7 Electronic Structure and Dynamics of the para-Dinitrobenzene Anion

The para-dinitrobenzene radical anion has been studied by 2D photoelectron imaging within the energy range of 2.5 eV above the detachment threshold. Supporting electronic structure calculations at the XMCQDPT2 level of the excited states and resonances are presented. The direct photodetachment channel has been observed and modelled and yields an electron affinity of 1.99 ± 0.01 eV. In addition to the direct channel, evidence of resonances is observed. These resonances, which are symmetry allowed for photoexcitation from the ground state and of Feshbach types with respect to the open continuum, result in fast internal conversion to bound electronic states, followed by statistical electron emission observed at very low kinetic energies as well as dissociation of the nitrite anion. The latter is seen in the photoelectron spectra, which can be modelled as a combination of direct detachment from the para-dinitrobenzene and nitrite anions. An additional dimension has been offered by the 2D photoelectron angular distribution that is particularly sensitive to a mechanism of electron detachment, allowing us to confidently interpret the production of the nitrite anion photofragment.

5.7.1 Introduction

Radical anions of dinitrobenzenes are fascinating because they are some of the simplest organic mixed valence systems. Meta- and para-dinitrobenzene (mDNB and pDNB) illustrate two examples of different classes of organic mixed-valence systems, as defined by the Robin-Day classification,⁵² which is based on the electronic interaction between two redox sites within a molecule (the two nitro-groups in DNBs). For pDNB, there is strong electronic coupling between the two sites and the charge is entirely delocalised (class III). In contrast, mDNB exhibits weak electronic coupling between the two redox sites and the excess charge is localised on one of the NO₂ groups. Mixed-valence systems and intervalence charge-transfer

transitions are extensively used in chemistry.^{53,54} Most of this work and our understanding of mixed-valence systems have come from solution phase work, where interactions with the solvent affect the electronic structure. To explore the intrinsic electronic structure of mixed-valence systems, studies on the isolated molecules are desirable. Here, we study the class III strongly coupled pDNB⁻, for which most of the excited states are not bound. The use of PE spectroscopy in combination with *ab initio* calculations allows us to gain insight into the intrinsic electronic structure of pDNB⁻ and the decay mechanisms of the resonances.

The most commonly used computational method for exploring the electronic structure and properties of organic mixed-valence systems is DFT. DFT is often hailed as a compromise between reasonable accuracy and computational cost, however, for mixed-valence systems, specific care must be taken when choosing the functional. For hybrid functionals with too little HF exchange, charge delocalization is consistently overestimated; whereas too much HF exchange over localizes the charge.^{55,56} A correct description of the Robin-Day classification can be obtained using these DFT methods, but it is not always due to a correct treatment of the intrinsic chemical physics of the molecule. While a thorough study by Sutton *et al.* showcases a reliable DFT methodology,⁵⁷ here we use XMCQDPT2⁵⁸ as a rigorous method that avoids any potential errors.

The study of pDNB⁻ here is also motivated by our longer-term goal of probing intervalence charge-transfer processes in real-time using time-resolved PE spectroscopy. This requires knowledge of the electronic “structure” of the continuum, because the probe energy may access resonances that alter the observed PE spectra and lead to incorrect interpretations. This is likely to be a problem for pDNB⁻ because of its high density of states.

Finally, while developing an understanding of the electronic structure of pDNB⁻ builds on an understanding of mixed-valence systems, aromatic nitro-compounds also have important industrial uses and form the basis of many explosives.^{59,60} Electron impact ionisation coupled

to mass-spectrometry is a common analytical method used to detect trace amounts of such explosives. Although cations are detected because 70 eV electron are used in the ionisation step, low energy electrons may provide more distinctive fragmentation patterns when probing negatively charged species.⁶¹ To understand the possible dissociative electron attachment channels, several electron attachment studies have been performed on aromatic nitro-compounds.^{62,63} Our work here complements these studies and the 2D PE spectra and 2D PADs combined with the computational work provides new insight into the resonances that lead to dissociative electron attachment in pDNB.

5.7.2 Methodology

The experiment has been described in detail in Section 3.1. Briefly, the ESI was used to produce anions from a ~1 mM solution of pDNB in methanol.

All initial ground state calculations of pDNB anion and neutral species were carried out using the QChem 5.0 package.⁴⁴ Geometries were obtained at the MP2/aug-cc-pVDZ level of theory and verified to be minimum energy structures by vibrational analysis. Both the anion and neutral have D_{2h} symmetry, although all calculations were not restricted to this symmetry. The ground state of the radical anion is a $^2B_{2u}$ state while the neutral has a 1A_g ground state.

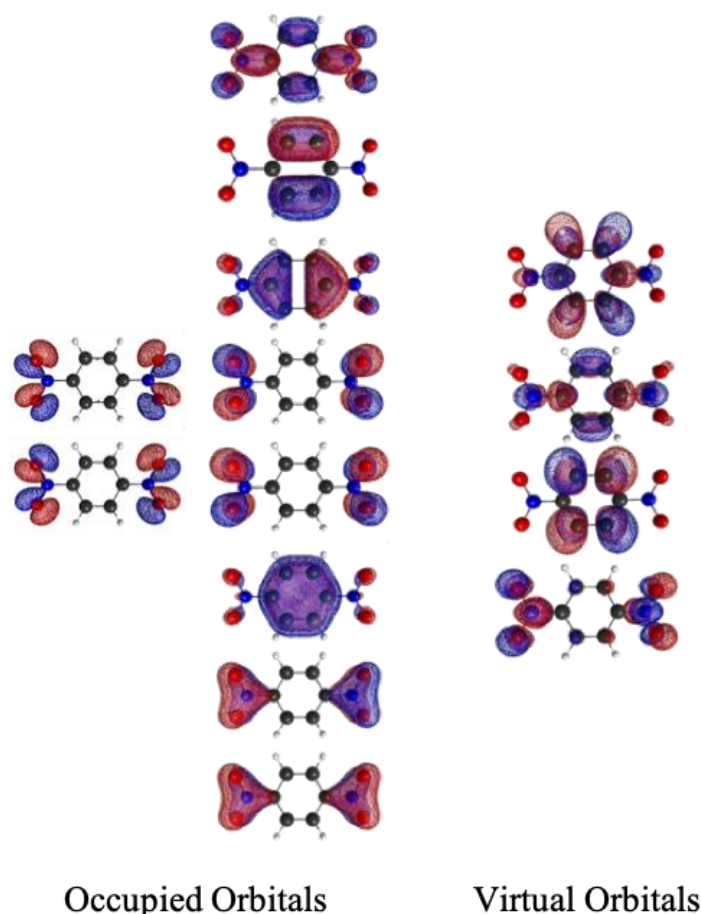


Figure 38 The relevant MOs used to form the both active spaces used in XMCQDPT2 calculations

VEEs were calculated with XMCQDPT2 using the Firefly computational package.⁶⁴ The excited states of pDNB^- were calculated using an active space of 12 valence π -orbitals and 15 electrons. In order to include all states within our experimental range, we employed the XMCQDPT2[11]/SA(9)-CASSCF(15,12) method with a reference space spanned by 11 CASCI wavefunctions, which were obtained through SA-CASSCF calculations. A DFT/PBE0-based one-electron Fock-type matrix was used to obtain energies of all CASSCF semi-canonical orbitals used in perturbation theory. For all calculations, the (aug)-cc-pVTZ basis set was used, where the augmented function was only affixed to the oxygen atoms of the nitro-groups. To calculate the VDE, an extremely diffuse p-function was added to one of the carbon atoms of the ring. A single p-orbital of this highly diffuse shell was included in the active space

and was used to mimic an electron-detachment process. The anion ground and bound excited states as well as the electron detached state were included in a state-averaging procedure for calculating the VDE at the XMCQDPT2[9]/SA(4)-CASSCF(15,13) level. Additionally, we performed the $n\text{-}\pi^*$ VEE calculations using the XMCQDPT2[11]/SA(11)-CASSCF(19,14) method by adding two n -orbitals to the π valence active space. All valence orbitals used in the active spaces are shown in Figure 38.

The PE spectra of the pDNB and nitrite anions were simulated at 300 K by direct evaluation of Franck-Condon integrals within the double harmonic parallel-mode approximation. Stick spectra were convoluted with Gaussian functions with a half width at half maximum of 13 meV. For this type of calculations, vibrational analysis and geometry optimization for the closed-shell species, pDNB and NO_2^- , were performed using MP2/(aug)-cc-pVTZ and MP2/aug-cc-pVTZ, respectively. Displacements between equilibrium geometries in the anion ground and detached states along each normal mode were estimated locally using the quadratic approximation, based on gradients calculated for the open-shell radical species, pDNB $^\cdot$ and NO_2 , at the Franck-Condon point at the MRMP2/CASSCF(15,12) and MRMP2/CASSCF(9,6) levels, respectively, using the same corresponding basis sets.

To model the angle-resolved data, the DNB anion was reoptimized using CCSD/aug-cc-pVDZ. Dyson orbitals were calculated using EOM-IP-CCSD/aug-cc-pVDZ, and the Dyson orbitals were used to model the direct detachment channels of pDNB $^\cdot$ and the nitrite anion using ezDyson v4.⁴⁵

5.7.3 Frequency- and Angle-Resolved Photoelectron Spectra

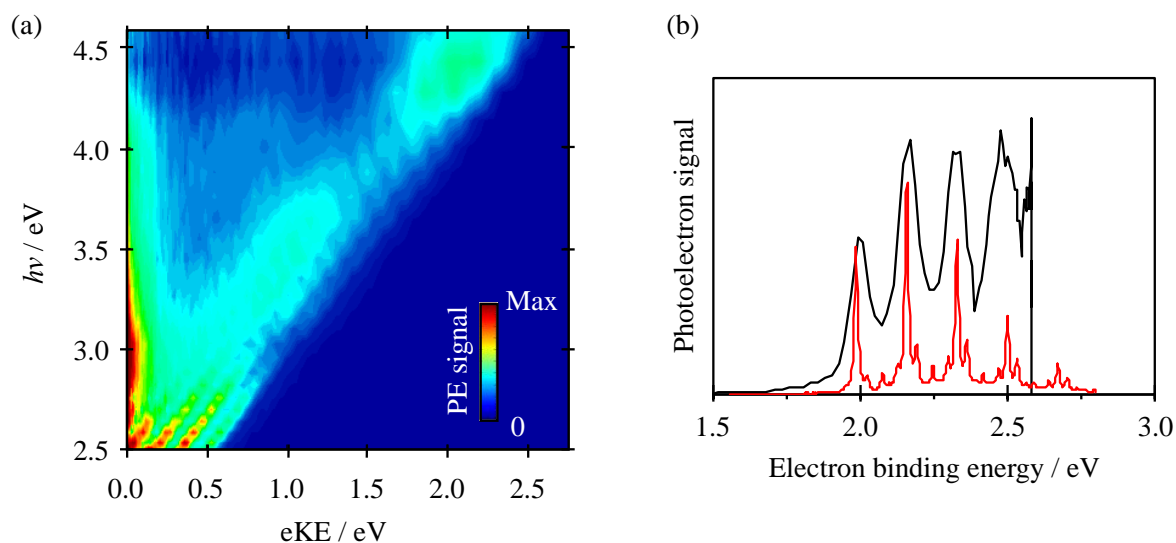


Figure 39 (a) 2D photoelectron spectra of pDNB⁻, where each spectrum has been normalised to its integrated PE signal. (b) Measured (black) and simulated (red) photoelectron spectra (a slice of (a) taken at $h\nu = 2.58$ eV

The frequency-resolved PE spectra for pDNB⁻ are shown as a 2D false-colour plot in Figure 39(a) for the range $2.5 \leq h\nu \leq 4.6$ eV (taken at 10 nm intervals). The PE spectra have been normalised to their total integrated intensity to emphasise spectral changes as a function of $h\nu$. The 2D PE spectra show a diagonal PE feature, the eKE of which increases linearly with increasing $h\nu$. This feature is attributed to a direct detachment channel that corresponds to an electron photodetached directly from the ground electronic state of the anion to form the ground state of the corresponding neutral species: ${}^2B_{2u} + h\nu \rightarrow {}^1A_g + e^-$. Figure 39(b) shows a representative PE spectrum at $h\nu = 2.58$ eV, in which the direct detachment is the predominant electron loss channel.

The direct detachment channel shows initial vibrational structure across the first ~ 0.75 eV of the continuum. Vibrational structure comes about from the differing anion and neutral ground state geometries, leading to a Franck-Condon profile that represents this difference. A computed PE spectrum of the direct detachment channel at $h\nu = 2.58$ eV is also included in

Figure 39 (b), where the ion temperature is taken to be 300 K, similar to that of the experiment. The overall agreement between the measured and computed PE spectra is very good.

However, there are also clear deviations from the direct detachment peak with the PE signal at lower eKE to the diagonal feature in Figure 39(a). Specifically, for $2.7 < h\nu < 4.3$ eV, a feature at very low eKE is visible. The appearance of very low eKE features typically indicates that a bound electronic state has been populated following internal conversion from photoexcited resonances.⁴¹

At $h\nu \sim 3.0$ eV the Franck-Condon profile for the direct detachment appears to change suddenly, as well as a loss of vibrational resolution, although the main vibrational progression from direct detachment can still be discerned. The PE spectra then change again around $h\nu \sim 3.8$ eV with more PE in the intensity of the direct detachment feature, as well as its broadening, is seen. For $h\nu > 4.3$ eV, no PE signal is seen at very low eKE.

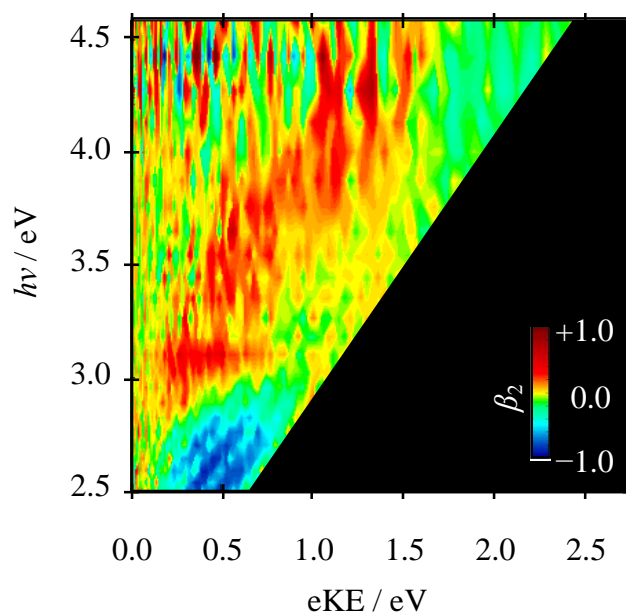


Figure 40 The 2D β_2 spectra of pDNB⁻. The shaded region is ignored as there is insufficient PE signal to define physically meaningful PADs.

In addition to the 2D PE, PE imaging yields PADs that give complementary information about the MO from which the electron is detached. The PADs are quantified by the anisotropy

parameters, β_2 , (Section 1.2.2). These are plotted as a 2D false-colour plot in Figure 40, where we have excluded data at eKE higher than that of the direct detachment feature, as there is no PE signal in this range and therefore no physically meaningful PADs can be extracted. Figure 40 shows that the direct detachment channel has a negative β_2 value (for $h\nu < 2.9$ eV). Qualitatively, this may be expected given that photodetachment is from the extended π -system of pDNB^- , where the SOMO in the ground electronic state is of a π^* -character.^{65,66} The qualitative agreement, however, fails in regions where the 2D PE spectra show deviations from direct detachment (*i.e.* $h\nu > 2.9$ eV). Finally, it is interesting to note that the vibrational structure of the direct detachment channel is preserved in the angle-resolved spectra as oscillations in β_2 values that match to the eKE of the vibrational bands.

5.7.4 Modelling Resonances Using XMCQDPT2

The results from the electronic structure calculations are collated in Figure 41, which provide the computed transition energies and their oscillator strengths. The energy of the continuum (in the anion geometry) is calculated to lie at 2.17 eV. Figure 40 shows that there are two bound excited states, 1^2A_u and 1^2B_{3g} , which are optically dark and bright, respectively. For $h\nu < 4.5$ eV there are additional 5 resonances. The first three resonances are clustered around 3 eV, which are the 2^2A_u , 1^2B_{1g} , and 1^2B_{2u} resonances. Only the 1^2B_{1g} state has some oscillator strength; photoexcitation to the other two resonances from the ground state is symmetry forbidden. The next 2^2B_{3g} resonance at $h\nu = 3.74$ eV is optically bright. Finally, at $h\nu = 4.16$ eV there is a 1^2B_{1g} resonance. All the optically active resonances are of Feshbach character in which autodetachment must be accompanied with an electronic transition in the neutral core to reach the $^1\text{A}_g$ ground state of the neutral.

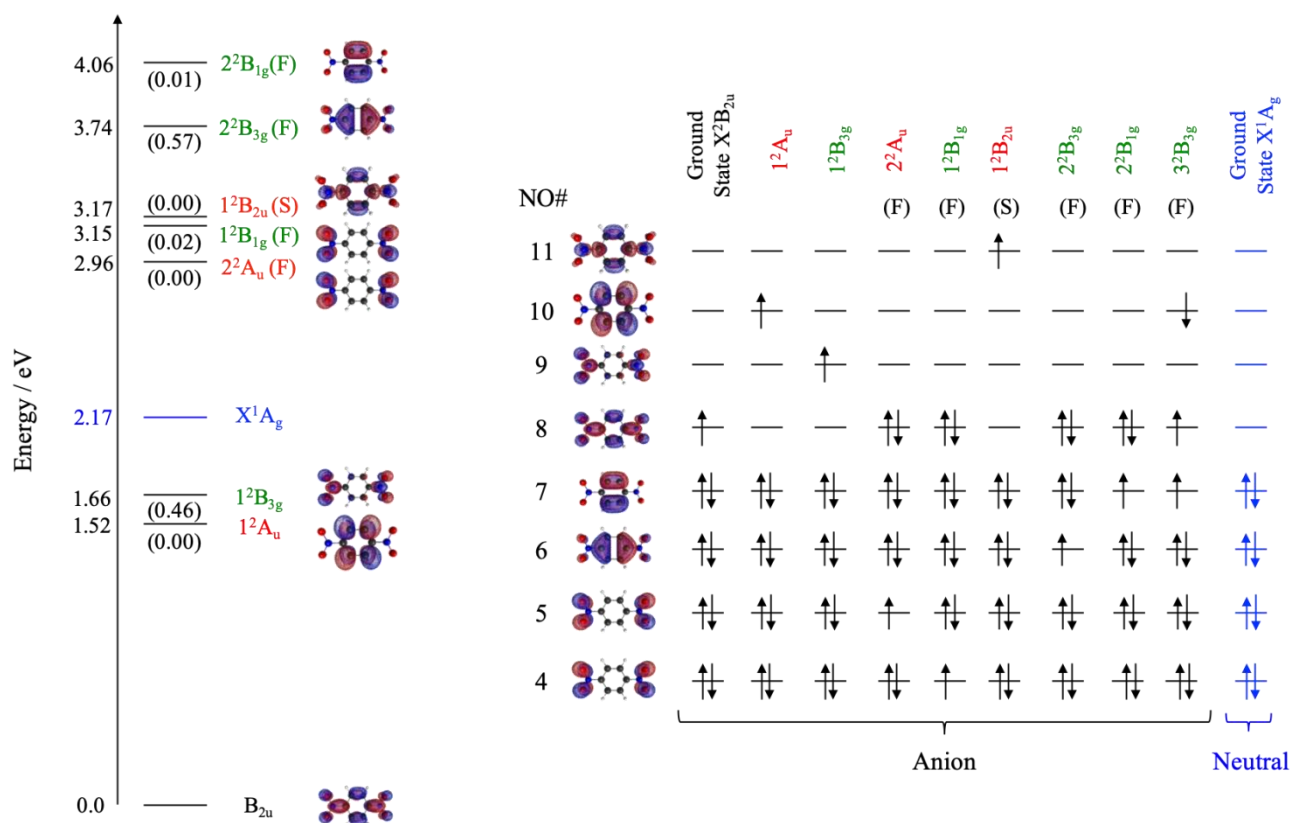


Figure 41 The calculated vertical excitation energies for $pDNB^-$ (eV). The oscillator strengths are shown in parenthesis for symmetry allowed transitions (green). The XMCQDPT2 natural orbitals that are singly occupied are shown for clarity, and the character of resonances is given alongside the symmetry label, where (F) and (S) indicate a Feshbach or shape resonance, respectively. The calculated vertical detachment energy is shown in blue. Within this energy range only the $\pi\pi^*$ excited states are shown; the $n\pi^*$ excited states, which are electronically bound and optically dark, are found to lie close to the detachment threshold at 1.90 and 1.97 eV. Note that symmetry forbidden electronic transitions (red) can gain intensity through coupling to vibrations. The full electronic configurations of all states are shown alongside for clarity.

Finally, we have computed the β_2 values using the Dyson orbital approach for the direct detachment $^2B_{2u} + h\nu \rightarrow ^1A_g + e^-$ channel. The results of this are shown in Figure 42. There is good agreement with the experimentally derived values at eKE less than 0.8 eV. However, coinciding with the appearance of the indirect detachment channels in Figure 39(a) and the computed resonance positions (also included in Figure 42), deviations are observed from the predicted behaviour, similar to our earlier observations.

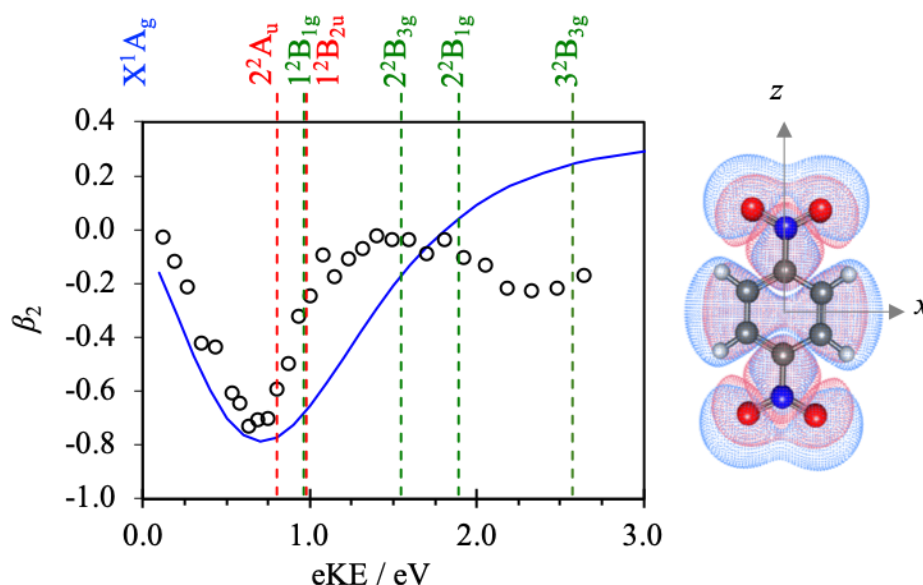


Figure 42 Measured (open circles) and computed (solid blue line) β_2 anisotropy parameters for the highest kinetic energy peak (i.e. the 0-0 transition). Location of resonances are shown as vertical dashed lines, including symmetry labels. The calculated β_2 parameter is derived from the Dyson orbital shown.

5.7.5 Evidence for Excited State Dynamics in pDNB⁻

Key physical properties of the pDNB can be determined from the experimental data, including the ADE, VDE, and the onset of resonances. Based on the excellent agreement between the computed and measured Franck-Condon profile of the PE spectrum in Figure 39(b), the 0-0 transition in Figure 39(b) can be identified as the peak at highest eKE (there are negligible contributions from hot-bands). From the experiment, we determine that ADE is 1.99 ± 0.01 eV. Our value agrees with a previous PE imaging study by the Sanov group and with data from ion/molecule reaction equilibria. Our experiment also provides the VDE, which is taken as the maximum of the Franck-Condon profile of the direct detachment feature (in the absence of any resonances). We find that VDE is 2.15 eV, being in excellent agreement with the computed VDE of 2.17 eV. The dominant vibrational progression observed in the PE spectrum is due to the symmetric stretch of the two NO₂ groups. The measured vibrational

spacing from Figure 39(b) is 163 meV which compares well with the calculated frequency of 171 meV.

In regions where spectral broadening has occurred, the apparent Franck-Condon profile is different, although the vibrational levels of the neutral can still be identified at high eKE. Deviation from direct detachment features are quite common in anion PE spectroscopy and typically come about from the excitation of an electronic resonance of the anion. Several mechanisms can lead to spectral broadening and/or red-shifting. Firstly, as the resonance has its own associated potential energy surface, the Franck-Condon factors between it and the final neutral electronic state may be different to a direct channel.¹ Secondly, as autodetachment is not instantaneous, the resonance lifetime may be sufficiently long that nuclear dynamics, including internal conversion, can take place. Autodetachment can occur from anywhere along the trajectory of the wavepacket, up to the point where the potential energy surface of the anion becomes bound. In its extreme case, the ground state of the anion may be recovered,^{67,68} and complete internal vibrational redistribution occurs. In the gas-phase, energy is conserved and so the total energy in this case remains above the ADE and electrons are lost by the statistical sampling of modes that may lead to electron emission.^{69–71} Alternatively, in competition with this statistical detachment is dissociation, leading to charged fragments. For $h\nu > 2.5$ eV, a feature that peaks at eKE ~ 0 eV is seen, thus suggesting that the ground or bound electronic states are recovered across this photon energy range.

The energetic onset of resonances can be determined in two ways: firstly, from the $h\nu$ at which an indirect signal is observed in the 2D PE spectra (Figure 39(a)); and secondly, by sudden changes in the PADs as a function of $h\nu$, that do not follow the expected direct detachment PADs (Figure 42). Specifically, the Dyson orbital approach is unable to account for autodetachment from resonances because the model is defined by only a single initial and final state: the ground state of the anion and the neutral, respectively, for the direct detachment

channel. From Figure 42, there are multiple energies at which there are deviations from the modelled PADs.

The first clear deviation from the direct detachment channel in both the PE spectra and the PADs is around $h\nu \sim 2.9$ eV (i.e. eKE ~ 0.9 eV). The Franck-Condon profile changes accompanied by broadening and a loss of apparent spectral resolution. According to our calculations, there are three resonances at $h\nu \sim 3$ eV, with the 1^2B_{1g} Feshbach resonance being the only optically bright state. The origin of the associated spectral broadening is now considered. Broadening due to rapid autodetachment can be modelled as a vertical transition (i.e. Franck-Condon) from resonance to the final state, as shown by Bochenkova *et al.* in the GFP chromophore.¹ The result is an indirect PE peak that does not change in eKE as $h\nu$ increases. For $2.8 < h\nu < 3.8$ eV, the eKE of the indirect peak is not constant with $h\nu$ and instead is increasing; it has a constant electron binding energy (eBE). We therefore consider an alternative explanation. As the initially excited resonance is of Feshbach character, the autodetachment may be expected to be relatively slow and significant nuclear dynamics can occur on the resonances. We have previously shown for radical anion quinones that internal conversion can take place prior to autodetachment and that, in the presence of a bound-electronic state, the ground electronic state can be recovered with extreme efficiency.³⁵ We note that $pDNB^-$ has available bound states (Figure 41) and that there is evidence of bound state recovery based on the observed statistical detachment peak near eKE = 0 eV. So how can we explain the apparent indirect PE signal that is red-shifted from the direct detachment?

5.7.6 Photodissociation of NO_2^-

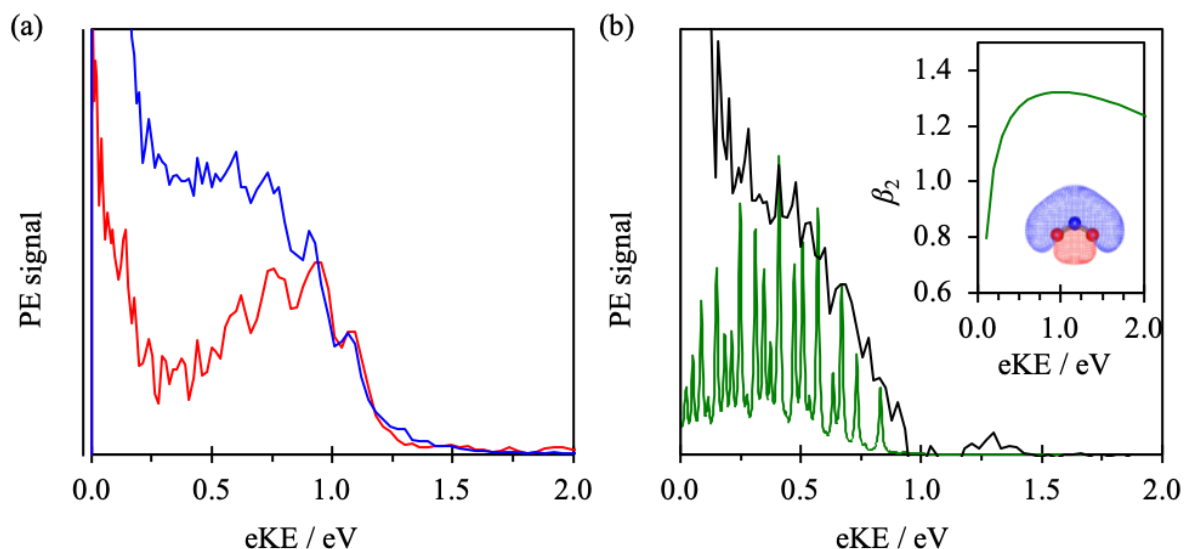


Figure 43 (a) PE spectra taken at $h\nu = 3.10$ eV. In (a), the PE spectra are taken using 5 ns pulses (blue) and 50 fs pulses (red). The PE spectrum in (b) is the difference between the two spectra (black) and includes a simulated PE spectrum of NO_2^- at $h\nu = 3.10$ eV (green). The inset graph shows the computed β_2 anisotropy parameters expected for the lowest-energy direct photodetachment channel from the n-orbital of NO_2^- . Note that the experimental difference between the VDE and ADE values observed here at eKE of 0.4 eV and 0.8 eV, respectively, matches the calculated one.

In Figure 43(a), the PE spectra of pDNB^- taken at $h\nu = 3.10$ eV with laser pulses of ~ 5 ns and ~ 50 fs duration are shown. The high eKE edge is similar between the two spectra. However, there are clear deviations for $\text{eKE} < 1$ eV. There is significantly more signal at very low eKE, but both spectra suggest that statistical emission occurs and the ground (or bound) state is recovered. The most striking difference between the spectra is that the indirect peak seen at $\text{eKE} \sim 0.5$ eV in the ns spectrum is not present in the fs spectrum. If this indirect feature arises from autodetachment of the initially populated resonances, then the duration of the excitation field should have no effect. Hence, the origin of the indirect process appears not to be autodetachment from resonances. Figure 43 (b) shows a difference spectrum between the 5 ns and 50 fs spectra, which recovers the spectral shape of the indirect peak. The VDE of the difference spectrum is at ~ 2.7 eV and the ADE at ~ 2.3 eV and has a striking resemblance to

the PE spectrum of NO_2^- taken by Ervin *et al.*, which has a broad peak with $\text{VDE} = 2.7$ eV and $\text{ADE} = 2.273 \pm 0.005$ eV.⁷² In Figure 43(b), we include a simulation of the expected PE spectrum at $h\nu = 3.10$ eV of NO_2^- , shifted so that the 0-0 transition lines up with the known ADE. Our simulated spectrum closely resembles that of Ervin *et al.* and shows good agreement with the difference PE spectrum shown in Figure 43(b). We do not have the resolution to observe the dense vibrational structure.

The NO_2^- PE spectrum can be generated by the absorption of a second photon during the 5 ns pulse. The dissociation is most likely a ground state or bound excited states process because there is clear evidence that the bound electronic states are recovered. Hence, NO_2^- loss is a relatively slow process and does not occur during the 50 fs pulse and can therefore not be seen in the PE spectrum using pulses shorter than the dissociation timescale. Similar dynamics have been observed following photoexcitation in anions that then undergo ground state reactions.⁷³

The NO_2^- PE spectrum can in fact explain much of the spectral broadening observed in Figure 39(a). In Figure 44, representative 1D PE spectra are shown along with simulated PE spectra for direct detachment from pDNB^- and NO_2^- . The simulated PE spectra have been arbitrarily scaled to the experimental data. The high eKE edge is consistent with direct detachment. The NO_2^- spectrum on the other hand is very broad, leading to the broad unresolved peak in Figure 44, that remains constant in eBE (and shifts linearly with eKE – see Figure 39). At CAM-B3LYP/aug-cc-pVDZ the binding energy of NO_2^- is 2.59 eV, which is consistent with the energy range, where the NO_2^- formation is observed.

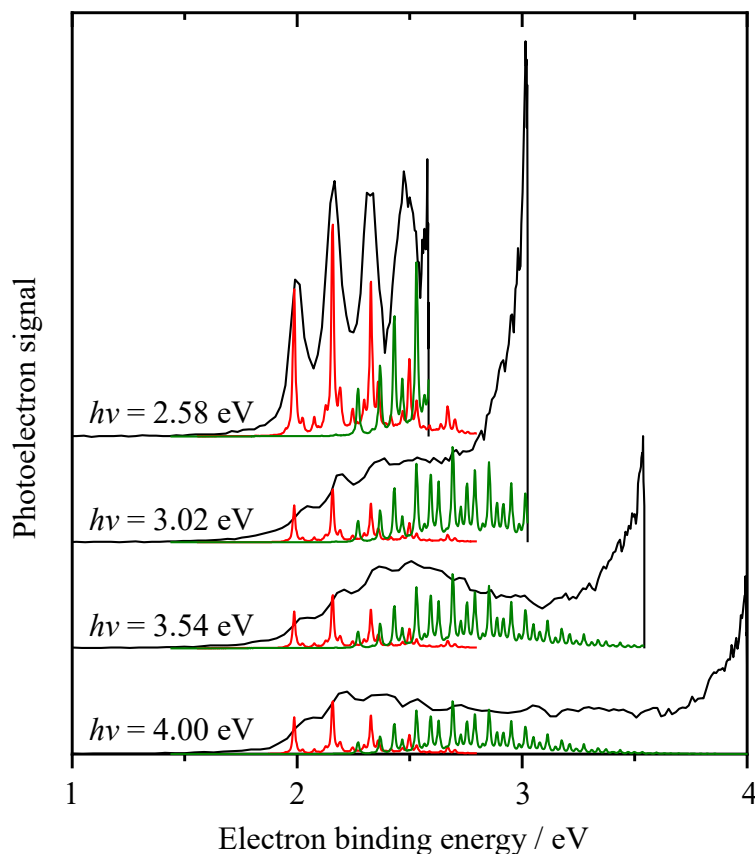


Figure 44 Slices of PE spectra (black) that are representative of regions where resonances play an important role as seen in Figure 1. The PE spectra have been offset with respect to one another to aid clarity in comparison. Included for each photon energy are the simulated direct PE spectrum for pDNB⁻ (red) and NO₂⁻ (green).

The PADs support the above interpretation. For $h\nu > 2.9$ eV, the β_2 anisotropy parameter is more positive ($\beta_2 \sim +0.5$) to the low eKE edge of the direct detachment peak. This low eKE edge corresponds to the signal that we assigned to the NO₂⁻ PE spectrum. As the photodetachment of NO₂⁻ and pDNB⁻ are incoherent, we expect to predominantly observe the PAD expected for NO₂⁻ at the eKE where this feature dominates. We have computed the PADs for photodetachment from NO₂⁻ and the expected β_2 as a function of eKE for this channel is shown in Figure 43(b). The detachment is very anisotropic with $\beta_2 > 0$ across the range probed here. This is consistent with the observed $\beta_2 \sim +0.5$ for the feature we assigned to NO₂⁻ photodetachment. The quantitative discrepancy is likely a consequence of the fact that other PE signals contribute over this energy range such as the high eKE channel and the very low

eKE peak – both of which are predominantly isotropic (see Figure 40) and thus reduce the observed β_2 from NO_2^- photodetachment. The isotropic nature of the direct detachment comes about because of the influence of the resonances that are excited.

From Figure 39(a) and Figure 44, the NO_2^- photodetachment feature is apparent up to $h\nu \sim 4.1$ eV. However, between $3.8 < h\nu < 4.1$ eV, additional PE signal can be seen essentially at all eKE between the direct detachment feature and the feature near 0 eV. Our calculations show that the 2^2B_{3g} resonance lies at 3.74 eV and is optically brighter than other resonances. The PE spectrum at $h\nu = 4.00$ eV (Figure 44) shows that even more spectral broadening has occurred beyond that predicted by the PE spectrum of NO_2^- . The 2^2B_{3g} resonance is of Feshbach character and autodetachment may occur along various parts of the potential energy surface. Note also that the peak at very low eKE is smaller here suggesting that more autodetachment has occurred (leading to less ground/bound electronic state recovery).

Finally, for $h\nu > 4.1$ eV, there is again a change in the PE spectra. The spectra are dominated by a single peak at high eKE and the statistical electron loss channel becomes a very minor component. The peak at high eKE is broadened relative to a simple direct detachment process. Hence, a new excitation channel appears to be accessed here. Our calculations show that the 2^2B_{1g} resonance lies at this energy and can account for the observed change. Note that β_2 for the high eKE peak is slightly negative (~ -0.2), while the predicted β_2 based on direct detachment is positive ($\sim +0.2$), again consistent with the excitation of a resonance.

Overall, the observed resonance dynamics in pDNB^- have many similarities with electron impact studies on pDNB. Specifically, these show that NO_2^- is a major dissociative electron attachment channel from ~ 1 eV above threshold below 1 eV, no NO_2^- was observed). This corresponds to $h\nu \sim 3$ eV in the 2D PE spectra, above which, indeed, the spectral feature corresponding to NO_2^- photodetachment is clearly observed. Sulzer *et al.* have shown that the yield of NO_2^- is essentially constant up to electron energies between 1.3 and 2.5 eV, above

which it rises sharply.⁶² In the 2D PE spectra, this energy corresponds to $h\nu > 4.5$ eV. At this energy, we still observe the NO_2^- photodetachment feature, but also observe another indirect (autodetachment) channel. However, there are also key differences between the PE spectroscopy and electron attachment. Specifically, the latter only shows parent anion formation over the electron energies near threshold (up to 0.2 eV). In contrast, we observe ground state recovery up to $h\nu \sim 4.3$ eV (corresponding to electron energies of 2.2 eV). Additionally, the electron impact studies showed many dissociative electron attachment channels.^{62,63} These are not observed here, but that does not mean that they are not active and we may simply be blind to other charged products in the experiment because of small photodetachment cross sections, too high electron affinities, or because the timescale for their formation is beyond that probed here (~ 5 ns). Note also that Rydberg electron transfer experiments point to the existence of a quadrupole-bound non-valence state in pDNB^- .⁷⁴ Here, we see no evidence for this in the PE spectra, although PE spectroscopy in general can be quite sensitive to such non-valence states.^{73,75}

5.7.7 Conclusions

The high density of resonances in pDNB^- has been probed experimentally and modelled computationally. The adiabatic detachment energy of pDNB is determined to be 1.99 ± 0.01 eV. The 2D photoelectron spectra as well as angular distributions show the presence of several resonances. Good overall agreement is achieved between experimental and theory. Bound electronic states recovery is inferred from the observation of statistical electron loss. Comparison between photoelectron spectra taken with our ns and fs excitation source allows us to identify a dissociative channel that leads to formation of the NO_2^- photofragment.

This study illustrates the breadth of processes that can be probed using 2D photoelectron imaging and highlights the necessity for computational models being able to disentangle the rich signatures observed. Vertical excitation energies and photoelectron spectra

of pDNB^- are calculated at the XMCQDPT2 level and angular distributions for direct electron detachment is modelled using the Dyson orbital approach. These provide qualitative and quantitative agreement with our experimental results. Through development of this joint computational and experimental approach to probing the electronic structure of anions in the gas phase, we will now be able to explore a wide range of intervalence charge transfer systems and elucidate their intrinsic properties with confidence.

5.8 Section B Conclusions and Outlook

This section presented two studies that showcase the insight into the intrinsic electronic structure and dynamics of anions that can be gained through 2D photoelectron spectroscopy. The two studies presented applied this ‘bottom-up’ technique to a chromophore common to many biochromophores and a simple mixed valence system, both systems represent the simplest meaningful components of the classes of system they belong to.

The first study, Section 5.1, presented a bottom-up investigation of a family of para-substituted phenolate anions of increasing complexity. A simple Hückel framework was used to explain incremental changes to the electronic structure, as a function of substituent. While quite rudimentary, such an approach provides a rather elegant insight into the overall electronic structure of the biochromophores. Specifically, using linear combination of molecular orbitals, the S_1 excited state can be identified with a transition of the para-substituent, while the higher-lying S_2 state is simply a localised excitation on phenolate. Remarkably, we have shown that the very different chromophores of PYP and GFP are in fact very closely related in terms of electronic structure.

Section 5.2 investigated the electronic structure and dynamics of pDNB^- , through a joint experimental and computational study. The complexity of the photoelectron features presented in the 2D photoelectron spectra required high-level *ab initio* calculations to be able to unravel the intrinsic dynamics of pDNB^- . This study aimed to provide a foundation for

probing the chemical physics of intervalence charge transfer systems. An interesting outcome of the study is that fragments can be identified and distinguished using the PADs information available from photoelectron imaging.

The two studies demonstrated the need for a computational toolkit to be able to extract and model different photoelectron signatures recorded experimentally. The electronic structure of the phenolate chromophores can be adequately represented through lower-level electronic structure calculations, and even a simple Hückel approach. Conversely, pDNB⁻ requires careful handling with multistate multireference approaches in order to accurately model high density of resonances.

5.9 References

- 1 A. V. Bochenkova, C. R. S. Mooney, M. A. Parkes, J. L. Woodhouse, L. Zhang, R. Lewin, J. M. Ward, H. C. Hailes, L. H. Andersen and H. H. Fielding, *Chem Sci*, 2017, **8**, 3154–3163.
- 2 C. R. S. Mooney, D. A. Horke, A. S. Chatterley, A. Simperler, H. H. Fielding and J. R. R. Verlet, *Chem. Sci.*, 2013, **4**, 921–927.
- 3 D. A. Horke, Q. Li, L. Blancafort and J. R. R. Verlet, *Nat. Chem.*, 2013, **5**, 711–717.
- 4 J. L. Woodhouse, M. Assmann, M. A. Parkes, H. Grounds, S. J. Pacman, J. C. Anderson, G. A. Worth and H. H. Fielding, *Phys. Chem. Chem. Phys.*, 2017, **19**, 22711–22720.
- 5 L. H. Andersen and A. V. Bochenkova, *Eur. Phys. J. D*, 2009, **51**, 5–14.
- 6 G. H. Patterson, S. M. Knobel, W. D. Sharif, S. R. Kain and D. W. Piston, *Biophys. J.*, 1997, **73**, 2782–2790.
- 7 R. Y. Tsien, *Annu. Rev. Biochem.*, 1998, **67**, 509–544.
- 8 M. A. van der Horst and K. J. Hellingwerf, *Acc. Chem. Res.*, 2004, **37**, 13–20.
- 9 U. K. Genick, S. M. Soltis, P. Kuhn, I. L. Canestrelli and E. D. Getzoff, *Nature*, 1998, **392**, 206–209.
- 10 S. R. Meech, *Chem. Soc. Rev.*, 2009, **38**, 2922–2934.
- 11 M. Chatteraj, B. A. King, G. U. Bublitz and S. G. Boxer, *Proc. Natl. Acad. Sci.*, 1996, **93**, 8362–8367.
- 12 M. Zimmer, *Chem. Rev.*, 2002, **102**, 759–782.
- 13 R. F. Gunion, M. K. Gilles, M. L. Polak and W. C. Lineberger, *Int. J. Mass Spectrom. Ion Process.*, 1992, **117**, 601–620.
- 14 J. Tay, M. A. Parkes, K. Addison, Y. Chan, L. Zhang, H. C. Hailes, P. C. Bulman Page, S. R. Meech, L. Blancafort and H. H. Fielding, *J. Phys. Chem. Lett.*, 2017, **8**, 765–771.
- 15 M. Almasian, J. Grzetic, J. Van Maurik, J. D. Steill, G. Berden, S. Ingemann, W. J. Buma and J. Oomens, *J. Phys. Chem. Lett.*, 2012, **3**, 2259–2263.
- 16 L. Lammich, J. Rajput and L. H. Andersen, *Phys. Rev. E*, 2008, **78**, 051916.
- 17 T. Rocha-Rinza, O. C. J. Rajput, A. Gopalan, D. B. Rahbek, L. H. Andersen, A. V. Bochenkova, A. A. Granovsky, K. B. Bravaya, A. V. Nemukhin, K. L. Christiansen and M. B. Nielsen, *J. Phys. Chem. A*, 2009, **113**, 9442–9449.
- 18 K. B. Bravaya and A. I. Krylov, *J. Phys. Chem. A*, 2013, **117**, 11815–11822.
- 19 S. Bonsma, R. Purchase, S. Jezowski, J. Gallus, F. Könz and S. Völker, *ChemPhysChem*, 2005, **6**, 838–849.

- 20 E. V. Gromov, I. Burghardt, H. Köppel and L. S. Cederbaum, *J. Am. Chem. Soc.*, 2007, **129**, 6798–6806.
- 21 A. V. Bochenkova, B. Klærke, D. B. Rahbek, J. Rajput, Y. Toker and L. H. Andersen, *Angew. Chem. - Int. Ed.*, DOI:10.1002/anie.201404609.
- 22 J. Rajput, D. B. Rahbek, L. H. Andersen, T. Rocha-Rinza, O. Christiansen, K. B. Bravaya, A. V. Erokhin, A. V. Bochenkova, K. M. Solntsev, J. Dong, J. Kowalik, L. M. Tolbert, M. Axman Petersen and M. Brøndsted Nielsen, *Phys. Chem. Chem. Phys.*, 2009, **11**, 9996.
- 23 M. A. Parkes, C. Phillips, M. J. Porter and H. H. Fielding, *Phys Chem Chem Phys*, 2016, **18**, 10329–10336.
- 24 C. R. S. Mooney, M. A. Parkes, A. Iskra and H. H. Fielding, *Angew. Chem. - Int. Ed.*, 2015, **54**, 5646–5649.
- 25 I.-R. Lee, W. Lee and A. H. Zewail, *Proc. Natl. Acad. Sci.*, 2006, **103**, 258–262.
- 26 L. H. Andersen, A. V. Bochenkova, J. Houmøller, H. V. Kiefer, E. Lattouf and M. H. Stockett, *Phys Chem Chem Phys*, 2016, **18**, 9909–9913.
- 27 P. B. Coto, D. Roca-Sanjuán, L. Serrano-Andrés, A. Martín-Pendás, S. Martí and J. Andrés, *J. Chem. Theory Comput.*, 2009, **5**, 3032–3038.
- 28 W. L. Ryan, D. J. Gordon and D. H. Levy, *J. Am. Chem. Soc.*, 2002, **124**, 6194–6201.
- 29 C. Ko, B. Levine, A. Toniolo, L. Manohar, S. Olsen, H. J. Werner and T. J. Martinez, *J Am Chem Soc*, 2003, **125**, 12710–12711.
- 30 S. Smolarek, A. Vdovin, D. L. Perrier, J. P. Smit, M. Drabbels and W. J. Buma, *J. Am. Chem. Soc.*, 2010, **132**, 6315–6317.
- 31 H. Kuramochi, S. Takeuchi and T. Tahara, *J. Phys. Chem. Lett.*, 2012, **3**, 2025–2029.
- 32 A. Toniolo, S. Olsen, L. Manohar and T. J. Martínez, *Faraday Discuss*, 2004, **127**, 149–163.
- 33 S. B. Nielsen, A. Lapierre, J. U. Andersen, U. V. Pedersen, S. Tomita and L. H. Andersen, *Phys. Rev. Lett.*, 2001, **87**, 228102.
- 34 E. Kamarchik and A. I. Krylov, *J. Phys. Chem. Lett.*, 2011, **2**, 488–492.
- 35 C. W. West, J. N. Bull, A. S. Hudson, S. L. Cobb and J. R. R. Verlet, *J. Phys. Chem. B*, 2015, **119**, 3982–3987.
- 36 J. Lazzari-Dean, A. I. Krylov and K. B. Bravaya, *Int. J. Quantum Chem.*, 2015, **115**, 1258–1264.
- 37 A. V. Bochenkova and L. H. Andersen, *Faraday Discuss.*, 2013, **163**, 297.
- 38 C. R. S. Mooney, M. A. Parkes, L. Zhang, H. C. Hailes, A. Simperler, M. J. Bearpark and H. H. Fielding, *J. Chem. Phys.*, 2014, **140**, 205103.
- 39 A. Svendsen, H. V. Kiefer, H. B. Pedersen, A. V. Bochenkova and L. H. Andersen, *J. Am. Chem. Soc.*, 2017, jacs.7b04987.
- 40 K. B. Bravaya, B. L. Grigorenko, A. V. Nemukhin and A. I. Krylov, *Acc. Chem. Res.*, 2012, **45**, 265–275.
- 41 C. S. Anstöter, J. N. Bull and J. R. R. Verlet, *Int. Rev. Phys. Chem.*, 2016, **35**, 509–538.
- 42 Y. Carissan, D. Hagebaum-Reignier, N. Goudard and S. Humbel, *J. Phys. Chem. A*, 2008, **112**, 13256–13262.
- 43 Y. Carissan, D. Hagebaum-Reignier, N. Goudard and S. Humbel, *HuLiS Code: Lewis embedded in Hückel Theory*, <http://www.hulis.free.fr>.
- 44 Y. Shao, Z. Gan, E. Epifanovsky, A. T. B. Gilbert, M. Wormit, J. Kussmann, A. W. Lange, A. Behn, J. Deng, X. Feng, D. Ghosh, M. Goldey, P. R. Horn, L. D. Jacobson, I. Kaliman, R. Z. Khaliullin, T. Kuš, A. Landau, J. Liu, E. I. Proynov, Y. M. Rhee, R. M. Richard, M. A. Rohrdanz, R. P. Steele, E. J. Sundstrom, H. L. Woodcock, P. M. Zimmerman, D. Zuev, B. Albrecht, E. Alguire, B. Austin, G. J. O. Beran, Y. A. Bernard, E. Berquist, K. Brandhorst, K. B. Bravaya, S. T. Brown, D. Casanova, C.-M. Chang, Y. Chen, S. H. Chien, K. D. Closser, D. L. Crittenden, M. Diedenhofen, R. A. DiStasio, H. Do, A. D. Dutoi, R. G. Edgar, S. Fatehi, L. Fusti-Molnar, A. Ghysels, A. Golubeva-Zadorozhnaya, J. Gomes, M. W. D. Hanson-Heine, P. H. P. Harbach, A. W. Hauser, E. G. Hohenstein, Z. C. Holden, T.-C. Jagau, H. Ji, B. Kaduk, K. Khistyayev, J. Kim, J. Kim, R. A. King, P. Klunzinger, D. Kosenkov, T. Kowalczyk, C. M. Krauter, K. U. Lao, A. D. Laurent, K. V. Lawler, S. V. Levchenko, C. Y. Lin, F. Liu, E. Livshits, R. C. Lochan, A. Luenser, P. Manohar, S. F. Manzer, S.-P. Mao, N. Mardirossian, A. V. Marenich, S. A. Maurer, N. J. Mayhall, E. Neuscamman, C. M. Oana, R. Olivares-Amaya, D. P.

- O'Neill, J. A. Parkhill, T. M. Perrine, R. Peverati, A. Prociuk, D. R. Rehn, E. Rosta, N. J. Russ, S. M. Sharada, S. Sharma, D. W. Small, A. Sodt, T. Stein, D. Stück, Y.-C. Su, A. J. W. Thom, T. Tsuchimochi, V. Vanovschi, L. Vogt, O. Vydrov, T. Wang, M. A. Watson, J. Wenzel, A. White, C. F. Williams, J. Yang, S. Yeganeh, S. R. Yost, Z.-Q. You, I. Y. Zhang, X. Zhang, Y. Zhao, B. R. Brooks, G. K. L. Chan, D. M. Chipman, C. J. Cramer, W. A. Goddard, M. S. Gordon, W. J. Hehre, A. Klamt, H. F. Schaefer, M. W. Schmidt, C. D. Sherrill, D. G. Truhlar, A. Warshel, X. Xu, A. Aspuru-Guzik, R. Baer, A. T. Bell, N. A. Besley, J.-D. Chai, A. Dreuw, B. D. Dunietz, T. R. Furlani, S. R. Gwaltney, C.-P. Hsu, Y. Jung, J. Kong, D. S. Lambrecht, W. Liang, C. Ochsenfeld, V. A. Rassolov, L. V. Slipchenko, J. E. Subotnik, T. Van Voorhis, J. M. Herbert, A. I. Krylov, P. M. W. Gill and M. Head-Gordon, *Mol. Phys.*, 2015, **113**, 184–215.
- 45 S. Gozem and A. I. Krylov, *ezDyson v4*, <http://iopenshell.usc.edu/downloads/ezdyson>.
- 46 L. H. Stanley, C. S. Anstöter and J. R. R. Verlet, *Chem. Sci.*, 2017, **8**, 3054–3061.
- 47 J. Schiedt and R. Weinkauf, *J. Chem. Phys.*, 1999, **110**, 304–314.
- 48 C. W. West, J. N. Bull, E. Antonkov and J. R. R. Verlet, *J. Phys. Chem. A*, 2014, **118**, 11346–11354.
- 49 D. J. Nelson, W. K. Gichuhi, E. M. Miller, J. H. Lehman and W. C. Lineberger, *J. Chem. Phys.*, 2017, **146**, 074302.
- 50 C. S. Anstöter, C. R. Dean and J. R. R. Verlet, *Phys. Chem. Chem. Phys.*, 2017, **19**, 29772–29779.
- 51 A. Acharya, A. M. Bogdanov, B. L. Grigorenko, K. B. Bravaya, A. V. Nemukhin, K. A. Lukyanov and A. I. Krylov, *Chem. Rev.*, 2017, **117**, 758–795.
- 52 M. B. Robin and P. Day, in *Advances in Inorganic Chemistry and Radiochemistry*, Academic Press, Waltham, MA, 1967, p. 247–422.
- 53 A. Heckmann and C. Lambert, *Angew. Chem. Int. Ed.*, 2012, **51**, 326–392.
- 54 J. Hankache and O. S. Wenger, *Chem. Rev.*, 2011, **111**, 5138–5178.
- 55 A. J. Cohen, P. Mori-Sánchez and W. Yang, *Chem. Rev.*, 2012, **112**, 289–320.
- 56 P. Mori-Sánchez, A. J. Cohen and W. Yang, *Phys. Rev. Lett.*, 2008, **100**, 146401.
- 57 C. Sutton, T. Körzdörfer, V. Coropceanu and J.-L. Brédas, *J. Phys. Chem. C*, 2014, **118**, 3925–3934.
- 58 A. A. Granovsky, *J. Chem. Phys.*, 2011, **134**, 214113.
- 59 S. F. Nelsen, M. N. Weaver, A. E. Konradsson, J. P. Telo and T. Clark, *J. Am. Chem. Soc.*, 2004, **126**, 15431–15438.
- 60 T. B. Brill and K. J. James, *Chem. Rev.*, 1993, **93**, 2667–2692.
- 61 E. de Hoffmann and V. Stroobant, *Mass Spectrometry - Principles and Applications*, John Wiley & Sons, Chichester, Second Edi., 2007.
- 62 P. Sulzer, A. Mauracher, S. Denifl, M. Probst, T. D. Märk, P. Scheier and E. Illenberger, *Int. J. Mass Spectrom.*, 2007, **266**, 138–148.
- 63 A. Mauracher, S. Denifl, A. Edtbauer, M. Hager, M. Probst, O. Echt, T. D. Märk, P. Scheier, T. A. Field and K. Graupner, *J. Chem. Phys.*, 2010, **133**, 244302.
- 64 A. A. Granovsky, *Firefly v8.2.1*, <http://classic.chem.msu.su/gran/firefly/index.html>.
- 65 A. Sanov, *Annu. Rev. Phys. Chem.*, 2014, **65**, 341–363.
- 66 E. R. Grumblin and A. Sanov, *J. Chem. Phys.*, 2011, **135**, 164302.
- 67 J. N. Bull, C. W. West and J. R. R. Verlet, *Phys. Chem. Chem. Phys.*, 2015, **17**, 16125–35.
- 68 J. N. Bull, C. W. West and J. R. R. Verlet, *Chem Sci*, 2015, **6**, 1578–1589.
- 69 O. W. Richardson, *Proc Camb. Philos Soc*, 1901, **11**, 286.
- 70 A. Amrein, R. Simpson and P. Hackett, *J. Chem. Phys.*, 1991, **95**, 1781–1800.
- 71 E. E. B. Campbell, G. Ulmer and I. V. Hertel, *Phys. Rev. Lett.*, 1991, **67**, 1986–1988.
- 72 K. M. Ervin, J. Ho and W. C. Lineberger, *J. Phys. Chem.*, 1988, **92**, 5405–5412.
- 73 J. N. Bull, C. W. West and J. R. R. Verlet, *Chem Sci*, 2016, **7**, 5352–5361.
- 74 C. Desfrancois, V. Périquet, S. A. Lyapustina, T. P. Lippa, D. W. Robinson, K. H. Bowen, H. Nonaka and R. N. Compton, *J. Chem. Phys.*, 1999, **111**, 4569.
- 75 J. N. Bull and J. R. R. Verlet, *Sci. Adv.*, 2017, **3**, e1603106.

Section C Non-valence States

In Section C, three studies are presented in which non-valence states are speculated to be important. Non-valence states are invoked in low energy electron capture mechanisms. The prevalence of non-valence states has been noted in past photoelectron spectroscopy studies. Notably, our group has recently probed the conversion of the correlation bound state of C_6F_6^- to the valence bound anion.¹⁻³ Here a study on the strength of the anion- π bond of the $\Gamma^-\cdot\text{C}_6\text{F}_6$ complex is presented. Investigation into whether the electronic structure of the nitrobenzene anion and a novel organic compound can host a dipole bound state are presented in the final two studies.

Work in this Section is based on the publication below, and unless stated otherwise I performed the experimental and computational work.

1. C. S. Anstöter, J. P. Rogers and J. R. R. Verlet
Spectroscopic Determination of an Anion- π Bond Strength
J. Am. Chem. Soc. **141**, 6132 (2019)

5.10 Investigating the Strength of the Anion- π Bond

5.10.1 Introduction

Noncovalent interactions are ubiquitous and a deterministic component of macromolecular and condensed phase structure. Noncovalent interactions include strong bonds such as hydrogen bonds, halogen bonds, π - π stacking interactions, and cation- π bonds.⁴⁻⁹ The full exploitation of noncovalent bonds in chemical design and reactivity is underpinned by a basic physical understanding of such interactions. Much of this basic physical chemistry has been built upon careful spectroscopic measurements on isolated (gas phase) systems that serve as a benchmark for theoretical models. For example, the cation- π bond was first discussed as an isolated system.¹⁰ A relatively new addition to the family of noncovalent interactions is the anion- π bond. First predicted theoretically,¹¹⁻¹³ the interaction arises between an electron deficient π -system and an anion. The anion- π bond is now recognized and exploited as a key interaction in anion-recognition and supramolecular chemistry.¹⁴⁻²³ However, while the exploitation of anion- π bonds is a rapidly growing field, the basic chemical physics of the interaction is not fully developed. For example, there is an ongoing debate about the relative importance of electrostatic and correlation forces in the bond description. The lack for this fundamental chemical understanding is in large part due to the lack of direct spectroscopic data on the anion- π bond.^{18,24} Here, we fill this void by using photoelectron spectroscopy in combination with high-level electronic structure calculations to determine the interaction strength of the archetypical anion- π bonded complex, iodide-hexafluorobenzene ($\text{I}^- \cdot \text{C}_6\text{F}_6$).

Cation- π bonds arise from the electrostatic quadrupole-charge interaction of an electron rich π -system with a cation.^{25,26} The electrostatic attraction between an anion and a π -system can be achieved by the addition of electron-withdrawing substituents that lead to a positive quadrupole moment along the axis perpendicular to the π -system, Q_{zz} .²⁷ As in the case of the cation- π bond, correlation forces play an important role. However, quantitative analyses of the

relative importance of these forces requires experimental data that is devoid from other interactions. Isolated anion- π complexes have been studied by mass spectrometry,^{16,28} providing qualitative information. Recently, Wang and coworkers performed photoelectron spectroscopy on a series of anions complexed to π -system tetraoxacalix[2]arene[2]triazine.²⁹ This revealed a large increase in the anion's electron binding energy when complexed, indicating that a strong cohesion energy between the two was present. However, a detailed analysis of the bond strength was not attempted. Here, such an analysis is provided on $\Gamma^- \cdot \text{C}_6\text{F}_6$, which was chosen not only as a benchmark anion- π bonded complex, but also because it is free from any other noncovalent interactions. While the anion- π bond strength has been considered in many computational studies, and benchmarking studies have been presented,³⁰ the lack of an experimental comparison has led to most studies focusing on how different interactions compete with the anion- π bond.

5.10.2 Methods

The experimental work was conducted by Dr J. P. Rogers, on the instrument detailed in Section 3.3. Briefly, Γ^- was condensed onto C_6F_6 using a molecular beam source.¹ A mixture of CF_3I and Ar (4 bar) was passed over liquid C_6F_6 and expanded into vacuum through a pulsed valve. The resultant expansion was crossed by an electron beam forming Γ^- by dissociative electron attachment to CF_3I , which subsequently clustered to C_6F_6 in the supersonic expansion to form $\Gamma^- \cdot \text{C}_6\text{F}_6$. An ion packet containing only $\Gamma^- \cdot \text{C}_6\text{F}_6$ complexes was mass-selected by time-of-flight and intersected with light from a tunable Nd:YAG pumped OPO. Resultant photoelectrons were analyzed using a velocity map imaging spectrometer,^{31,32} which was calibrated to the known photoelectron spectrum of Γ^- . The use of a molecular beam source ensures that the complex is relatively cold (on the order of 10s K).

The $\Gamma^- \cdot \text{C}_6\text{F}_6$ complex was also treated computationally using EOM-IP-CCSD(dT)/aug-cc-pVDZ.^{33,34} The complex was optimized and verified to be the minimum energy structure by

vibrational analysis. All calculations employed the frozen-core approximation and were carried out using the QChem 5.0 computational package.³⁵ A rigid potential energy scan was calculated at this level of theory by changing the distance between the I^- and the center of the C_6F_6 ring. This provided both potential energy curves for the anion ground state and for the detachment threshold of the neutral in the same geometry (*i.e.* the neutral ground state curve).

5.10.3 Indirect Measurement of the Anion- π Bond with Photoelectron Spectroscopy

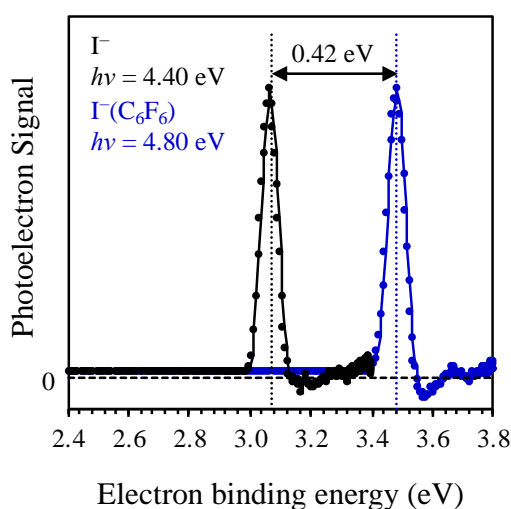


Figure 45 Photoelectron spectra of I^- and $\text{I}^-\cdot\text{C}_6\text{F}_6$ taken at 4.40 and 4.80 eV, respectively. The vertical dashed lines indicate the peak positions, which are separated by 0.42 eV.

Figure 45 shows the photoelectron spectra of I^- and $\text{I}^-\cdot\text{C}_6\text{F}_6$ taken with photon energy of 4.40 and 4.80 eV, respectively, so that both peaks have similar electron kinetic energies. The spectra are plotted in electron binding energy and clearly show that there is a blue-shift in the eBE of $\text{I}^-\cdot\text{C}_6\text{F}_6$ relative to I^- . From Figure 45, this shift, $\Delta\text{eBE} = 0.42 \pm 0.02 \text{ eV}$. Additionally, both spectra have essentially the same spectral profile.

The similarity between the I^- and $\text{I}^-\cdot\text{C}_6\text{F}_6$ spectra suggest that the charge is predominantly located on the iodide with the C_6F_6 simply solvating this anion.¹ Therefore, to

a first approximation, ΔeBE can be assigned to the cohesion energy of the anionic complex – *i.e.* the anion- π bond. However, photoelectron spectroscopy accesses the neutral potential energy surface (PES) in the geometry of the anion (*i.e.* a vertical transition) and, therefore, the interaction between the final $I\cdot C_6F_6$ is ignored in that approximation. Iodide is polarizable and one may expect the neutral complex to have a non-negligible interaction. Hence, *ab-initio* electronic structure calculations are essential to assess both the anion PES and the neutral PES and to determine an accurate anion- π bond strength.

5.10.4 Determining the Strength of the Anion- π Bond

Figure 46(a) shows the minimum energy geometry of the $I^- \cdot C_6F_6$ complex. The I^- resides above the C_6F_6 ring at a distance of 3.69 Å. The charge is almost exclusively on the iodide, as implicated from the experimental photoelectron spectra. To map the PES, the distance between the centroid of the ring and I^- , R , was varied and the resulting energy calculated. The result of such a scan is shown in Figure 46(b) and (c) for the neutral and anionic complexes, respectively. As $R \rightarrow \infty$, the difference between the neutral and anion PES is simply the electron affinity of I. Our calculations yield an energy difference of 3.13 eV (at $R = 30$ Å), very close to the known electron affinity, 3.06 eV. We have shifted the neutral surface so that it reproduces the correct value. All energies in Figure 46 are referenced to the minimum of the anion PES.

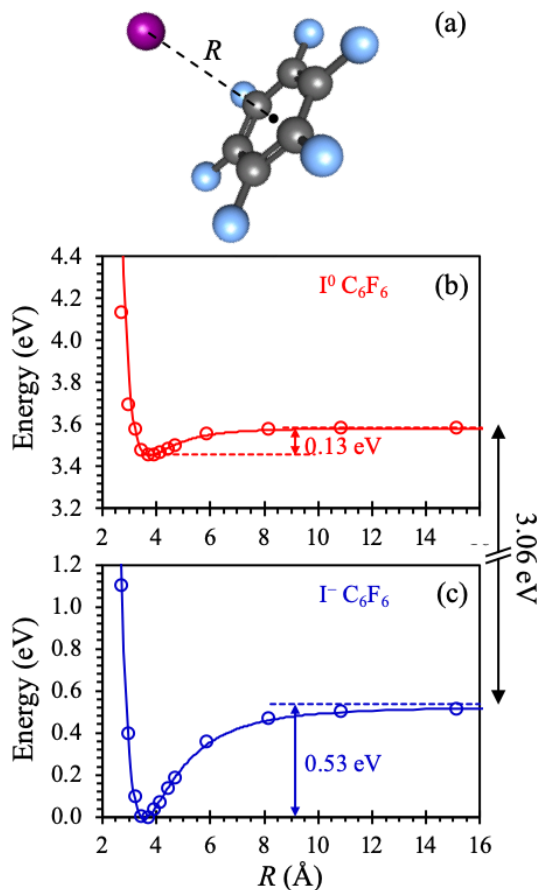


Figure 46 (a) Minimum energy structure of $\text{I}^- \cdot \text{C}_6\text{F}_6$ and potential energy curves for (b) $\text{I} \cdot \text{C}_6\text{F}_6$ and (c) $\text{I}^- \cdot \text{C}_6\text{F}_6$ as a function of separation between the I and the center of the C_6F_6 ring. The solid lines in (b) and (c) are Leonard-Jones potential energy functions with parameters defined in the text.

Figure 46(b) and (c) also includes fits of the calculated bond energies to a Leonard-Jones potential, V_{LJ} , of the form:

$$V_{\text{LJ}}(R) = D_e \left[\left(\frac{R_0}{R} \right)^{2n} - 2 \left(\frac{R_0}{R} \right)^n \right], \quad (28)$$

where ε is the dissociation energy, R_0 is the internuclear distance at the minimum of the curve, and n is an index that provides a physical description of the interaction. The overall fit to the calculated energies for the anion is excellent. Deviations at small R arise because of the (well-known) incorrect description of the repulsive component in $V_{\text{LJ}}(R)$. For the anion- π bond, the Leonard-Jones parameters are: $D_e = 0.53$ eV, $R_0 = 3.56$ Å; and $n = 3.34$. If the interaction is purely electrostatic charge-quadrupole in nature, then one would expect that $n = 3$ (*i.e.* R^{-3} long-

range dependence). The determined Leonard-Jones parameter is close to charge-quadrupole but also includes some higher order contributions (*e.g.* dispersion, induction etc. that scale as $n = 6$). The fitted R_0 value is some way off the equilibrium 3.69 Å distance calculated in Figure 46(a). However, the potential is relatively flat and the energy difference at $R = 3.45$ Å and 3.69 Å is only 2.5 meV.

The fit of the computed neutral PES to $V_{\text{LJ}}(R)$ is slightly poorer (see Figure 46 (b)), but we nevertheless included this to enable comparison. The Leonard-Jones parameters for the neutral complex are $D_e = 0.13$ eV, $R_0 = 3.76$ Å; and $n = 4.35$. The larger value for n is consistent with the loss of the charge. Clearly, the interaction is weaker than in the anion. However, the interaction remains significant and simply assuming that the anion- π bond equates to the increase in electron binding of the anion (*i.e.* 0.42 eV) would be erroneous. Interestingly, although the neutral complex interaction is significantly weaker than in the anion, R_0 has not increased by a large amount, especially given the flatness of the PES as described previously.

In photoelectron spectroscopy, it is the vertical difference between the anion and neutral that is measured, starting from the anion geometry. From Figure 46, this computed energy difference at $R_0 = 3.56$ Å is 0.40 eV, in excellent agreement with the measured $\Delta\text{eBE} = 0.42 \pm 0.02$ eV. We conclude that the calculated PES for the anion and neutral are representative of the complexes and that the calculated anion PES describes the anion- π bond accurately. From the anion PES (Figure 46(c)), the bond dissociation energy of the anion- π bond, $D_e = 0.53$ eV (51 kJ mol⁻¹). It is not possible to determine an accurate error on this value because it is in part derived from the computational work. However, given the overall agreement between experiment and theory, the uncertainty is likely to be less than ± 0.03 eV. Hence, we have determined the anion- π bond to chemical accuracy.

In arriving at the anion- π bond strength, a number of assumptions have been made. It is assumed that R is a unique coordinate and ignores the associated angular (*i.e.* bend) motion.

However, the PES overall is very flat in this region and therefore, such motion is not likely to have a large impact on the result. We have also ignored the zero-point energy contribution of the anion- π bond. A particularly useful aspect of $V_{\text{LJ}}(R)$ is that the harmonic frequency of the vibration can be defined based on the parameters:

$$\nu_e = (n / 2\pi R_0) \sqrt{(D_e / \mu)}, \quad (29)$$

where μ is the reduced mass of $\Gamma \cdot \text{C}_6\text{F}_6$. Using the anion PES parameters, the (harmonic) zero-point energy of the vibration is 2.5 meV (20 cm^{-1}). Hence, the correction to ΔeBE is very small and well within our estimated error. A further approximation made is that we have simply used the difference in energies between the PESs at the anion geometry and not calculated the Franck-Condon factors. However, given the relative flatness of the PESs, this also does not introduce a very large error. By inspection of the anion PES, the turning points for the $\nu = 0$ level are at $R \sim 3.48$ and 3.63 \AA . Vertical projection from these points to the neutral PES results in changes in the observable ΔeBE of less than 0.01 eV. Hence, this too is a small effect. This insensitivity also accounts for similarity in width of the photoelectron spectra of Γ^- and $\Gamma \cdot \text{C}_6\text{F}_6$.

5.10.5 Disentangling the Contributions to the Anion Binding Energy

Our results highlight that the key physical interactions are well-accounted for by the calculations. The calculations now also allow us to disentangle the dominant contributions to the total binding energy. In Figure 47, we show an analysis of the main contributions to the anion- π bond. The SCF energy can be further decomposed into electrostatic, polarization and charge-transfer interactions using the ALMO-EDA approach. At the minimum energy geometry, the SCF binding is 0.31 eV, of which 0.12 eV is electrostatic, and 0.15 eV is due to polarization interactions (a further 0.04 from delocalization/charge-transfer). The purely electrostatic interaction arises between the negative charge localized on Γ^- and the positive

quadrupole-moment of C_6F_6 ($Q_{zz} = +9.50$ B). In terms of overall contributions to the total anion- π binding, the relative ratio of electrostatic:polarization:correlation is 23:28:41 (at the calculated minimum energy geometry). Hence, while the positive quadrupole is an important driver for the anion- π bond, the correlation energy is the dominant contributor, accounting for ~40% of the total anion- π bond strength. Correlation has been recognized as a key component to the interaction (even for electron binding)^{1,2,36}, but without spectroscopic data, the relative contribution has become a source of debate.³⁷

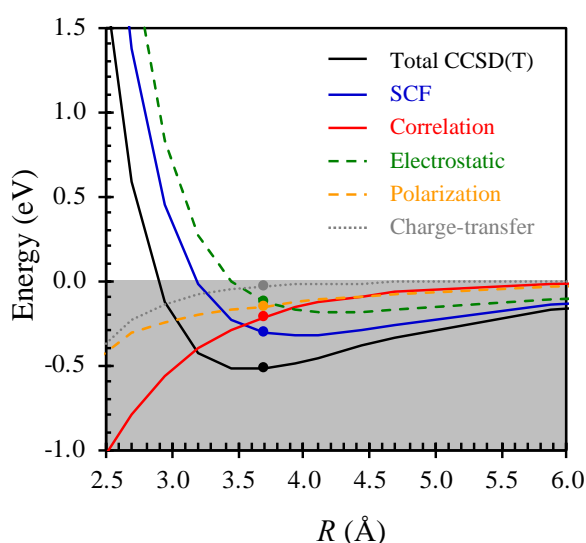


Figure 47 Contributions to the calculated total energy from the SCF and correlation energies. The SCF energy is further decomposed into contributions from electrostatic, polarization and charge-transfer interactions. The points indicate the decomposed energies at the calculated minimum energy geometry. The grey area indicates regions of attractive interactions.

Many previous experimental studies have focused on unravelling the interplay of anion- π and other non-covalent interactions in the binding of anions to π -rich molecules, partly because it is often difficult to study pure anion- π complexes. We have demonstrated here that the anion- π bond by itself is strong, cementing its importance as a non-covalent interaction. We note that molecules with much larger Q_{zz} have been synthesized and with large π -systems for which both the electrostatic and correlation interaction will be even larger.³⁸ The identity of the anion is also important. For the smaller halides, the bond distance to the ring centroid is

smaller. For example, benchmarking computational studies have probed the variation of bond strengths with the anion complexed to C_6F_6 .^{11,30} This suggested that the bond strength increases with smaller halide size so that the $\text{I}^- \cdot \text{C}_6\text{F}_6$ may be expected to be the weakest in the halide series. Probing other anion- π complexes using the methods presented here will provide the key physical insight to build a comprehensive understanding of the relative factors contributing to the intrinsic anion- π bond.

5.10.6 Conclusions

In conclusion, we have determined the anion- π bond dissociation energy in $\text{I}^- \cdot \text{C}_6\text{F}_6$ to be 0.53 eV (51 kJ mol⁻¹) using a combination of anion photoelectron spectroscopy and high-level electronic structure theory. The bond has a ~60% electrostatic quadrupole-charge contribution, with the rest (~40%) arising from correlation forces. To the best of our knowledge, this presents the first rigorous spectroscopic determination of an anion- π bond energy. The strength of the interaction suggests that anion- π bonds are important non-covalent interactions in their own right, even though they are often observed in competition with other non-covalent interactions. The use of anion photoelectron spectroscopy coupled with accurate electronic structure calculations is applicable to a wide host of anion- π bonded complexes and paves the way to studying how competing effects alter the anion- π bond.

5.11 The Nitrobenzene Anion: 2D Photoelectron and Electron Energy Loss Spectroscopy Study

5.11.1 Introduction

Electron attachment processes are of fundamental importance in many fields of science and technology, ranging from astrophysics to biology^{39,40} and electrical power distribution to semiconductor fabrication.^{41,42} For many decades, mechanistic details of electron capture have been studied by electron spectroscopic methods.^{43–49} More recently, anion photoelectron (PE) spectroscopy has also been used to provide complementary information.^{50,51} Specifically, 2D electron energy loss (EEL) and 2D PE spectroscopy have many parallels and provide clear signatures of the non-adiabatic dynamics of resonances. However, they can also contain unexpected features that remain unexplained. For example, outgoing electrons with very low kinetic energy (i.e. high electron energy loss) often appear to have structure in their energy spectrum.^{36,52–54} This is surprising because such features are commonly interpreted as arising from the statistical electron emission from the ground state of the anion for which the emission should appear as a Boltzmann distribution (i.e. unstructured).^{55–58} A tentative explanation for these low energy features was provided in studies on specific anionic clusters of quinone-derivatives, where the transient formation of a non-valence state had been associated with the observed low energy structure in the electron emission.³⁶ Unfortunately, because of the size of those systems, no definitive explanation or clear insight could be gained. Here, a reductionist approach is taken by considering the electron attachment to nitrobenzene, NB, forming electronic resonances of the NB radical anion, NB^{•−}, as a model system. In both 2D PE and 2D EEL spectroscopy, structured low energy emission is observed, and the origin of these features is explored.

5.11.2 Methodology

The 2D EEL spectroscopy was carried out by Dr Juraj Fedor at the J. Heyrovský Institute of Physical Chemistry and are included as a comparator to the 2D PE spectroscopy.

PE spectroscopy was carried out in the cluster anion PE spectrometer detailed in Section 3.2. Briefly, a molecular beam with NB was produced by passing 4.0×10^5 Pa of Ar over a sample of liquid NB and expanded into vacuum through a pulsed valve. NB^- was produced by crossing the expansion with a 380 eV electron beam, mass-selected in a time-of-flight mass spectrometer, and irradiated with light from a tunable nanosecond Nd:YAG pumped OPO providing ~ 5 ns pulses. Photodetached electrons were collected using perpendicular velocity-map imaging PE spectrometer. Raw PE images were reconstructed using the polar onion peeling algorithm and calibrated using the known PE spectrum of O_2^- . The spectral resolution is $\Delta \text{eKE}/\text{eKE} < 3\%$. The 2D PE spectrum was constructed by taking individual PE spectra over a wavelength range from $1.2 < h\nu < 2.0$ eV with 25 meV intervals. The PE spectra presented was retaken by Golda Mensa-Bonsu.

An IR spectrum of nitrobenzene was taken in a Perkin Elmer FT-IR Spectrum Two Spectrometer.

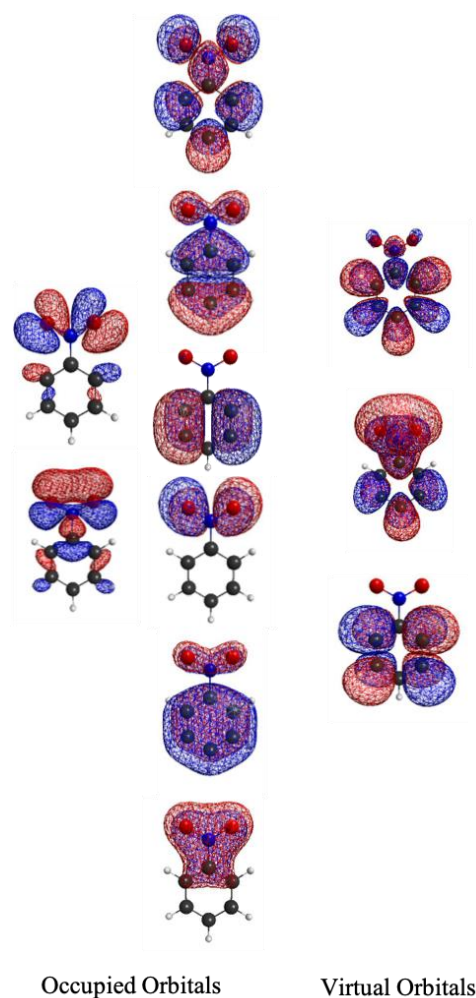


Figure 48 The valence orbitals used in the XMCQDPT2 calculations of nitrobenzene.

To aid interpretation of the experimental data, *ab initio* calculations were used to model the valence resonances of NB^- . Initial ground state calculations were carried out on NB using MP2/aug-cc-pVDZ in the Q-Chem 5.0 package.³⁵ Geometries of the ground state were optimized and verified to be geometric minima by vibration frequency analysis. The ground states NB and NB^- have C_{2v} symmetry but were not constrained to this symmetry for any calculation. VEEs were calculated using XMCQDPT2⁵⁹ in the Firefly package.⁶⁰ All orbitals used in the calculations of valence states are shown in Figure 48. The $^2\pi\pi^*$ excited states of NB^- were calculated using an active space of 9 valence π -orbitals and 11 electrons. The XMCQDPT2[9]/SA[9]-CASSCF(11,9) method was used with a reference space spanned by 9 CASCI wavefunctions obtained through CASSCF-SA to ensure all states experimentally

accessible were modelled. Additionally, the first $^2n\pi^*$ resonance was calculated by expanding this active space to include 2 n-orbitals using the XMCQDPT2[7]/SA(7)-CASSCF(13,11) method. The effective Hamiltonian was then modified to average over only the D_0 and D_{1n} states within the XMCQDPT2[2]/SA(2)-CASSCF(13,11) method. All XMCQDPT2 calculations used the (aug)-cc-pVTZ basis set, where the augmented function was only affixed to the oxygen atoms of the nitro-group.

Additional calculations to determine the binding energy of the dipole bound state were carried out using XMCQDPT2 and EOM-EA-CCSD. The C_{2v} symmetry of nitrobenzene was used in all dipole bound state calculations. Details of the general methodology for the calculation of non-valence states is given in Section 3.7.1 A more detailed explanation is offered in the section below, alongside results from both methods.

Additional exploration of the resonance energy landscapes and the binding energy of the dipole bound state using XMCQDPT2 were carried out at Moscow State University by Dr Anastasia V. Bochenkova and Anton Boichenko.

5.11.3 Comparison of 2D Photoelectron and Electron Energy Loss Spectra

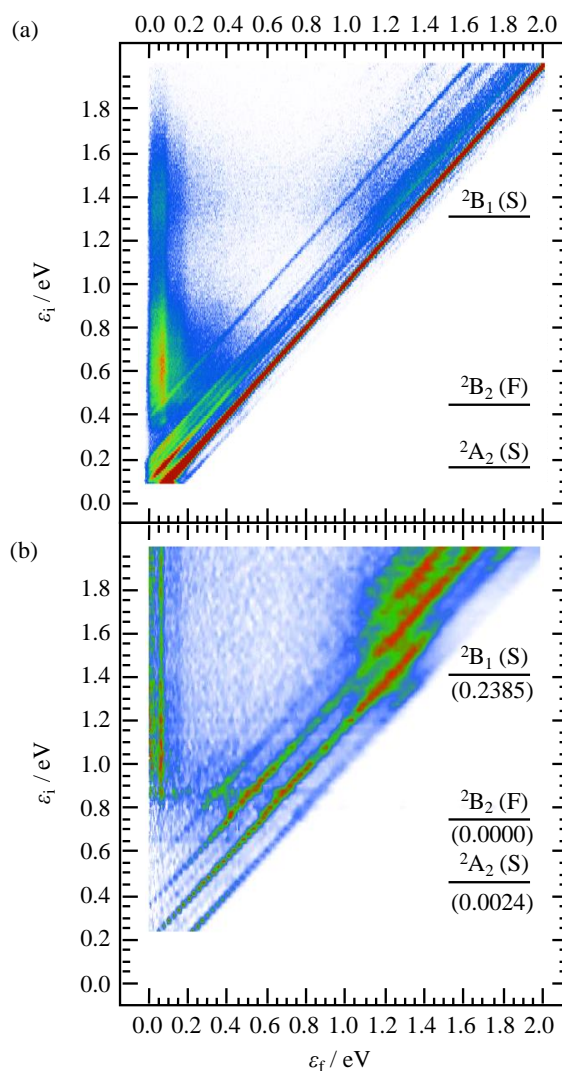


Figure 49 2D photoelectron and electron energy loss spectra of the nitrobenzene anion, (a) and (b), respectively. Each spectrum in the PE plot has been normalised to its total integrated signal.

In 2D EEL spectroscopy, the kinetic energy of the outgoing electron (ϵ_{out}) is measured as a function of an incoming electron (ϵ_{in}) impacting on NB. In 2D PE spectroscopy, NB^- is photodetached and the outgoing electron kinetic energy, equivalent to ϵ_{out} , is measured as a function of photon energy, $h\nu$. The 2D PE and 2D EEL spectra for NB are shown in Figure 49(a) and (b), respectively. To aid comparison between the two, we have plotted the 2D PE spectra as a function of ϵ_{in} : analogy can be drawn between $h\nu$ and ϵ_{in} by recognising that the photon accesses the continuum at an energy above the adiabatic electron affinity (AEA)

defined as $\varepsilon_{\text{in}} = h\nu - \text{AEA}$. From the PE spectra, $\text{AEA} = 0.95$ eV. The PE spectra have been normalized to total integrated signal levels to emphasis spectral changes as a function of excitation energy. The key features shown in Figure 49 are diagonal features with $\varepsilon_{\text{out}} = \varepsilon_{\text{in}}$ and $\varepsilon_{\text{out}} = \varepsilon_{\text{in}} - \varepsilon_{\text{vib}}$, where ε_{vib} is the energy of a vibrational mode excited in the neutral. In the 2D PE spectrum, these diagonal features correspond to direct detachment, whereby the electron is photodetached from the ground state of NB^- to form the ground state of the neutral. The intensity profile of specific levels in the neutral defined by ε_{vib} is determined by the Franck-Condon factors. In the 2D EEL spectrum, the bright $\varepsilon_{\text{out}} = \varepsilon_{\text{in}}$ diagonal feature arises from elastic scattering, with weaker transitions leading to vibrational excitation of the neutral (with ε_{vib}).

Both 2D PE and 2D EEL spectroscopy are sensitive to the presence of resonances. These appear as off-diagonal features; ε_{in} is converted to vibrational energy by nuclear motion on the resonance potential energy surfaces. In Figure 49(a), a broadening of the direct detachment feature, accompanied by a change in Franck-Condon factors, can be seen clearly at $\varepsilon_{\text{in}} > 1.3$ eV. Similar broadening of the ε_{out} spectrum can also be seen in the 2D EEL spectrum around the same ε_{in} (Figure 49 (b)).

A second off-diagonal feature is seen in both 2D spectra, with electrons emitted with $\varepsilon_{\text{out}} < 0.2$ eV. This channel only turns on at $\varepsilon_{\text{in}} > 0.8$ and $\varepsilon_{\text{in}} > 0.4$ eV for the 2D PE and 2D EEL spectrum, respectively, and persists over all higher excitation energies. More surprisingly, this channel shows structured bands that remain at constant ε_{out} despite a large increase in ε_{in} . The structure peak comprises a sharp band in the 2D PE spectra at 60 meV and a broad peak with a rough maximum at 130 meV. The 2D EEL spectrum is broadly similar with sharp peaks at ~ 50 and a broader mostly unresolved peak at ~ 140 meV.

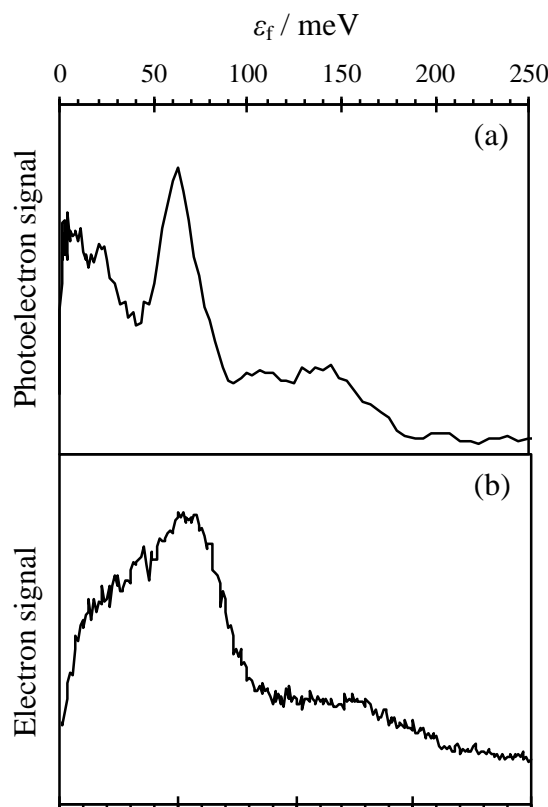


Figure 50 The structured low energy feature is shown for both the photoelectron spectra (a) and the electron energy loss spectra (b). Both plots are averaged across the range the low energy feature is present.

In Figure 50(a), the PE spectrum of the low energy feature is shown, where we have taken an average of all the spectra in the range $0.8 < \varepsilon_{\text{in}} < 2.0$. Similarly, a low energy EEL spectrum is presented in Figure 50(b), which shows overall agreement with the features seen in the PE spectrum, albeit with lower overall resolution.

5.11.4 Interpreting Structured Low Energy Electron Emission

Anions with extended π -delocalised systems often show electron emission at 0 eV as there are a number of valence resonances able to undergo nuclear dynamics and internally convert to reform the vibrationally excited ground state.^{61,62,62,63} Once in the ground state of the anion, the high excess internal energy leads to electron loss by the statistical sampling of vibrational modes above the AEA, producing an ε_{out} spectrum that peaks at 0 eV and has a

Boltzmann (exponential) distribution.^{55–58} The fact that there is structure in the low ϵ_{out} spectrum of NB therefore cannot be assigned as thermionic emission. Instead, the structured ϵ_{out} spectrum is suggestive of vibrational mode-specific electron emission. Autodetachment from a valence resonance is typically broad because of the large geometric differences between the resonance and neutral potential energy surfaces and because of nuclear dynamics occurring on the resonance surface. Therefore, it is unlikely that the observed structure arises from a valence resonance. There are a few scenarios that could potentially lead to low energy electrons with structure. Two of these are outlined below.

5.11.4.1 Evidence of a Dipole Bound State?

Mode-specific autodetachment can potentially arise from non-valence states, as suggested in recent time-resolved measurements on quinone-derivative cluster anions.³⁶ The best-known example of a non-covalent state is a dipole-bound state (DBS), in which the excess electron is loosely bound in a diffuse s-type orbital, located off the positive side of the permanent dipole moment of the neutral molecule.⁶⁴ Because of the weak interaction between the dipole-bound electron and the valence electrons of the neutral core, the potential energy surface associated with the DBS is very similar to that of the neutral molecule. Neutral NB has a large dipole moment of 4.2 D, in excess of the ~ 2.5 D required to observe such states experimentally. Indeed, Rydberg electron transfer experiments by Desfr  ois *et al.* have verified that NB^- has a DBS and they estimated a binding energy of 28 meV from Rydberg electron transfer experiments.⁶⁵ Hence, the DBS in NB^- may be a candidate for the source of the observed structure. But why should this lead to structured emission and which modes facilitate the emission?

Given that the DBS is bound by the permanent dipole moment of the neutral core, chemical intuition suggests that the modes that strongly modulate this dipole moment may be expected to lead to electron emission. These are of course the same modes as the IR active

modes in vibrational spectroscopy. Hence, one might anticipate that signatures of the IR spectrum of the neutral molecule may be apparent in this electron loss channel.

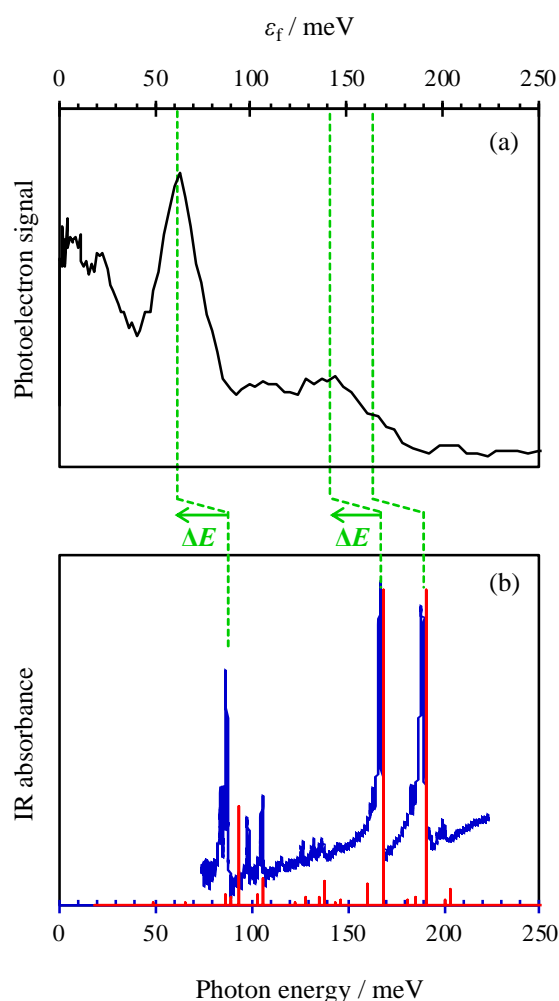


Figure 51 (a) The averaged photoelectron spectra across the low energy region and (b) the measured (blue) and calculated MP2/aug-cc-pVDZ (red) IR spectra of nitrobenzene.

Figure 51 compares the low energy PE spectrum with the IR spectrum of neutral NB. The IR spectrum is dominated by the peaks at 702, 1347 and 1521 cm^{-1} . These correspond to vibrational modes ν_4 , ν_8 and ν_9 , respectively. The ν_4 mode is a symmetric stretch of the hydrogens out of the aromatic plane and the ν_8 and ν_9 modes involve the symmetric and asymmetric stretch of the nitro group, respectively. At first glance, there is little agreement with the photoelectron spectra in Figure 51(a) and the IR spectrum in (b). However, if the IR spectrum is displaced by $\Delta E = -218 \text{ cm}^{-1}$ (-27 meV), as shown in Figure 51, then a clear

correlation can be seen between the dominant features of the electron emission spectra and IR spectrum. Specifically, the ν_4 mode aligns well with the peak at 60 meV, whereas the broader peak at ~130 meV encompasses both the ν_8 and ν_9 modes, suggesting that the width of this feature in the electron emission spectra contains both modes. However, there is also some signal at ~110 meV which is not reproduced.

5.11.4.1.1 Calculating the DBS

NB was specifically chosen as a model system because it is a relatively simple molecule that has a rich electronic structure including non-valence states and valence resonances, to which high-level theory can be applied. Previously XMCQDPT2 valence VEEs have shown excellent agreement with experimental values^{63,66} and so this method has been applied here to calculation of the binding energy of the dipole bound state for the first time.

Details of the general procedure for calculation of a dipole bound state are given in Section 3.1.7. Briefly, a ghost atom, affixed with diffuse basis functions, was placed in the centre of mass of the nitrobenzene molecule. The diffuse basis functions comprised of XsXpXd primitive Gaussian functions to represent the dipole bound state orbital and three p-character extremely diffuse orbitals that represented the continuum. The dipole bound state should be of A_1 symmetry, therefore all representative dipole bound state orbitals included in the active space were of this symmetry. At least one of the ‘continuum’ orbitals was also included in the active space, as the binding energy of the dipole bound state was found through comparison of the relative energies of the continuum and dipole bound states.

Method	Basis Set	Active space beside $\pi\pi^*$	DBS BE / meV	VDE / eV
XMCQDPT2[4]/ SA(4)-CASSCF(11,11)	(aug)*-cc-pVTZ+3s3p	IP+DBS	-17	0.61
XMCQDPT2[4]/ SA(4)-CASSCF(11,11)	(aug)*-cc-pVTZ+4s4p	IP+DBS	-2.9	0.61
XMCQDPT2[4]/ SA(4)-CASSCF(11,11)	(aug)*-cc-pVTZ+5s5p	IP+DBS	0.5	0.61
XMCQDPT2[4]/ SA(4)-CASSCF(11,11)	(aug)*-cc-pVTZ+6s6p	IP+DBS	4.6	0.61
XMCQDPT2[5]/ SA(5)-CASSCF(11,13)	(aug)*-cc-pVTZ+6s6p6d	3IP+DBS	6.5	0.63

Table 3 The calculated dipole bound state binding energies (DBS BE) and vertical detachment energies (VDE) changing the basis set on the ghost atom and active space. All calculations

were carried out on the neutral geometry of nitrobenzene. The valence basis set only has the augmented function on the oxygen atoms.

Table 3 shows the results of increasing the size of the basis set on the binding energy of the dipole bound state. Initially the dipole bound state was unbound, but through increasing the basis set the dipole bound state became energetically bound. Inclusion of d-functions caused non-negligible mixing of the continuum and dipole bound state orbitals, to remedy this all three of the continuum functions were included in the active space. The relative energy of the continuum with respect to the anion, VDE, is shown alongside the calculated DBS BE as a measure of how accurately the model was performing. The experimental VDE is double the calculated VDE, 1.14 and 0.61 eV, respectively. While it was possible to calculate a bound dipole bound state through improving the description of the dipole bound state orbital, it was not possible to reproduce a binding energy in agreement with previous experimental findings (~28 meV). Various parameters were changed in order to gauge if the model was missing a component in the description and to improve the description of the continuum. It was found that the geometry used in the calculation caused the biggest change to binding energy of the dipole bound state. These additional calculations were performed by Anton Boichenko at Moscow State University and are presented in Table 4 without further analysis.

Method	Geometry	Basis Set	Active space beside $\pi\pi^*$	DBS BE / meV	VDE / eV
XMCQDPT2[5]/ SA(5)-CASSCF(11,13)	Anion	(aug)*-cc-pVTZ+6s6p6d	3IP+DBS	7	0.95
XMCQDPT2[5]/ SA(5)-CASSCF(11,13)	Anion	(aug)*-cc-pVQZ+6s6p6d	3IP+DBS	7.8	1.24
XMCQDPT2[5]/ SA(5)-CASSCF(11,13)	Anion	(aug)*-cc-pVQZ+6s6p6d	2IP+2DBS	8.5	1.24
XMCQDPT2[6]/ SA(6)-CASSCF(11,14)	Anion	(aug)*-cc-pVQZ+6s6p6d	3IP+2DBS	8.7	1.17
XMCQDPT2[6]/ SA(6)-CASSCF(11,14)	DBS (neutral)	aug-cc-pVTZ+6s6p6d	3IP+2DBS	6.8	0.6

Table 4 The calculated DBS BE and VDE of nitrobenzene with respect to changing the reference geometry, active space and valence basis set. These calculations were carried out by Anton Boichenko.

The binding energy was also calculated using EOM-EA-CCSD, using the same methodology as Jordan's group.^{67,68} This method calculated a DBS BE of 33 and 47 meV, for the neutral and anion geometries, respectively.

5.11.4.2 Exploration of the Resonance Landscape

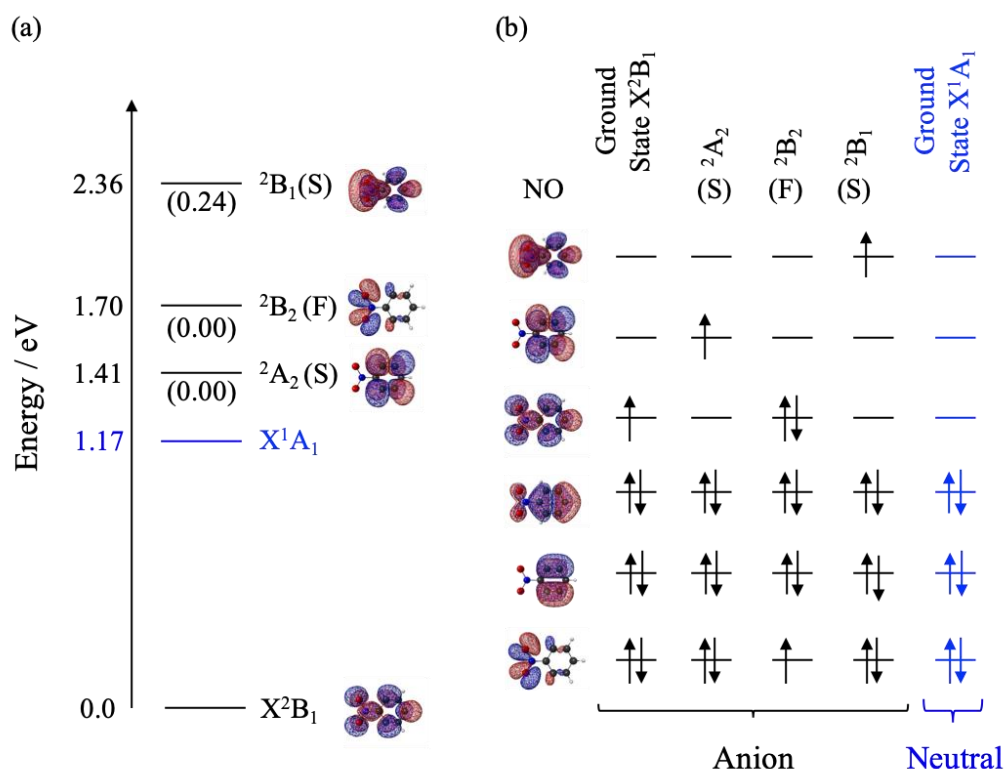


Figure 52 (a) The XMCQDPT2 calculated VEEs for the nitrobenzene anion (eV). The oscillator strengths, natural orbitals that are single occupied and character of the resonance are given alongside the symmetry label for clarity. Feshbach and shape resonances are indicated by (F) and (S), respectively. The calculated VDE is shown in blue. The full electronic configurations of all states are given in full in (b).

Preliminary XMCQDPT2 calculations confirm there are multiple valence resonances within the experimental energy range probed, Figure 52. The energies of the anion resonances are included in Figure 49(a) and (b) in the equilibrium anion and neutral geometry, respectively. Two π^* -resonances are calculated to lie at $\epsilon_{in} = 0.46$ and 1.41 eV (based on VEE = 1.41 and 2.36 eV, respectively) for the anion geometry, as probed in the 2D PE spectrum. The same two resonances lie at $\epsilon_{in} = 0.16$ and 1.31 eV (VEE = 0.81 and 1.96 eV, respectively)

for the anion in the neutral geometry, as probed in the 2D EEL spectrum. Both π^* -resonances are of shape type with respect to the neutral X^1A_1 ground state. The broadening observed in both 2D spectra is associated with the 2B_1 state, which has a considerable oscillator strength. The 2B_2 resonance is optically dark and is not apparent in the 2D spectra. Additionally, a 2B_2 Feshbach resonance was calculated by considering the $^2n\pi^*$ excited states. The onset of this resonance is found to be at $\epsilon_{in} = 0.75$ eV (VEE = 1.70 eV) and 0.18 eV (VEE = 0.83 eV) for the anion and neutral geometries as probed in the 2D PE and 2D EEL spectrum, respectively. While this electronic transition is symmetry forbidden, B_1 and B_2 modes, out of plane and in plane, respectively, make this transition vibronically allowed. The location of this resonance is in good agreement with the onset of the low energy electron loss channel. Hence, it appears that the low energy electron emission occurs from a state mediated by the initial excitation of resonances, be it by photoexcitation or electron impact.

5.11.5 Mode-Specific Vibrational Autodetachment

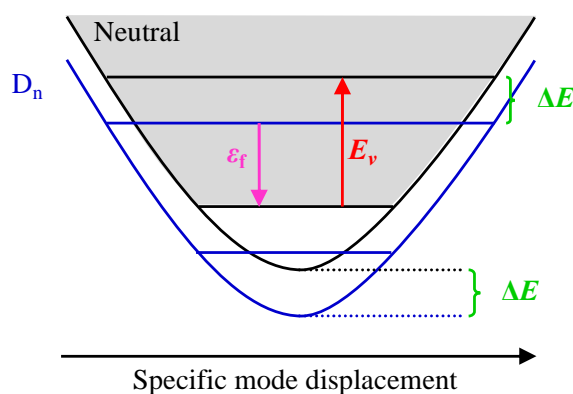


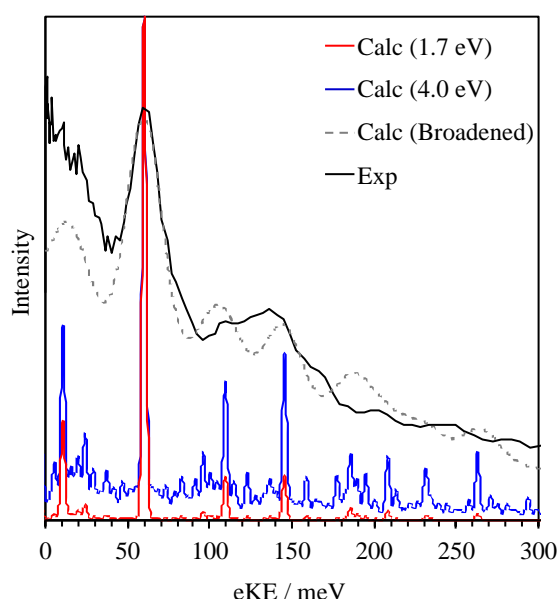
Figure 53 Schematic showing the proposed mechanism for mode facilitated electron loss from an excited state of the anion. The potential energy surface is shown as a blue curve, and that of the neutral ground state as black. The continuum is represented by the shaded grey. The displacement between the two surfaces is equal to the binding energy of the excited state.

The structure in the low energy PE spectrum suggests that electron emission is mediated by the specific modes of the neutral. This could be consistent with IR-mode specific emission from a DBS. However, it could also be compatible with electron emission from a valence state that lies close to the neutral and has a potential energy surface that is very similar to that of the neutral. The propensity rule associated with vibrational autodetachment from an anion excited state is to lose one quantum of vibrational energy, $\Delta v = -1$, in going from the excited state to the neutral.⁶⁹ As shown schematically in Figure 53, this vibrational autodetachment (in a harmonic picture) will then lead to specific electron emission energies that equal the vibrational frequency (*i.e.* $\Delta E = h\nu_e(v + 1) - h\nu_e(v) = h\nu_e$), but offset by the binding energy of the state autodetached from.

The proposed mechanism accounts for mode-specific vibrational autodetachment from either the DBS or a valence resonance, either of which can be formed following initial excitation of the D_{1n} state. However, nonadiabatic coupling of the final excited state of the anion to the neutral ground state must be large to leave the photoelectron signature observed. Let us first consider the coupling of a non-valence DBS to a valence ground state.

For there to be non-zero coupling, the vibrational mode must be of A_1 symmetry, as the DBS state (and hence the corresponding continuum wavefunction) is totally symmetric (A_1). The DBS is bound by the dipole moment of the neutral core, along the molecular C_2 (z) axis, therefore any changes along this axis will modulate the binding energy of the DBS. The most active IR modes, ν_4 , ν_8 and ν_9 , are of B_1 , A_1 and B_2 symmetry, respectively. Displacement along these modes corresponds to changes of the dipole moment along the x (B_1), z (A_1), and y (B_2) axes, respectively. It is expected that only the ν_8 mode, corresponding to CN symmetric stretch, would modulate the DBS binding energy and have a non-zero nonadiabatic coupling. This is supported by the finding of calculations performed by Dr Anastasia V. Bochenkova, which confirmed negligible couplings for only the ν_8 mode. Assignment of the ν_4 , ν_8 and ν_9 IR

modes to the structure seen at low energy in the PE spectra, Figure 51, attributes the highest intensity peak at 60 meV to vibrational autodetachment from the ν_4 (B_1) mode. Following the



symmetry argument outlined above, the B_1 mode is not expected to be the most active autodetachment mode from the DBS. Indeed, vibrational autodetachment from the DBS should yield only a peak corresponding to loss from the ν_8 mode at $167 - 27 = 140$ meV. Further electronic structure calculations by Dr Anastasia V. Bochenkova suggested that vibrational autodetachment is more likely to occur from the optically dark 2A_2 state, following internal conversion from higher lying resonances, 2B_2 and 2B_1 . Population of a low-lying state by internal conversion through a conical intersection from a valence resonance has been seen in quinone-derivative anions. An optimization calculation revealed the geometries of the 2A_2 and X^1A_1 to be very similar, and indeed so are the respective potential energy curves. This can be rationalized through inspection of the natural orbitals in Figure 52. Both the 2A_2 and X^1A_1 states are formed through removal of an electron from the CN π -bonding SOMO in the X^2B_1 ground state. Therefore, relaxation from the anion geometry to the respective geometries of the 2A_2 and X^1A_1 states will involve elongation of the CN bond.

Figure 54 Simulated photoelectron spectra for autodetachment out of the 2A_2 resonance and averaged photoelectron spectra. The modelled spectra were calculated by Anastasia Bochenkova.

Simulation of the autodetachment spectrum for the $^2A_2 \rightarrow X^1A_1$ channel yields a spectrum dominated by the 0-0 transition at all excitation energies, shown in Figure 54. The different excitation energies were considered through changing the internal energy of the anion. The 0-0 transition was assigned to the dominant peak seen at 60 meV in the photoelectron spectra, while the broad peak around 140 meV is assigned to autodetachment from hot bands. The population of each mode was calculated as a function of internal energy, and it was found that the intensity of hot bands changed with increasing excitation energy. Furthermore, the simulated photoelectron spectra appear to explain a peak at even lower kinetic energy (e.g. around 10 meV). We note that some thermionic emission may be contributing to the low ϵ_{out} signal as the signal rises at very low ϵ_{out} .

The density of resonances in nitrobenzene is reflected in the complex 2D PE and EEL spectra presented in this study. While we are certain that the structured low energy electron emission arises from mode specific electron loss, confident assignment of the final anion excited state that couples to the neutral ground state remains difficult. While the DBS of the nitrobenzene anion has been calculated and provides a reasonable explanation of the low energy structured spectra, it does not account for all features seen and is inconsistent with the expected non-adiabatic coupling between the DBS and neutral continuum. The low energy electron loss channel is in more convincing agreement with vibrational autodetachment from the 2A_2 resonance, however, this is only the case for the 2D PE spectrum. The observed energetics of the 2D EEL spectra do not support proposed autodetachment from the 2A_2 resonance.

5.11.6 Conclusions

In conclusion, we have presented a detailed analysis of the origin of structure in low energy electron loss channels observed in both electron attachment and electron detachment spectroscopy. Specifically, we study this phenomenon in the nitrobenzene radical anion using 2D EEL and 2D PE spectroscopy. The structure arises from vibrational mode specific electron loss from an excited state of the anion. High-level *ab initio* calculations show the emission requires the presence of valence resonances. Through comparison of the low energy channel measured in anion PE spectroscopy with the simulated photodetachment spectra, the specific modes that participate in electron loss can be assigned. Two interpretations of the origin of the structured emission have been presented, while emission from the 2A_2 state, formed following internal conversion from higher lying resonances, is in excellent agreement with the PE spectra, the energetics measured by the EEL experiment contradict this interpretation. Our preliminary results demonstrate the invaluable additional insight that can be gained through complimentary spectroscopic techniques, and the caution one must exhibit in interpretation of indirect PE signal in complex molecules.

5.12 Probing the Dipole Bound State of a Novel Organic Anion

5.12.1 Introduction

Non-valence electronic states of anions represent an important mode for electron binding, which is fundamentally different to that of typical valence anions.^{70–73} In these, the excess electron is weakly bound by long-range charge-dipole, -quadrupole, or correlation interactions. As a result, the non-valence orbital is very diffuse and localised away from the nuclear framework of the molecule. This is in stark contrast with valence-bound anions where the excess electron resides in molecular orbitals located on the molecular framework. The most studied non-valence anionic state is a dipole-bound state (DBS) in which the permanent dipole moment of the neutral is sufficient (> 2 Debye) to hold the excess electron in a sigma-type

orbital.⁷⁴ While DBSs have been observed in many systems, either as ground or excited states, it is challenging to probe these states experimentally using PE spectroscopy. The difficulties arise from the presence of valence excited states that are able to outcompete formation and autodetachment from a non-valence state. Here, we explore the binding of a DBS in a specifically synthesised small molecule with a permanent dipole moment sufficient to host a DBS, and with no energetically close valence excited states. Small molecules are useful as they are tractable by high level electronic structure calculations.

Exotic anions can be made *in situ* in molecular beam, in electrospray ionisation processes, or by collision-induced dissociation.⁷⁵ While it is well-known that ESI can lead to reactions and these ideas have been exploited in mass-spectrometry, the use of such reactivity has – to the best of our knowledge – not been exploited to generate anions with specific properties to be probed by spectroscopy. Here we generate an ESI-synthesised organic compound with a large dipole-moment that we probe by photoelectron spectroscopy and model using a complementary computational toolkit. We determine the structure of the compound through analysis photoelectron spectra and angular distributions. Further, we probe the DBS of the anion using 2D photoelectron spectroscopy and show a novel means of how this method can be used to determine the binding energy of the DBS. Using this interpretation, we calculate the binding energy of DBS to be ~30 meV.

5.12.2 Methodology

The details of the experiment can be found in Section 3.1. Briefly, anions were produced by ESI of ~1 mM solution of tetracyanoethylene (TCNE) in methanol and acetonitrile.

All calculations were carried out using the QChem 5.0 computational package.³⁵ Initial calculations of the neutral and anion ground states geometries of three mass-degenerate isomers were optimized using CAM-B3LYP/aug-cc-pVDZ level of theory. The geometries obtained

were verified to be global minimum energy structures by vibrational analysis. All energetics were corrected for zero-point energy. The photoelectron spectrum at 300 K was simulated using the ezSpectrum v3.⁷⁶ A rigid shift was applied to the vibrational origins of all the bands to align with experimental values.

Additional EOM-IP-CCSD calculations were used to obtain Dyson Orbitals. Dyson orbitals were used to model the direct detachment channels for the anion using the ezDyson v4.⁷⁷ EOM-EE-CCSD calculations were performed to find the VEEs of the anion excited states.

5.12.3 Gas-phase Synthetic Chemistry

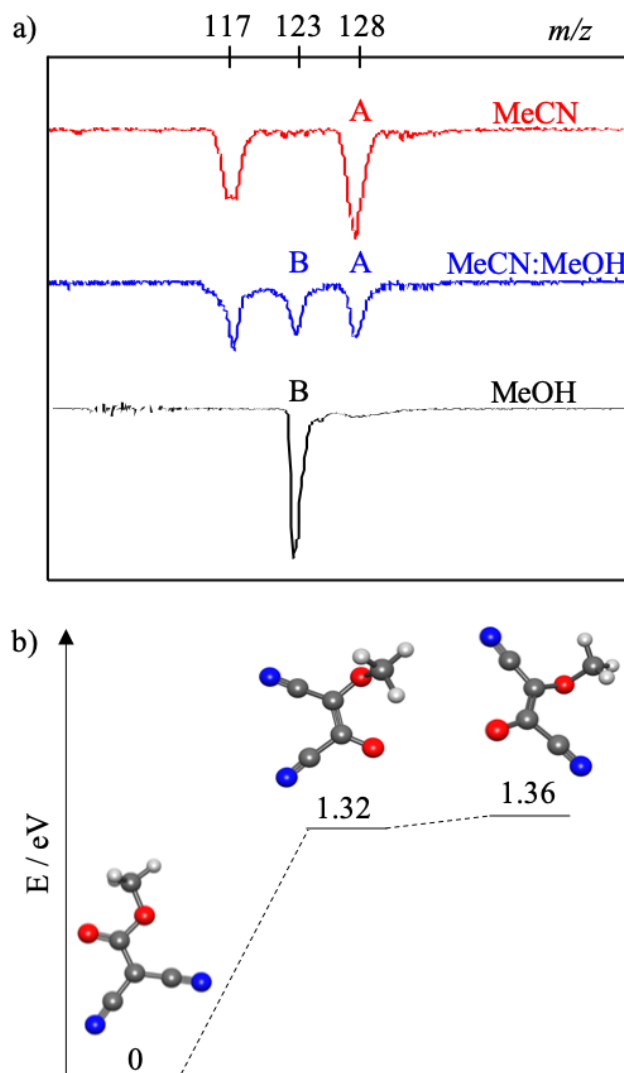


Figure 55 (a) The TOF mass spectrum of TCNE cosprayed in pure acetonitrile (MeCN), acetonitrile and methanol, and pure methanol (MeOH), shown in red, blue and black, respectively. Peak A corresponds to TCNE⁻ and peak B to the product methyl-2,2-dicyanoacetate (MDCA⁻). (b) Relative energies of the three isomers of the product formed following ESI. Geometric optimisations were carried out using CAM-B3LYP/aug-cc-pVDZ and were verified to be global minimum energy structures by vibrational analysis.

Figure 55(a) shows the TOF mass spectra for TCNE sprayed in pure acetonitrile, a 1:1 acetonitrile:methanol mixture and pure methanol, respectively. TCNE⁻ has a mass m/z = 128 amu and is clearly seen when sprayed in pure acetonitrile. When ESI is performed in the acetonitrile:methanol mixture, additional peaks are present, while in methanol, only one peak m/z = 123 amu. The cyano-anion has been shown to be a readily formed fragment following

collisionally induced dissociation in ESI source. Although the fragment seen here is probably not formed by this route, the mass difference corresponds to the loss of two cyano groups from TCNE and their substitution with two oxygens and a methyl group, forming hydrogen cyanide as a by-product. Apparently, the reaction is very facile and proceeds with almost unit efficiency within our experiment.

While the mass provides a chemical formula for the ESI-synthesised compound, in the present case, there are three isomers. The two cyano groups can be substituted on a single carbon or one on each carbon, with the latter having a cis and trans isomer. According to DFT calculations (Figure 55(b)), the isomer formed from substitution of the cyano groups on the same carbon, methyl-2,2-dicyanoacetate anion (MDCA^-), is the most energetically stable. The other two geometric isomers lie more than 1.3 eV higher in energy. This large difference in relative energies between MDCA^- and the other two isomers means that even at 300 K, the contribution of these isomers to the total anion packet at $m/z = 123$ amu is expected to be negligible. This conclusion appears to also be supported by the photoelectron imaging results below.

Figure 56 shows the photoelectron spectrum of MDCA^- taken at $h\nu = 4.20$ eV. From the PE spectra, the adiabatic detachment energy (ADE) and vertical detachment energy (VDE) of the anion can be determined. The ADE was found to be 3.60 ± 0.10 eV and the VDE 3.77 ± 0.05 eV. Both are in excellent agreement with calculated values: DFT calculations predict values of 3.76 and 3.91 eV for the ADE and VDE, respectively. The higher-level EOM-IP-CCSD calculation predicted a VDE of 3.81 eV. The ADE and VDE of the other two isomers are 3.27 and 3.72 eV, and 3.15 and 3.69 eV for the cis and trans isomers, respectively, calculated at CAM-B3LYP/aug-cc-pVDZ.

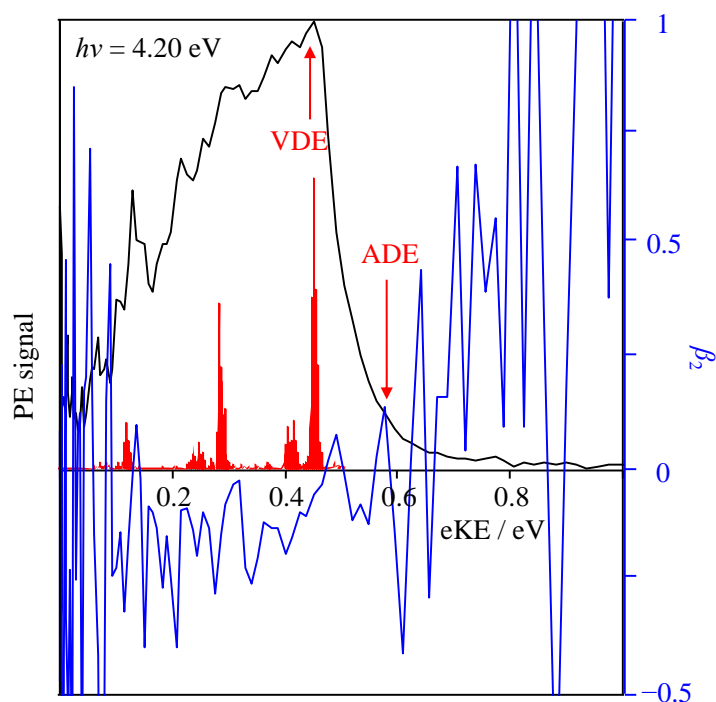


Figure 56 PE spectrum of MDCA^- at $h\nu = 4.2$ eV with the corresponding PE angular distributions superimposed, shown as black and blue lines, respectively. The PE signatures of the physical quantities of the adiabatic and vertical detachment energies, ADE and VDE, are indicated by the red arrows on the PE spectrum. The Franck-Condon envelope, calculated using ezSpectrum v3 at 300 K, is shown as a red stick spectrum.

In addition to the above energetic arguments, further support for the assignment can be gained from the PADs, which contain complementary information about the electronic structure of the system studied.^{63,78,79} The experimentally determined anisotropy parameter, β_2 , is shown alongside the PE spectrum in Figure 56, determined by averaging the β_2 values across the highest intensity region of the direct detachment peak. Over the kinetic energy range in which there is meaningful photoelectron signal, the PADs have broadly negative values of β_2 .

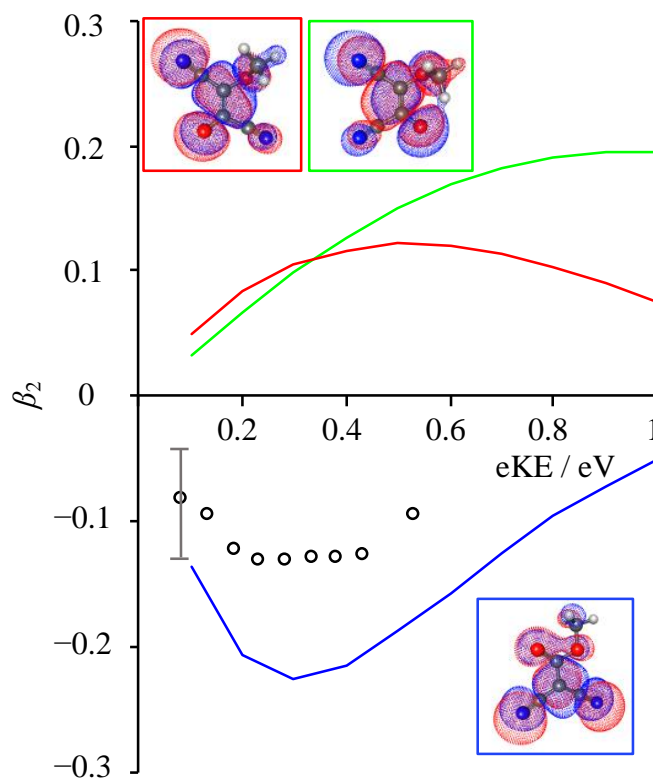


Figure 57 Plot of the experimental (circles) and computed (solid lines) β_2 parameters as a function of eKE for the direct detachment channel of the three isomers of the ESI product. The lowest energy isomer, MDCA⁻, is shown in blue, while the cis- and trans-isomers are shown in green and red respectively. The relevant Dyson orbitals are inset and follow the same colour scheme.

The calculated PADs of the three isomers are shown in Figure 57. The higher energy cis- and trans-isomers both have broadly positive values of β_2 over the experimental energy range. In contrast, MDCA⁻ shows negative β_2 values in the same energetic range in reasonable agreement with the experimental trends in PADs. In the present case, the PADs are a sensitive diagnostic of structure, as changes to positions of functional groups cause drastic changes to the electronic structure that directly determine the Dyson orbital.⁷⁸ Negative values of β_2 are broadly interpreted to arise from photodetachment from a molecular orbital with π -character. From simple inspection of the Dyson orbitals in Figure 57, it is not obvious why only one of the three isomers have negative computed PADs. All three isomers appear to have Dyson orbitals of predominantly π -character. However, consideration of the geometries of the isomers

gives insight into the physical origin of these values. Only the MDCA anion has a planar geometry, the methoxy groups are rotated out of the plane in the cis- and trans-isomers. PADs have previously been demonstrated to be extremely sensitive to the rotation of a substituent out of the π -plane. The modelled PADs for two conformers of para-ethyl phenolate demonstrated the sensitivity of PADs to subtle changes in geometry that introduce even partial s- or σ -mixing in the Dyson orbital.⁷⁸ Taken together, the relative energies, photoelectron spectra and PADs provide a definitive assignment of the experimentally probed isomer.

5.12.4 Evidence of a Dipole Bound State?

Figure 58 shows a waterfall plot of the photoelectron spectra taken for MDCA⁻ over a range of the photon energies, $3.70 \leq h\nu \leq 4.35$ eV. The kinetic energy of the dominant peak at $h\nu = 4.35$ eV decreases proportional to the decrease in photon energy and ultimately can no longer be distinguished for $h\nu < 3.80$ eV. Photoelectron features that show such linear dependence on photon energy arise from direct photodetachment, in this case corresponding to photoelectron loss from the ground state of the anion to form the ground state of the neutral MDCA.

In addition to the direct detachment channel, there are a number of peaks apparent at low kinetic energy that do not show a shift in energy despite the varying photon energy. From Figure 58, it is apparent that the low energy part of the photoelectron spectrum does not bear a resemblance of a statistical (unstructured Boltzmann distribution) process as there are clear peaks in the spectrum at kinetic energies of 14, 66 and 126 meV. However, these peaks do not appear all at once and successively higher lying peaks become apparent at higher photon energies.

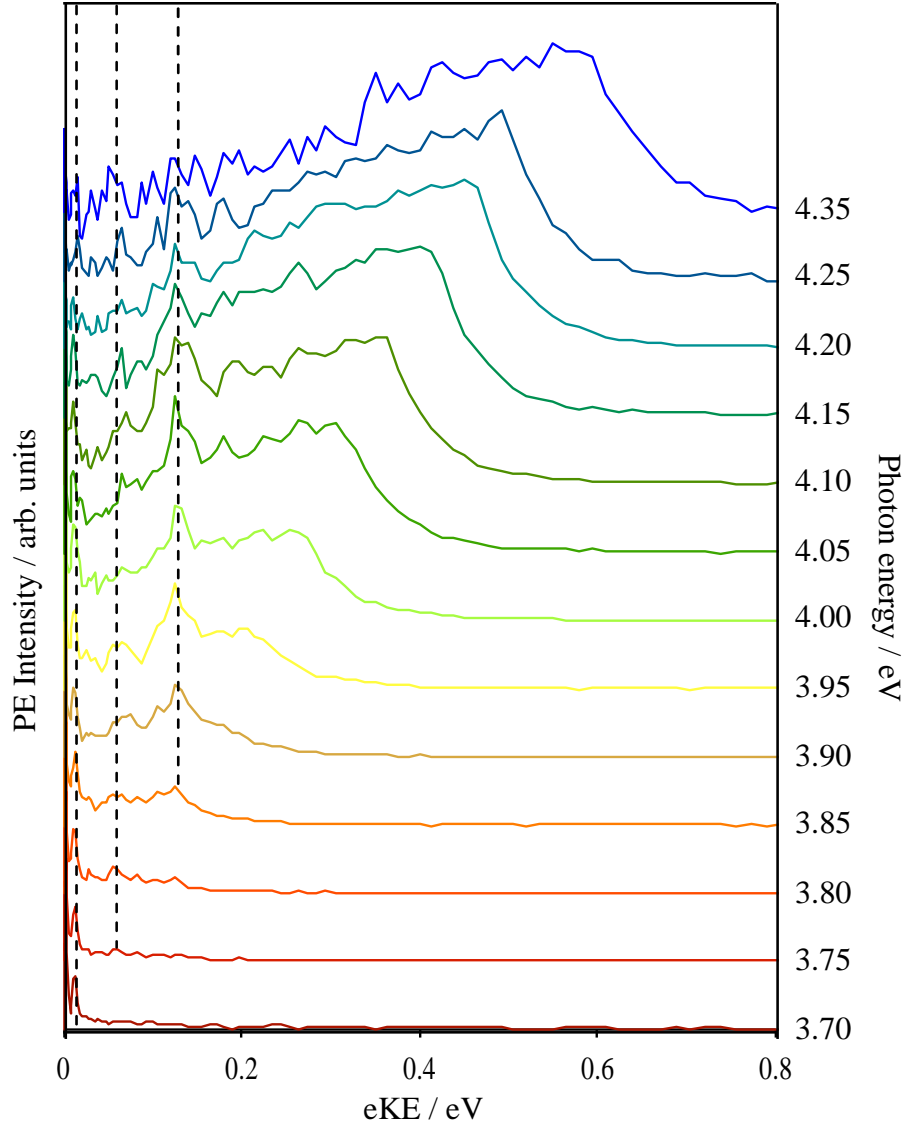


Figure 58 PE spectra of the MDCA⁻ as a function of increasing photon energy. Low energy structured features that remain static in eKE space are highlighted.

From Figure 58, the spectrum at $h\nu = 3.70$ eV shows only evidence of the peak at 14 meV. As the photon energy increases, we begin to see electron emission occur from the second (66 meV) and third (126 meV) peaks at $h\nu = 3.75$ and 3.80 eV, respectively. These channels remain visible at most $h\nu$ but disappear at higher $h\nu$, with the 14 meV peak becoming indistinguishable at $h\nu \sim 4.20$ eV, followed by the peak at 66 meV at $h\nu \sim 4.25$ eV and finally the peak at 124 meV at $h\nu \sim 4.35$ eV. Hence, there is a limited photon energy window over which the specific low-energy peaks are visible.

Peaks at constant kinetic energy have been observed previously and assigned to autodetachment from resonances.^{2,66,80} Here, the fact that the peaks are narrow is suggestive of mode-specific vibrational autodetachment, which is common in the autodetachment from non-valence states. Vibronic structure could also be seen in weakly-bound anionic clusters, where specific modes of the cluster essentially “shake” the non-valence electron off the cluster.³⁶ In MDCA, the calculated dipole-moment (4.7 D) implies that a DBS will exist. To probe whether a mechanism involving valence to non-valence transitions is operable in MDCA, we have performed excited state calculations on the anion. These show that there are no excited states or resonances in the experimental range over which electron loss from modes of the DBS occur. The lowest-lying resonance has a calculated VEE of 4.35 eV with an oscillator strength of 8.5×10^{-5} . The observation of the vibronic structure at photon energies as low as $h\nu = 3.8$ eV is inconsistent with the calculated energy of the valence resonances and, therefore, the route to mode-specific electron loss from a DBS is not via such a process. Instead, the DBS could be directly photoexcited.

Even though direct excitation of a DBS is expected to have a low oscillator strength because of the poor overlap between valence and non-valence orbitals, direct excitation has been clearly observed in many cases.^{81–85} In particular, mode-specific vibrational autodetachment has been accurately probed following resonant excitation using cryo-slow electron velocity map imaging as shown on a number of DBS and more recently a quadrupole-bound state by the Wang group.^{86–88} Because the potential energy surface of the non-valence state and the neutral final state are essentially parallel, the vibrational modes resonantly excited in the DBS are to be similar to those in the neutral upon photodetachment and the Franck-Condon factors between the DBS and the final neutral states are highly diagonal. As a consequence, vibrational autodetachment of the DBS to the corresponding levels of the neutral tend to obey the $\Delta v = -1$ propensity rule.⁶⁹ Moreover, the rate of vibrational autodetachment is

sensitive to the specific mode and Simons has provided the essential theoretical framework in which the nonadiabatic coupling can be calculated. In a zeroth-order picture, it is those modes that are strongly coupled to the non-valence that are facile in shaking off the electron. For a DBS, these are the modes that strongly modulate the dipole-moment of the neutral core – i.e. the IR active modes of the neutral. The strong coupling between the IR active modes and the DBS have been clearly shown in direct photodetachment from dipole-bound anions that show the IR active vibronic peaks in the photoelectron spectra.

Based on the above considerations, we may anticipate that IR active modes of MDCA may be apparent in the photoelectron spectrum. Initial photoexcitation populates all the vibrational levels in the DBS with good Franck-Condon overlap between the initial anion and the neutral. This should lead to a broad spectrum as indicated by the direct detachment (Figure 56) on which are superimposed autodetachment of the specific IR-active modes. As the DBS and neutral states are essentially parallel, direct excitation of the DBS vibrational levels will follow that of the neutral Franck-Condon envelope. That is to say that once the direct detachment leads to photoelectrons with significant kinetic energy, then we do not expect to be able to photoexcite the DBS. This is in agreement with Figure 58 which shows how the vibrational levels appear only when sufficient photon energy is present to directly excite them and that they subsequently disappear because the photon energy is above those vibrational levels of the DBS for which there is good overlap.

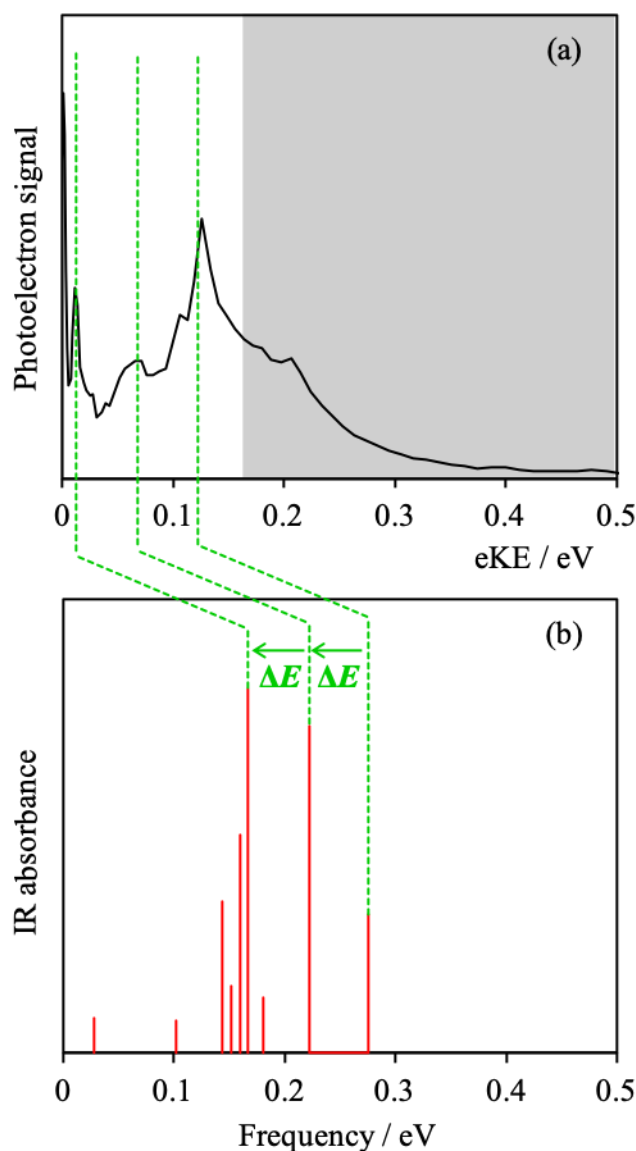


Figure 59 (a) The averaged photoelectron spectra across the low energy region and (b) the calculated IR spectra of MDCA. The grey shaded region in the PE spectra (a) denotes signal from direct detachment.

The mechanism described above would lead to peaks in the photoelectron spectrum corresponding to the IR-active modes, but red-shifted by the binding energy of the DBS (see Section 5.11.4.1). To the best of our knowledge there is no experimental IR spectrum recorded for MDCA, however, it has previously been shown that the calculated vibrational spectra provide reasonable agreement with experiment (Section 5.11.4.1). Indeed, there are similarities seen between the calculated IR spectrum of MDCA and the low energy structured electron loss

channel, shown in Figure 59. When offsetting the energy of the calculated spectra, the three main vibrational modes correlate well with the observed peaks in the photoelectron spectra. It should be noted that, unlike the previous nitrobenzene case, MDCA does not have symmetry restrictions. As MDCA does not have symmetry governing non-adiabatic coupling of the DBS and neutral ground state, in principle any IR active modes may be able to have non-zero couplings. The difference in energy between the photoelectron spectra and the vibrational spectrum corresponds to the offset in energy between the potential energy surfaces of the DBS and the neutral ground state, which is equivalent therefore to the binding energy of the DBS. Following this method, we determine a binding energy of ~30 meV for the dipole bond excited state of MDCA⁻.

As an aside, signatures of IR modes have also been seen in the direct photodetachment from DBS or non-valence states more generally. Bailey *et al.* observed weak redshifted features of the direct PE spectrum of the dipole-bound anion CH₃CN⁻, where the shifts amounted to the vibrational frequencies of the IR modes of CH₃CN.⁸⁹ Their appearance was attributed to vibrational modes of the neutral that are strongly coupled to the non-valence state – i.e. IR active modes. Similar features have recently been observed in the non-valence correlation-bound state of C₆F₆⁻, where both IR and Raman modes could be strongly coupled.⁹⁰ However, while this process similarly is based on non-adiabatic coupling between the dipole-bound orbital and specific vibrations, the mechanism presented here fundamentally differs as it is an autodetachment rather than photodetachment process.

The above proposed scheme is a general feature of anion photoelectron spectroscopy near threshold as long as the neutral has a sufficient dipole-moment (or multipole and correlation energy). Surprisingly, however, to the best of our knowledge, these features have not been explicitly observed or explained in a clear picture. There may be several reasons for this. Firstly, typical anion photoelectron spectroscopy is not performed near threshold because

(i) detachment cross sections are small and (ii) the entire Franck-Condon envelope may not be apparent. With the application of SEVI, threshold effects have of course been seen and most notable exploited by the Wang group.^{83,86,88,91–93} Secondly, it is only through 2D photoelectron spectroscopy that such peaks stand out. Thirdly, resonant excitation cross sections to the DBS are typically small compared to direct detachment. In the present case, we appear to have a relatively large excitation cross section for the DBS, which may be a consequence of the large-dipole moment that binds the DBS more strongly leading to better overlap between the valence and non-valence orbitals.

5.12.5 Conclusions

In conclusion, we present a novel organic anion designed to have a large dipole moment, synthesized through solvent dependent electrospray ionisation source. Through photoelectron imaging we assign its structure and extract the intrinsic physical properties of the anion, and model them using *ab initio* methods. We propose an interpretation of the low energy structured emission consistent mode specific electron emission, with a new mechanism for the formation of a DBS.

5.13 Section C Conclusions and Outlook

This section presented three studies in which the importance of non-valence states has been investigated, through PE spectroscopy and quantum chemistry calculations. The first of the studies presented a computational investigation of the strength of the anion- π bond, while the second two studies focused on investigating the prevalence of dipole bound states in anions.

The anion- π bond study, Section 5.10, laid the foundation for understanding the components of this non-valence bond. Further computational work is underway and there are plans to explore the anion- π bond with complementary experiments.

The second study, Section 5.11, used 2D photoelectron spectroscopy and 2D electron energy loss to probe the electronic structure and dynamics of the nitrobenzene anion. The photoelectron signatures were unraveled using high-level quantum chemistry calculations. The results of the XMCQDPT2 calculations allowed interpretation of the structure low energy electron loss channel observed in both spectroscopic techniques. It was proposed that this emission is the result of mode specific vibrational autodetachment from the 2A_2 state following internal conversion from resonances. While evidence of the dipole bound state of nitrobenzene was not seen, XMCQDPT2 was used to calculate the binding energy of a dipole bound state for the first time.

In the final study, Section 5.12, a novel organic compound was synthesized by electrospray ionization. This anion was designed to have a large dipole moment and no low-lying excited states of the anion, to allow the dipole bound state to be probed. The synthesized anion was characterized through modelling of its intrinsic physical properties with *ab initio* methods. Finally, a new mechanism was proposed to explain the low energy structured emission from the dipole bound state.

5.14 References

- 1 J. P. Rogers, C. S. Anstöter and J. R. R. Verlet, *Nat. Chem.*, 2018, **10**, 341–346.
- 2 J. P. Rogers, C. S. Anstöter and J. R. R. Verlet, *J. Phys. Chem. Lett.*, 2018, **9**, 2504–2509.
- 3 J. P. Rogers, C. S. Anstöter, J. N. Bull, B. F. E. Curchod and J. R. R. Verlet, *J. Phys. Chem. A*, 2019, **123**, 1602–1612.
- 4 E. A. Meyer, R. K. Castellano and F. Diederich, *Angew. Chem. Int. Ed.*, 2003, **42**, 1210–1250.
- 5 L. M. Salonen, M. Ellermann and F. Diederich, *Angew. Chem. Int. Ed.*, 2011, **50**, 4808–4842.
- 6 H.-J. Schneider, *Angew. Chem. Int. Ed.*, 2009, **48**, 3924–3977.
- 7 S. Mecozzi, A. P. West and D. A. Dougherty, *Proc. Natl. Acad. Sci.*, 1996, **93**, 10566–10571.
- 8 S. E. Wheeler and J. W. G. Bloom, *J. Phys. Chem. A*, 2014, **118**, 6133–6147.
- 9 C. A. Hunter and J. K. M. Sanders, *J. Am. Chem. Soc.*, 1990, **112**, 5525–5534.
- 10 J. Sunner, K. Nishizawa and P. Kebarle, *J. Phys. Chem.*, 1981, **85**, 1814–1820.
- 11 D. Quiñero, C. Garau, C. Rotger, A. Frontera, P. Ballester, A. Costa and P. M. Deyà, *Angew. Chem. Int. Ed.*, 2002, **41**, 3389–3392.
- 12 I. Alkorta, I. Rozas and J. Elguero, *J. Am. Chem. Soc.*, 2002, **124**, 8593–8598.

- 13 M. Mascal, A. Armstrong and M. D. Bartberger, *J. Am. Chem. Soc.*, 2002, **124**, 6274–6276.
- 14 A. Frontera, P. Gamez, M. Mascal, T. J. Mooibroek and J. Reedijk, *Angew. Chem. Int. Ed.*, 2011, **50**, 9564–9583.
- 15 C. Garau, A. Frontera, D. Quiñonero, P. Ballester, A. Costa and P. M. Deyà, *ChemPhysChem*, 2003, **4**, 1344–1348.
- 16 D.-X. Wang and M.-X. Wang, *J. Am. Chem. Soc.*, 2013, **135**, 892–897.
- 17 Y. Zhao, Y. Domoto, E. Orentas, C. Beuchat, D. Emery, J. Mareda, N. Sakai and S. Matile, *Angew. Chem. Int. Ed.*, 2013, **52**, 9940–9943.
- 18 M. Giese, M. Albrecht and K. Rissanen, *Chem. Commun.*, 2016, **52**, 1778–1795.
- 19 H. T. Chifotides and K. R. Dunbar, *Acc. Chem. Res.*, 2013, **46**, 894–906.
- 20 B. L. Schottel, H. T. Chifotides and K. R. Dunbar, *Chem. Soc. Rev.*, 2007, **37**, 68–83.
- 21 S. Guha and S. Saha, *J. Am. Chem. Soc.*, 2010, **132**, 17674–17677.
- 22 R. E. Dawson, A. Hennig, D. P. Weimann, D. Emery, V. Ravikumar, J. Montenegro, T. Takeuchi, S. Gabutti, M. Mayor, J. Mareda, C. A. Schalley and S. Matile, *Nat. Chem.*, 2010, **2**, 533–538.
- 23 S. Chakravarty, A. R. Ung, B. Moore, J. Shore and M. Alshamrani, *Biochemistry*, 2018, **57**, 1852–1867.
- 24 S. Guha, F. S. Goodson, L. J. Corson and S. Saha, *J. Am. Chem. Soc.*, 2012, **134**, 13679–13691.
- 25 J. C. Ma and D. A. Dougherty, *Chem. Rev.*, 1997, **97**, 1303–1324.
- 26 D. Papp, P. Rovó, I. Jákl, A. G. Császár and A. Perczel, *J. Comput. Chem.*, 2017, **38**, 1762–1773.
- 27 A. Bauzá, D. Quiñonero, P. M. Deyà and A. Frontera, *Chem. Phys. Lett.*, 2013, **567**, 60–65.
- 28 M. Göth, F. Witte, M. Quennet, P. Jungk, G. Podolan, D. Lentz, W. Hoffmann, K. Pagel, H.-U. Reissig, B. Paulus and C. A. Schalley, *Chem. – Eur. J.*, 2018, **24**, 12879–12889.
- 29 J. Zhang, B. Zhou, Z.-R. Sun and X.-B. Wang, *Phys. Chem. Chem. Phys.*, 2015, **17**, 3131–3141.
- 30 P. D. Mezei, G. I. Csonka, A. Ruzsinszky and J. Sun, *J. Chem. Theory Comput.*, 2015, **11**, 360–371.
- 31 A. T. J. B. Eppink and D. H. Parker, *Rev. Sci. Instrum.*, 1997, **68**, 3477–3484.
- 32 G. M. Roberts, J. L. Nixon, J. Lecointre, E. Wrede and J. R. R. Verlet, *Rev. Sci. Instrum.*, 2009, **80**, 053104.
- 33 P. Piccuch and M. Włoch, *J. Chem. Phys.*, 2005, **123**, 224105.
- 34 T. H. Dunning, *J. Chem. Phys.*, 1989, **90**, 1007–1023.
- 35 Y. Shao, Z. Gan, E. Epifanovsky, A. T. B. Gilbert, M. Wormit, J. Kussmann, A. W. Lange, A. Behn, J. Deng, X. Feng, D. Ghosh, M. Goldey, P. R. Horn, L. D. Jacobson, I. Kaliman, R. Z. Khaliullin, T. Kuś, A. Landau, J. Liu, E. I. Proynov, Y. M. Rhee, R. M. Richard, M. A. Rohrdanz, R. P. Steele, E. J. Sundstrom, H. L. W. III, P. M. Zimmerman, D. Zuev, B. Albrecht, E. Alguire, B. Austin, G. J. O. Beran, Y. A. Bernard, E. Berquist, K. Brandhorst, K. B. Bravaya, S. T. Brown, D. Casanova, C.-M. Chang, Y. Chen, S. H. Chien, K. D. Closser, D. L. Crittenden, M. Diedenhofen, R. A. D. Jr, H. Do, A. D. Dutoi, R. G. Edgar, S. Fatehi, L. Fusti-Molnar, A. Ghysels, A. Golubeva-Zadorozhnaya, J. Gomes, M. W. D. Hanson-Heine, P. H. P. Harbach, A. W. Hauser, E. G. Hohenstein, Z. C. Holden, T.-C. Jagau, H. Ji, B. Kaduk, K. Khistyayev, J. Kim, J. Kim, R. A. King, P. Klunzinger, D. Kosenkov, T. Kowalczyk, C. M. Krauter, K. U. Lao, A. D. Laurent, K. V. Lawler, S. V. Levchenko, C. Y. Lin, F. Liu, E. Livshits, R. C. Lochan, A. Luenser, P. Manohar, S. F. Manzer, S.-P. Mao, N. Mardirossian, A. V. Marenich, S. A. Maurer, N. J. Mayhall, E. Neuscamman, C. M. Oana, R. Olivares-Amaya, D. P. O’Neill, J. A. Parkhill, T. M. Perrine, R. Peverati, A. Prociuk, D. R. Rehn, E. Rosta, N. J. Russ, S. M. Sharada, S. Sharma, D. W. Small, A. Sodt, T. Stein, D. Stück, Y.-C. Su, A. J. W. Thom, T. Tsuchimochi, V. Vanovschi, L. Vogt, O. Vydrov, T. Wang, M. A. Watson, J. Wenzel, A. White, C. F. Williams, J. Yang, S. Yeganeh, S. R. Yost, Z.-Q. You, I. Y. Zhang, X. Zhang, Y. Zhao, B. R. Brooks, G. K. L. Chan, D. M. Chipman, C. J. Cramer, W. A. G. III, M. S. Gordon, W. J. Hehre, A. Klamt, H. F. S. III, M. W. Schmidt, C. D. Sherrill, D. G. Truhlar, A. Warshel, X. Xu, A. Aspuru-Guzik, R. Baer, A. T. Bell, N. A. Besley, J.-D. Chai, A. Dreuw, B. D. Dunietz, T. R. Furlani, S. R. Gwaltney, C.-P. Hsu, Y. Jung, J.

- Kong, D. S. Lambrecht, W. Liang, C. Ochsenfeld, V. A. Rassolov, L. V. Slipchenko, J. E. Subotnik, T. V. Voorhis, J. M. Herbert, A. I. Krylov, P. M. W. Gill and M. Head-Gordon, *Mol. Phys.*, 2015, **113**, 184–215.
- 36 J. N. Bull and J. R. R. Verlet, *Sci. Adv.*, 2017, **3**, e1603106.
- 37 S. E. Wheeler and K. N. Houk, *J. Phys. Chem. A*, 2010, **114**, 8658–8664.
- 38 C. Wang, F. N. Miros, J. Mareda, N. Sakai and S. Matile, *Angew. Chem. Int. Ed.*, 2016, **55**, 14422–14426.
- 39 M. F. Hohmann-Marriott and R. E. Blankenship, *Annu. Rev. Plant Biol.*, 2011, **62**, 515–548.
- 40 J. Jortner and M. Bixon, *Advances in Chemical Physics; Electron Transfer - From Isolated Molecules to Biomolecules*, John Wiley & Sons, 1999, vol. 106.
- 41 T. M. Figueira-Duarte and K. Müllen, *Chem. Rev.*, 2011, **111**, 7260–7314.
- 42 X. Guo, M. Baumgarten and K. Müllen, *Prog. Polym. Sci.*, 2013, **38**, 1832–1908.
- 43 G. J. Schulz, *Rev. Mod. Phys.*, 1973, **45**, 378–422.
- 44 K. D. Jordan and P. D. Burrow, *Chem. Rev.*, 1987, **87**, 557–588.
- 45 K. D. Jordan and P. D. Burrow, *Acc. Chem. Res.*, 1978, **11**, 341–348.
- 46 H. Hotop, M.-W. Ruf, M. Allan and I. I. Fabrikant, in *Advances in Atomic Molecular and Optical Physics*, 2003, vol. 49, pp. 85–216.
- 47 E. Illenberger, in *Photoionization and Photodetachment*, ed. C. Y. Ng, World Scientific, Singapore, 2000, pp. 1063–1160.
- 48 G. E. Caledonia, *Chem. Rev.*, 1975, **75**, 333–351.
- 49 E. Illenberger and B. M. Smirnov, *Phys.-Uspekhi*, 1998, **41**, 651–685.
- 50 W. C. Lineberger, *Annu. Rev. Phys. Chem.*, 2013, **64**, 21–36.
- 51 K. M. Ervin and W. C. Lineberger, in *Advances in Gas Phase Ion Chemistry*, eds. N. G. Adams and L. M. Babcock, JAI Press, Greenwich, 1992, p. 121.
- 52 M. Allan, .
- 53 A. Henley, M. E. Diveky, A. M. Patel, M. A. Parkes, J. C. Anderson and H. H. Fielding, *Phys. Chem. Chem. Phys.*, 2017, **19**, 31572–31580.
- 54 C. S. Anstöter, C. W. West, J. N. Bull and J. R. R. Verlet, *Unpublished Results*, .
- 55 A. Amrein, R. Simpson and P. Hackett, *J. Chem. Phys.*, 1991, **94**, 4663–4664.
- 56 A. Amrein, R. Simpson and P. Hackett, *J. Chem. Phys.*, 1991, **95**, 1781–1800.
- 57 B. Baguenard, J. C. Pinaré, C. Bordas and M. Broyer, *Phys. Rev. A*, 2001, **63**, 023204.
- 58 J. U. Andersen, E. Bonderup and K. Hansen, *J Phys B Mol Opt Phys*, 2002, **35**, R1–R30.
- 59 A. A. Granovsky, *J. Chem. Phys.*, 2011, **134**, 214113.
- 60 A. A. Granovsky, *Firefly v8.2.1*, <http://classic.chem.msu.su/gran/firefly/index.html>.
- 61 V. Blanchet, M. Z. Zgierski, T. Seideman and A. Stolow, *Nature*, 1999, **401**, 52–54.
- 62 C. W. West, J. N. Bull, E. Antonkov and J. R. R. Verlet, *J. Phys. Chem. A*, 2014, **118**, 11346–11354.
- 63 C. S. Anstöter, T. E. Gartmann, L. H. Stanley, A. V. Bochenkova and J. R. R. Verlet, *Phys. Chem. Chem. Phys.*, 2018, **20**, 24019–24026.
- 64 K. D. Jordan and F. Wang, *Annu. Rev. Phys. Chem.*, 2003, **54**, 367–396.
- 65 C. Desfrancois, V. Périquet, S. A. Lyapustina, T. P. Lippa, D. W. Robinson, K. H. Bowen, H. Nonaka and R. N. Compton, *J. Chem. Phys.*, 1999, **111**, 4569.
- 66 A. V. Bochenkova, C. R. S. Mooney, M. A. Parkes, J. L. Woodhouse, L. Zhang, R. Lewin, J. M. Ward, H. C. Hailes, L. H. Andersen and H. H. Fielding, *Chem Sci*, 2017, **8**, 3154–3163.
- 67 V. K. Voora, A. Kairalapova, T. Sommerfeld and K. D. Jordan, *J. Chem. Phys.*, 2017, **147**, 214114.
- 68 M. Gutowski, P. Skurski, K. D. Jordan and J. Simons, *Int. J. Quantum Chem.*, 1997, **64**, 183–191.
- 69 J. Simons, *J. Am. Chem. Soc.*, 1981, **103**, 3971–3976.
- 70 G. L. Gutsev and R. J. Bartlett, *J. Chem. Phys.*, 1996, **105**, 8785–8792.
- 71 R. N. Compton, H. S. Carman, C. Desfrancois, H. Abdoul-Carime, J. P. Schermann, J. H. Hendricks, S. A. Lyapustina and K. H. Bowen, *J. Chem. Phys.*, 1996, **105**, 3472–3478.
- 72 L. Lehr, *Science*, 1999, **284**, 635–638.
- 73 J. H. Hendricks, S. A. Lyapustina, H. L. de Clercq and K. H. Bowen, *J. Chem. Phys.*, 1998, **108**, 8–11.

- 74 K. D. Jordan and W. Luken, *J. Chem. Phys.*, 1976, **64**, 2760–2766.
- 75 S. W. Froelicher, B. S. Freiser and R. R. Squires, 1986, 2853–2862.
- 76 V. Mozhayskiy and A. I. Krylov, *ezSpectrum v3.0*, <http://iopenshell.usc.edu/downloads>
- 77 S. Gozem and A. I. Krylov, *ezDyson v4*, <http://iopenshell.usc.edu/downloads/ezdyson>.
- 78 C. S. Anstöter, C. R. Dean and J. R. R. Verlet, *J. Phys. Chem. Lett.*, 2017, **8**, 2268–2273.
- 79 J. L. Woodhouse, A. Henley, M. A. Parkes and H. H. Fielding, *J. Phys. Chem. A*, 2019, **123**, 2709–2718.
- 80 J. N. Bull, C. W. West and J. R. R. Verlet, *Phys. Chem. Chem. Phys.*, 2015, **17**, 16125–35.
- 81 P. B. Comita and J. I. Brauman, *J. Am. Chem. Soc.*, 1987, **109**, 7591–7597.
- 82 J. N. Bull, C. W. West and J. R. R. Verlet, *Chem Sci*, 2016, **7**, 5352–5361.
- 83 D.-L. Huang, H.-T. Liu, C.-G. Ning, G.-Z. Zhu and L.-S. Wang, *Chem. Sci.*, 2015, **6**, 3129–3138.
- 84 C. E. H. Dessent, J. Kim and M. A. Johnson, *Faraday Discuss.*, 2000, **115**, 395–406.
- 85 J. N. Bull, J. T. Buntine, M. S. Scholz, E. Carrascosa, L. Giacomozzi, M. H. Stockett and E. J. Bieske, *Faraday Discuss.*, 2019, **217**, 34–46.
- 86 D.-L. Huang, H.-T. Liu, C.-G. Ning, P. D. Dau and L.-S. Wang, *Chem. Phys.*, 2017, **482**, 374–383.
- 87 G. Z. Zhu, Y. Liu and L. S. Wang, *Phys. Rev. Lett.*, 2017, **119**, 1–5.
- 88 H. T. Liu, C. G. Ning, D. L. Huang, P. D. Dau and L. S. Wang, *Angew. Chem. - Int. Ed.*, 2013, **52**, 8976–8979.
- 89 C. G. Bailey, C. E. H. Dessent, M. A. Johnson and K. H. Bowen, 1996.
- 90 J. P. Rogers, C. S. Anstöter and J. R. R. Verlet, *Nat. Chem.*, 2018, **10**, 341–346.
- 91 D.-L. Huang, H.-T. Liu, C.-G. Ning and L.-S. Wang, *J. Chem. Phys.*, 2015, **142**, 124309.
- 92 H.-T. Liu, C.-G. Ning, D.-L. Huang and L.-S. Wang, *Angew. Chem. Int. Ed.*, 2014, **53**, 2464–2468.
- 93 G.-Z. Zhu, L. F. Cheung, Y. Liu, C.-H. Qian and L.-S. Wang, *J. Phys. Chem. Lett.*, 2019, **10**, 4339–4344.

6 Conclusion and Outlook

This thesis has presented a number of studies that have aimed to show recent advances and new challenges in anion photoelectron imaging.

In Section A, the studies presented have shown the wealth of information that can be extracted from the photoelectron angular distributions of a molecular anion. However, there are still regimes in which this information is being lost. Most notably, it is not possible to model the photoelectron angular distributions for autodetachment channels from resonances. Within the studies presented, the photoelectron angular distributions have been demonstrated to be sensitive to the onset of resonance (see also Section A). However, if this current qualitative interpretation could be developed to be qualitative it would afford a new dimension of insight into resonances. Specifically, the ability to assign resonances based on their orbital character would be a major advantage over traditional EELS type experiments for which no such information is available. Additionally, developing methods to understand angular distributions into the time domain is desirable to build on the work begun in Section A, and work toward a fully time-resolved photoelectron imaging model.

The studies presented in Section B of the results have highlighted the benefits of the ‘bottom-up’ approach to investigating the intrinsic dynamics of complex biological molecules. When going bigger there are still some limitations, both experimentally and computationally. The three dinitrobenzene (DNB) isomers have been probed by PE spectroscopy, however even these small, ‘simple’, mixed-valence systems have complex electronic structures and dynamics. Work is ongoing to unravel the PE signatures recorded for the meta- and ortho-isomers computationally and for this reason, these experimental results were omitted from the thesis. Once the intrinsic dynamics of the para- and meta-DNB are understood, additional experiments that would build upon this project would be to incrementally add single water molecules to DNB anions to gain insight into how solvation affects the intrinsic dynamics. This

is desirable as it ties the findings of gas phase studies to the Marcus theory picture of ET in solution phase, demonstrating the importance of the ‘bottom-up’ approach. Specifically, as the donor/acceptor in the intervalence charge transfer (IVCT) are at the same energy, it is expected that a single water molecule will skew this balance. Additionally, for the delocalised cases (class III) in para- and ortho-DNB, addition of a water molecule is expected to localise the charge bringing the system to a less strongly coupled regime. These “bottom-up” studies should prove very useful to understand coupling in IVCT systems and how solvation affects the coupling. Furthermore, it would be of interest to study the ultrafast dynamics of IVCT, for which these studies lay the foundation.

Finally, Section C discussed how low energy electrons inform about resonance dynamics and non-valence states. The resolution offered at low energy suggests that these features can be generally assigned offering new insight into autodetachment dynamics. However, we have shown that one should treat this with caution as it is not immediately clear at first glance whether the dynamics are originating from valence or non-valence states. This highlights the importance of computational chemistry as a means to understand the true photophysics. Performing 2D PE spectroscopy near the detachment continuum on specifically designed molecules, with large dipole moments without extensive delocalised π -systems, should offer insight into the IR active modes of the neutral molecule. Finally, in this section, we also showed how anion- π bonds could be measured and extending this to a wide range of anions (halogens, molecular anions, and multiply charged anions) as well as different anion- π bond acceptors is likely to provide a general physical chemists understanding of the nature of this interaction. To this end, we have started to perform the required computational work on the different halogens bonded to C_6F_6 .